Development and Application of Stellar Wind Models to T Tauri Stars

Leandro J. R. Machado

Tese de Doutoramento em Astronomia

2001

Leandro José Rodrigues Machado

Development and application of stellar wind models to T Tauri stars

Departamento de Matemática Aplicada
Faculdade de Ciências da Universidade do Porto
Junho de 2001

Leandro José Rodrigues Machado

Development and application of stellar wind models to T Tauri stars

Tese submetida à Faculdade de Ciências da Universidade do Porto para obtenção do grau de Doutor em Astronomia

Departamento de Matemática Aplicada
Faculdade de Ciências da Universidade do Porto
Junho de 2001

To my wife

and

our daugther

Acknowledgements

My gratitude to Profs. Doutores M. Teresa Lago and João Lima, my thesis supervisors, for the continuous support and encouragement. It started with the opportunity of my MSc dissertation on the subject of TTS wind models, to proceed to a PhD level, in order to further develop those wind models. It continued with stimulating discussions on the results and the work to be done, and ended in the careful reading (and the many tips given) of this manuscript. It has been a privilege to work with them.

I also thank Prof. Alan Hood from the University of St. Andrews for his help and insights on the energy equation. I must also thank everyone from the Solar Theory Group of this University for their warm welcome in my stay. In particular Prof. Eric Priest, Luca dell Zanna, Jack Ireland, Robert Walsh, and my office mates David Brown, Duncan Mackay and Jason Smith.

Prof. Kanaris Tsinganos from the University of Crete is to be acknowledged for organizing the very fruitful 1998 Summer School "Dynamical MHD Phenomena, in Solar and Astrophysical Plasmas". Amongst the lecturers, I must cite Dr. Daniel Spicer from the Goddard Space Flight Center for his talks on numerical integration methods.

A word of recognition also goes to Manuel Monteiro, CAUP's system manager, for his work on improving our internal computer network. And to António Pedrosa for his tips on the XMGR graphic program, and all remaining CAUP members not yet mentioned.

The excellent work of NASA's Astrophysics Data System Abstract Service on providing on-line articles difficult to find (`http://adsabs.harvard.edu`) is acknowledged. So are the authors of the many useful (and used) LaTeX packages available at the Comprehensive TeX Archive Network - CTAN (`http://www.tex.ac.uk`), as well as the maintainers of the database.

And finally, my most special thank to my beloved wife. For everything.
Another special thank to our daughter and our parents.

Sumário

As estrelas são o constituinte mais abundante do universo visível. Desde sempre fascinaram a humanidade, e contiuam a fazê-lo. Actualmente, acredita-se que quase todos os elementos químicos, com excepção dos mais leves, foram criados no interior dos núcleos estelares, ou em explosões de novas ou supernovas. Em particular alguns elementos essenciais para a vida, como C, O ou Fe. Durante o decurso das suas vidas, as estrelas enriquecem o meio interestelar com estes e outros elementos químicos, através da perca de massa nos seus ventos. Quando as estrelas de elevada massa terminam as suas vidas numa explosão de supernova enriquecem também o meio interestelar e podem, eventualmente, despoletar a formação de estrelas em nuvens moleculares próximas.

Quase toda a vida na Terra depende da existência de uma estrela de pequena massa, da sequência principal e de meia idade: o Sol. As interpretações teóricas fundamentadas em observações mostram que existe uma classe de estrelas variáveis e muito activas, de pequena massa como o Sol, e que ainda não fazem parte da sequência principal: as estrelas T Tauri. O facto de estas estrelas possuirem massas similares à do Sol e de estarem ainda na fase de evolução para a sequência principal constituiem motivações extras, que aliadas às suas qualidades intrínsecas, tornam o seu estudo ainda mais relevante. Esse estudo pode possibilitar a visualização das condições prováveis para a formação dos sistemas planetários, e para uma melhor caracterização da evolução seguida pelo Sol.

Este trabalho começa com uma breve revisão das propriedades das estrelas T Tauri, seguindo-se uma extensa pesquisa bibliográfica das suas taxas de rotação. As taxas de rotação obtidas através da espectroscopia ($v \sin i$) ou da fotometria ($P_{\rm rot}$) são ambas usadas. Esta pesquisa bibliográfica foi motivada pelo eventual papel da força centrífuga na equação do momento que descreve os modelos de vento estelar para as estrelas T Tauri. Porém, mostrar-se-á que a força centrífuga devida à rotação estelar pode ser desprezada na equação do momento quando aplicada aos ventos das estrelas T Tauri. Três tipos pricipais de modelos de vento estelares hidrodinâmicos serão desenvolvidos. O primeiro tipo com o perfil de temperatura prescrito, o segundo possui uma equação de energia detalhada, enquanto que o terceiro é uma generalização do segundo, mas incluindo os efeitos da propagação de ondas de Alfvén.

Summary

Stars are the most abundant constituent of the visible universe. They have always fascinated mankind and continue to do so. It is now believed that almost all chemical elements, apart from the lighter ones, have been created inside the core of stars, or in novæ or supernovæ explosions, particularly some elements essential to life, such as C, O and Fe. During the course of their lives the stars enrich the interstellar medium with these and other chemical elements through mass loss in their winds. When high-mass stars end their lives in a supernova explosion they enrich the interstellar medium and, eventually, trigger star formation in nearby molecular clouds.

Almost all life on earth depends on the existence of a low-mass, main-sequence, middle age star: the sun. Observations coupled with theoretical interpretations have shown that there exists a class of very active, variable stars, of low-mass, like the sun, that have not yet reached the main-sequence: the T Tauri stars. Having mass similar to the sun's and being still evolving towards the main sequence is an extra motivation, added to their intrinsic qualities, that makes their study even more interesting since it allows the study of the probable conditions for the formation of planetary systems and to better characterize the evolution undertaken by the sun.

This work begins with a brief review of the properties of T Tauri stars, followed by an extensive bibliographic survey of their rotation rates. The rotations rates obtained through spectroscopy ($v \sin i$) or photometry ($P_{\rm rot}$) are both used. The motivation for this bibliographic survey was the eventual role of the centrifugal force on the momentum equation describing stellar wind models for the T Tauri stars, which constitute the main goal of this work. It will be shown that the centrifugal force due to stellar rotation can be neglected in the momentum equation in the case of the winds of TTS. Three main types of hydrodynamical stellar wind models will be developed. The first has a prescribed temperature profile, the second including a detailed energy equation, while the third is a generalization of the second one including the effects of Alfvén wave propagation.

Résumé

Les étoiles sont le constituant le plus abondant de l'univers visible. Elles ont fascinées l'humanité et continuent a être des objects très fascinants. La plupart des éléments chimiques, l'exception des plus légers, sont creés à l'intérieur des étoiles, or dans l'explosions de novae ou de supernovae. Ceci est aussi vrai quand on parle des éléments essentiels à la vie, comme nous la connaissons, comme par exemple les éléments C, O et Fe. Ainsi, pendant la vie des étoiles, il y a un enrichissement du milieu interstellaire avec de nouveaux éléments chimiques, produits par la perte de masse dans les vents stellaires. Quand les étoiles les plus massives finissent en supernovae, elles vont enrichir le milieu interstéllaire et, dans de certaines conditions, provoquer la formation stellaire dans les plus proches nuages moléculaires.

La vie dans la planète Terre dépend de l'éxistence d'une étoile de petite masse, qui fait partie de la séquence principale et est à moitié de son existence: le soleil. L'observation et l'interprétation théorique ont montré qu'il y a des étoiles très actives, variables, de petite masse comparable au soleil et qui ne font pas partie de la séquence principale: les étoiles T Tauri. Ces étoiles se trouvent en pleine évolution vers la séquence principale, et présentent un intérêt complémentaire, associé à des spectres caractéristiques et au fait qu'elles representent le soleil dans sa jeunesse. Ainsi l'étude de l'évolution du soleil et la propre formation du système planétaire sont faits par l'analyse des T Tauri.

Ce travail commence par un bref résumé des propriétées des étoiles T Tauri, suivi par une compilation bibliographique des taux de rotation. Les taux de rotation, obtenus en spectroscopie ($v \sin i$) ou photometrie ($P_{\rm rot}$) sont utilisés pour mieux caractériser la rotation des T Tauri. L'étude bibliographique a été motivé par l'éventuel rôle de la force centrifuge dans l'équation du moment, qui décrit les modèles de vent stellaire dans le cas des étoiles T Tauri. Cette étude a permis de démontrer que la force centrifugue causée par la rotation stellaire des étoiles T Tauri est négligeable dans le cas des modèles de vent stellaire. Trois modèles hydrodynamiques de vent stellaire ont été développés. Dans le premier groupe, la variation de température est prescrite, le deuxième cas utilise une équation d'énergie détaillée, le troisième modèle est une généralisation du deuxième avec l'inclusion de la propagation d'ondes Alfvén.

Contents

List of Tables

List of Figures

Chapter 1

Introduction

1.1 Overview of T Tauri stars

In this Chapter a concise description of the main characteristics of T Tauri stars (hereafter TTS) is presented. Particular emphasis is given to their rotation rates and their winds.

1.1.1 General characteristics

T Tauri stars are young ($<10^7$ years), low-mass stars ($<3\,M_\odot$) still evolving towards the main-sequence (MS). The in-depth study of this class of stars is very interesting and rewarding since it gives us knowledge on the conditions of formation and evolution of solar like low-mass stars, as well as hints on planetary formation. This last topic being a bonus in these days when there are more planets known to orbit other solar-type stars than planets in the solar system itself.

Alfred H. Joy (1942; 1945; 1949) was the first to define as a new class these variable stars he discovered in the Taurus-Auriga dark clouds, named after its brightest member: T Tauri.

Over the years the hypothesis that TTS are newly formed stars still evolving towards the MS has gained consistency. In his classical review Herbig (1962), presented observational evidence of their youth, namely: (1) in some of the regions with TTS their space density being 10–100 times higher than that of field stars of similar luminosity; (2) the largest number of TTS occurring in association with O and B stars; (3) in the HR-diagram the TTS being located above the MS. The results of the proper motion studies made by Herbig (1977) and by Jones and Herbig (1979) confirmed the kinematical association between TTS and the dark clouds from which they were born.

However, it must be realized that the unambiguous inclusion of a star in the TTS class is based on its spectroscopic characteristics. Following again Herbig (1962) these are:

- the hydrogen and the Ca II H & K lines in emission;
- the presence of fluorescent Fe I emission lines $\lambda\lambda$4063, 4132;
- [S II] emission lines $\lambda\lambda$4068, 4076 usually present;
- strong Li I λ6707 absorption line, when there is an absorption spectrum.

With few exceptions, namely the 'group' of isolated TTS that includes TW Hydræ (Hoff et al., 1998), the stars with such spectral characteristics are found in or around nebulosity and are variable in light.

The term T Tauri star is used to designate the pre-main sequence (PMS) low-mass optical stellar objects, as TTS have only recently become visible in the optical range, while the term young stellar object (YSO), first introduced by Strom (1972), is used for all PMS stellar objects, optically visible or not. Therefore TTS represent an important class between embedded PMS sources that can only be studied at infrared and radio wavelengths and solar-type MS stars. In fact, TTS represent the first stage of low-mass stellar evolution that can be studied at *all* wavelengths, making possible to build a clearer picture of the star and its immediate environment.

1.1.2 Rotation

The measure of the rotational velocity of stars has proven to be important in the understanding of the phenomena occurring in the interior of the stars. One of the most well known features of the rotation of MS stars is the fast rotation rates of the early type stars and the very slow rotation rates of the late type stars (Gray, 1992, for example). This difference in the rotation rate is connected with the existence of a convective envelope in late type stars. The complex motions in this outer convection zone generate a global magnetic field through the dynamo mechanism. The interaction of the stellar magnetic field with the stellar ionized wind will decelerate the star's rotation rate (Weber and Davis, 1967, for example).

A rather common spectral characteristic of TTS is the veiling, that is, the filling in of the absorption lines by an enhanced continuum originated above the photosphere and/or the blending of weak emission lines. For the TTS with most severe veiling, and consequently almost without photospheric absorption lines, it is very difficult, if not impossible, to determine the value of the projected equatorial velocity of axial rotation ($v \sin i$, where

v is the equatorial rotational velocity and i is the inclination angle between the stellar rotation axis and the line of sight). Vogel and Kuhi (1981) made the first measurements of $v \sin i$ for a large sample of PMS leading to the unexpected result that most TTS are slow rotators, with $v \sin i$ below $25\,\mathrm{km\,s^{-1}}$. The lowest value for $v \sin i$ that could be measured in this first survey was in the range 25–30 $\mathrm{km\,s^{-1}}$. Later on more sensitive surveys both of $v \sin i$ and of the photometric rotational period (P_{rot}) confirmed that TTS are indeed slow rotators.

This slow rotation rate appears to be a characteristic of TTS, whether they are classified as Classical TTS (CTTS) or Weak-line TTS (WTTS), as the results of Walter et al. (1988) indicate, although the stellar mass seems to be an important factor in the determination of the rotation rate, as suggested by Bouvier et al. (1986). In the latter sample of TTS, those with $M_\star < 1.2\,M_\odot$ rotate slower ($6\,\mathrm{km\,s^{-1}} < v \sin i < 30\,\mathrm{km\,s^{-1}}$) than higher mass TTS ($6\,\mathrm{km\,s^{-1}} < v \sin i < 70\,\mathrm{km\,s^{-1}}$).

The commonly accepted picture for stellar formation is based on the accretion of material from the molecular cloud by the protostellar core. Most, if not all, of this material comes from the surrounding rotating disk/envelope, and has high specific angular momentum. Consequently, the TTS were expected to be fast rotators. However, in general their rotation rate is well below the break-up velocity. Therefore, the angular momentum problem must have already been solved before the star reveals itself as a TTS.

1.1.3 Winds

The realization that TTS represent a stage of stellar evolution before the MS was of major importance as it allowed the confrontation between theoretical evolutionary models and observations of the ongoing process. Due to their characteristics, namely their low mass, TTS are usually considered as solar analogues just before the MS. What are the characteristics required for a star to be a solar analogue? Quoting Soderblom (1999)

> What makes a star "solar-type" is the presence of a convection zone (CZ) in the surface layers, for the CZ lies at the heart of the many fascinating phenomena that we associate with the Sun. Most of those phenomena are related to the "activity" in one form or another – sunspots, flares, the corona, etc. – and activity is an observable manifestation of the Sun's magnetic field. The magnetic field exists because of the complex circulation patterns created by the interaction of convection with rotation, especially differential rotation. This simplified description is the current paradigm for studying and understanding the behaviour of stars like the Sun.

> So the essence of "solar-typeness" is the intimate connection between rotation and activity.

The study of the TTS spectra has revealed that some of them show a classical P Cygni profile for certain emission lines (Kuhi, 1964) which clearly indicate the presence of a wind outflow from the star. The first estimates of the mass loss rate were made by Kuhi (1964) based on the modelling of the H_α P Cygni profile. Through the spectroscopic analysis of the TTS, mass loss rates between 10^{-9} and $10^{-6}\, M_\odot\, \mathrm{yr}^{-1}$ (DeCampli, 1981, for example) have been proposed.

This high mass loss rates (the solar value is only $10^{-14} M_\odot\, \mathrm{yr}^{-1}$ - Lim and White (1996), for example) were not expected for these late type and low luminosity stars. The bolometric flux is not enough to produce the inferred kinetic energy flux of the wind. The solution to this problem can be found in the magnetic activity created by a dynamo mechanism. Again using the solar analogy, the presence of a magnetic field and a convective envelope, will result in the generation of Alfvén waves. These waves could help to drive a wind with high mass loss rates. Pursuing this possibility, in Chapter 6 a wind model with the inclusion of Alfvén waves will be developed.

1.2 Brief description of this work

As seen in the previous Sections, TTS are very active and energetic stars that show clear signs for mass outflow.

The purpose of this work is to investigate the mechanism, or mechanisms, responsible for the outflows. Possible solutions to this question will be sought by developing several spherical symmetric stellar wind models.

In order to find out if the centrifugal force due to the stellar rotation is the source for the wind acceleration an extensive bibliographical survey of the TTS rotation is presented in Chapter 2. This large database is used to study the behaviour of rotation rate as function of spectral type, age, mass and classification as CTTS or WTTS.

Chapter 3 begins with a short review of the theory of ideal MHD and the oscillatory modes of a magnetized plasma, followed by a review of wind models for solar-type stars. In Chapter 4 wind models with a prescribed temperature profile are developed.

The search for possible sources of the wind driving mechanism is continued in Chapter 5 with a wind model which includes a detailed energy equation. This equation has terms due to thermal conductivity, radiative losses and a mechanical heating function. This model is generalized in Chapter 6 to include the effects of Alfvén wave propagation in

both the momentum and energy equations.

Finally, Chapter 7 is devoted to the general conclusions of this work and to future prospects.

Chapter 2

Rotation of T Tauri stars

The main goal of this work is to develop stellar wind models for T Tauri stars. Nevertheless, before starting with the physical-mathematical modelling some previous steps must be taken. The first is to choose the type of stellar wind model: a thermally driven wind, a radiation driven wind, a dust driven wind, or other. The study of the general characteristics of TTS, particularly their mass and surface temperature of 'solar-type' values, suggests that TTS' winds should be similar to the solar wind: a wind where the thermal pressure gradient and the magnetic forces play the major role, radiation pressure being almost absent.

One issue remains: the role of the centrifugal force. The sun has a very low rotational velocity ($\sim 2\,\mathrm{km\,s^{-1}}$), typical for the stars of its mass and age; therefore, as a first approach the centrifugal force may be neglected in solar wind models. In order to find out whether or not the centrifugal force should be included in TTS stellar wind models a bibliographical survey, aimed at the characterization of the rotational velocity for TTS, was undertaken.

In this survey both the photometric periods (P_{rot}) and the projected equatorial velocity ($v \sin i$) are used to better characterize the rotation of TTS. With the help of this database the behaviour of the rotation rate of TTS across the spectral sequence and in the HR-diagram are studied. For the TTS in the sample with enough parameters measured, the radii and equatorial velocity are computed. To complete the picture of the rotation rate evolution from the TTS phase until the zero-age main-sequence (ZAMS), the relevant observational properties of nearby open clusters are overviewed at the end of the Chapter.

2.1 Introduction

As mentioned in the previous Chapter, TTS were classified as a separate class of variable stars by Joy in the early forties. The evidence for their youth has built up during the following years, and eventually the quest for the rotational properties of TTS begun. Herbig (1952; 1957; 1962) was the first to measured the widths of some absorption lines of four TTS: T Tau, UX Tau (A), RY Tau and SU Aur. Although some doubts remained about the cause of the line broadening, whether it was due to the stellar rotation or not, the line widths were converted into projected equatorial velocity ($v \sin i$) of the star. His results were:

star's name	$\boldsymbol{v \sin i}$ ($\mathrm{km\,s^{-1}}$)
T Tau	20
UX Tau	20–25
RY Tau	45–50
SU Aur	65

A possible analysis of Herbig results is that both T Tau and UX Tau could be considered slow rotators and that SU Aur is a fast rotator. This analysis does not reveal much about the rotational properties of the TTS, mainly due to the very small sample size.

Another piece of evidence, although indirect, about the rotation rate of TTS was the Skumanich law: $\Omega \propto t^{-1/2}$, where Ω is the stellar rotation rate and t is the age in gigayears (Skumanich, 1972). This law was based on the solar rotation rate ($\overline{v \sin i} \sim 2\,\mathrm{km\,s^{-1}}$), the mean rotation rate for the Hyades G stars ($\overline{v \sin i} \sim 10\,\mathrm{km\,s^{-1}}$), and that for the Pleiades G stars ($\overline{v \sin i} \sim 20\,\mathrm{km\,s^{-1}}$). Being TTS younger than the Pleiades they should be faster rotators. With only four TTS with rotational velocity measurements it was impossible to confirm or reject this assumption. Nevertheless TTS were since referred as fast rotators.

The assumption that TTS were fast rotators remained until Vogel and Kuhi (1981) published the measurements of $v \sin i$ for 64 PMS stars in the NGC 2264 and the Taurus-Auriga star forming regions (SFR). This first survey revealed the unexpected result that about three quarters of the sample stars showed rotation velocities below the threshold of the survey (between 25 and $35\,\mathrm{km\,s^{-1}}$). Later more sensitive surveys corroborated this fact, and therefore it may be foreseen that the centrifugal force plays a minor role in the dynamics of a stellar wind model in TTS.

One step further towards a better knowledge of the rotation rate of young stars was the discovery by Alphenaar and van Leeuwen (1981) that some stars in the Pleiades cluster have periodic variations in several photometric bands. For most of these stars the periodic variations were interpreted as the rotational period of the star.

T Tauri stars were known to be irregular photometric variables, but later systematic and frequent observations confirmed that some TTS show periodic light variations which could be interpreted as a measure of the rotational period of the star. One interesting result of this study was the presence of a bimodality in the histogram of the rotational periods, with one peak around 2–3 days and another at 7–8 days (Attridge and Herbst, 1992).

2.2 The database

There is a large number of publications with measurements of the rotation rates for young stars. In general, they present the results of $v \sin i$ from spectroscopic observations, or of $P_{\rm rot}$, obtained from photometry, for stars of a given association or SFR. The compilation of all these dispersed measurements in a large database is very important for several reasons, namely it allows the comparison of the observational uncertainty and others which are intrinsic to each type of technique. A statistical analysis of the rotational measurements included in this database is sufficient to determine the role of the centrifugal force on the dynamics of a stellar wind model, which constituted the leading motivation to build this database. Further to that, more information about the rotation rate of the TTS and its eventual dependence on stellar parameters can also be gathered from it. The broad study of the rotation rate of TTS is the goal of this Chapter.

The stars included in the sample are mainly from the Taurus-Auriga, Orion, Monoceros and Chamaeleon SFR. They are all pre-main-sequence stars, although some may be too close to the zero-age main-sequence to be considered as TTS. Not all stars have colour, spectral type and bolometric luminosity measurements and thus cannot be placed in the HR diagram to confirm their nature. The TTS with observed spectra show PMS characteristics, namely the strong absorption line of Li λ6707. The stars without measured spectra are kinematically linked to the same nebula/SFR as the others and therefore should most probably be PMS stars as well.

As referred in the previous Chapter, the TTS have spectral types G, K and M (Herbig, 1983). This places an arbitrary classification boundary (F9/G0) that coupled with the uncertainties in the spectral classification suggests that at least the F8-F9 PMS stars are, most probably, TTS as well. The earlier PMS stars should be classified as Herbig Ae/Be stars. In the data surveyed only 14 stars out of 232 with measured rotational velocity are of spectral class F, 7 of which are of type F8–F9. These were considered as TTS, and consequently included in the analysis. One of these F8 TTS also has a $P_{\rm rot}$ measurement, and is the earliest spectral type among the TTS with $P_{\rm rot}$ measurements in the database.

Efforts have been made to try to include every star only once. However TTS are presented

in various catalogues and it is not always easy to follow all cross references. In any case only a few stars may appear more than once under different names.

The next Sections present the observations and the possible correlations between the rotation rate and stellar parameters, then some physical parameters for certain TTS are computed, and finally the results are discussed and the evolution of the rotation rate from the T Tauri phase to the MS is overviewed.

2.3 The observations

This Section begins with the presentation of the measurements included in the database. The results for $v \sin i$ and $P_{\rm rot}$ are given separately since different observational techniques are involved in their acquisition.

2.3.1 Data on the projected equatorial rotational velocities

The projected equatorial rotational velocity, $v \sin i$, can be recovered from the stellar spectrum by two methods: using the Fourier transform (Vogel and Kuhi, 1981; Gray, 1992) or a cross-correlation technique (Benz and Mayor, 1981; Bouvier et al., 1986).

The histogram shown in Fig. 2.1 combines all the measurements of $v \sin i$ available in the literature, including a total of 225 stars (Vogel and Kuhi, 1981; Mundt et al., 1983; Smith et al., 1983; Bouvier et al., 1986; Hartmann et al., 1986; Hartmann et al., 1987; Walter et al., 1988; Franchini et al., 1988; Hartmann and Stauffer, 1989; Duncan, 1993; Gameiro and Lago, 1993; Dubath et al., 1996). Twelve TTS lie outside this histogram with $v \sin i$ between 100 and 225 $\mathrm{km\,s^{-1}}$ (for seven there is a measurement, while for the remaining five only a lower limit is available).

In this histogram the observations classified as 'uncertain measurements' result from one of the following reasons:

- only one or two spectra are available to construct the FFT;
- a large observational error (exceeding 10 $\mathrm{km\,s^{-1}}$);
- the star is suspected of being a close binary (spectroscopic).

Some TTS were excluded from this histograms and the analysis, namely, the TTS members of close binary systems, and the TTS for which different authors have published disagreeing measures of $v \sin i$.

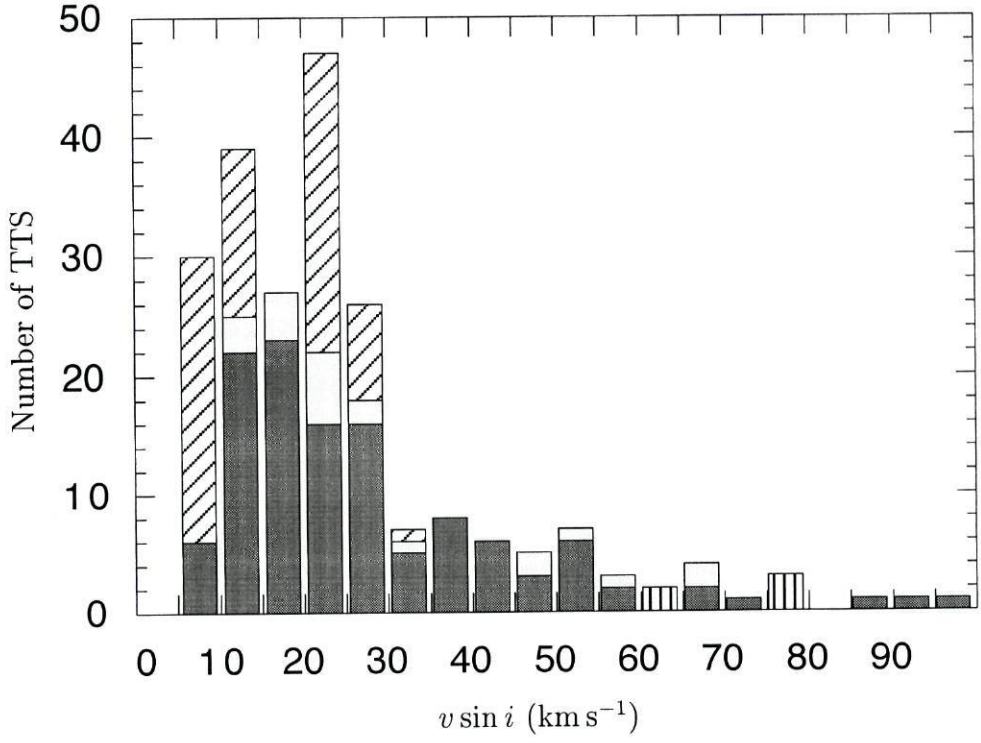

Figure 2.1: Histogram of the projected equatorial rotational velocity of TTS. Dark grey represents the reliable measurements, light grey the uncertain measurements, the oblique stripes represent the upper limits and the vertical stripes the lower limits of $v \sin i$.

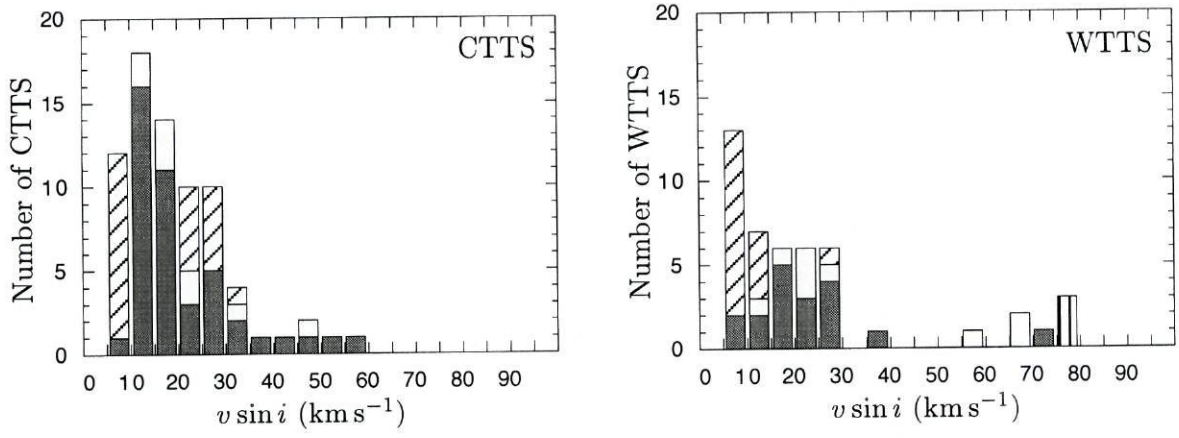

Figure 2.2: Histogram of the projected rotational velocity of CTTS and WTTS. Symbols have the same meaning as in Fig. 2.1.

In the subsample of TTS with reliable measurements of $v \sin i$, 67 stars (55% of them) have $v \sin i \leq 25\,\mathrm{km\,s^{-1}}$. If the subsample of TTS which have upper limits less than $25\,\mathrm{km\,s^{-1}}$ (62 stars) is added to the previous subsample, then 70% of the stars (129) show $v \sin i \leq 25\,\mathrm{km\,s^{-1}}$. This number is too large to be the result of a projection effect. TTS are therefore mainly slow rotators.

Figure 2.2 displays the same data but separating between Classical (CTTS) and Weak-line TTS (WTTS). The reason to make this separation when dealing with the rotation rate of the TTS arises from the commonly cited physical difference between them: the existence or absence of a circumstellar disk. Historically, after Joy's classification, the first TTS were found by systematic searches using objective prism surveys, in which the stars that showed $W_\lambda(H_\alpha) > 10$Å were tentatively classified as TTS. Later observations in the infrared region showed that most of these TTS also have an IR excess. With the advent of X-ray observations another class of T Tauri stars was found . These TTS also showed PMS characteristics, namely the Li λ6707 absorption line, however they lack the IR excess and the strong H_α line. The former are now known as CTTS and the later as WTTS. Examples of the spectral energy distribution for the CTTS and the WTTS are shown in Fig. 2.3. The most common picture for the CTTS system is a PMS star surrounded by a (accretion) disk, while the WTTS would be solely a PMS star (Walter et al., 1988; Edwards et al., 1993). The presence or absence of a circumstellar disk will certainly affect the stellar rotation rate through the interaction between the star and the disk, mediated by the stellar magnetic field. Consequently, in this Chapter plots are presented where the separation between CTTS and WTTS is made. A few TTS classified as WTTS by some authors and as CTTS by other authors were not included in Fig. 2.2.

CTTS (Fig. 2.2 - left) show a similar behaviour to that of Fig. 2.1, 31 in 44 stars (70%) with a reliable measurement having $v \sin i \leq 25\,\mathrm{km\,s^{-1}}$. If CTTS with only upper limits to the rotation velocity known are also included then 78% of the CTTS (47 stars in a total of 60) display $v \sin i \leq 25\,\mathrm{km\,s^{-1}}$.

The histogram for the WTTS is not much different. The number of stars is smaller and only 12 of the 18 stars (67%) with reliable measurements of the rotational velocity have $v \sin i \leq 25\,\mathrm{km\,s^{-1}}$. The inclusion of the stars with only upper limits results in 27 out of 33 WTTS (82%) with $v \sin i \leq 25\,\mathrm{km\,s^{-1}}$.

2.3.2 Data on the photometric period

Some TTS show periodic changes in several photometric bands. These periodic changes are assumed to be due to the presence of spots (hot and/or cool), or groups of spots on the stellar surface. As the star rotates the spot causes the modulation of the light curve.

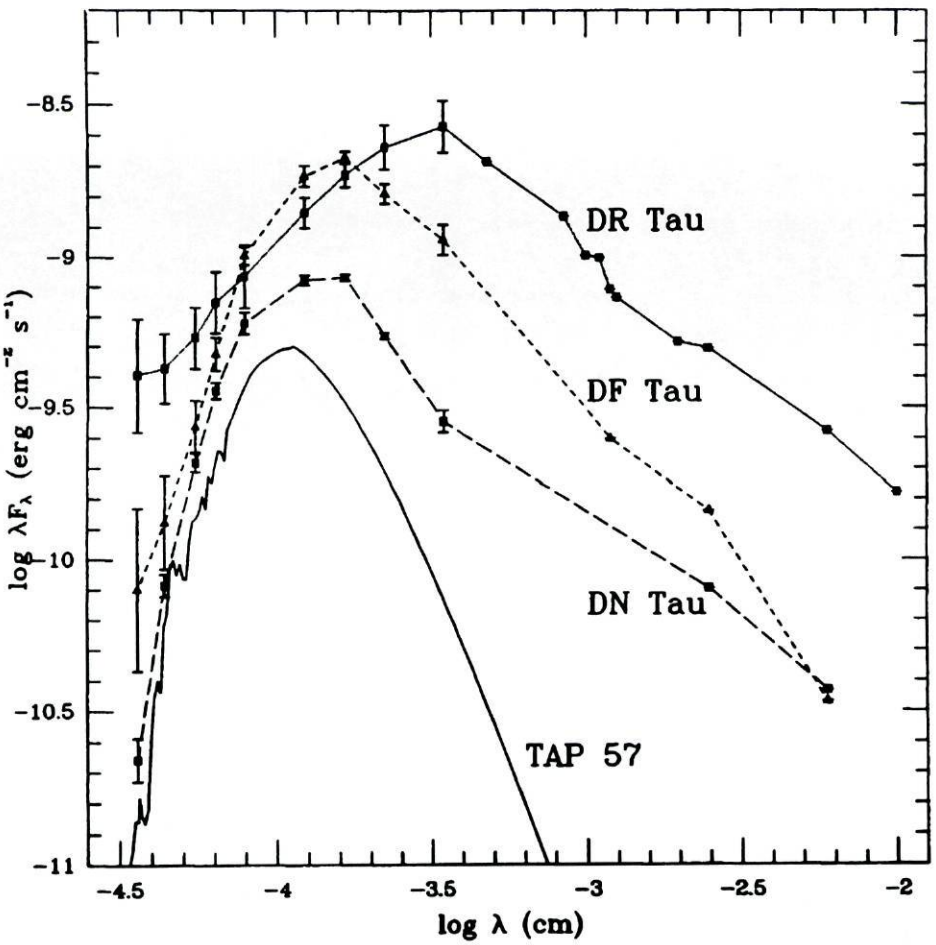

Figure 2.3: Examples of spectral energy distribution for the CTTS and the WTTS. TAP 57 is a WTTS, and its energy distribution has been displaced downward by 0.3 dex. DR Tau, DF Tau and DN Tau are all CTTS (adapted from Bertout (1989)).

To determine the period a periodogram is computed using the observations.

The histogram shown in Fig. 2.4 was obtained by combining the measurements of the rotational periods available in the literature (Rydgren and Vrba, 1983; Rydgren et al., 1984; Bouvier et al., 1986; Herbst et al., 1986; Vrba et al., 1986; Bouvier and Bertout, 1989b; Bouvier and Bertout, 1989a; Vrba et al., 1989; Simon et al., 1990; Walker, 1990; Grankin et al., 1991; Mandel and Herbst, 1991; Attridge and Herbst, 1992; Bouvier et al., 1993; Grankin, 1993; Vrba et al., 1993; Zakirov et al., 1993; Grankin, 1994; Bouvier et al., 1995; Eaton et al., 1995; Prosser et al., 1995; Choi and Herbst, 1996; Grankin, 1996; Osterloh et al., 1996; Kearns et al., 1997). Five TTS lie outside this histogram with measured periods between 16.25 and 34.51 days, and another with an uncertain period of 15 days.

The uncertainties in the measurements are caused either by:

- lack of a good coverage of all phases of the light curve;
- the star was observed during less than two photometric periods;
- the amplitude of the variations is very small, even in the U-band;
- the star is, or is suspected of being, a close binary (spectroscopic).

For certain stars the periodogram displayed several significant peaks, corresponding to periods of 1 to 2 or 3 days. In these cases the largest period was used as an upper limit in the histogram (although this is not very meaningful). These stars are not used in the remaining of this Chapter.

Figure 2.4 shows that there are clearly two groups of TTS, the period of 4 days being the dividing line. Taking into consideration only TTS with reliable measurements of $P_{\rm rot}$, the first group peaks around 2–3 days and the second group between 6 and 7 days. Of the 112 TTS with reliable measurements for the photometric period only 6 (5% of the total) have $P_{\rm rot}$ between 4 and 5 days. The existence of this bimodality in the histogram for $P_{\rm rot}$ demands further analysis. Among the possible causes for the separation of the period of TTS in two groups are the stellar mass, the stellar age, and the eventual presence of a circumstellar (accretion) disk. As previously mentioned, the disk hypothesis lead to the study of rotation rate for CTTS and WTTS, while the stellar mass and age possibilities demand the comparison of the position of TTS in the HR-diagram with theoretical evolutionary tracks. This latter study will be the subject of Section 2.5.

Recently an article by Stassun et al. (1999) includes measurements of $P_{\rm rot}$ for over 250 TTS in Orion. The results for the TTS in this work will be compared to those of Stassun et al. at the end of this Chapter.

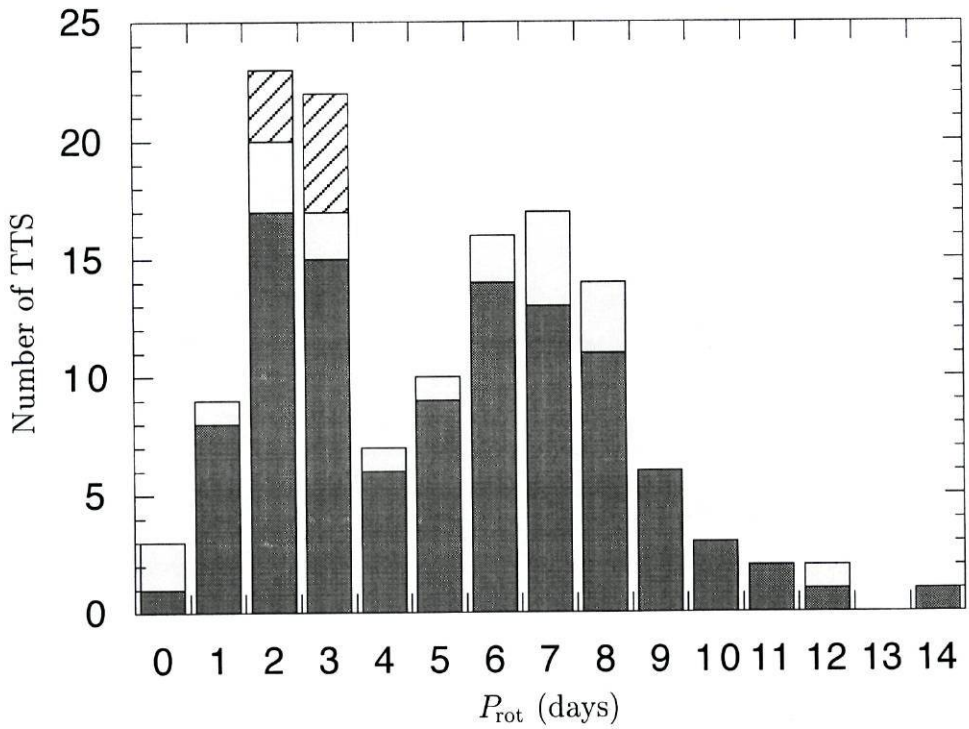

Figure 2.4: Histogram of the rotational period of TTS. Symbols as in the previous figures, but for measurements of $P_{\rm rot}$.

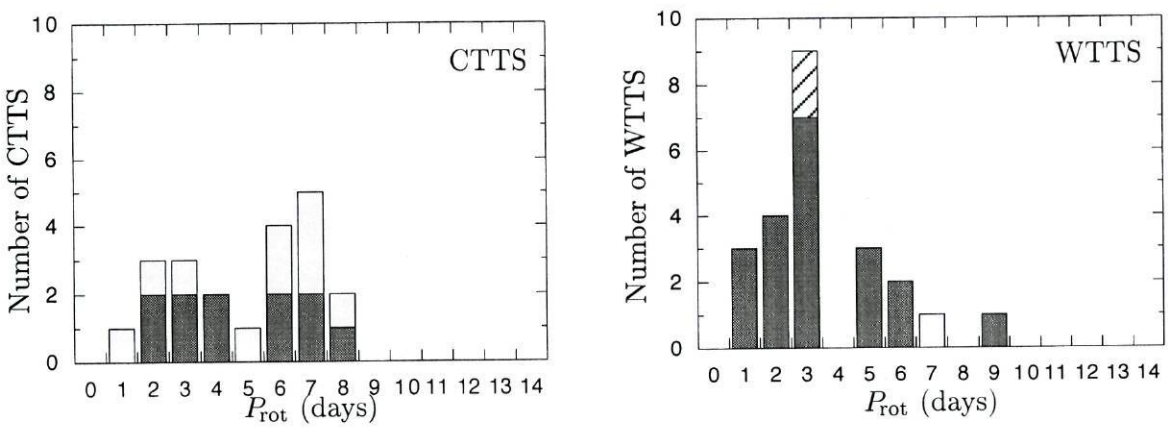

Figure 2.5: Histogram of the rotational period of CTTS (left) and WTTS (right). Symbols as in the previous figures.

Figure 2.5 shows the separation between WTTS and CTTS. There is one WTTS with a period of 17.25 days which lies outside the histogram. There are 11 CTTS and 21 WTTS with reliable measurements of the photometric period. In these two small sub-samples, the WTTS tend to be dominated by 'fast' rotators ($P_{\rm rot} \leq 4$ days), while the distribution for CTTS is very flat, with no preferred rotation period.

2.4 The behaviour of $v \sin i$ and $P_{\rm rot}$ with spectral type

The behaviour of $v \sin i$ and $P_{\rm rot}$ with spectral type for the large sample being studied will now be analysed, excluding TTS with uncertain values of $v \sin i$ or $P_{\rm rot}$. However, it is relevant to recall that in the case of some TTS there may be some uncertainty in the spectral classification. This is usually smaller than two to three subclasses, even if in some extreme cases no spectral type can be assigned at all to the star.

2.4.1 $v \sin i$ versus $T_{\rm eff}$

The analysis of the distribution of $v \sin i$ with $T_{\rm eff}$ demands the conversion from spectral type into effective temperature ($T_{\rm eff}$), and for that purpose Table 7 in Cohen and Kuhi (1979) will be used. Fig. 2.6 shows that fast rotators are more abundant amongst the earlier type and almost absent in the later type TTS. Table 2.1 presents some statistical results for the TTS of Fig. 2.6, where neighbouring spectral types have been grouped together to provide stronger statistics. This Table shows results for the reliable measurements of $v \sin i$, as well as the results obtained with the Kaplan-Meier estimators, which take into consideration both the reliable measurements and the upper limits. The ASURV package (Feigelson and Nelson, 1985; Isobe et al., 1986) was used for the computations. It is clear that earlier type TTS rotate faster than later type ones and also that the dispersion is higher for the earlier type stars.

If the sub-samples of the CTTS and WTTS are analysed separately (Fig. 2.7), then the former includes more than 30 stars with reliable measurements of $v \sin i$ which are distributed between spectral types G2 and M5, while the later has less than 20 stars distributed between the spectral types K1 and M5.5. The CTTS distribution resembles that of the complete sample while that of the WTTS is flatter.

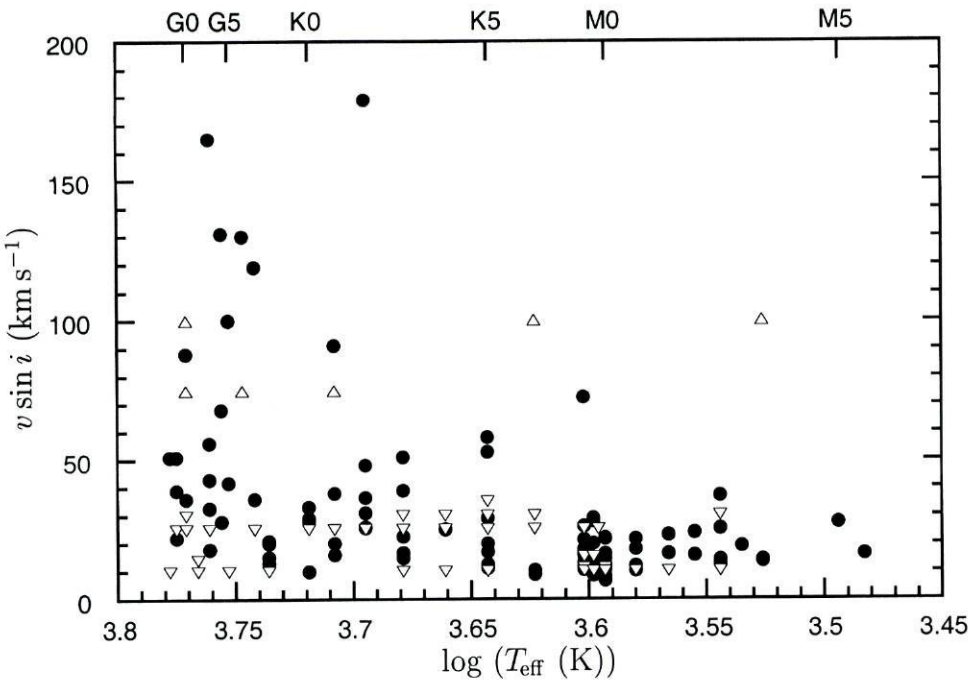

Figure 2.6: $v \sin i$ as a function of $T_{\rm eff}$. Circles represent TTS with reliable measurements of $v \sin i$, triangles down the upper limits and triangles up the lower limits on $v \sin i$.

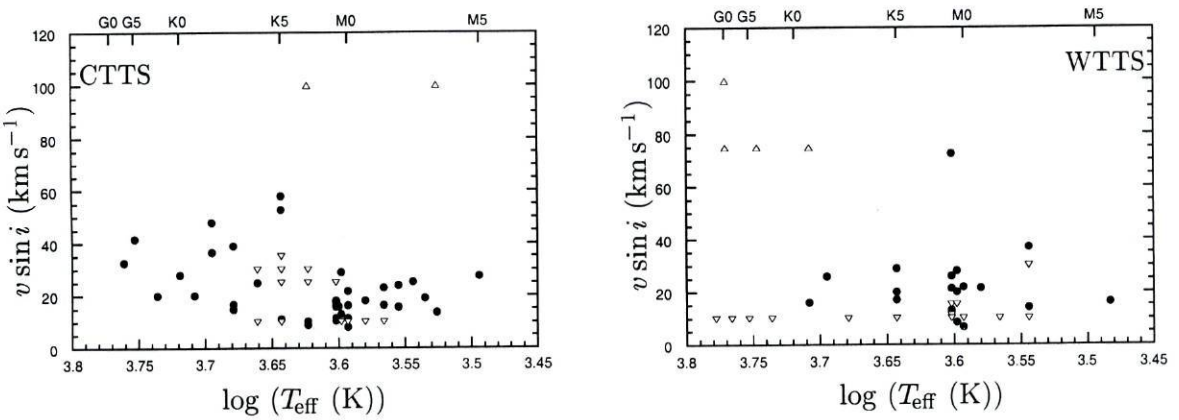

Figure 2.7: $v \sin i$ as a function of $T_{\rm eff}$ for CTTS (left) and WTTS (right). Symbols have the same meaning as in Fig. 2.6.

	reliable				limits						
Sp. Types	number	median	mean	σ	$N_<$	$N_>$	N_{tot}	median	mean	σ	c
	(#)	($km\,s^{-1}$)	($km\,s^{-1}$)	($km\,s^{-1}$)	(#)	(#)	(#)	($km\,s^{-1}$)	($km\,s^{-1}$)	($km\,s^{-1}$)	
F8 to G0	6	45.0	47.8	22.4	5	nc	11	20.0	32.8	7.10	f
					5	ir	13	29.0	41.2	8.24	f
G2 & G4	8	49.5	67.7	52.8	3	0	11	30.4	54.2	14.3	
G5 & G6	3	100	90.6	44.9	1	nc	4	41.7	70.4	23.6	f
					1	ir	5	58.4	71.3	18.9	f
G7 & G8	6	20.5	37.3	40.8	2	0	8	16.7	31.2	12.0	f
K0 & K1	9	28.0	32.6	23.6	3	nc	12	20.1	28.3	6.04	
					3	ir	13	22.1	31.9	6.56	
K2 & K3	12	28.5	43.0	44.3	5	0	17	24.9	34.9	9.22	f
K4 to K6	10	18.5	24.5	17.6	15	nc	25	10.8	17.0	2.73	
					15	ir	26	11.0	20.2	4.08	
K7	12	16.2	20.8	16.9	7	0	19	12.2	17.3	3.16	f
K7-M0	6	17.9	19.1	8.23	5	0	11	8.83	14.6	2.32	
M0 & M0.5	13	12.0	14.2	5.22	6	0	19	10.4	12.1	1.21	
M1 to M2.5	9	19.0	20.7	7.62	6	0	15	13.9	16.8	2.00	f
M3 to M5.5	4	15.4	17.8	6.56	0	1	5	15.1	34.2	14.9	l

Comments: f - the first (smallest) upper limit on $v \sin i$ has been changed to a reliable measurement for the computations of the Kaplan-Meier estimators, thus biasing the mean; l - same as 'f', but for the last (largest) lower limit on $v \sin i$; nc - lower limit not considered in the computations; ir - lower limit included as a reliable measurement.

Table 2.1: Statistics for the TTS. For each spectral type range (column 1), are presented the number of TTS per range with reliable measurements of $v \sin i$ (column 2), their median $v \sin i$ (column 3), mean (column 4) and standard deviation (column 5), all in units of $km\,s^{-1}$, the number of TTS with upper limits on $v \sin i$ known (column 6), a comment about the treatment of the TTS with lower limits on $v \sin i$ known (column 7), the total number of TTS used in the Kaplan-Meier statistics (column 8), their median $v \sin i$ (column 9), mean (column 10) and standard deviation (column 11), all in units of $km\,s^{-1}$, and a comment about the Kaplan-Meier statistics (column 12).

Sp.Type	number	median	mean	σ
F8 to G1	2	2.20	2.20	1.41
G6 to G8	3	1.81	2.22	0.96
K0 & K1	9	2.80	5.52	5.31
K2 & K3	5	3.43	4.31	2.81
K4 to K6	5	3.90	4.45	2.81
K7	13	5.60	5.23	2.45
K7-M0	4	5.25	5.36	2.54
M0 & M0.5	14	6.85	8.12	7.85
M1 & M2	4	8.21	7.60	3.03
M3 & M4	5	6.86	6.53	2.51

Table 2.2: Median, mean, standard deviation (σ) as well as the number of TTS with reliable measurements of $P_{\rm rot}$ for several spectral classes ranges.

2.4.2 $P_{\rm rot}$ versus $T_{\rm eff}$

As expected, the behaviour of $P_{\rm rot}$ versus $T_{\rm eff}$ shown in Fig. 2.8 is similar: there is a predominance of fast rotators for the earlier types, and of slow rotators amongst the later type TTS (also compare Table 2.2 with Table 2.1).

Another interesting feature is the large number of TTS (31 stars, almost half of the total sample) in the spectral classes K7 to M0.5. This subsample has both fast and slow rotators, as well as the presence of the general characteristic for the rotation rate to decrease for the later spectral types. Future observations will certainly populate other spectral bins in Table 2.2 and it will be then possible to find out whether these other bins will be equally populated by both fast and slow rotators, or if there will be a predominance of fast rotators in the early spectral type bins and a prevalence of slow rotators for the later spectral type bins. The analysis of the behaviour of the median in Table 2.2 hints in favour of the second hypothesis.

Figure 2.9 displays the behaviour of the photometric period of rotation along the spectral sequence which is similar for the WTTS and CTTS considered: a predominance of fast rotators for the earlier spectral types, and the appearance of slower rotators at the K7-M0 spectral region.

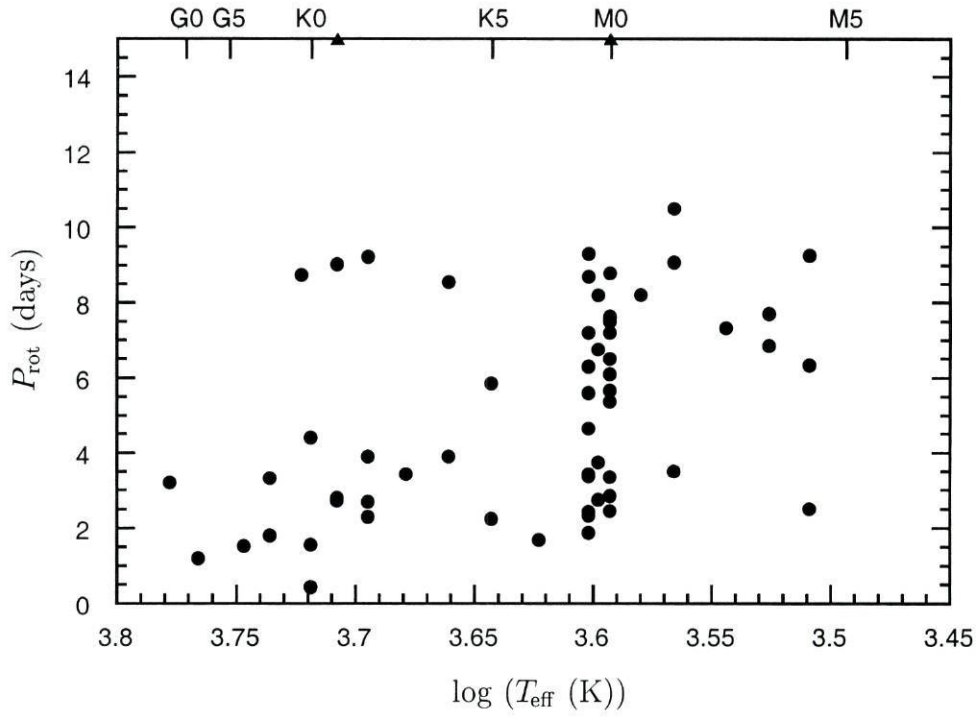

Figure 2.8: Rotational period versus $T_{\rm eff}$ for TTS. Circles represent TTS with reliable measurements of $P_{\rm rot}$. The triangle near $\log(T_{\rm eff}) = 3.7$ represents a K1 TTS with a reliable measurement for $P_{\rm rot}$ of 17.25 days, and the other near $\log(T_{\rm eff}) = 3.6$ a M0 TTS with a reliable measurement of 34.41 days.

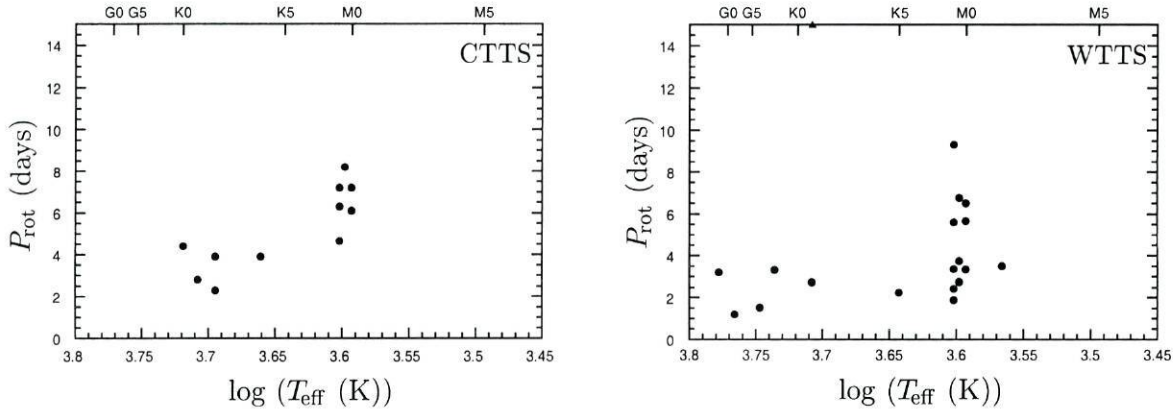

Figure 2.9: Rotational period versus spectral type for CTTS (left) and WTTS (right). The triangle near $\log(T_{\rm eff}) = 3.7$ represents a K1 WTTS with a reliable measurement for $P_{\rm rot}$ of 17.25 days.

2.5 $P_{\rm rot}$ and $v \sin i$ on the HR-diagram

To correctly place a star in the HR-diagram the *stellar luminosity* must be known. However, some TTS show a large IR excess, as well as an excess in the blue band, when compared to a main-sequence star. This effect is more common among CTTS than WTTS, the later showing a spectral energy distribution closer to that of a main-sequence star, as shown in Fig. 2.3. Since both the blue and IR excesses are considered to have a non-stellar origin, they should be removed when computing the stellar luminosity.

Several authors have presented different ways of computing the *true* TTS luminosity. For example, Cohen et al. (1989) assumed that the luminosity detected in the V filter (L_V) is only of stellar origin. From main-sequence stars of the same spectral type as the TTS they also compute mean (L_V/L_{sum}), where L_{sum} results from the integration under the energy distribution from 1000 Å to 25 μm and the extrapolation to larger wavelengths by Rayleigh-Jeans distributions. The authors multiplied the measured value for L_V by the appropriate mean (L_V/L_{sum}), and identified the result as the total stellar luminosity. Strom et al. (1989) adopted a similar procedure using however the R-band filter. Alternatively, Kenyon and Hartmann (1990) used the J-band filter to recover the true TTS luminosity. The differences in the derived luminosities are rather high, and $\Delta \log(L_{max} - L_{min}) \sim 0.5$ was not a rare situation.

Another approach is to adopt the sum of the luminosity measured in the different photometric bands (L_{sum}) as the total stellar luminosity, with a small correction (in general) for the long wavelengths, for which L is not measured. The values of the total stellar luminosity derived in this way by different authors are usually in good agreement, with $\Delta \log(L_{max} - L_{min}) < 0.1$. Frequently, the values of the luminosity based on L_{sum} are encompassed by the values computed from the fits to the photometric bands described in the previous paragraph.

In this work L_{sum}, or the mean when several measurements are available, is adopted as the stellar luminosity. The observational results for the rotation of TTS in the HR-diagram are shown in Figs. 2.10 and 2.11 where the position of the TTS with measurements of $v \sin i$ or $P_{\rm rot}$ are superimposed on the theoretical evolutionary tracks of Palla and Stahler (1999). These Figures show that the more massive TTS seem to be faster rotators than the less massive ones. In order to quantify the behaviour of the rotation rate for the TTS as function of mass or age Tables 2.3 and 2.4 were built using these HR-diagrams. Considering only the more populated bins, the rotation rate seems to increase with increasing mass, as well as increasing age. These trends are valid for both the $v \sin i$ (with or without inclusion of the limits) and the $P_{\rm rot}$ measurements.

In these Tables the effects of mass and age are mixed, being desirable to separate them.

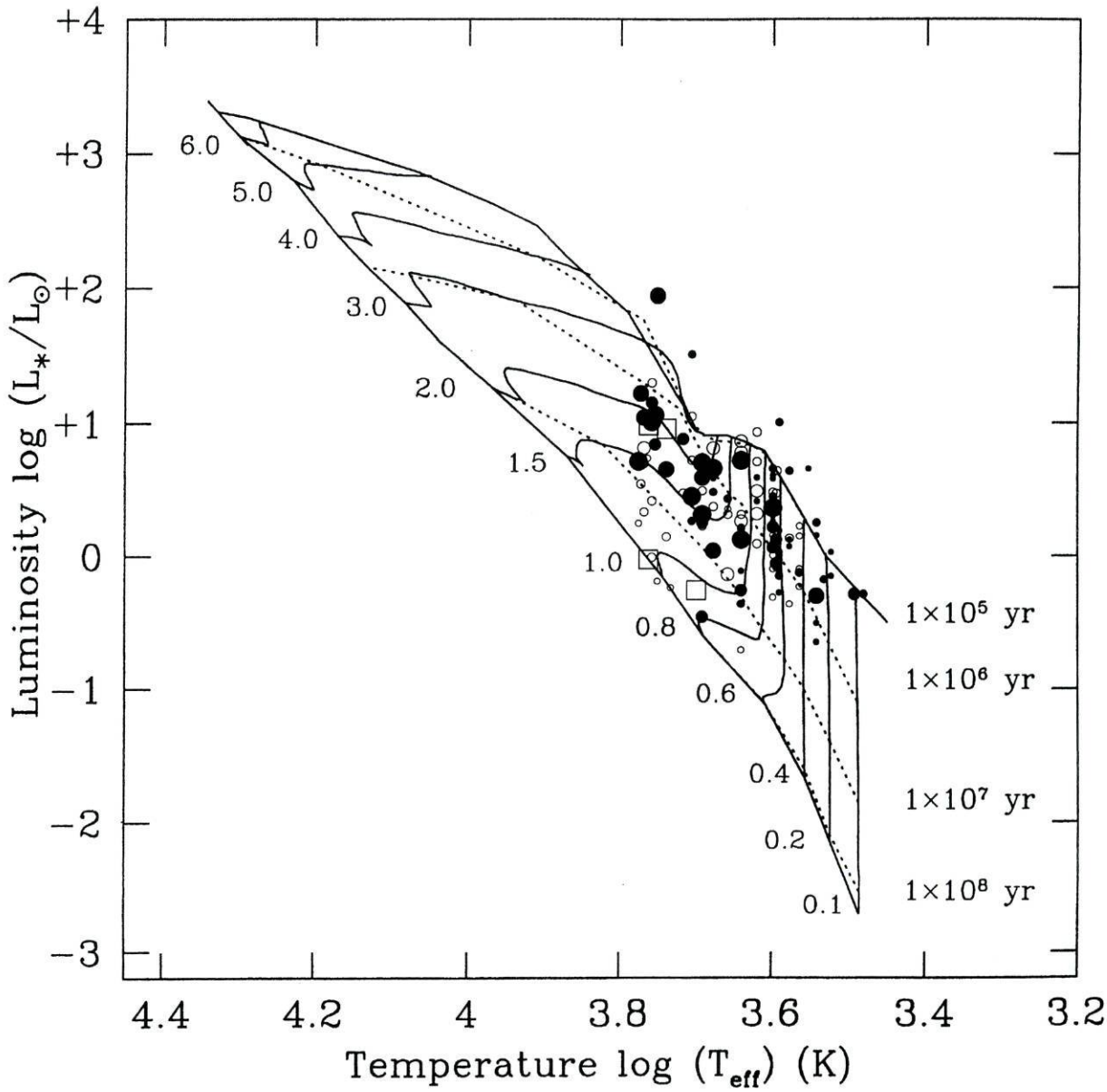

Figure 2.10: HR-diagram of TTS with measurements of $v \sin i$. Filled circles are for reliable measurements ($v \sin i$ bins:• 0–15, • 15–25, • 25–35, • 35–45, • >45 km s^{-1}), empty circles for the upper limits ($v \sin i$ bins:◦ <10, <11 or <15, ◦ <25, ◦ <30 or 35 km s^{-1}), and empty squares for the lower limits on $v \sin i$ of 75 km s^{-1}. The theoretical evolutionary tracks are adapted from Palla and Stahler (1999).

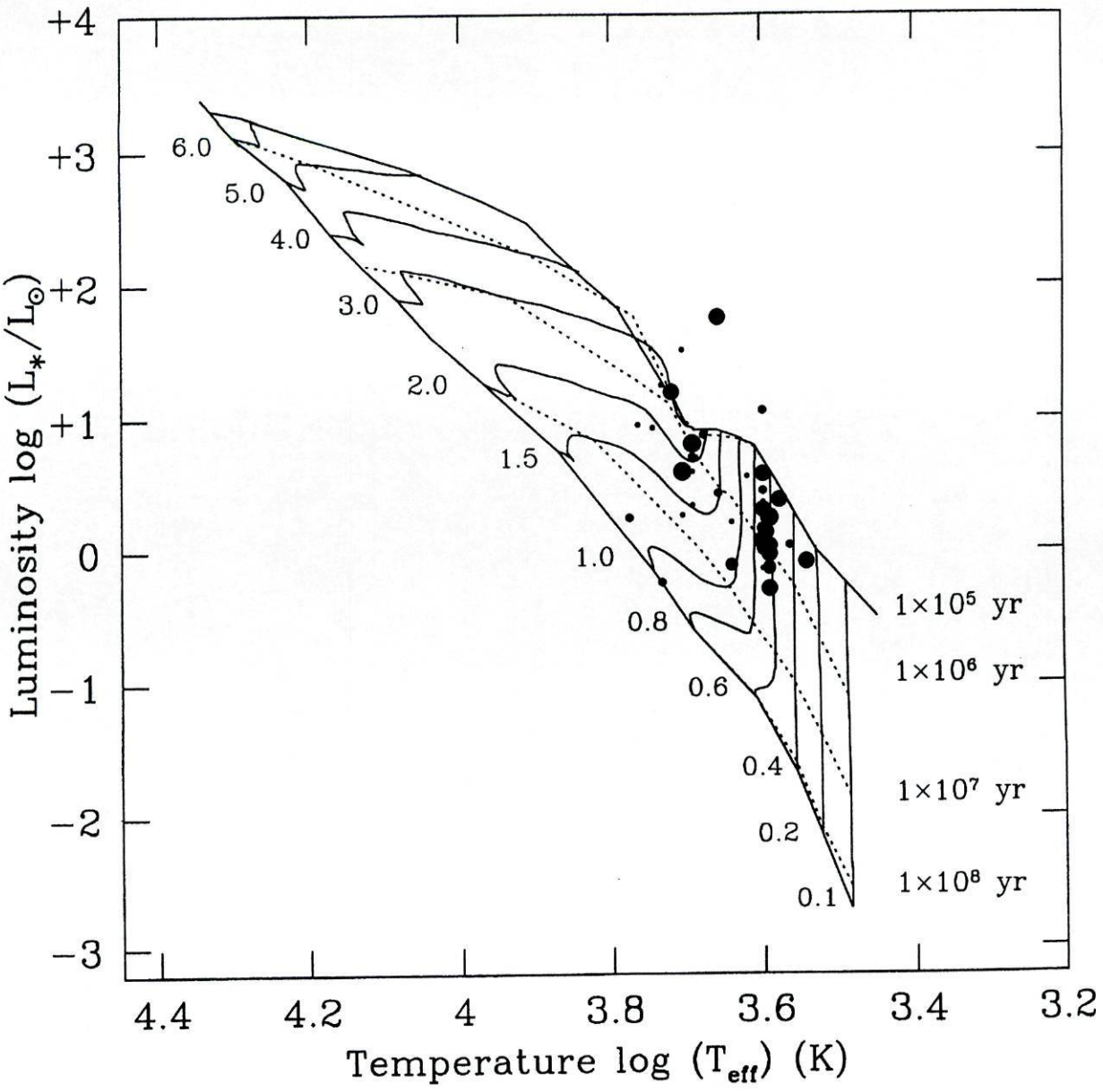

Figure 2.11: HR-diagram of TTS with $P_{\rm rot}$ measurements. $P_{\rm rot}$ bins:• 0–3, • 3–5, • 5–7, • 7–9, • >9 days). The theoretical evolutionary tracks are adapted from Palla and Stahler (1999).

	reliable				limits						
mass range	number	median	mean	σ	$N_<$	$N_>$	N_{tot}	median	mean	σ	c
($M_\odot$)	(#)	(km s^{-1})	(km s^{-1})	(km s^{-1})	(#)	(#)	(#)	(km s^{-1})	(km s^{-1})	(km s^{-1})	
$2.0 < M_\star$	3	32.7	33.2	5.52	1	0	4	28.0	31.2	2.64	f
$1.5 < M_\star \leq 2.0$	12	36.3	47.5	33.4	7	nc	19	23.1	35.2	6.96	f
					7	ir	21	26.8	40.2	7.19	f
$1.0 < M_\star \leq 1.5$	11	26.0	44.7	47.7	16	0	27	12.3	25.7	6.43	f
$0.8 < M_\star \leq 1.0$	4	13.7	16.3	9.18	5	nc	9	9.37	13.8	2.75	
					5	ir	10	9.73	19.9	6.31	
$0.6 < M_\star \leq 0.8$	21	15.8	18.9	14.0	15	0	36	10.5	14.6	1.97	
$0.4 < M_\star \leq 0.6$	3	16.3	16.6	4.81	6	0	9	7.50	12.2	1.28	f
$0.2 < M_\star \leq 0.4$	3	19.0	23.3	12.1	1	0	4	14.0	20.0	5.16	f
$M_\star \leq 0.2$	2	20.8	20.8	9.55	0	0	2	—	20.8	4.77	

age range	number	median	mean	σ	$N_<$	$N_>$	N_{tot}	median	mean	σ	c
(year)	(#)	(km s^{-1})	(km s^{-1})	(km s^{-1})	(#)	(#)	(#)	(km s^{-1})	(km s^{-1})	(km s^{-1})	
$10^7 < \text{age} \leq 10^8$	2	21.5	21.5	6.36	7	nc	9	—	13.3	2.01	f
					7	ir	10	8.33	19.5	6.12	f
$10^6 < \text{age} \leq 10^7$	30	28.0	38.6	36.6	24	nc	54	14.8	25.5	4.20	
					24	ir	56	15.5	27.7	4.35	
$10^5 < \text{age} \leq 10^6$	27	16.3	21.7	15.9	20	0	47	11.4	16.9	1.98	

Table 2.3: Statistics for the TTS with $v \sin i$ measurements, that could be placed in the HR diagram. For each mass or age range (column 1, obtained from Fig. 2.10) the same quantities shown in Table 2.1 are presented here.

mass range	number	median	mean	σ
($M_\odot$)	(#)	(day)	(day)	(day)
$2.0 < M_\star$	3	3.43	4.82	3.90
$1.5 < M_\star \leq 2.0$	6	3.10	3.64	2.88
$1.0 < M_\star \leq 1.5$	5	2.73	3.34	1.44
$0.8 < M_\star \leq 1.0$	2	2.51	2.51	1.15
$0.6 < M_\star \leq 0.8$	22	5.63	6.75	6.59
$0.4 < M_\star \leq 0.6$	2	5.86	5.86	3.33
$0.2 < M_\star \leq 0.4$	1	7.33	7.33	—
$M_\star \leq 0.2$	0	—	—	—

age range	number	median	mean	σ
(year)	(#)	(day)	(day)	(day)
$10^7 < \text{age} \leq 10^8$	2	3.26	3.26	0.08
$10^6 < \text{age} \leq 10^7$	18	3.33	4.16	2.30
$10^5 < \text{age} \leq 10^6$	21	5.66	6.86	6.84

Table 2.4: For each mass or age range (column 1) it is shown the number of TTS per range (column 2), their median $P_{\rm rot}$ (column 3), mean (column 4) and standard deviation (column 5), all in units of days.

This differentiation is shown in Tables 2.5 and 2.6 where the same statistical quantities are presented, but for only two mass ranges and, simultaneously, two age ranges. Due to the uneven distribution of the number of TTS per bin in Table 2.5 ($v \sin i$ measurements) it is difficult to draw precise conclusions. Nevertheless, the results hint that higher mass and older TTS rotate faster than the lower mass and younger ones. The more massive TTS of Table 2.6 rotate faster than the less massive ones, while no age differentiation is unambiguously detected.

2.6 TTS radii and equatorial velocities

Some of the TTS have measurements of $T_{\rm eff}$, luminosity, $v \sin i$ and $P_{\rm rot}$ that may be used to learn more about them, in particular to determine their radius, equatorial velocity and inclination angle. This Section deals with these computations and the corresponding results.

From the values of $v \sin i$ and $P_{\rm rot}$ it is possible to get the projected equatorial radius ($R_{\rm eq} \sin i$)

$$R_{\rm eq} \sin i = \frac{P_{\rm rot} v \sin i}{2\pi} \quad . \tag{2.1}$$

To obtain the true equatorial radius, the following relation between L, $T_{\rm eff}$ and $R_{\rm eq}$

$$L = 4\pi R_{\rm eq}^2 \sigma {T_{\rm eff}}^4 \tag{2.2}$$

is used. In this equation it is assumed that the star is spherical and is emitting as a black-body, which is not necessarily a valid approximation for all TTS. The luminosity in this equation is the stellar luminosity which, as referred before, is difficult to determine for some TTS.

The equatorial velocity can be recovered from the expression

$$V_{\rm eq} = \frac{2\pi R_{\rm eq}}{P_{\rm rot}} \tag{2.3}$$

and the inclination angle from

$$\sin i = \frac{v \sin i}{V_{\rm eq}} = \frac{R_{\rm eq} \sin i}{R_{\rm eq}} \quad . \tag{2.4}$$

$1.0 < M_\star \leq 2.0$											
		reliable			limits						
age range	number	median	mean	σ	$N_<$	$N_>$	N_{tot}	median	mean	σ	c
(year)	(#)	($km\,s^{-1}$)	($km\,s^{-1}$)	($km\,s^{-1}$)	(#)	(#)	(#)	($km\,s^{-1}$)	($km\,s^{-1}$)	($km\,s^{-1}$)	
$10^6 < age \leq 10^7$	21	36.0	45.3	41.7	14	nc	35	17.3	32.7	5.98	f
					14	ir	37	18.7	35.7	6.03	f
$10^5 < age \leq 10^6$	2	54.5	54.5	4.95	4	0	6	—	24.8	8.60	f

$0.6 < M_\star \leq 0.8$											
		reliable			limits						
age range	number	median	mean	σ	$N_<$	$N_>$	N_{tot}	median	mean	σ	c
(year)	(#)	($km\,s^{-1}$)	($km\,s^{-1}$)	($km\,s^{-1}$)	(#)	(#)	(#)	($km\,s^{-1}$)	($km\,s^{-1}$)	($km\,s^{-1}$)	
$10^6 < age \leq 10^7$	4	13.9	15.6	9.13	6	0	10	5.03	10.4	2.11	
$10^5 < age \leq 10^6$	16	15.8	19.3	15.4	8	0	24	11.3	16.0	2.70	

Table 2.5: Statistics for the TTS. For each age range (column 1) and mass range (top and middle rows) the same quantities shown in Table 2.1 are presented here.

	$1.0 < M_\star \leq 2.0$				$0.6 < M_\star \leq 0.8$			
age range	number	median	mean	σ	number	median	mean	σ
(year)	(#)	(day)	(day)	(day)	(#)	(day)	(day)	(day)
$10^6 < \text{age} \leq 10^7$	10	2.72	3.54	2.35	8	5.49	4.94	2.12
$10^5 < \text{age} \leq 10^6$	0	—	—	—	14	5.98	7.78	8.04

Table 2.6: For each age and mass ranges (column 1 and top row, respectively) it is shown the number of TTS per range (columns 2 and 6), their median $P_{\rm rot}$ (columns 3 and 7), mean (columns 4 and 8) and standard deviation (columns 5 and 9).

Another interesting quantity is the break-up velocity of the star, that is, the value of $V_{\rm eq}$ for which the gravitational acceleration and the centrifugal force at the the stellar equator are equal in magnitude

$$V_{\rm br} = \sqrt{\frac{GM_\star}{R_\star}} \tag{2.5}$$

The results are summarized in Tables 2.7 and 2.8. In Table 2.8 the stellar mass ranges were obtained from the comparison of the stellar $T_{\rm eff}$ and $L_{\rm sum}$ ranges on the HR-diagram with the theoretical evolutionary tracks of Palla and Stahler. The analysis of these Tables shows some general results for the TTS properties, namely: most of the TTS in this sample have $M_\star < M_\odot$, nevertheless they all have $R_\star > R_\odot$, hinting that they are still in the contraction phase prior to the main-sequence. Another property of this sample of TTS is their low rotation rates, well below the break-up velocity for most of the stars.

One exception to these general trends is the star T Tau. However, T Tau is a multiple system, constituted of an optically visible star, T Tau N, an infrared companion to the south, T Tau S (Dyck et al., 1982) and a probable third member north of T Tau N, discovered in 1985 by Nisenson and co-workers (Nisenson et al., 1985) and confirmed by Maihara and Kataza in 1991, but never seen again. T Tau N luminosity dominates at optical wavelengths, while T Tau S dominates in the far infrared (Maihara and Kataza, 1991; Ghez et al., 1991). The separation between T Tau N and T Tau S is 0.″6 and that between T Tau N and the possible third component is 0.″4 (Maihara and Kataza, 1991). Since the distance to the Taurus-Auriga complex exceeds 100 pc, the linear separation between T Tau N and any of its companions is larger than 50 a.u.. With such large separation both the photometric period and the $v \sin i$ values are due to the stellar rotation of T Tau N (the only optically visible component) and not to the orbital motions.

Without making any assumptions about the T Tauri system, Table 2.9 shows the values of $R_{\rm eq}$, $V_{\rm eq}$ and the inclination angle for the hypothetical cases where T Tau N accounts for 1/4, 1/2 or 3/4 of the total luminosity of the system. Smaller values of the luminosity

TTS name	Spectral Type range	$\log(L/L_\odot)$ min	max	$P_{\rm rot}$ (days)	$v \sin i$ (km s^{-1})	$r \sin i$ ($R_\odot$)	$R_{\rm eq}^{\rm min}$ $R_{\rm eq}^{\rm max}$ ($R_\odot$)	$V_{\rm eq}^{\rm min}$ $V_{\rm eq}^{\rm max}$ (km s^{-1})	$\sin i$ min	max	i (deg) min	max
AA Tau	K7[17]↔K7-M0[6]	0.110[25]↔0.140[6]		8.20[28]	13.0[a]	2.11	2.36↔2.49	14.6↔15.4	0.845↔0.891		57.7↔63.0	
DI Tau	M0[6]	-0.030[7]↔0.080[25]		7.50[4]	10.6[14]	1.57	2.10↔2.38	14.2↔16.1	0.660↔0.749		41.3↔48.5	
FK 2	K7[29]↔K7-M0[22]	0.040[29]↔0.150[25]		3.75[b]	20.0[c]	1.48	2.18↔2.52	29.4↔34.0	0.588↔0.679		36.0↔42.8	
GI Tau	K6[20]↔K7[d]	0.280[6]↔0.300[e]		7.20[27]	11.4[f]	1.62	2.61↔2.94	18.3↔20.7	0.551↔0.621		33.5↔38.4	
GK Tau	K7[6]	0.340[25]↔0.540[6]		4.65[g]	17.5[f]	1.61	3.08↔3.88	33.5↔42.2	0.415↔0.522		24.5↔31.5	
LHa 332-21	G8[16]↔K0[1]	0.870[3]		4.40[h]	28.0[3]	2.43	3.06↔3.31	35.2↔38.1	0.736↔0.796		47.4↔52.7	
Lk Ca 4	K7[18]	0.010[29]↔0.100[25]		3.37[i]	26.1[15]	1.74	2.11↔2.34	31.6↔35.1	0.744↔0.825		48.0↔55.6	
Lk Ca 15	K5[18]	-0.120[29]		5.85[4]	12.5[15]	1.44	1.50	13.0	0.962		74.1	
ROX 29	K6[3]↔K7[6]	0.550[3]↔0.590[6]		6.30[h]	15.8[3]	1.97	3.56↔4.11	28.6↔33.0	0.479↔0.552		28.6↔33.5	
RY Lup	K1[21]↔K4[1]	0.420[3]		3.90[3]	25.0[3]	1.93	2.07↔2.57	26.9↔33.4	0.748↔0.929		48.4↔68.3	
Sz 6	K2[j]	0.580[3]		2.30[h]	36.5[k]	1.66	2.65	58.2	0.627		38.8	
TAP 35	K1[29]	0.220[29]↔0.280[25]		2.73[i]	16.0[29]	0.863	1.65↔1.76	30.5↔32.7	0.489↔0.524		29.3↔31.6	
T Tau	K0[20]↔K1[6]	1.45[6]↔1.55[25]		2.80[19]	20.1[l]	1.11	6.45↔7.61	117↔138	0.146↔0.172		8.40↔9.93	
UX Tau A	K2[6]	0.280[6]↔0.380[25]		2.70[h]	25.7[m]	1.37	1.87↔2.10	35.1↔39.4	0.652↔0.732		40.7↔47.0	
V410 Tau	K3[5]↔K7[6]	0.280[23]↔0.420[n]		1.87[12]	70.7[14]	2.61	2.02↔3.38	54.6↔91.4	0.773↔1.30		50.7↔???	
WK 2	K7[29]↔K7-M0[22]	-0.150[3]↔0.020[25]		2.75[o]	28.0[c]	1.52	1.75↔2.17	32.3↔40.0	0.701↔0.868		44.5↔60.2	

keys: a=10,13,14; b=3,12; c=3,22,29; d=5,6; e=7,25; f=13,14; g=4,27; h=2,3; i=11,12; j=1,9; k=3,8,9; l=3,10,13,14,26; m=3,13,14; n=6,25; o=2,3,12,24.

References: 1- Appenzeller et al. (1983); 2- Bouvier & Bertout (1989a); 3- Bouvier et al. (1986); 4- Bouvier et al. (1993); 5- Bouvier et al. (1995); 6- Cohen & Kuhi (1979); 7- Cohen et al. (1989); 8- Dubath et al. (1996); 9- Franchini et al. (1988); 10- Gameiro & Lago (1993); 11- Grankin (1993); 12- Grankin (1994); 13- Hartmann & Stauffer (1989); 14- Hartmann et al. (1986); 15- Hartmann et al. (1987); 16- Henize & Mendoza (1973); 17- Herbig (1977); 18- Herbig et al. (1986); 19- Herbst et al. (1986); 20- Herbst et al. (1994); 21- Liseauet al. (1987); 22- Mundt et al. (1983); 23- Rydgren & Vrba (1983); 24- Rydgren et al. (1984); 25- Strom et al. (1989); 26- Vogel & Kuhi (1981); 27- Vrba et al. (1986); 28- Vrba et al. (1993); 29- Walter et al. (1988).

Table 2.7: List of the TTS that have measurements of $T_{\rm eff}$, luminosity, $P_{\rm rot}$ and $v \sin i$, and the derived values for the equatorial radius and velocity, value of $\sin i$ and the inclination angle.

TTS name	$M_\star^{\min}$ $M_\star^{\max}$ ($M_\odot$)	$V_{\rm br}^{\min}$ $V_{\rm br}^{\max}$ ($\mathrm{km\,s^{-1}}$)	$\frac{V_{\rm eq}^{\max}}{V_{\rm br}^{\min}}$
AA Tau	0.60↔0.80	214↔254	0.07
DI Tau	0.60↔0.80	219↔269	0.07
FK 2	0.60↔0.80	213↔264	0.16
GI Tau	0.50↔0.70	180↔226	0.12
GK Tau	0.60↔0.80	171↔222	0.25
LHa 332-21	1.90↔2.10	330↔361	0.12
Lk Ca 4	0.60↔0.80	221↔269	0.16
Lk Ca 15	1.00↔1.20	356↔390	0.04
ROX 29	0.70↔0.90	180↔219	0.18
RY Lup	1.50↔1.70	333↔395	0.10
Sz 6	1.80↔2.00	360↔379	0.16
TAP 35	1.30↔1.50	374↔416	0.09
T Tau	3.00↔???	274↔???	0.50
UX Tau A	1.40↔1.60	356↔403	0.11
V410 Tau	0.70↔1.70	198↔400	0.46
WK 2	0.60↔0.80	229↔295	0.17

Table 2.8: List of the TTS that have measurements of $T_{\rm eff}$, luminosity, $P_{\rm rot}$ and $v \sin i$, and the inferred values for the stellar mass range obtained from the position of the TTS in the HR-diagrams of Figs. 2.10 and 2.11, the break-up velocity and the ratio $V_{\rm eq}^{\max}/V_{\rm br}^{\min}$.

$\frac{L_N}{L_{tot}}$	$\log(L/L_\odot)$	R_{eq}^{min} R_{eq}^{max}	V_{eq}^{min} V_{eq}^{max}	$\sin i$	i (deg)	$M_\star^{min}$ $M_\star^{max}$	V_{br}^{min} V_{br}^{max}	$\frac{V_{eq}^{max}}{V_{br}^{min}}$
	min max	($R_\odot$)	($\mathrm{km\,s^{-1}}$)	min max	min max	($M_\odot$)	($\mathrm{km\,s^{-1}}$)	
1/4	0.85↔0.95	3.23↔3.82	58.4↔69.0	0.291↔0.344	16.9↔20.1	2.0↔3.0	316↔420	0.22
1/2	1.15↔1.25	4.57↔5.39	82.5↔97.4	0.206↔0.243	11.9↔14.1	3.0↔???	325↔???	0.30
3/4	1.32↔1.42	5.55↔6.56	100↔119	0.170↔0.200	9.76↔11.5	3.0↔???	295↔???	0.40

Table 2.9: Derived values for the equatorial radius and velocity, inclination angle and break-up velocity and the inferred stellar mass for the star T Tau N, in the hypothetical cases were it accounts for 1/4, 1/2 or 3/4 of the total luminosity of the system.

result in a decrease of the equatorial radius and velocity of T Tau, its mass and the ratio $V_{eq}^{max}/V_{br}^{min}$, placing all these quantities in closer agreement with the corresponding values for the other TTS in Tables 2.7 and 2.8.

An awkward result of Table 2.7 is the value of 1.30 for $\sin i$ of V410 Tau. This maximum value of $\sin i$ results from the combination of the minimum of the luminosity and the maximum of the effective temperature (Eqs. (2.2) and (2.4)). V410 Tau has a negligible UV excess (Herbig and Goodrich, 1986), as well as a very small IR excess (Rydgren & Vrba 1981; Ghez, White & Simon 1997), therefore Eq. (2.2) can be used with confidence. V410 Tau is also a member of a multiple stellar system (Ghez, Neugebauer & Matthews 1993; Ghez et al. 1997) although none of the secondary stars (B & C) seems to contribute significantly to the total luminosity of the system. The angular separation between V410 Tau A and B is 0.″07, and that between V410 Tau A and C is 0.″26 (Ghez et al., 1997). These angular separations exceed 10 a.u. of linear separation between any of the system components at the distance of the Taurus–Auriga complex. Therefore the measurements of P_{rot} and $v \sin i$ are due to the rotation of V410 Tau and not to the orbital motions. As a consequence, the effects of the companion stars, as far as this work is concerned, will be to decrease by a small amount the value of the total luminosity of V410 Tau, thus causing an increase in the value of $\sin i$.

As the measurements of both P_{rot} and $v \sin i$ are the smallest found in the literature, the use of higher values results in an increase of the maximum value of $\sin i$. Therefore the cause of the abnormal value of $\sin i$ must be either the luminosity, the spectral type classification or the conversion between the spectral type and T_{eff}. Starting with the spectral type classification of V410 Tau, a K7 type leads to a maximum value of $\sin i < 1$.

The use of other Tables to convert between the spectral type and T_{eff} is not helpful. For example, the values of Table 4 of Hartigan et al. (1994) are so similar to those of Table 7 of Cohen and Kuhi (1979) that, again, only a classification of K7 to V410 Tau makes the maximum value of $\sin i$ smaller than one.

Three values of $\log(L/L_\odot)$ for V410 Tau have been found in the literature: 0.28 (Rydgren

and Vrba, 1983; Strom et al., 1989, R-band fit); 0.38 (Cohen and Kuhi, 1979; Strom et al., 1989); 0.42 (Bouvier et al., 1986). If somehow the lower value is not correct and is rejected then the value of 0.38 is to be used as a minimum. Then V410 Tau could not be earlier than K5 since it would result in a maximum value of $\sin i$ above 1. Therefore the K3 classification of V410 Tau must be questioned.

A K7, or even K6, spectral classification for V410 Tau also solves the indeterminacy to its mass shown in Table 2.8, were it ranges from 0.7 to 1.7 $M_{\odot}$. Restricted to these spectral classifications the mass range for V410 Tau is from 0.7 to 0.9 $M_{\odot}$, in agreement with the ranges for the other TTS in this sample.

The procedure outlined by Eqs. (2.1) to (2.4) has already been used by Weaver (1987) to obtain the equatorial velocity and radius of TTS and their inclination angle to the line of sight. The agreement between his Table 1 and Table 2.7 is good, yet some TTS in his Table are not included in Table 2.7. The reasons to exclude them from Table 2.7 are the following:

undetermined $P_{\rm rot}$:

BP Tau $P_{\rm rot}=$ 6.1 days, (Simon et al., 1990)
$P_{\rm rot}\sim$ 7.6 days, (Simon et al., 1990)
$P_{\rm rot}=$ 7.6 days, (Vrba et al., 1986)
$P_{\rm rot}\sim$ 7.7 days, (Osterloh et al., 1996)

DF Tau $P_{\rm rot}\sim$ 8.5 days, (Bouvier and Bertout, 1989a; Bouvier et al., 1993)
$P_{\rm rot}\sim$ 9.8 days, (Bouvier et al., 1995)
no $P_{\rm rot}$ observed, (Rydgren et al., 1984)

DN Tau $P_{\rm rot}=$ 6.0 days, (Bouvier et al., 1986; Bouvier and Bertout, 1989a)
$P_{\rm rot}=$ 6.3 days, (Vrba et al., 1993)
$P_{\rm rot}=$ 6.6 days, (Vrba et al., 1986)

HP Tau/G2 uncertain $v \sin i$
$v \sin i\sim$ 100 km s^{-1}, (Hartmann et al., 1986; Hartmann and Stauffer, 1989)

ROX 21 undetermined $v \sin i$
$v \sin i=$ 21 km s^{-1}, (Bouvier et al., 1986)
$v \sin i \sim$ 43 km s^{-1}, (Bouvier et al., 1986)

RW Aur spectral type of A component $\sim$ K1, (Herbig and Bell, 1988)
spectral type of B component $\sim$ K3, (Herbig and Bell, 1988)
no spectral type, 'continuous star', (Cohen and Kuhi, 1979)

From the analysis of these examples it is found that some care must be taken for the measurement of $P_{\rm rot}$ for the TTS. It seems that in some cases the periodicity does not correspond to the period of rotation of the stellar surface, which should remain almost constant in time, but to the rotational period of some circumstellar material, whatever its origin. As mentioned, in the hypothesis of magnetospheric accretion, a hot spot forms above the photosphere at the locus of the accretion shock; in this case it will be the rotational period of the hot spot that is measured and not the photospheric rotational period.

In the case of uncertain values for $v \sin i$ new observations are needed to improve the precision in its determination. For the TTS RW Aur it was not possible to determine unequivocally its spectral type, since the spectra of both components is highly veiled, and therefore the photospheric absorption lines are difficult to measure.

The TTS LH$_\alpha$332-20 is named Sz 6 in Table 2.7, while TW Cha was not included in the analysis since it was not possible to look at the original sources for its $P_{\rm rot}$ cited by Bouvier et al. (1986).

2.7 Discussion

In the previous Sections the rotation of TTS was studied. It was shown that TTS are slow rotators, an unexpected result by the time of publication of the first survey of their rotation rate (Vogel and Kuhi, 1981). Another interesting result was the bimodality present in the histogram of the rotational periods. The absence of bimodality in the histogram of $v \sin i$ may be explained by the existence of a projection effect ($\sin i$), and the fact that TTS with different radii are included in the same plot.

How to explain the presence of two main peaks for the $P_{\rm rot}$ values for the TTS? A tentative explanation put forward by Edwards et al. (1993) is that the slow rotating TTS are surrounded by an accretion disk (CTTS), the star being magnetically synchronized to a point in the disk and thus prevented to spin up while contracting towards the MS. The stars not surrounded by a disk (WTTS) can spin up while contracting, therefore having shorter periods. It was shown that, even in the very small samples considered, WTTS tend to have shorter periods of rotation than CTTS, in agreement with the suggestion by Edwards et al. (1993). However, the separation in these classes is not the only factor, since there is a non-negligible number of exceptions.

To investigate this further was studied the distribution of $P_{\rm rot}$ along the spectral sequence and in the HR-diagram. The earlier-type, as well as the more massive, TTS tend to be faster rotators. These two cases are in fact just one, as the earlier-type TTS are also

		number of TTS in the $P_{\rm rot}$ range (day)								
mass range	age range	1–2	2–3	3–4	4–5	5–6	6–7	7–8	8–9	9–10
($M_\odot$)	(year)	(#)	(#)	(#)	(#)	(#)	(#)	(#)	(#)	(#)
1.0–2.0	10^6–10^7	2	4	2	0	1	0	0	0	1
0.6–0.8	10^6–10^7	0	3	0	0	2	1	2	0	0
0.6–0.8	10^5–10^6	1	1	2	1	2	1	2	2	1

Table 2.10: For each age and mass ranges are presented the number of TTS with $P_{\rm rot}$ in the referred ranges (top row).

the more massive ones (please refer to Fig. 2.11). This tentative explanation is tested in Table 2.10 where the TTS of Table 2.6 are distributed in given $P_{\rm rot}$ ranges. It is clear that the subsample of the more massive TTS is dominated by the faster rotators, while the subsample of the less massive ones has both fast and slow rotators, independently of age. Yet this tentative explanation is not completely satisfactory either.

The $v \sin i$ measurements also show the tendency for the earlier-type, as well as more massive and older TTS to be the faster rotators. Yet this is only a tendency, contrary to the case of the single MS stars. The study of the changes in $v \sin i$ from the T Tauri phase to the MS is the subject of next Section.

2.7.1 $v \sin i$ in open clusters

To characterize the evolution of the rotation rate between the TTS phase and the main sequence (MS) it is adequate to study open clusters. This characterization demands the determination of the the open clusters ages. The differential age of the clusters is relatively easy to determine using the turnoff point. However, the absolute age of the clusters is more difficult to determine, since it depends on theoretical evolutionary models. Soderblom et al. (1993) proposed an age of 50 Myr for the α Persei cluster, 70 Myr for the Pleiades, 600 Myr for the Hyades and 300 Myr for the Ursa Major cluster (Soderblom and Mayor, 1993).

Figure 2.12 shows that both α Persei and Pleiades clusters have a large scatter in the distribution of $v \sin i$ for a given spectral type, with slow rotators ($v \sin i \leq 10\,{\rm km\,s^{-1}}$) and fast rotators with $v \sin i \geq 30\,{\rm km\,s^{-1}}$, some in excess of $100\,{\rm km\,s^{-1}}$.

For the older open clusters shown in Fig. 2.13 the rotational velocity displays some convergence: by 300 Myr (Ursa Major cluster) the rotational velocity has converged to the lower values, for the G and later type stars, while by 600 Myr (Hyades cluster) all stars of a given spectral type (mass) have converged to a narrow range of $v \sin i$, dependent on

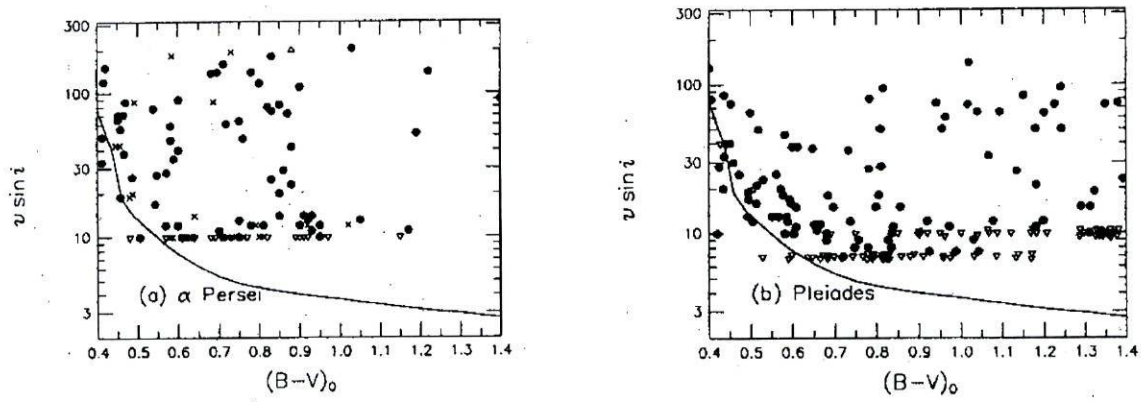

Figure 2.12: α Persei and Pleiades clusters $v \sin i$ as function of spectral type. The curve in both plots is a mean relation for the Hyades. These figures are adapted from Soderblom et al. (1993)

the stellar spectral type, with the exception of the very late M-type stars that have long evolutionary timescales.

These observations show that a broad range of rotation rates for a given stellar mass is a common characteristic of the young stellar clusters. They also give hints to the angular momentum problem: if there was angular momentum conservation the stars should increase their rotation rates while contracting from the TTS phase to the MS, contrary to what the observations seem to indicate. Consequently, the stars must lose angular momentum from their surface layers. The angular momentum loss mechanism must be strong enough to prevent the fast rotating TTS to arrive at the MS rotating near the breakup velocity. However, it must not be so efficient that the slow rotating TTS are 'stopped' before arriving at the MS.

Some theoretical models

There are several theoretical evolutionary models that follow the evolution of the internal structure of the star and also its rotation rate. One of the most complete sets of models for solar-type stars are those of Krishnamurthi et al. (1997). They developed evolutionary models with solid body rotation throughout the stellar interior, as well as evolutionary models with solid body rotation in the convective envelope and differential rotation in the radiative core. In the latter models the core and the envelope were decoupled (in the sense of having different rotation rates), being the core a reservoir of angular momentum. The difference in the rotation rate at the interface core/envelope is allowed to increase until the diffusion coefficients become large enough to transport angular momentum from the core to the envelope.

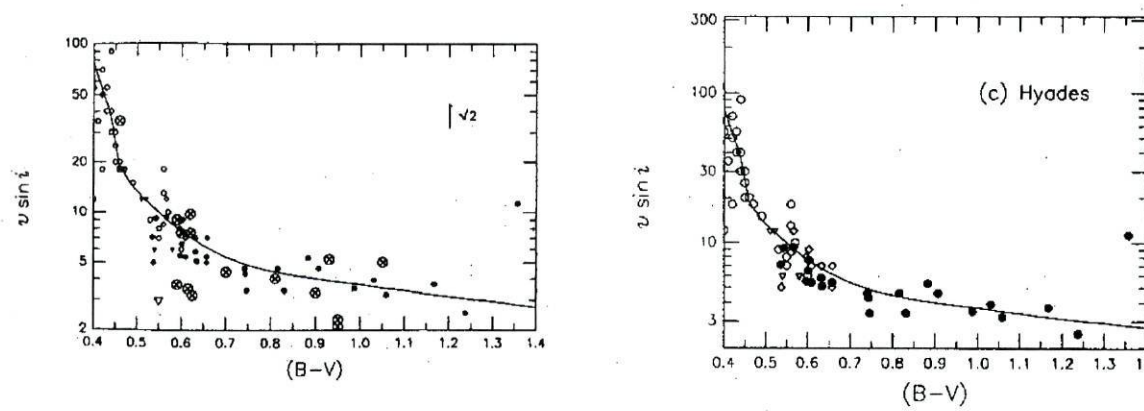

Figure 2.13: Ursa Major (left) and Hyades clusters $v \sin i$ as function of spectral type. The curve in both plots is a mean relation for the Hyades. Circles with a cross in them represent Ursa Major members and the large triangle an upper limit. The small symbols are for Hyades members. In Hyades graphic open symbols are $v \sin i$ measurements and filled symbols are period measurements converted to equatorial velocities and multiplied by $\pi/4$ (mean of $\sin i$). The figure on the left is adapted from Soderblom and Mayor (1993) and that on the right from Soderblom et al. (1993)

The core/envelope decoupling constitutes a possible solution to the angular momentum problem: in this case the convective envelope can have a lower rotation rate than the core and the mechanism for the angular momentum loss does not need to be as efficient as in the case of a solid body rotating star.

Some of the main general features that result from the set of models from Krishnamurthi et al. (1997) are:

- there is a need for an angular momentum loss mechanism from the surface layers, for example, a magnetized stellar wind;
- the saturation threshold of the angular momentum loss mechanism is mass-dependent;
- the differential rotation evolutionary models provide a better fit to the observations of the young open clusters, on the whole, than do the solid body rotation models.

2.8 Conclusion

The leading conclusion of this Chapter, and the one that has implications for the stellar wind models of TTS which is the main subject of this work, is the confirmation that

TTS are slow rotators, with only a few fast rotators. This conclusion results from a bibliographical survey, in which more than 200 TTS with $v \sin i$ measurements were included. The low rotation rate of the TTS allows, as a first approximation, to neglect the centrifugal force in the stellar wind models that will be developed in the following Chapters. Therefore, these stellar wind models should not be compared with observational parameters derived from fast rotating TTS.

Other general trends for the rotation rate of TTS were found, in particular that faster rotators are more abundant among the WTTS, the earlier-type TTS, the more massive and the older TTS. As all subsamples considered in this work have both slow and fast rotators in different proportions, it may be concluded that the rotation rate of TTS is not uniquely determined by its present characteristics (mass, age, radius, $T_{\rm eff}$, luminosity) but also from its formation history in the molecular cloud, prior to become an optically visible object. Although, as for single MS stars, the stellar mass seems to be one of the most important factors in the regulation of the rotation rate.

In this work several hypothesis were tested in order to explain the bimodality present in the $P_{\rm rot}$ histogram, yet none of them was satisfactory, as there were always a significant number of exceptions. A closer look at the histogram of the photometric periods (Fig. 2.4) reveals that there are 6 TTS in the 4–5 days bin, corresponding to about 5% of the total number of TTS in that sample. This is a small, but non negligible, number, and it must be questioned if the lack of TTS with $P_{\rm rot}$ in the range 4–5 days would remain in larger samples of TTS with measurements of $P_{\rm rot}$.

In fact, Stassun et al. (1999) published values of $P_{\rm rot}$ for over 250 TTS in the Orion nebula region. To compare their results with those presented in this Chapter, their histogram of $P_{\rm rot}$ for the TTS is shown in Fig. 2.14. A visual inspection of this figure does not reveal a clear bimodality in the histogram for their sample. Through the use of statistical test the authors argue that the distribution of $P_{\rm rot}$ in the range 1–8 days for the TTS of their sample is consistent with a uniform distribution of $P_{\rm rot}$ in the quoted range.

This conclusion does not contradict the conclusions of this Chapter, since, as mentioned before, the number of TTS in the 4–5 days bin of the sample analysed in this Chapter is small, but not vanishingly small. They also corroborate our conclusion that there is not a characteristic of the star (line strengths, IR excess, colour, class, mass, age) that allows the classification of a given TTS as a slow or a fast rotator. Whatever the criteria used, there are always slow and fast rotators in varying degrees.

The fraction of TTS with $P_{\rm rot} < 2$ days is larger in the Stassun et al. (1999) sample than in the sample studied in this Chapter. This might indicate that the fraction of fast rotating TTS is larger than previously thought, at least in the Orion SFR. If this conclusion is further confirmed, the stellar wind models developed for these fast rotating TTS would

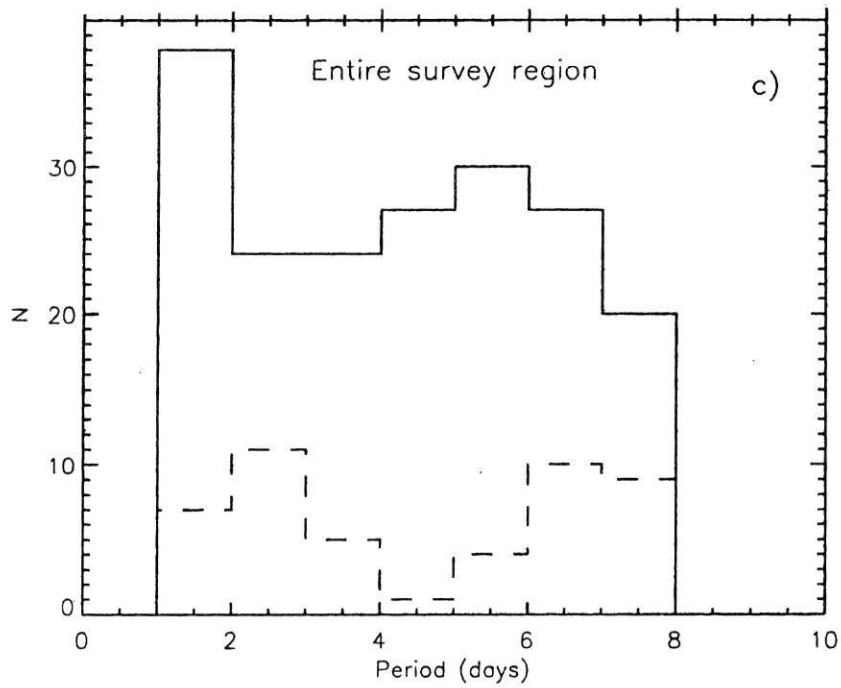

Figure 2.14: Histograms of $P_{\rm rot}$ in the Stassun et al. (1999) sample (solid lines), and in the Choi and Herbst (1996) sample (dashed lines). This Figure is adapted from Stassun et al. (1999).

most probably need to account for the effects of the centrifugal force.

Chapter 3

Review of stellar wind models

As already mentioned, the TTS are low-mass and cool stars, of solar-like nature. Therefore, a review of proposed wind models for the sun and the TTS will be made.

The main goal of this work is to construct stellar wind models for TTS with a detailed energy equation. Consequently, this review concentrates on the evolution of the energy equation used in the stellar wind models, starting with the simple isothermal assumption of the Parker model. This review is not exhaustive, but rather puts emphasis on the works that add new ingredients to the energy equation, and in particular to the one-fluid and steady state wind models. A very short review of stellar wind models including the effects of the global magnetic field is also made, and a first application to the TTS is made using a wind model proposed by Tsinganos and Trussoni. The review finishes with relevant observations and proposed stellar wind models for TTS.

3.1 Plasmas, magnetic fields and waves

It seems appropriate to present at this point, and for future reference, some definitions and approximations that led to the equations of ideal MHD, as well as to the concept of Alfvén waves. This Section addresses this issue, following the works of Choudhuri (1998), Cook (1975), Cross (1982), Kraus and Carver (1986), Priest (1982) and Tsinganos (1994), in alphabetical order.

3.1.1 Characteristic quantities in a plasma

Since Maxwell's equations for electromagnetism will be often needed they are presented here for future reference. It must be noted that Gaussian units will be used throughout

this thesis.

$$\nabla \times \vec{B} = \frac{1}{c}\frac{\partial \vec{E}}{\partial t} + \frac{4\pi}{c}\vec{J}_{\rm c} \quad , \tag{3.1}$$

$$\nabla \cdot \vec{B} = 0 \quad , \tag{3.2}$$

$$\nabla \times \vec{E} = -\frac{1}{c}\frac{\partial \vec{B}}{\partial t} \quad , \tag{3.3}$$

$$\nabla \cdot \vec{E} = 4\pi\rho_{\rm e} \quad . \tag{3.4}$$

Three of these equations are also named: generalized Ampere's law, Eq. (3.1), Faraday's law, Eq. (3.3) and Gauss' law, Eq. (3.4). In these equations, and throughout this thesis, $\vec{B}$ is the magnetic field[1], $\vec{E}$ is the electric field, c is the speed of light in vacuum, $J_{\rm c}$ is the conduction current density and $\rho_{\rm e}$ is the electric charge density.

These are the basic equations for the study of electromagnetic phenomena, and are supplemented by some other relations, in particular Ohm's law:

$$\vec{J}_{\rm c} = \sigma \vec{E}_{\rm t} \tag{3.5}$$

where σ is the electric conductivity, $\vec{E}_{\rm t}$ is the total electric field acting on the particle. Another relation is the force that the electric and the magnetic field exert on a particle of electric charge q, known as the Lorentz force:

$$\vec{F} = q\left(\vec{E} + \frac{\vec{V} \times \vec{B}}{c}\right) \tag{3.6}$$

where $\vec{V}$ is the velocity of the particle. And the constitutive relations between the fields:

$$\vec{D} = \epsilon \vec{E} \tag{3.7}$$

where $\vec{D}$ is the electric displacement and ϵ is the dielectric constant, and

$$\vec{H} = \mu \vec{B} \tag{3.8}$$

[1] $\vec{B}$ is in fact the magnetic induction, while the magnetic field is $\vec{H}$. However the tradition in Astronomy is to call $\vec{B}$ the magnetic field.

where $\vec{H}$ is the magnetic field[2] and μ is the magnetic permeability. In this work both ϵ and μ are set equal to their values in vacuum ($\epsilon = 1$ and $\mu = 1$[3]), consequently, there is no distinction between the $\vec{E}$ and $\vec{D}$ fields nor between the $\vec{B}$ and $\vec{H}$ fields and the polarization and magnetization of the medium are neglected, an assumption already used in Eqs. (3.1) to (3.4). These assumptions will be used throughout this thesis.

The electric and the magnetic fields measured by two observers in relative motion

It is well known that two observers, say $\mathcal{O}$ and $\mathcal{O}'$, where $\mathcal{O}'$ is moving with a velocity $V \ll c$ relative to $\mathcal{O}$, measure the electric - $\vec{E}$; $\vec{E}'$ - and magnetic - $\vec{B}$; $\vec{B}'$ - fields in a certain region of space and time, related by

$$\vec{E}' = \vec{E} + \frac{\vec{V} \times \vec{B}}{c} \quad , \tag{3.9}$$

and

$$\vec{B}' = \vec{B} \quad . \tag{3.10}$$

Consequently, in the non-relativistic case, it is not necessary to specify the frame of reference when indicating the value of the magnetic field, while it is always necessary to specify the frame of reference for the measurements of the electric field.

In the non-relativistic limit Ohm's law (Eq. (3.5)) becomes

$$\vec{J}_c = \sigma \left(\vec{E} + \frac{\vec{V} \times \vec{B}}{c} \right) \tag{3.11}$$

where $\vec{E}$ is measured by a stationary observer.

The Debye length

If a charge q is placed in the plasma it will create an electric field, whose electrostatic potential ϕ is

$$\phi = q \frac{\exp\left(-\frac{R}{\lambda_D}\right)}{R} \tag{3.12}$$

[2]refer to previous note for the nomenclature used

[3]In the rationalized mks system these conditions are $\epsilon = \epsilon_0$ and $\mu = \mu_0$

where R is the radial distance from the charge Q, and the Debye length is

$$\lambda_{\rm D} = \sqrt{\frac{K_{\rm B}T}{8\pi n e^2}} \quad . \tag{3.13}$$

This equation expresses the fact that the effects of a charged particle inside the plasma are screened by charges of opposite sign within a distance $\lambda_{\rm D}$. Therefore deviations from charge neutrality can only appear inside a sphere with the Debye radius.

The gyrofrequency and the plasma frequency

In a cyclotron a particle of charge q has its velocity $\vec{V}$ perpendicular to the external magnetic field $\vec{B}$, therefore the particle describes a circle with radius $R = \frac{mcV}{qB}$ at an angular frequency

$$\omega_{\rm g} = \frac{qB}{mc} \tag{3.14}$$

that is known as the gyrofrequency or cyclotron frequency. When a plasma is traversed by electromagnetic waves with $\omega \approx \omega_{\rm g}$ they strongly interact with each other.

Another typical oscillatory interaction between a plasma and an electromagnetic wave is the plasma or Langmuir wave, characterized by a frequency:

$$\omega_{\rm p} = \sqrt{\frac{4\pi n q^2}{m}} \tag{3.15}$$

where n is the plasma density.

The basic physical mechanism originating these oscillations is the difference in the mass of the ions to that of the electrons: the mass of the ions is much larger than that of the electrons, therefore as a first approximation the ions can be considered immobile, while the electrons are oscillating due to the perturbation electric field. Consequently there are places with excess and other with lack of electrons, thus giving rise to electrostatic forces that drive the oscillations.

3.1.2 The MHD approximations

Large electrical conductivity

The electrical conductivity of a plasma depends on its temperature (Spitzer, 1952):

$$\sigma_{\rm e} \propto T^{3/2} \quad . \tag{3.16}$$

Consequently, in high temperature plasmas the electrical conductivity is very high. In this case, Ohm's law (Eq. (3.11)), becomes:

$$\frac{\vec{J}}{\sigma} = \vec{E} + \frac{\vec{V} \times \vec{B}}{c} \approx 0 \tag{3.17}$$

where $\vec{E}$ is the electric field measured in a fixed referential. Therefore the electric field seen by a stationary observer can be approximated by the expression:

$$\vec{E} \approx -\frac{\vec{V} \times \vec{B}}{c} \quad . \tag{3.18}$$

Neglect of the displacement current

Considering the generalized Ampere's law (Eq. (3.1)):

$$\nabla \times \vec{B} = \frac{1}{c}\frac{\partial \vec{E}}{\partial t} + \frac{4\pi}{c}\vec{J}_{\mathrm{c}} \tag{3.19}$$

where the first term on the right-hand side is the displacement current. This term can be neglected in Ampere's law when dealing with low frequency phenomena. In particular the angular frequency must obey $\omega \ll \omega_{\mathrm{p}}$.

Quasi-charge neutrality

For non-relativistic velocities, and for systems with $L \gg \lambda_{\mathrm{D}}$ the approximation $n_{\mathrm{i}} \simeq n_{\mathrm{e}} = n$ is valid.

The fluid limit

When the particles of a plasma are collision dominated the fluid approximation can be used with confidence. For the particles to be collisionally dominated the mean free path must be much smaller than the characteristic length scale, i.e.,

$$\lambda \ll L \quad . \tag{3.20}$$

For the particular case of the solar wind, the condition of small mean free path is obeyed in the inner corona, however in the distant solar wind, say at the earth's orbit, the mean free path is of the order of the typical length scale ($\lambda \sim L$), and therefore the fluid approximation seems not to be valid. However if there is a strong magnetic field present,

then the particles will spiral along it, and its motion in the direction perpendicular to the magnetic field is highly forbidden. Consequently in the times scales of interest being studied a particle will remain in the vicinity of its neighbourhood particles.

The frozen-in approximation

The magnetic Reynolds number is defined as

$$R_{\rm m} \equiv \frac{4\pi\sigma V L}{c^2} \quad , \tag{3.21}$$

where σ is the electrical conductivity, V and L are a velocity and a length characteristic of the plasma system under study. Large values of the magnetic Reynolds number ($R_{\rm m} \gg 1$), as is the case for most astrophysical plasmas, imply that

$$\frac{\partial \vec{B}}{\partial t} = \nabla \times \left(\vec{V} \times \vec{B}\right) \quad , \tag{3.22}$$

which expresses the fact that the plasma and the magnetic field 'move together', i.e., the magnetic field lines are also streamlines for the plasma.

3.1.3 The equations of ideal MHD

Under the assumptions and approximations made in the previous Sections the equations of MHD in the ideal limit are:
the mass continuity equation

$$\frac{\partial \rho}{\partial t} + \nabla \cdot (\rho \vec{V}) = 0 \tag{3.23}$$

the momentum equation

$$\rho \left(\frac{\partial}{\partial t} + \vec{V} \cdot \nabla\right) \vec{V} = -\nabla P - \rho \frac{GM}{R^2}\, \hat{e}_{\rm r} + \frac{\left(\nabla \times \vec{B}\right) \times \vec{B}}{4\pi} \tag{3.24}$$

the equation for the nonexistence of magnetic monopoles

$$\nabla \cdot \vec{B} = 0 \tag{3.25}$$

Ampere's law

$$\nabla \times \vec{B} = \frac{4\pi}{c} \vec{J} \tag{3.26}$$

and Faraday's law

$$\frac{\partial \vec{B}}{\partial t} = -c\nabla \times \vec{E} = \nabla \times \left(\vec{V} \times \vec{B}\right) \quad . \tag{3.27}$$

Ohm's law for infinite conductivity may be used to recover the value of the electric field

$$\vec{E} = -\frac{\vec{V} \times \vec{B}}{c} \quad . \tag{3.28}$$

To be solved, this system of differential equations must be supplemented by an equation of state, some assumptions on the system geometry, and eventually an energy equation.

The term of the Lorentz force in the momentum equation can be written in several different forms,

$$\frac{\vec{J} \times \vec{B}}{c} = \frac{\left(\nabla \times \vec{B}\right) \times \vec{B}}{4\pi} = \frac{\left(\vec{B} \cdot \nabla\right) \vec{B}}{4\pi} - \nabla\left(\frac{B^2}{8\pi}\right) \tag{3.29}$$

where the identity

$$\nabla\left(\vec{F} \cdot \vec{G}\right) = \left(\vec{F} \cdot \nabla\right) \vec{G} + \left(\vec{G} \cdot \nabla\right) \vec{F} + \vec{F} \times \left(\nabla \times \vec{G}\right) + \vec{G} \times \left(\nabla \times \vec{F}\right) \tag{3.30}$$

has been used. In the last equality of Eq. (3.29) the first term is due to the magnetic tension and the last one is due to the magnetic pressure.

3.1.4 Brief overview of magnetic waves

When a gas, for example the air, is perturbed/excited sound waves are generated. Similarly, when a magnetized plasma is perturbed electromagneticacoustic waves are generated.

A straightforward way to obtain mathematical expressions for the magnetic waves originating on a perturbation of the plasma is to consider the ideal MHD equations (Eqs. (3.23) to (3.27)), but neglecting the gravitational term in the momentum equation. Assuming that the motion is adiabatic, i.e.,

$$\left(\frac{\partial}{\partial t} + \vec{V} \cdot \nabla\right)\left(\frac{P}{\rho^\gamma}\right) = 0 \quad , \tag{3.31}$$

and that the initial state of the plasma is uniform, i.e., $\vec{B} = B_0\vec{n}$, $|\vec{n}| = 1$, $P = P_0$, $\rho = \rho_0$ and selecting a referential moving with the plasma, i.e., $\vec{V} = \vec{0}$. The plasma is then perturbed, and these quantities take the form:

$$\rho = \rho_0(1+\alpha) \ , \quad P = P_0(1+p) \ , \quad \vec{B} = B_0(\vec{n} + \vec{b}) \ , \quad \vec{V} = \vec{v} \tag{3.32}$$

where the perturbation quantities have small magnitude.

After linearizing the equations, and assuming solutions of the form

$$\exp\left[i\left(\omega t - \vec{k}\cdot\vec{r}\right)\right] \tag{3.33}$$

two main modes are generated: the Alfvén mode (incompressible) and the two magnetoacoustic modes (compressible). Before further analysis of the properties of these waves modes it is convenient to choose a coordinate system such that

$$\vec{n} = (0,1,0) \ , \qquad \vec{k} = (k_{\rm x}, k_{\rm y}, 0) = (k\sin\psi, k\cos\psi, 0) \ , \qquad \vec{v} = (v_{\rm x}, v_{\rm y}, v_{\rm z}) \tag{3.34}$$

where ψ is the angle between the direction of propagation and the ambient magnetic field, and to introduce the wave phase and group velocities,

$$V_{\rm ph} = \frac{\omega}{k} \ , \tag{3.35}$$

$$\vec{V}_{\rm gr} = \frac{\partial\omega}{\partial\vec{k}} = \left(\frac{\partial\omega}{\partial k_{\rm x}}, \frac{\partial\omega}{\partial k_{\rm y}}, \frac{\partial\omega}{\partial k_{\rm z}}\right) \ , \tag{3.36}$$

as well as the sound and Alfvén speeds,

$$V_{\rm s}^2 = \gamma\frac{P}{\rho} \qquad \text{and} \qquad V_{\rm A}^2 = \frac{B^2}{4\pi\rho} \ . \tag{3.37}$$

Alfvén mode

One of the wave modes is an oblique Alfvén wave, with phase and group velocities:

$$V_{\rm ph} = V_{\rm A}\cos\psi \qquad \text{and} \qquad \vec{V}_{\rm gr} = (0, V_{\rm A}, 0) \ . \tag{3.38}$$

For this wave mode

$$\vec{v} = (0,0,v_{\rm z}) \quad \Longrightarrow \quad \vec{v}\cdot\vec{k} = 0 \qquad \text{and} \qquad \vec{v}\cdot\vec{n} = 0 \tag{3.39}$$

therefore the plasma motion is perpendicular to both the direction of propagation and the direction of the ambient magnetic field, i.e., Alfvén waves are transverse waves. Since

$$\alpha = \frac{\vec{k}\cdot\vec{v}}{\omega} = 0 \tag{3.40}$$

the Alfvén waves do not involve any compression of the plasma.

For Alfvén waves the energy density is equally distributed between the magnetic and the velocity perturbations[4],

$$\frac{B_0^2 b^2}{8\pi} = \frac{1}{2}\rho v^2 \tag{3.41}$$

The energy is not alternating between the magnetic and the kinetic forms, since both disturbance vectors ($\vec{v}$ and $\vec{b}$) are in phase. Therefore the total energy density is:

$$\mathcal{E} = \frac{B_0^2 b^2}{4\pi} \quad . \tag{3.42}$$

An important property of the Alfvén waves is that they are not limited to small amplitude disturbances, which means that Alfvén waves are more difficult to dissipate.

The Poynting vector, giving the direction and magnitude of the instantaneous flux of electromagnetic energy through a surface, is

$$\vec{S} = \frac{c}{4\pi}\vec{e} \times B_0\vec{b} = \left(0, \frac{B_0^2 b^2 V_\mathrm{A}}{4\pi}, 0\right) = \left(0, \mathcal{E}V_\mathrm{A}, 0\right) = \mathcal{E}V_\mathrm{A}\vec{n} \quad . \tag{3.43}$$

Consequently, energy is carried in the direction of the unperturbed magnetic field, regardless of the direction of $\vec{k}$, and its magnitude is equal to the product of the energy density by the group velocity.

Magnetoacoustic modes

The other two wave modes are characterized by the phase velocities

$$V_\mathrm{ph}^2 = \frac{V_\mathrm{A}^2 + V_\mathrm{s}^2}{2}\left[1 \pm \left(1 - \frac{4V_\mathrm{A}^2 V_\mathrm{s}^2 \cos^2\psi}{\left(V_\mathrm{A}^2 + V_\mathrm{s}^2\right)^2}\right)^{1/2}\right] \tag{3.44}$$

The $+$ sign corresponds to the fast magnetosound mode, while the $-$ sign corresponds to the slow magnetosound mode. For these modes

$$\vec{v} = (v_\mathrm{x}, v_\mathrm{y}, 0) \quad \Longrightarrow \quad \vec{k}\cdot\vec{v} \neq 0 \quad \Longrightarrow \quad \alpha \neq 0 \tag{3.45}$$

therefore both these waves modes involve compression of the plasma.

The magneto-acoustic waves have many interesting properties, however these properties will not be presented here since the wave mode considered in the stellar wind model to be developed in Chapter 6 is the Alfvén mode.

[4]The energy stored in the perturbation electric field only becomes important for V_A near c.

The WKB approximation

The expressions for the plasma response to a perturbation obtained in the previous Sections rely on the assumption of a uniform background on which the disturbances propagate. However situations of astrophysical interest are not usually uniform. Under what circumstances is it still possible to use the formalism developed so far in these non-uniform media?

The eikonal or WKB approximation (Weinberg, 1962) places the following condition for the applicability of the expressions for uniform media to non-uniform media:

$$hk \gg 1 \tag{3.46}$$

where h is a typical scale length for appreciable variations of the quantities, in particular, the Alfvén speed for the case of Alfvén waves, and k is the wave number. Since $k = 2\pi/\lambda$, being λ the wavelength, then the condition (3.46) is equivalent to:

$$h \gg \lambda \tag{3.47}$$

i.e., the wave sees an almost uniform plasma, and therefore the expressions for uniform plasmas can be applied.

3.1.5 The Alfvén wave flux in a fixed frame of reference

In the previous Sections the frame of reference was a co-moving one, and only a wave at a single frequency was considered. When considering more realistic cases it is convenient to follow the behaviour of the average perturbations due to waves with all allowed frequencies and wavenumbers, in all polarizations, i.e.,

$$\delta B = (\langle \delta B^2 \rangle)^{1/2} \qquad \text{and} \qquad \delta V = (\langle \delta V^2 \rangle)^{1/2} \tag{3.48}$$

where δB is the average wave magnetic field amplitude, δV is the average wave velocity field amplitude.

The energy density flux associated with Alfvén waves has two components: the Poynting flux (Eq. (3.43)) and the advected kinetic energy density due to the velocity perturbations of the plasma,

$$f_{\rm w} = \frac{\langle \delta B^2 \rangle}{4\pi} (V + V_{\rm A}) + \frac{1}{2} \rho \langle \delta V^2 \rangle V \tag{3.49}$$

where V is the velocity of the plasma. It is recalled that in a fixed frame of reference the group velocity for Alfvén waves is $V_{\rm gr} = V_{\rm A} + V$. For Alfvén waves the energy density is equally distributed between the magnetic and the velocity perturbations (cf. Eq. (3.41))

$$\frac{\langle \delta B^2 \rangle}{8\pi} = \frac{1}{2}\rho \langle \delta V^2 \rangle \quad . \tag{3.50}$$

Therefore

$$f_{\rm w} = \frac{\langle \delta B^2 \rangle}{8\pi} \frac{3M_{\rm A} + 2}{M_{\rm A}} V \tag{3.51}$$

where

$$M_{\rm A} = \frac{V}{V_{\rm A}} \tag{3.52}$$

is the Alfvénic Mach number.

3.1.6 Undamped propagation of Alfvén waves

When the Alfvén waves propagate undamped there is no direct wave heating of the plasma, i.e., $Q_{\rm w} = 0$. The vanishing of the wave heating determines the functional form of the wave magnetic amplitude, under spherical symmetry.

Following Hollweg (1973), the wave heating is

$$Q_{\rm w} = -\nabla \cdot \left[\vec{S} + \frac{1}{2}\rho \langle \delta V^2 \rangle \vec{V} \right] + \vec{V} \cdot \nabla \left(\frac{\langle \delta B^2 \rangle}{8\pi} \right) \tag{3.53}$$

where $\vec{S}$ is the Poynting vector (Eq. (3.43)), and is given by

$$\vec{S} = \frac{\langle \delta B^2 \rangle}{4\pi} (\vec{V} \pm \vec{V}_{\rm A}) \tag{3.54}$$

the + sign is for an outward propagating Alfvén wave, while the − sign is for inward propagation.

The term in square brackets in Eq. (3.53) is the energy flux density of the Alfvén waves, its divergence represents the rate at which the waves loose energy to the plasma. Since the waves loose energy by damping (resulting in the conversion of wave energy into thermal energy of the plasma) and also by doing work, the latter effect must be removed from the expression of wave heating, justifying the extra term in Eq. (3.53).

Under spherical symmetry (Eq. (3.53)) becomes

$$Q_{\rm w} = -\frac{1}{R^2}\frac{\mathrm{d}}{\mathrm{d}R}\left[R^2\frac{\langle\delta B^2\rangle}{4\pi}(V+V_{\rm A}) + R^2 V\frac{\langle\delta B^2\rangle}{8\pi}\right] + \frac{V}{8\pi}\frac{\mathrm{d}\langle\delta B^2\rangle}{\mathrm{d}R} \quad . \tag{3.55}$$

In the WKB regime, and for Alfvén waves with small amplitudes ($\langle\delta B^2\rangle < \epsilon B^2$, where ϵ is usually taken to be $1/2$) it is assumed that there is no wave damping, therefore $Q = 0$, i.e.,

$$2VR^2\left(1+\frac{V_{\rm A}}{V}\right)\frac{\mathrm{d}\langle\delta B^2\rangle}{\mathrm{d}R} + 3\langle\delta B^2\rangle\frac{\mathrm{d}(VR^2)}{\mathrm{d}R} + 2\langle\delta B^2\rangle\frac{\mathrm{d}(V_{\rm A}R^2)}{\mathrm{d}R} = 0 \quad . \tag{3.56}$$

From the continuity equation under spherical symmetry,

$$R^2 V\rho = Z \tag{3.57}$$

where Z is a constant, the magnetic induction equation,

$$B = \frac{B_0 R_0^2}{R^2} \quad , \tag{3.58}$$

and the Alfvén velocity (Eq. (3.37)), Eq. (3.56) becomes

$$\frac{\mathrm{d}\ln\left(\langle\delta B^2\rangle\right)}{\mathrm{d}R} - \frac{3}{2}\frac{\mathrm{d}\ln(\rho)}{\mathrm{d}R} + 2\frac{\mathrm{d}\ln}{\mathrm{d}R}\left(1+\frac{V_{\rm A}}{V}\right) \quad . \tag{3.59}$$

This integrates immediately to

$$\frac{\langle\delta B^2\rangle}{\langle\delta B^2\rangle_0} = \left(\frac{\rho}{\rho_0}\right)^{3/2}\left(\frac{1+V_{\rm A_0}/V_0}{1+V_{\rm A}/V}\right)^2 \tag{3.60}$$

where the subscript denotes some reference level R_0, or

$$\frac{\langle\delta B^2\rangle}{\langle\delta B^2\rangle_0} = \frac{M_{\rm A_0}}{M_{\rm A}}\left(\frac{1+M_{\rm A_0}}{1+M_{\rm A}}\right)^2 \quad . \tag{3.61}$$

Introducing

$$F_{\rm w} \stackrel{\rm def}{=} R^2 f_{\rm w} = \frac{\langle\delta B^2\rangle Z}{8\pi\rho}\frac{2+3M_{\rm A}}{M_{\rm A}} \quad , \tag{3.62}$$

and solving for $\langle\delta B^2\rangle_0$, changes Eq. (3.61) to

$$\langle\delta B^2\rangle = \frac{8\pi F_{\rm w_0}}{Z}\frac{\rho M_{\rm A}}{2+3M_{\rm A_0}}\left(\frac{1+M_{\rm A_0}}{1+M_{\rm A}}\right)^2 \tag{3.63}$$

that is the expression to be used in this work for the undamped propagation of Alfvén waves.

Having finished this preliminary presentation, it is now time to begin with the review of stellar wind models starting with the first successful solar wind model: the Parker model.

3.2 Parker's solar wind model

In 1958 Parker published a remarkable article that could be divided in three parts: in the first he showed that a static, hot, solar corona could not exist, in the second he proposed the first hydrodynamic solar wind model and in the third he deduced the shape of the solar magnetic field lines.

3.2.1 The impossibility of a static corona

The solar corona was known to have temperatures in excess of a million degrees, deduced from the observation of highly ionized ions (for example the forbidden lines of Fe XIV).

Parker (1958) computed the thermal pressure at a very large distance from the solar surface arising from a hot ($T_0 = 1.5 \times 10^6$ K) corona in a static equilibrium. This static model uses the classic expression for the thermal conduction ($\kappa(T) \propto T^n$, where $n = 2.5$ for ionized hydrogen) and a temperature profile sufficiently far from the solar surface (where there are no heating sources) given by the heat conduction equation $\nabla \cdot [\kappa(T) \nabla T] = 0$. The resulting thermal pressure at infinity is of the order of $10^{-5}\,\mathrm{dyn\,cm^{-2}}$. This pressure is much larger than a reasonable gas pressure of the interstellar medium of $10^{-13}\,\mathrm{dyn\,cm^{-2}}$. Due to this pressure imbalance the corona must expand.

3.2.2 The solar wind model

In the decade of 1950 Biermann (1957) argued that the solar radiation was not enough to explain the motion of comet tails and that a flow of particles outward from the sun was needed. Based on this arguments and in the impossibility of a static corona, Parker proposed a hydrodynamic solar wind model.

To build his solar wind model, Parker assumed spherical symmetry and an isothermal plasma ($T(R) = T_0$). He used the equations for the perfect gas law, mass continuity and

momentum:

$$P = \frac{nK_{\mathrm{B}}T}{\mu} \tag{3.64}$$

$$nVR^2 = Z = \text{const} \tag{3.65}$$

$$\rho V \frac{\mathrm{d}V}{\mathrm{d}R} = -\frac{\mathrm{d}P}{\mathrm{d}R} - \rho \frac{GM_{\odot}}{R^2} \tag{3.66}$$

where the symbols have their usual meaning, and $\mu = 1/2$ for ionized hydrogen. These equations, together with the isothermal condition, formed the system of equations describing Parker's hydrodynamic solar wind model. A single ordinary differential equation can be obtained from this system of equations, namely

$$\left(V^2 - \frac{2K_{\mathrm{B}}T}{m_{\mathrm{H}}}\right) \frac{1}{V} \frac{\mathrm{d}V}{\mathrm{d}R} = \frac{4K_{\mathrm{B}}T}{m_{\mathrm{H}}R} - \frac{GM_{\odot}}{R^2} \quad . \tag{3.67}$$

At the radial distance R_{c} defined by

$$R_{\mathrm{c}} = \frac{GM_{\star}m_{\mathrm{H}}}{4K_{\mathrm{B}}T_0} \tag{3.68}$$

the right-hand side of Eq. (3.67) is zero, consequently the left-hand side must also vanish. There are two possibilities for this to happen, either

$$V_{\mathrm{c}}^2 = \frac{2K_{\mathrm{B}}T_0}{m_{\mathrm{H}}} \tag{3.69}$$

or

$$\frac{\mathrm{d}V}{\mathrm{d}R} = 0 \quad . \tag{3.70}$$

The point $(R_{\mathrm{c}}, V_{\mathrm{c}})$ is called a critical point, and its properties determine the topology of the possible solutions for Eq. (3.67).

The topology of the solutions for the velocity resulting from the Parker model are shown in Fig. 3.1 where the symbol B marks the position of the critical point. The solutions of type ④ obey condition (3.70) at $R = R_{\mathrm{c}}$. They start with a low value of the velocity at the coronal base, attain a maximum at $R = R_{\mathrm{c}}$ and then decreases for larger distances in region ⓑ. These solutions are called breeze-type solutions. The solutions of type ③ also obey condition (3.70). However they start with a very high (supersonic) velocity at the

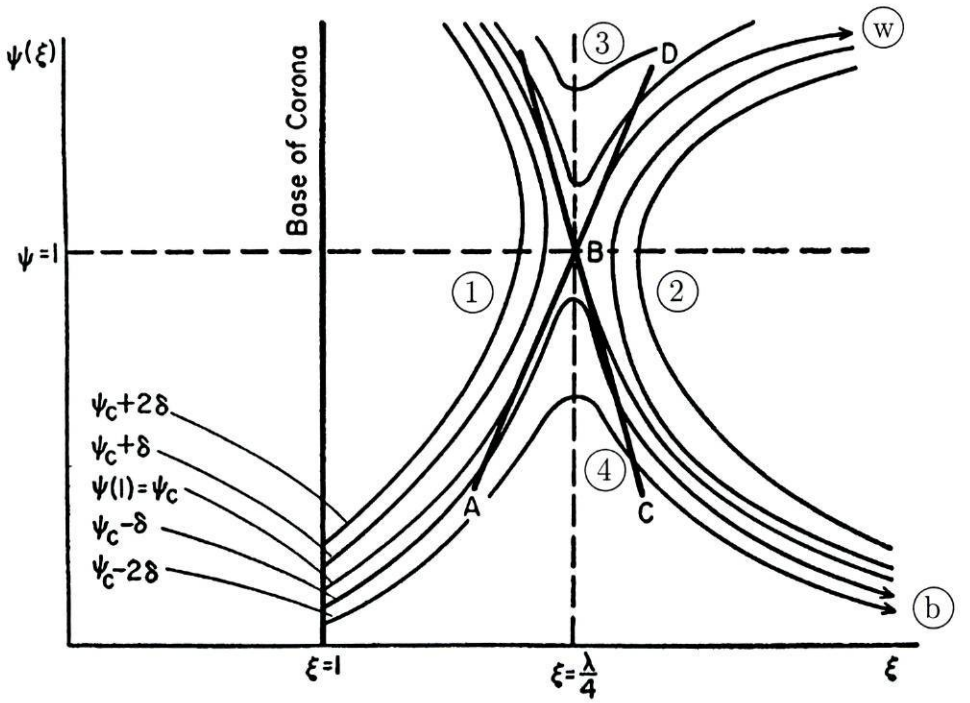

Figure 3.1: Topology of the velocity solutions obtained with the Parker model. The symbols have the following meaning: $\xi = R/R_a$, R_a is the radial distance of the coronal base, $\lambda = GM_\star m_H/(K_B T_0 R_a)$ and $\psi = m_H V^2/(2K_B T_0)$, while the other are explained in the text. This Figure is adapted from Parker (1960).

coronal base, attain a minimum at $R = R_c$ and increase their velocity afterwards. They are ruled out since the observed solar wind velocity at the coronal base is subsonic.

The solutions of type ① are double valued between the stellar surface and a certain $R < R_c$ and do not exist afterwards, while the solutions of type ② do not exist between the stellar surface and a certain $R > R_c$ and are double valued afterwards. The solutions of these two types are therefore ruled out.

The remaining solutions obey condition (3.69) at $R = R_c$, i.e., they cross the critical point. In the case of Parker's solar wind model, and also for the stellar wind models in general, the critical point is an X-type critical point. It is known (Boyce and DiPrima, 1986, for example, and also Appendix A) that an X-type critical point is crossed by two solutions, one with a negative slope and another with a positive slope. The solution with a negative slope can be thought as an accretion solution while the one with a positive slope is called the wind solution. The wind solution starts with a low (subsonic) value of the velocity at the coronal base, labelled $\psi(1) = \psi_c$ in Fig. 3.1, crosses the critical point and attains high (supersonic) values for the velocity at large distances, in region ⓦ. It is appropriate to stress that the critical point acts like a filter: of all the possible solutions it filters just one wind solution connecting the low velocity region near the star to the high velocity region

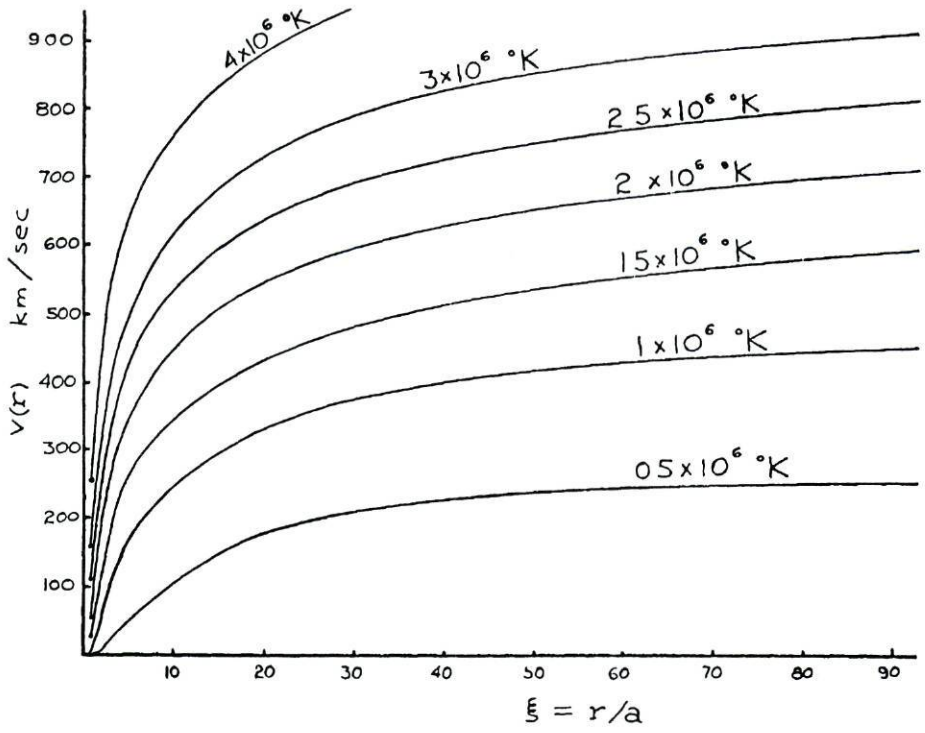

Figure 3.2: Examples of wind velocity profiles obtained with the Parker solar wind model. This Figure is adapted from Parker (1958).

far from the star. Some examples of velocity profiles for the Parker solar wind model are shown in Fig. 3.2.

Although very simple, Parker's solar wind model already displayed some general features of the stellar wind models. One of the most prominent features is the existence of at least one X-type critical point that filters the wind solution from all the possible solutions to the differential equation. In the simple case of a polytropic relation between the gas pressure and density the critical point(s) occurs when the velocity equals one of the characteristic wave speed(s) of the perturbations in the gas. An example where the wind solution crosses three critical points is the Weber and Davis (1967) solar wind model.

3.2.3 Shape of the magnetic field lines

The solar wind is the flow of a highly ionized plasma in a medium permeated by a global magnetic field. It is therefore reasonable to assume the frozen-in approximation, i.e., that particles move along the magnetic field lines. In Parker's model the particles move radially outward, however, as he pointed out, the footpoints of the magnetic field lines are anchored on the solar surface and the sun is itself rotating. The conjunction of these facts results in the shape of an Archimedean spiral for the solar magnetic field lines, as

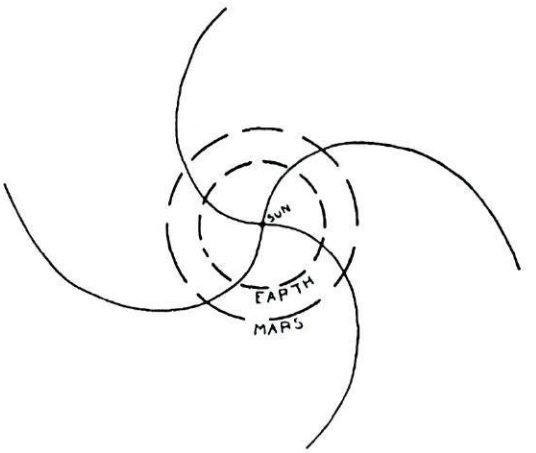

Figure 3.3: Examples of magnetic field lines in the geometry proposed by Parker. This Figure is adapted from Parker (1958).

shown in Fig. 3.3.

3.3 Coronal (conductive) stellar wind models

In an attempt to prove that the selected solution should be one of the breeze solutions, rather than the wind solution, Chamberlain (1961) used a more complete energy equation instead of the isothermal assumption. This energy equation can be written as

$$\frac{\mathrm{d}}{\mathrm{d}R}\left\{R^2\left[\rho V\left(\frac{1}{2}V^2+\frac{A\gamma}{\gamma-1}T-\frac{GM}{R}\right)+q\right]\right\}=0 \tag{3.71}$$

where the first three terms arise from the advection by the flow of the kinetic energy, the enthalpy, the gravitational potential energy, while the last represents the thermal conductivity flux. The classical expression for the thermal conductivity flux (Spitzer, 1956; Spitzer, 1962) with constant κ was used

$$q=-\kappa_0 T^{5/2}\frac{\mathrm{d}T}{\mathrm{d}R} \quad . \tag{3.72}$$

Equations (3.64) to (3.66) complete the wind model. These stellar wind models start at the 'coronal base' the thermal flux from this high temperature region being the source powering the wind. Therefore, these stellar wind models are usually named 'conductive' stellar winds. In this work they are also named 'coronal' stellar winds, since they originate in a hot corona.

The breeze solutions obtained by Chamberlain (1961) from this solar wind model have $P \rightarrow 0$ as $R \rightarrow \infty$, being therefore admissible in this aspect. However, the work of Axford

et al. (1963) showed, based solely on energetic considerations and the presence of a global magnetic field, that the only possible solution was the wind solution.

Nevertheless, the inclusion of an energy equation in the theory of hydrodynamic solar wind models has proved to be fruitful. Noble and Scarf (1963) were the first authors to present wind solutions for these solar wind models. The theoretical study of the system of equations Eqs. (3.64) to (3.66) and (3.71) allowed the formulation of some important results on the behaviour of wind solutions. A major result was the discovery of the asymptotic expansions of the temperature for large R: $T \propto R^{-2/7}$, Parker (1965), $T \propto R^{-2/5}$, Wang and Chang (1965), and $T \propto R^{-4/3}$, Durney (1971). The value of the exponent in the asymptotic expansions depends on the leading term(s) in Eq. (3.71) (Roberts and Soward, 1972). These asymptotic laws for wind solutions and the domain of existence for the breeze solutions were studied in a comprehensive way by Roberts and Soward (1972). Asymptotic expansions for two fluid models (electrons and protons) have also been worked out (Lucas, 1973; Roxburgh, 1974).

Another important result, also relevant for this work, is the existence of upward and downward divergent solutions (Weber, 1970; Couturier, 1977, among others) as shown in Fig. 3.4. This divergent behaviour is characteristic of the numerical procedures of integration that start at the critical point (Cuperman et al., 1975), and is mainly due to the classical form of the thermal conductivity flux (Couturier, 1977).

Another important issue raised by coronal wind models was the form and the value of the thermal conductivity. The first models used the classical (collisional) expression for the thermal conductivity (Spitzer, 1956; Spitzer, 1962) with a constant κ_0. However, as pointed out by Parker (1964) there are reasons to expect the thermal conductivity value to be below the collisional value. This is related with the assumptions made in deriving the classical expression for the thermal conductivity, namely a large number of collisions between the particles, a Maxwellian velocity distribution and the absence of magnetic fields. The main effect of the magnetic field when dealing with the thermal conduction is to channel the thermal conductivity along the magnetic field lines and to prevent it across them. The two other assumptions, the large number of collisions and the Maxwellian distribution, are very good approximations in the low corona near the sun. However, their validity weakens with the distance from the sun.

More arguments for a reduced thermal conductivity came from two fluid solar wind models that treat separately the energy equations for the electrons and for the protons (Hartle and Sturrock, 1968; Durney, 1973). When comparing the results obtained from these wind models with the observations at the earth's orbit it was found that the plasma velocity and the proton temperature were lower than observed, while the electron temperature was higher than observed. This suggested that the electron thermal conductivity should be

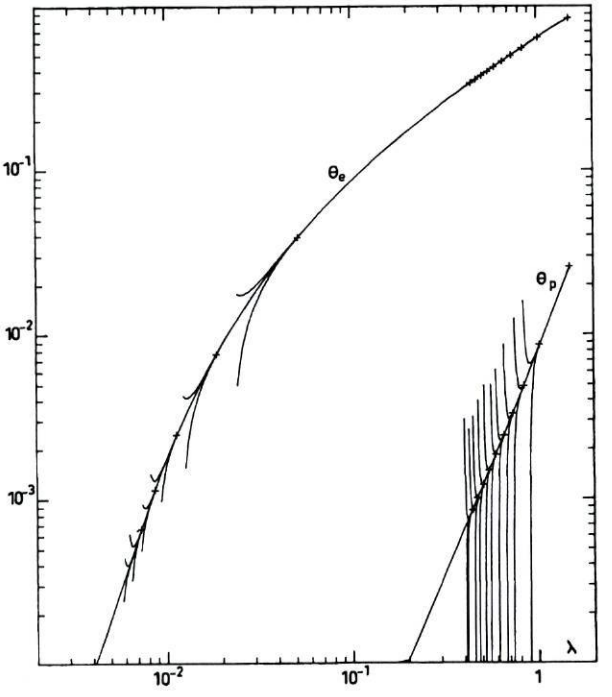

Figure 3.4: Example of the implementation of the shooting-splitting integration method of Couturier. The upward and downward diverging solutions are clearly seen. The symbols are: $\lambda = \dfrac{GM}{\varepsilon_{\mathrm{T}} R}$, $\theta = \dfrac{q}{\rho V \varepsilon_{\mathrm{T}}}$, q given by Eq. (3.72), and ε_{T}, the total energy flux per unit mass, $\varepsilon_{\mathrm{T}} = \dfrac{1}{2}V^2 + \dfrac{A\gamma}{\gamma - 1}T - \dfrac{GM}{R} + \dfrac{q}{\rho V}$, a integral of Eq. (3.71). This Figure is adapted from Couturier (1977).

decreased, while the proton thermal conductivity should be increased, when compared to the collisional values.

This drawback of the theory motivated the study of alternative forms for the thermal conductivity. Cuperman, Harten and Dryer (1972), Cuperman and Metzler (1973; 1975) used an expression of the form $q = -R^{\alpha}\kappa_0 T^{5/2}\,\mathrm{d}T/\mathrm{d}R$, where α is a constant. Hollweg (1974; 1976) has developed a more detailed theory for the thermal conductivity by considering in a qualitative way the interactions between plasma particles and MHD waves, and the escape of the electrons in the high velocity tail of their Maxwellian velocity distribution. He proposed the electron collisionless heat conduction, $q_{\mathrm{e}} = \frac{3}{2} n_{\mathrm{e}} K_{\mathrm{B}} T_{\mathrm{e}} V \alpha$, where α is a constant. The agreement between the models and the observations of the solar wind improved with the inclusion of the non-classical expressions for the thermal conductivity in the solar wind models.

Holzer and Leer (1980) made an exploration of the parameter space for the coronal wind models with collision and collisionless heat conduction, as well as with overspherical expansion. Their main conclusion is for the impossibility of matching simultaneously the observations of the solar wind at the earth's orbit and at the coronal base.

3.3.1 Coronal stellar wind models with Alfvén waves

A different approach to bring the models in better agreement with the observations was to include the effects of MHD waves, and in particular, the effects of the Alfvén waves in solar wind models.

Under spherical symmetry, the momentum equation is modified to include a term due to the Alfvén wave pressure gradient (cf. Eq. (3.66)),

$$\rho V \frac{\mathrm{d}V}{\mathrm{d}R} = -\frac{\mathrm{d}P}{\mathrm{d}R} - \rho \frac{GM_{\odot}}{R^2} - \frac{\mathrm{d}}{\mathrm{d}R}\left(\frac{\langle \delta B^2 \rangle}{8\pi}\right) \tag{3.73}$$

where $\langle \delta B^2 \rangle$ is the average wave magnetic field amplitude, related to the Alfvén wave energy density by

$$\varepsilon_{\mathrm{w}} = \frac{\langle \delta B^2 \rangle}{4\pi} \quad . \tag{3.74}$$

Alazraki and Couturier (1971) and Belcher (1971) have proposed solar wind models with the inclusion of the effects of Alfvén waves in the momentum equation. In both models the authors followed the evolution of the wave amplitude in the WKB limit, without wave damping, i.e., without transfer of energy directly from the waves to the plasma in the

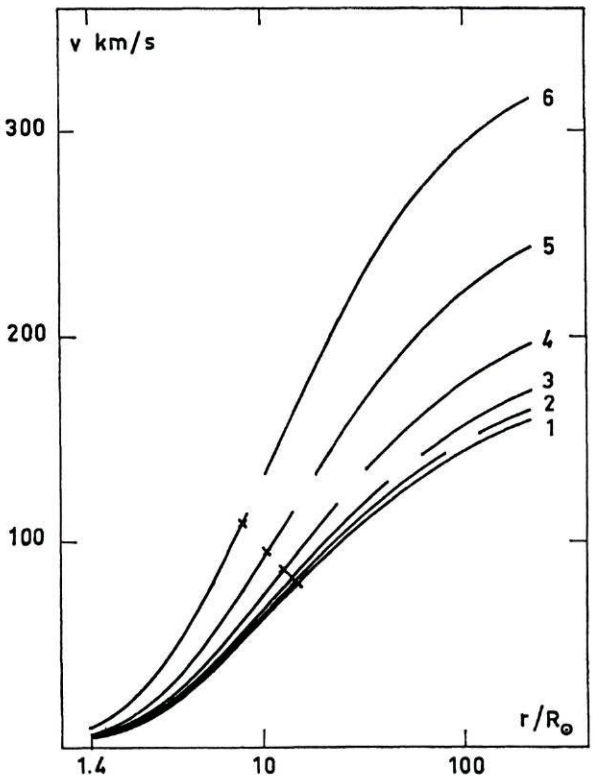

Figure 3.5: Effect of the Alfvén wave pressure gradient on the velocity profiles. Curve labelled '1' has no Alfvén wave flux, while this flux increases from curve labelled '2' to curve labelled '6'. This Figure is adapted from Alazraki and Couturier (1971).

form of heat. In this case $\langle \delta B^2 \rangle \equiv \langle \delta B^2 \rangle_1$ is given by Eq. (3.63). Those authors did not consider any damping mechanism for the Alfvén waves and have used a polytropic relation ($P \propto \rho^\alpha$, α a constant) as the energy equation. The equations for the perfect gas law (Eq. (3.64)), mass continuity (Eq. (3.65)) and magnetic flux conservation

$$B\,R^2 = \text{const} \tag{3.75}$$

close the system of equations describing both solar wind models.

The main conclusion of both works is shown in Fig. 3.5, that is, the Alfvén wave pressure gradient helps driving the solar wind causing the terminal velocity to increase relative to models without Alfvén waves. The other positive feature of the models was the existence of wind solutions for values of the base temperature (T_0) lower than those possible in solar wind models without Alfvén waves. Also the agreement between the model predictions at the coronal base and at the earth's orbit with the observations improved (Belcher, 1971).

Hollweg (1973) proposed a two-fluid (electrons and protons) solar wind model with the inclusion of Alfvén waves as sources of momentum and energy. He also treated the wave propagation in both the undamped and the damped regimes. The energy equation had

the form

$$\frac{\mathrm{d}}{\mathrm{d}R}\left\{R^2\left[\rho V\left(\frac{1}{2}V^2+\frac{A\gamma}{\gamma-1}T_\mathrm{s}-\frac{GM}{R}\right)+q_\mathrm{s}+f_\mathrm{w}\right]\right\}=\pm R^2 H_\mathrm{T} \tag{3.76}$$

where H_T is the energy transfered between the electrons and the protons, and the subscript 's' denotes the species (protons or electrons) concerned. Equation (3.76) is not the most suitable for the analysis, the following form being preferred

$$\rho V\frac{K_\mathrm{B}}{\mu m_\mathrm{H}}\left(\frac{1}{\gamma-1}\frac{\mathrm{d}T_\mathrm{s}}{\mathrm{d}R}-T_\mathrm{s}\frac{\mathrm{d}\ln(\rho)}{\mathrm{d}R}\right)=-\frac{1}{R^2}\frac{\mathrm{d}}{\mathrm{d}R}\left((R^2 q_\mathrm{s})\right)+Q_\mathrm{ws}\pm H_\mathrm{T} \tag{3.77}$$

where Q_w is the heating by the Alfvén waves

$$Q_\mathrm{w}=V\frac{\mathrm{d}}{\mathrm{d}R}\left(\frac{\langle\delta B^2\rangle}{8\pi}\right)-\frac{1}{R^2}\frac{\mathrm{d}}{\mathrm{d}R}\left((R^2 f_\mathrm{w})\right)\quad . \tag{3.78}$$

Hollweg (1973) assumed that the Alfvén waves directly heated only the protons, i.e., $Q_\mathrm{we}=0$, $Q_\mathrm{wp}=Q_\mathrm{w}$, and that the thermal conductivity flux was solely due to the electrons, i.e., $q_\mathrm{e}=q$, $q_\mathrm{p}=0$. He further assumed that the magnetic wave amplitude was limited to a certain fraction of the ambient magnetic field

$$\frac{\langle\delta B^2\rangle_\mathrm{B}}{B^2}=\epsilon^2 \tag{3.79}$$

i.e., when $\langle\delta B^2\rangle_1<\langle\delta B^2\rangle_\mathrm{B}$ then $\langle\delta B^2\rangle=\langle\delta B^2\rangle_1$ (Eq. (3.63)), and when $\langle\delta B^2\rangle_1>\langle\delta B^2\rangle_\mathrm{B}$ then $\langle\delta B^2\rangle=\langle\delta B^2\rangle_\mathrm{B}$. The first condition was met near the sun and in this region the Alfvén waves propagate undamped ($Q_\mathrm{w}=0$), while at larger distances from the sun the second condition was met and the waves damped, directly heating the protons ($Q_\mathrm{w}>0$).

Some representative results of Hollweg (1973) are shown in Fig. 3.6. In this Figure the profiles of T_e, T_p, V and n are shown for some values of the Alfvén wave energy flux. The most prominent feature is the sharp rise of the proton temperature at the point where damping of the Alfvén waves starts. This abrupt rise of the temperature is a characteristic of stellar wind models that divide the space in regions with undamped propagation of the waves and regions with damped propagation, without intermediate regions in between.

The good features of this solar wind model are the increase of the proton temperature and the decrease of the electron temperature far from the sun (at earth's orbit) when compared to wind models without the inclusion of Alfvén waves. And, as already known from the works of Alazraki and Couturier (1971) and Belcher (1971), the flow speed also increases. These effects represent changes in better agreement with the observations.

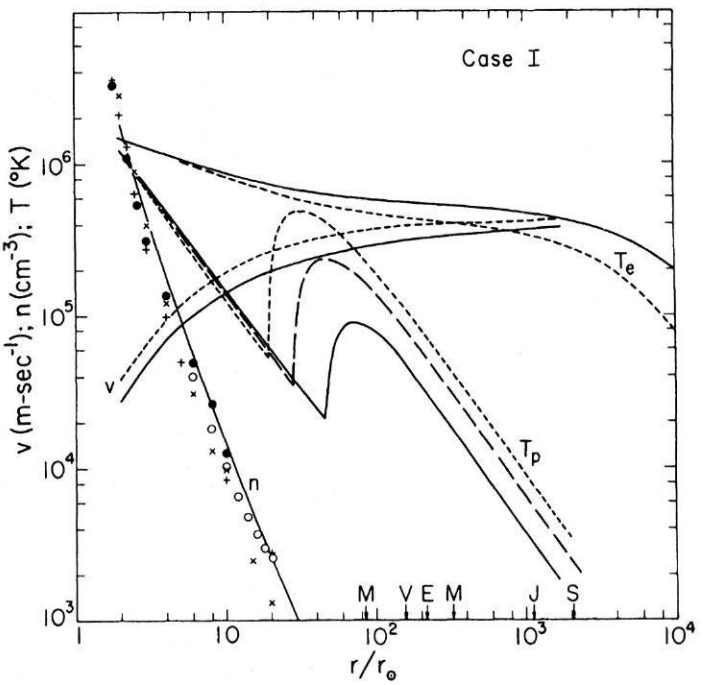

Figure 3.6: Effect of the Alfvén wave energy flux on the electron and proton temperatures (T_e and T_p), velocity and number density profiles. The Alfvén wave energy flux increases from the solid lines (—), to the long-dashed lines (– –), to the dashed lines (---). This Figure is adapted from Hollweg (1973).

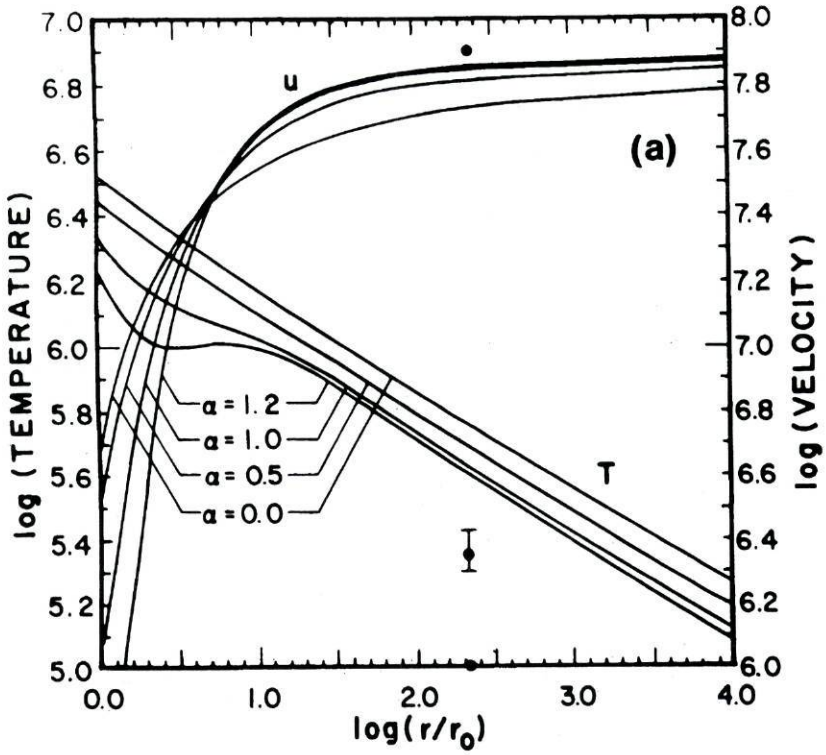

Figure 3.7: Effect of the Alfvén wave energy flux on the temperature and velocity. The quantity α is proportional to the Alfvén wave energy flux. This Figure is adapted from Jacques (1978).

Jacques (1977) presented the formalism for the inclusion of the effects of all types of MHD waves in stellar wind models. He later applied this formalism to a one fluid spherically symmetric solar wind model with Alfvén waves (Jacques, 1978). He used Eq. (3.73) for the momentum equation, and Eq. (3.76) without subscript 's' and with $H_{\rm T} = 0$, as the energy equation. To guarantee a smooth transition from undamped to damped propagation of Alfvén waves the following combination of the wave magnetic amplitudes (Eqs. (3.63) and (3.79)) was used

$$\langle \delta B^2 \rangle = \frac{\langle \delta B^2 \rangle_{\rm I} \langle \delta B^2 \rangle_{\rm B}}{\langle \delta B^2 \rangle_{\rm I} + \langle \delta B^2 \rangle_{\rm B}} \quad . \tag{3.80}$$

Some examples of temperature and velocity profiles obtained with this model are shown in Fig. 3.7. Comparison of the temperature profiles with those of $T_{\rm p}$ in Fig. 3.6 shows that the former are much smoother. As in the work of Hollweg (1973) the values of T, V and n obtained with the model were in good agreement with the observations.

More details of the coronal wind models can be found on the works of Holzer (1977), Holzer and Leer (1980), Esser et al. (1986), Tu (1987) and Sandbæk and Leer (1994).

3.4 Stellar wind models with a detailed energy equation

A further step was given by Hammer (1982a; 1982b) with a model for the energy balance of the solar corona. The energy equation of this model can be written as

$$\frac{\mathrm{d}}{\mathrm{d}R}\left\{R^2\left[\rho V\left(\frac{1}{2}V^2+\frac{A\gamma}{\gamma-1}T-\frac{GM}{R}\right)+q\right]\right\}=R^2\left(H_\mathrm{m}-n^2\chi T^\alpha\right) \tag{3.81}$$

where $n^2\chi T^\alpha$ represents the radiative losses in the optically thin regime and H_m is the mechanical volumetric heating rate. Since the coronal heating mechanism was poorly known, a prescribed negative exponential form was chosen[5]

$$H_\mathrm{m}=H_0\exp\left(-\frac{R-R_0}{L}\right) \tag{3.82}$$

where L is the damping length. This model was not static, but used Eq. (3.67) as the momentum equation. The equations of continuity and the perfect gas law complete the system of equations describing the model. Therefore this model unifies the two related fields of coronal heating and energy balance to the field of solar wind models.

Hammer was mostly interested in the coronal energy balance and not in the solar wind. Nevertheless, his work showed that it was possible to extend solar wind models to the transition region ($T\sim 10^4$-10^5 K) and not just to the 'coronal base' ($T\sim 10^6$ K).

Hollweg (1986) proposed a one-fluid solar wind model with the inclusion of Alfvén waves using Eq. (3.73) as the momentum equation and Eq. (3.81) as the energy equation. However, he proposed that the coronal heating was due to the dissipation of Alfvén waves in a turbulent cascade, the heating rate being governed by the equation

$$E_\mathrm{H}\equiv H_\mathrm{m}=\frac{\Gamma\rho\langle\delta V^2\rangle^{3/2}}{L_\mathrm{corr}} \tag{3.83}$$

where Γ is a dimensionless constant of order one and L_corr is a measure of the correlation length of the Alfvén waves. In this model the Alfvén waves were assumed to cascade from small wave numbers to large wave numbers, being then absorbed by the plasma as heat, in a Kolmogorov-type turbulence.

To simplify the numerical problem the equations were solved in the equatorial plane. The cross section of the flux tube was assumed to be that deduced by Munro and Jackson (1977) for a polar coronal hole. Inside $10\,R_\odot$ the magnetic field was assumed to be radial and the classical form of the thermal conductivity flux was used, while outside $10\,R_\odot$ the

[5] In Hammer's notation it is $\int H_\mathrm{m}$ that is given by Eq. (3.82)

magnetic field would have the spiral shape deduced by Parker (1958) and the collisionless form of of the thermal conductivity flux (Hollweg, 1976) was used.

The results obtained were qualitatively correct, in the sense of mimicking the temperature profiles of the transition region and corona, and a mass loss rate in agreement with the observed value. However, the models that fit well the observations at the base of the wind give a poor fit to the observations at the earth's orbit, and vice-versa.

An improvement to the model of Hollweg (1986) was developed by Hollweg and Johnson (1988). This is a two-fluid model, where the electrons and protons are assumed to be coupled through Coulomb collisions inside $2\,R_\odot$, i.e. $T_\mathrm{e} = T_\mathrm{p}$, but completely decoupled outside $2\,R_\odot$. They further assume that outside $2\,R_\odot$ the waves heat only the protons. The results were essentially the same as those of Hollweg (1986), i.e., it was not possible to fit simultaneously the observations at the base of the wind and at 1 a.u. in a reasonable manner.

Withbroe (1988) proposed a solar wind model with the following energy equation

$$\frac{\mathrm{d}}{\mathrm{d}R}\left\{R^2\left[\rho V\left(\frac{1}{2}V^2+\frac{A\gamma}{\gamma-1}T-\frac{GM}{R}\right)+q+f_\mathrm{w}\right]\right\}=R^2\left(H_\mathrm{m}-n^2\chi T^\alpha\right)\quad . \tag{3.84}$$

This energy equation has two energy sources: a mechanical energy source of the form given by Eq. (3.82) and the Alfvén wave energy flux. The dissipation length L in the volumetric mechanical heating was kept small and the Alfvén wave propagation assumed to occur in the undamped regime (Eq. (3.63)) throughout the wind. With this choice of parameters the initial push on the plasma was provided by the mechanical heating, while the effect of the Alfvén waves was to increase the terminal velocity of the wind. The momentum equation was of the form of Eq. (3.73) and the system of equations was closed by the perfect gas law equation and the mass continuity equation. The thermal heat conduction was given by the classical form between the base of the wind and 5–10 $R_\odot$, depending on the model, and thereafter by the collisionless expression proposed by Hollweg (1976).

With this model, Withbroe was able to fit reasonably well the observations both near the solar surface and at the earth's orbit. This hinted that solar wind models with a complete energy equation should use two different energy sources, one acting very near the base of the wind to give the initial accelerating and heating of the plasma, and another further out, whose effects are still felt outward of the critical point, to increase the plasma terminal velocity.

Another solar wind model following this line of investigation was proposed by Cuseri et al. (1999). The model includes the effects of Alfvén waves resulting from the mechanism of gravitational damping proposed by Khabibrakhmanov and Mullan (1994). Cuseri et al.

(1999) used the perfect gas law, the mass continuity equation and a momentum equation of the form

$$\rho V \frac{\mathrm{d}V}{\mathrm{d}R} = -\frac{\mathrm{d}P}{\mathrm{d}R} - \rho \frac{GM_\odot}{R^2} - \frac{\langle \delta V^2 \rangle}{V_\mathrm{A}^2} \frac{\mathrm{d}P}{\mathrm{d}R} \quad . \tag{3.85}$$

Comparison of the previous equation with Eq. (3.73) shows that they have neglected the term due to the Alfvénic wave pressure gradient and have included a term due to the gravitational damping of Alfvén waves. The neglect of the Alfvénic pressure gradient is justified by the authors on the grounds that this term is important far from the sun, when the plasma has already a high velocity, while the aim was the driving mechanism that initiates the plasma heating and acceleration. The energy equations for protons has the form

$$\rho V \frac{K_\mathrm{B}}{\mu m_\mathrm{H}} \left(\frac{1}{\gamma - 1} \frac{\mathrm{d}T_\mathrm{p}}{\mathrm{d}R} - T_\mathrm{p} \frac{\mathrm{d}\ln(\rho)}{\mathrm{d}R} \right) = -\frac{1}{R^2} \frac{\mathrm{d}}{\mathrm{d}R} \left((R^2 q_\mathrm{p}) \right) + H_\mathrm{m} + Q_\mathrm{wg} + H_\mathrm{T} \tag{3.86}$$

and that for the electrons

$$\rho V \frac{K_\mathrm{B}}{\mu m_\mathrm{H}} \left(\frac{1}{\gamma - 1} \frac{\mathrm{d}T_\mathrm{e}}{\mathrm{d}R} - T_\mathrm{e} \frac{\mathrm{d}\ln(\rho)}{\mathrm{d}R} \right) = -\frac{1}{R^2} \frac{\mathrm{d}}{\mathrm{d}R} \left((R^2 q_\mathrm{e}) \right) + H_\mathrm{m} - n_\mathrm{e}^2 \chi T^\alpha - H_\mathrm{T} \tag{3.87}$$

where Q_wg is the heating due to the gravitational damping of the Alfvén waves, H_m is the volumetric mechanical energy input, of the form $H_\mathrm{m} = H_0 \exp(-(R - R_\odot)^2/\sigma^2)$, and H_T is the energy transfer between the electrons and the protons. The analysis of these energy equations shows that the gravitational damping was assumed to directly heat the protons, while the electrons were responsible for the radiative losses. It was further assumed that, when present, the mechanical energy input caused the heating of the electrons and the protons equally.

The fit to the observations was reasonable both at the wind base and at the earth's orbit. The best fit to the observations included a contribution from the mechanical energy input near the base of the wind.

More aspects of the stellar wind models with a detailed energy equation can be found in the works of Wang (1993; 1994), Sandbæk et al. (1994), and Sandbæk and Leer (1995).

3.5 Some analytical MHD stellar wind models

An alternative to the stellar wind models reviewed in the previous sections is to find wind solutions by solving the MHD equations under some reasonable simplifying assumptions.

The stellar wind models that will be described use the steady state equations of ideal MHD. The relevant equations for these models are (cf. Eqs. (3.23) to (3.28))

$$
\begin{aligned}
& P = \frac{K_{\mathrm{B}}}{\mu m_{\mathrm{H}}} \rho T \\
& \nabla \cdot (\rho \vec{V}) = 0 \\
& \rho \left(\vec{V} \cdot \nabla \right) \vec{V} = -\nabla P - \rho \frac{GM}{R^2} \hat{e}_{\mathrm{r}} + \frac{\left(\nabla \times \vec{B} \right) \times \vec{B}}{4\pi} \\
& \nabla \cdot \vec{B} = 0 \\
& \nabla \times \vec{B} = \frac{4\pi}{c} \vec{J} \\
& \vec{E} = -\frac{\vec{V} \times \vec{B}}{c} \\
& \nabla \times \left(\vec{V} \times \vec{B} \right) = 0 \quad .
\end{aligned}
\tag{3.88}
$$

The first successful solar wind model of this type was that of Weber and Davis (1967). They assumed complete axysymmetry while the MHD equations were only solved on the equatorial plane. Under these simplifying assumptions the only independent variable was the radial distance from the stellar centre. They used a polytropic relation between the gas pressure and density ($P \propto \rho^{\alpha}$).

In this model the radial component of the momentum equation was reduced to

$$
\begin{aligned}
& \frac{\mathrm{d}V_{\mathrm{r}}}{\mathrm{d}R} = \frac{\mathcal{N}}{\mathcal{D}} \\
& \mathcal{N} = \frac{V_{\mathrm{r}}}{R} \left\{ \left(\frac{2\alpha P_*}{\rho_* M_{\mathrm{A}}^{2(\alpha-1)}} - \frac{GM_{\odot}}{R} \right) \left(M_{\mathrm{A}}^2 - 1 \right)^2 + \right. \\
& \qquad \left. \Omega^2 R^2 \left(\frac{V_{\mathrm{r}}}{V_{\mathrm{r}}^*} - 1 \right) \left[\left(M_{\mathrm{A}}^2 + 1 \right) \frac{V_{\mathrm{r}}}{V_{\mathrm{r}}^*} - 3M_{\mathrm{A}}^2 + 1 \right] \right\} \\
& \mathcal{D} = \left[\left(V_{\mathrm{r}}^2 - \frac{\alpha P_*}{\rho_* M_{\mathrm{A}}^{2(\alpha-1)}} \right) \left(M_{\mathrm{A}}^2 - 1 \right)^3 - \Omega^2 R^2 M_{\mathrm{A}}^2 \left(\frac{R_*^2}{R^2} - 1 \right) \right] \quad .
\end{aligned}
\tag{3.89}
$$

where Ω is the angular velocity of the magnetic field lines at the sun, R_* and V^* are the position and velocity of the Alfvénic critical point. This differential equation has three critical points: the slow and fast magnetosonic and the Alfvénic critical points. The topology is shown in Fig. 3.8. Due to the existence of three critical points the topology is rather complex, nevertheless, the two X-type critical points are filtering just one wind solution from all the possible solutions. The wind solution is labelled $u_{\alpha 1}$ in Fig. 3.8.

Weber and Davis selected boundary conditions at earth's orbit and the fit to the observed values near the sun was very poor. Nevertheless this solar wind model allowed the direct

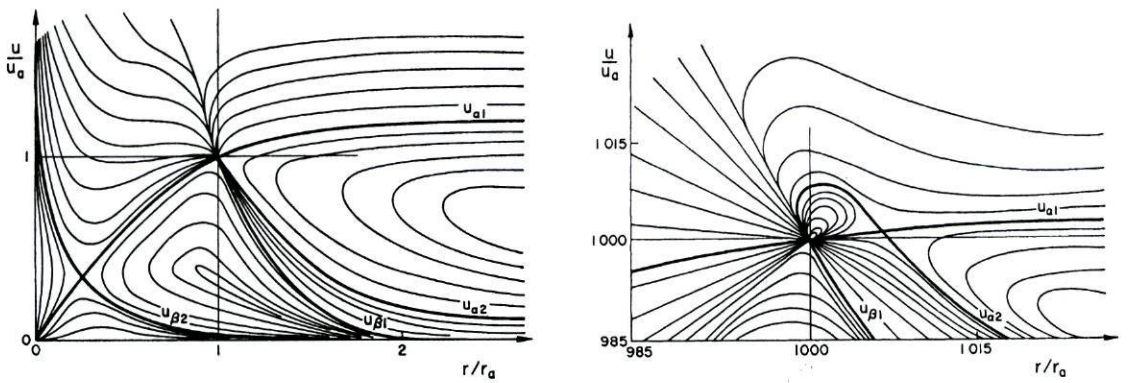

Figure 3.8: Topology of the velocity solutions from the Weber and Davis solar wind model. These Figures are adapted from Weber and Davis (1967).

computation of the angular momentum loss from the sun through the expression

$$\frac{\mathrm{d}J_\odot}{\mathrm{d}t} = \frac{3}{2}\Omega R_*^2 \frac{\mathrm{d}M_\odot}{\mathrm{d}t} = -\frac{J_\odot}{\tau} \tag{3.90}$$

where $J_\odot$ is the the total angular momentum of the sun, and τ is a characteristic time for the variations of $J_\odot$. From the values appropriate to their solar wind model they found $\tau \sim 7 \times 10^9$ years, a reasonable value when compared to the solar age of about 5×10^9 years. These results hinted that the magnetic torque was very important in removing angular momentum from the sun.

The Weber and Davis solar wind model has some major drawbacks, namely, the equations are solved only on the equatorial plane and in fact it is only valid for cylindrical stars (Suess and Nerney, 1973; Nerney and Suess, 1975) to avoid meridional flows. Nevertheless, this stellar wind model is still used in stellar evolutionary models (MacGregor and Brenner, 1991; Soderblom et al., 1993) to give the rate of angular momentum loss from the surface layers of the star. The motivations are its simplicity and the correct order of magnitude for the changes of the solar angular momentum. An exploration of the space parameter of the Weber and Davis solar wind model has been made by Belcher and MacGregor (1976).

An independent and more complete MHD solar wind model has been proposed by Mestel (1968a). This model was axisymmetric but not restricted to the equatorial plane. It was further developed (Mestel, 1968b; Mestel and Selley, 1970) to include the effects of the magnetic axis being inclined to the rotation axis of the star, the oblique rotator model.

A different approach to solve the MHD equations is to assume that only one of the coordinates is ignorable, instead of considering two ignorable coordinates (spherical symmetry). It can then be proved that some exact integrals of the MHD equations can be found (Tsinganos, 1981; Tsinganos, 1982). Tsinganos and co-workers (Low and Tsinganos, 1986; Tsinganos and Low, 1989; Hu and Low, 1989; Tsinganos and Trussoni, 1990; Tsinganos

and Trussoni, 1991; Trussoni and Tsinganos, 1993; Tsinganos and Sauty, 1992a; Tsinganos and Sauty, 1992b; Sauty and Tsinganos, 1994; Trussoni et al., 1997; Sauty et al., 1999; Lima et al., 2001) have followed this line of research and built several analytical stellar wind models by assuming an ignorable ϕ-coordinate (no ϕ-dependence or axysymmetry). Either by carefully choosing the functional form of some quantities, like $\vec{V}$, $\vec{B}$, ρ and P, and in particular their co-latitudinal (θ) dependence, using a magnetic field with both open and closed field regions, or by deducing more general functional forms of those same quantities with co-latitude using now a magnetic field with only open field lines, they were able to built self-consistent stellar wind models that extended to all space around the star. The energetics of the flow were studied *a posteriori* using the first law of thermodynamics.

A good review of MHD stellar wind models can be found in Sauty (1993) and Sauty and Tsinganos (1994).

The stellar wind model of Tsinganos and Trussoni (1991) will be studied in more detail in next section.

3.6 The stellar wind model of Tsinganos and Trussoni (1991): application to TTS

The stellar wind model of Tsinganos and Trussoni (1991) is studied in more detail by two main reasons: one of its input parameters is a measure of the stellar rotation rate, and to test the routine of integration HEMODES (Nobili and Turolla, 1988). From the results of the previous Chapter it was concluded that TTS are mostly slow rotators. Nevertheless, some TTS have $v \sin i > 50\,\mathrm{km\,s^{-1}}$ and this stellar wind model can be used to learn about the effects of the rotation rate in the dynamics of the winds for these faster rotating TTS.

In this stellar wind model the various quantities are assumed to be separable functions of the independent variables[6] r and θ, i.e.,

$$f(r,\theta) = f_1(r) \cdot f_2(\theta) \tag{3.91}$$

The radial velocity, the radial magnetic field and the mass density have the following functional forms

$$V_\mathrm{r}(R,\theta) = V_0 Y(R) \frac{\cos\theta}{[1+\omega\sin^2\theta]^{1/2}} \tag{3.92}$$

$$B_\mathrm{r}(R,\theta) = \frac{B_0}{R^2}\cos\theta \tag{3.93}$$

[6]The original notation of Tsinganos and Trussoni (1991) will be used in this Section

$$\rho(R,\theta) = \frac{\rho_0}{Y(R)R^2}[1+\omega\sin^2\theta] \tag{3.94}$$

where $R = r/r_0$ is the adimensional radial coordinate, in terms of the stellar radius (r_0), and Eq. (3.94) defines the input parameter ω. This parameter determines the overdensity of the equatorial plasma to the polar plasma.

By assuming that the angular momentum efflux (angular momentum loss rate per infinitesimal solid angle at the angle θ) has the form

$$\dot{l}(\theta) = \lambda\beta^2\rho_0 V_0^2 r_0^3 \cos\theta \sin^2\theta \tag{3.95}$$

where

$$\beta = \frac{V_{A_0}}{V_0} \qquad \text{and} \qquad V_{A_0} = \frac{B_0}{\sqrt{4\pi\rho_0}} \tag{3.96}$$

where V_{A_0} is the base Alfvén speed, and the parameter β can be used as a measure of the stellar magnetic field. Using this in the MHD equations result in the following azimuthal components of the velocity and magnetic fields

$$V_\phi(R,\theta) = \lambda V_0 \frac{R\sin\theta}{[1+\omega\sin^2\theta]^{1/2}} \frac{Y_* - Y(R)}{1-M_A^2} \tag{3.97}$$

$$B_\phi(R,\theta) = \lambda B_0 \frac{\sin\theta}{R} \frac{R^2/R_*^2 - 1}{1-M_A^2} \tag{3.98}$$

where

$$M_A^2 = \left(\frac{V_r}{V_A}\right)^2 = \frac{YR^2}{\beta^2} \tag{3.99}$$

is the Alfvénic Mach number. There exists a point $R = R_*$ where $M_A = 1$, i.e.,

$$Y_* R_*^2 = \beta^2 \quad . \tag{3.100}$$

This equation defines the normalized velocity Y_*, and Eq. (3.97) defines the input parameter λ. This parameter is a measure of the stellar rotation rate.

By further assuming that the gas pressure can be separated in two components of the form:

$$P(r,\theta) = P_0(r) + P_1(r)\sin^2\theta \tag{3.101}$$

a single first order differential equation for Y(R) is obtained:

$$\frac{\mathrm{d}Y}{\mathrm{d}R} = \frac{F(R,Y)}{G(R,Y)} \tag{3.102}$$

where

$$F = \frac{\omega\nu^2}{YR^4} - \frac{4\beta^2}{R^5} + \frac{2\lambda^2 Y}{RM_{\mathrm{A}}^2(1-M_{\mathrm{A}}^2)^2}\left[\frac{(2M_{\mathrm{A}}^2-1)}{M_{\mathrm{A}}^2}\frac{R^4}{R_*^4} - (3M_{\mathrm{A}}^2-2)\right] \tag{3.103}$$

$$G = \frac{2}{R^2} - \frac{\lambda^2}{(1-M_{\mathrm{A}}^2)^2}\left[\frac{(2M_{\mathrm{A}}^2-1)}{M_{\mathrm{A}}^4}\frac{R^4}{R_*^4} - 1\right] \tag{3.104}$$

and

$$\nu = \frac{\sqrt{2GM/r_0}}{V_0} \tag{3.105}$$

is the ratio of the escape speed to the radial velocity at the polar base.

Equation (3.102) has two critical points, with coordinates (R,Y) for which $F(R,Y) = G(R,Y) = 0$, i.e., points where the differential equation has an indetermination of type 0/0. The critical point closest to the stellar surface is the Alfvénic critical point, where $M_{\mathrm{A}}^2 = 1$. Its topology is of type node, and is denoted by (R_*, Y_*). The other critical point is located farther out and topologically is an X-type critical point. It is denoted $(R_{\mathrm{x}}, Y_{\mathrm{x}})$. As already mentioned, the X-type critical point will filter and select the wind type solution from all the possible solutions.

3.6.1 Topology of the velocity solutions

The topology of the solutions to Eq. (3.102) is shown in Fig. 3.9. Due to the existence of two singular points the global topology is rather complex. Nevertheless, the analysis of the wind-type solutions (the thick lines in each plot) shows that the initial plasma acceleration is stronger for the low-β models. Observational results, for example Mundt (1984), suggest that the wind of some TTS in his sample experiences a strong acceleration near the base, namely for the TTS DG Tau, As 205, AS 353A, Lk H_α 321 and V 1331 Cyg. This result motivates the study of the low-β models, that is the subject of next section.

3.6.2 Some applications of the stellar wind model

The first example of the wind solution from the stellar wind model of Tsinganos and Trussoni is an example presented by the authors in page 164 of their article. For a star

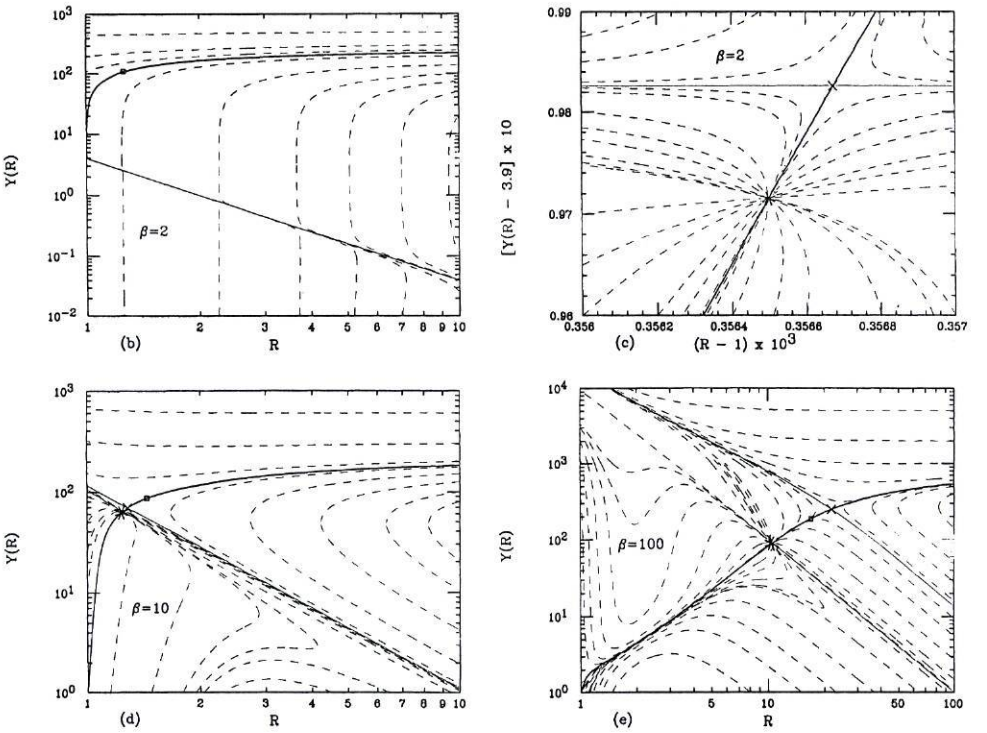

Figure 3.9: Examples of the topology of the velocity solutions obtained with the Tsinganos and Trussoni stellar wind model. This Figure is adapted from Tsinganos and Trussoni (1991).

with solar mass and radius and the input parameters $\omega = 4$, $\beta = 2$, $\lambda = 0.5$, $\nu = 120$, $n_0 = 5 \times 10^8\,\mathrm{cm}^{-3}$ the position of the critical points and two values of the plasma velocity are shown in the first data row of Table 3.1, while the profiles of the velocity, number density, thermal pressure and the plasma temperature (computed from the perfect gas law, Eq. (3.64)) are displayed by the solid lines in Fig. 3.10. It is seen that the plasma experiences a large initial acceleration, and that the temperature profile mimics well the transition region, where the temperature raises from $\sim 2 \times 10^5$ K to $\sim 10^7$ K within a short distance, although the maximum temperature is higher than typical coronal values.

Table 3.1 also shows the positions of the critical points which occur very near the base for these low-β models, and two values of the plasma velocity for wind models with one of the input parameters (ν, λ, orβ) changed. Analysis of this Table shows that changes in ν or λ induce small changes on the solutions, while the increment of β induces a larger change. The profiles of temperature, number density, velocity and thermal pressure from this last model are shown in Fig. 3.10 (dotted lines). Comparison of the two models displayed in Fig. 3.10 shows that the model with $\beta = 4$ has a smaller value of $T_{\max}$ (although the temperature becomes higher for larger distances) and has a velocity profile slightly below that of the model with $\beta = 2$, except near the base, as shown in Table 3.1.

The parameter β is proportional to the stellar magnetic field (Eq. (3.96)). TTS are usually

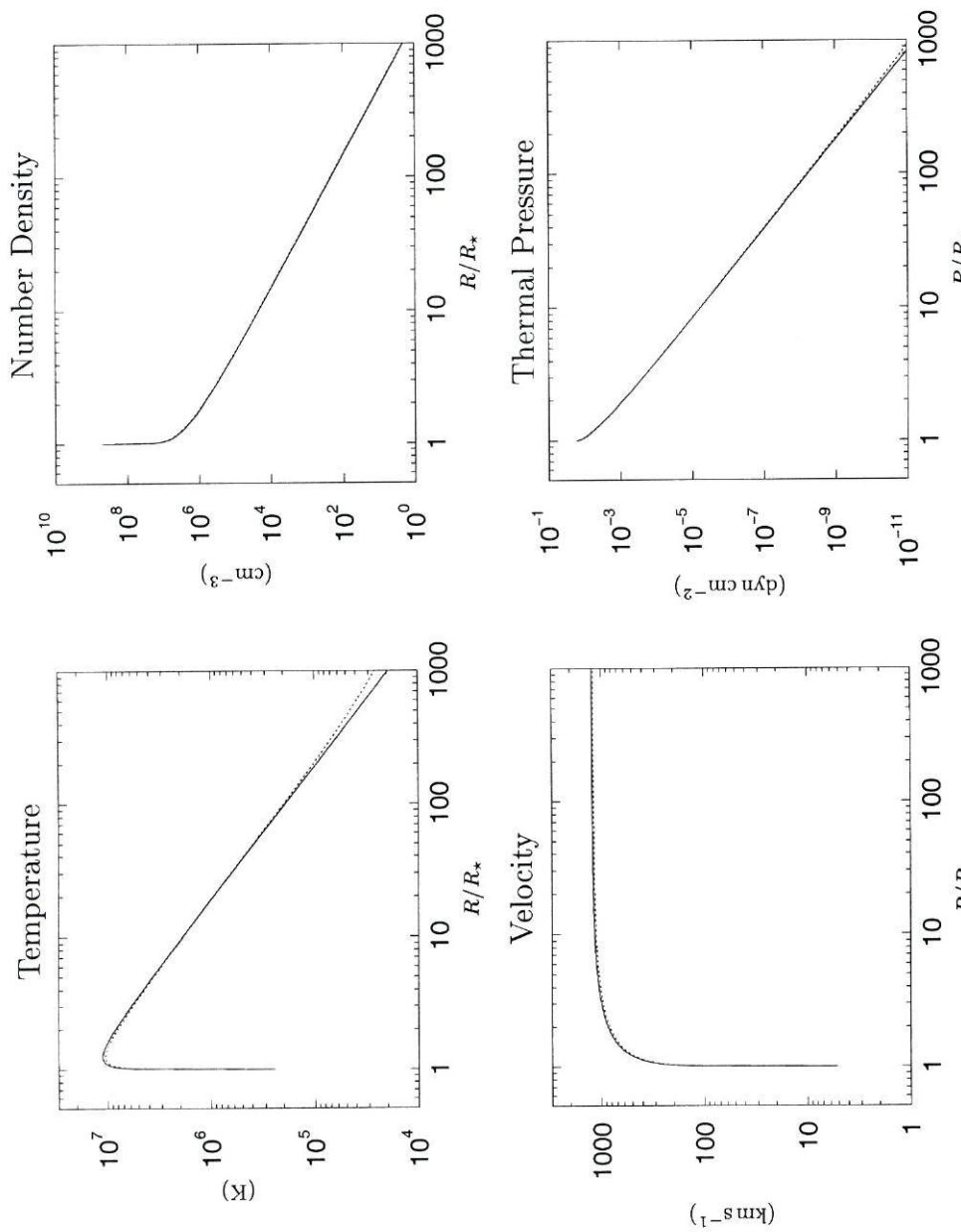

Figure 3.10: Effects in the profiles of temperature, number density, velocity and thermal pressure when β is increased. The following values of the input parameters are common to both models: $r_0 = R_\odot$, $M_\star = M_\odot$, $\omega = 4$, $\lambda = 0.5$, $\nu = 120$, $n_0 = 5 \times 10^8\,\mathrm{cm}^{-3}$. (—): $\beta = 2$, $(\cdots)$: $\beta = 4$.

ν	λ	β	R_*	R_x	$V_r(R=1)$ ($km\,s^{-1}$)	$V_r(R=1000)$ ($km\,s^{-1}$)
120	0.5	2	1.0003565	1.0003567	5.14	1223
90	0.5	2	1.0006338	1.0006344	6.86	1220
120	1	2	1.0006449	1.0006458	5.15	1222
120	0.5	4	1.00743266	1.00747648	5.15	1188

Table 3.1: Normalized radial distance from the stellar centre of the Alfvén critical point (R_*) and the X-type critical point (R_x), as well as the radial velocity at the base and at a distance of 1000 stellar radii.

assumed to have large surface magnetic fields, of the order of several hundred Gauss and more. Some measurements giving values above one kiloGauss have been made (Guenther et al., 1999). These facts motivate the study of a more magnetized model, and the results for a model with $\beta = 10$ are shown in Fig. 3.11. From the analysis of this Figure, the major drawback of the model comes from the temperature profile, as the temperature remains very high at large distances from the stellar surface. This behaviour of the temperature is not observed in the solar wind, thus preventing the use of the solar analogy.

Concerning the stellar rotation rate, the value 0.5 for the parameter λ is adequate for the sun, with a rotation rate $\sim 2\,km\,s^{-1}$. TTS are mostly slow rotators, nevertheless a significant fraction of them has rotation rates several times above the solar value. Therefore, higher values of the parameter λ seem adequate for TTS. Two models with larger values of λ are shown in Fig. 3.12. From the analysis of the profiles of velocity it is seen that the initial acceleration and the terminal velocity of the wind decrease with increasing rotation rate. The temperature profile of the model with $\lambda = 10$ starts to develop a high temperature region far from the star, as in the model shown in Fig. 3.11 for $\beta = 10$.

From the various examples shown it can be concluded that this is not the most appropriate stellar wind model for TTS. The major drawback is the high temperature at very large distances from the stellar surface obtained from the models with higher surface values for the magnetic field, as well as for the models with rotation rate several times larger than the solar value.

3.7 Winds from T Tauri stars

This Section deals with the winds of TTS, both the observations and the proposed models are reviewed.

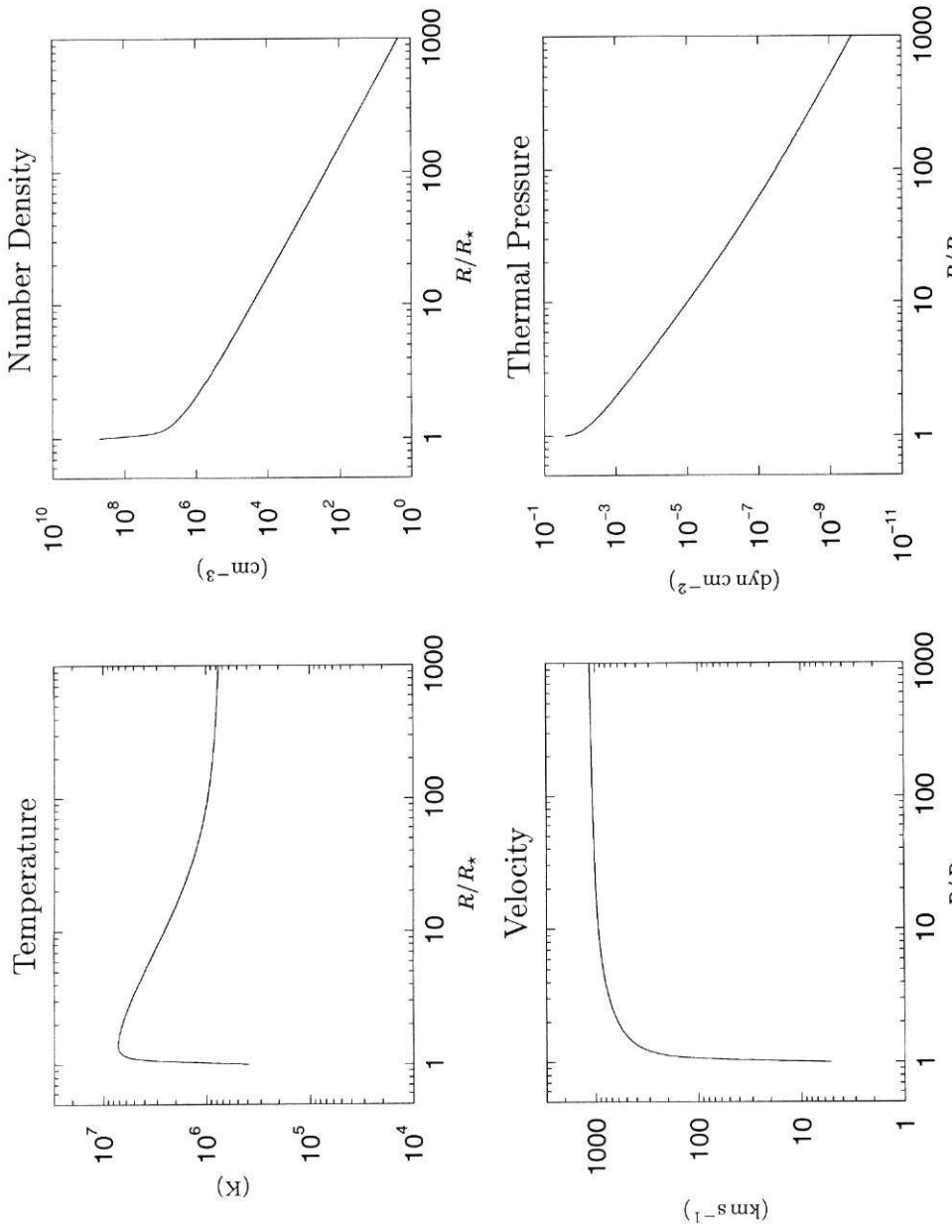

Figure 3.11: Profiles of temperature, number density, velocity and thermal pressure for the model with the following values for the input parameters: $r_0 = R_\odot$, $M_\star = M_\odot$, $\omega = 4$, $\beta = 10$, $\lambda = 0.5$, $\nu = 120$, $n_0 = 5 \times 10^8\,\mathrm{cm}^{-3}$.

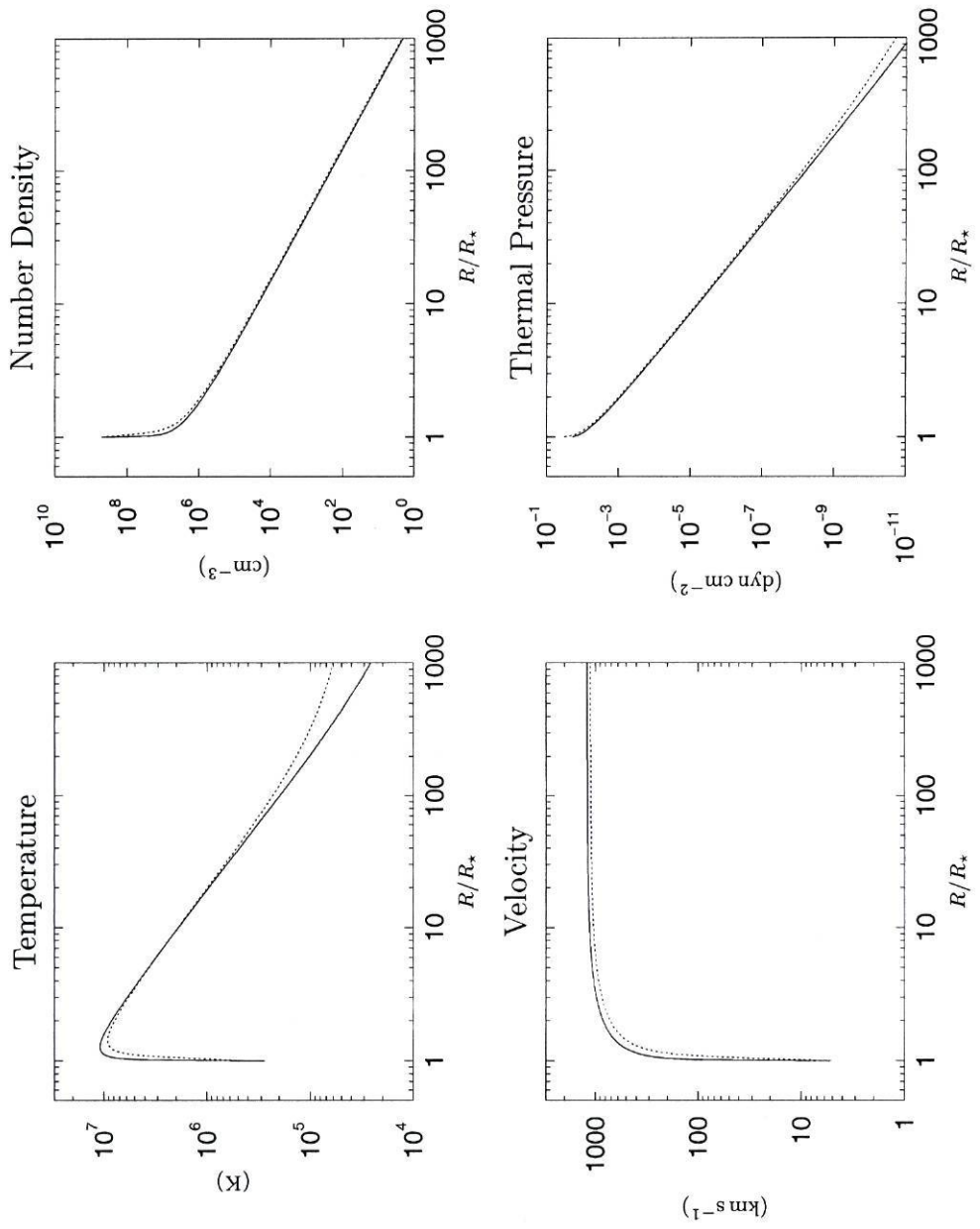

Figure 3.12: Profiles of temperature, number density, velocity and thermal pressure for the models with the following values for the input parameters in common: $r_0 = R_\odot$, $M_\star = M_\odot$, $\omega = 4$, $\beta = 2$, $\nu = 120$, $n_0 = 5 \times 10^8\,\mathrm{cm}^{-3}$. (—): $\lambda = 4$, $(\cdots)$: $\lambda = 10$.

3.7.1 The observations

One of the most compelling evidences for the existence of winds in TTS is the classical P Cygni profile displayed by some spectral lines in about 30% of the stars classified as TTS (Natta, 1989). Namely, the optical lines of H_α, Ca II H and K and the Na I doublet (Kuhi, 1964; Hartmann, 1982; Mundt, 1984), and the UV lines of Mg II and Fe II (Lago, 1988). The classical P Cygni profile is easily explained in terms of an expanding spherical wind, as shown by Beals (1950, his type I profile).

The detailed study of the Na I D profiles of some TTS led Mundt (1984) to conclude for a strong initial acceleration of the stellar wind. The observed line profiles show that the velocity at the red edge of emission (V_R) is smaller than that of the blue edge of the P Cygni absorption (V_B), i.e., $|V_R| < |V_B|$. If this 'asymmetry' is due to occultation effects, as the author argues, then the Na I D lines are formed within one stellar radii above the stellar surface. In four of the stars the absorption component of the P Cygni profile is very broad (FWHM $\sim$ 100–200 $\mathrm{km\,s^{-1}}$), therefore suggesting a very strong initial plasma acceleration.

Another evidence for the existence of winds in the TTS is the presence of forbidden lines of low ionization species in the spectra of about 20% of the TTS (Natta, 1989). Examples of these forbidden lines are: [O I] λ6300Å, [S II] $\lambda\lambda$6717, 6731Å, [N II] λ6584Å and [F II] $\lambda\lambda$4069, 4076Å (Lago, 1982; Jankovics et al., 1983; Appenzeller et al., 1984; Edwards et al., 1987). These lines are formed in low density regions ($n_e \sim 10^5$–$10^6\,\mathrm{cm^{-3}}$ (Lago, 1982)) occurring in the outer regions of a stellar wind, under the reasonable assumption of a density profile that decreases with distance. These lines are very broad, being the most cited cause for this line broadening the flow velocity of the particles. Under this assumption the velocities derived are in the range 100–150 $\mathrm{km\,s^{-1}}$ (Penston and Lago, 1982; Edwards et al., 1987).

There is also evidence for flows of cold neutral matter near young stellar objects as observed in radio and IR lines, see for example the review by Lada (1985) and the article by Giovanardi et al. (1992).

Another piece of evidence for the existence of winds from TTS comes from their X-ray emission. There are many X-ray emitting sources in and around star forming regions (Neuhäuser et al., 1995; Neuhäuser, 1996; Alcalá et al., 1997; Neuhäuser et al., 1997; Preibisch, 1997; Gregorio-Hetem et al., 1998; Grosso et al., 2000; Wichmann et al., 2000) although not all of them are TTS (Favata et al., 1997). Nevertheless, there are confirmed X-ray emitting TTS and it is pertinent to recall that the WTTS were mainly discovered by their X-ray emission.

The origin of the TTS X-rays remains a matter of debate. This is particularly true for

the CTTS, for which the two most cited causes are thermal origin in a hot corona, or in an accretion shock. The hot corona hypothesis is based on a scaled up version of the solar corona that radiates in the X-ray range due to its temperature in excess of one million degrees Kelvin. The accretion shock origin for the X-rays relies on the common picture for the CTTS system, namely, the interaction between a star and a circumstellar disk. These two pictures for the origin of the TTS X-ray emission are discussed in Guenther et al. (2000, and references therein). In this article the authors also present observations in several wavelength ranges for the WTTS V773 Tau that led them to conclude for the hot corona origin of the X-ray emission of this TTS.

The proposed corona of this WTTS, and the eventual corona of other TTS, must be larger than the solar corona. As pointed out by Schmitt et al. (1995) the sensibility of the ROSAT all-sky survey (RASS) allows the detection of a corona like the solar corona within a distance of 9.20 pc. Nevertheless, the X-ray emission of TTS is detected with the same instrument out to hundreds of parsecs away from the source. Therefore, the TTS are much stronger X-ray emitters than the sun. And, indeed, the X-ray luminosity of the detected TTS (Gahm, 1980; Montmerle et al., 1983; Alcalá-Estrada, 1995; Preibisch, 1997; Costa, 2000, for example) is 10^2–10^3 higher than the solar maximum value of $2 \times 10^{27}\,\mathrm{erg\,s^{-1}}$ (Schmitt et al., 1995).

If the TTS have a hot corona then, as for the solar case (Parker, 1958), it is difficult, if not impossible, to maintain the corona in static equilibrium. Therefore, the TTS X-ray emission is an indirect evidence for the existence of a stellar wind in TTS.

The line profiles of some TTS are very complex and difficult to interpret. Some authors have argued that this complexity is partially due to the simultaneous existence of outflow (a stellar wind) and inflow (accretion) of matter around these TTS (Calvet et al., 1992; Natta, 1992; Beristain et al., 2001). The more detailed models proposed for the TTS RU Lupi (Lamzin et al., 1996) and SU Aur (Petrov et al., 1996) also invoke both inflow and outflow of matter.

The same complexity of TTS line profiles led Grinin and Mitskevich (1991) to propose the stochastic stellar wind models. In these models the wind is not continuous, but is rather constituted by a series of 'blobs' that emanate from the stellar surface. At any given time only about 10% of the stellar surface acts as a source of the wind. These blobs must have the property of being accelerated until a certain distance above the stellar surface, and being thereafter decelerated, implying that the velocity attains a maximum.

3.7.2 The models

There are several stellar wind models with different assumptions about the wind structure that have been proposed to explain the observed properties of TTS, from radio to X-ray wavelengths. These stellar wind models can be grouped in three main categories: solar-like wind models, neutral wind models and stochastic wind models.

Solar-like stellar wind models

One of the first sets of stellar wind models proposed for the TTS was that of DeCampli (1981). The equations describe a steady state stellar wind for a rotating star with a global magnetic field. The forces responsible for driving the wind are: the thermal pressure gradient, the Lorentz force, the gravitational force and the pressure gradient due to the Alfvén waves. However, due to the complexity of the equations describing the model, DeCampli showed only examples where the star was assumed to be non-rotating, which resulted in a spherical symmetric geometry of the model. It was further assumed that the thermal pressure and the mass density were related by a polytropic law: $P = K\rho^{\gamma}$, where both K and γ are constant. Two of the examples shown were isothermal, with a wind temperature equal to 17 000 K, while in the other example it was assumed a polytropic relation between the temperature and the mass density. In all examples the Alfvén waves were assumed to propagate undamped until their amplitude becomes comparable to the amplitude of the global magnetic field, at which point they were assumed to rapidly dissipate.

With this framework, DeCampli was able to present stellar wind models with a high initial acceleration, and a relatively low terminal speed of the order of $300\,\mathrm{km\,s^{-1}}$, following the observations of the line widths. In all the models the velocity at the critical point was assumed to be around $83\,\mathrm{km\,s^{-1}}$. These wind models were able to explain some of the properties of the TTS winds, namely the high number density in excess of $10^{12}\,\mathrm{cm^{-3}}$ at the base of the wind, although other properties, such as the X-ray emission, remained unexplained, since the wind temperature was too low to generate thermal X-rays. And, of course, no constrain on the wind thermal structure could be given as the temperature law was prescribed.

Hartmann et al. (1982) proposed a stellar wind model that also assumed a steady state and spherical symmetry, as well as the propagation of Alfvén waves. However it included an energy equation, and therefore the thermal structure of the wind is now an output of the model and not an input for it. The energy equation was split in two parts: near the base of the wind the energy input due to the dissipation of the Alfvén waves is 'lost' by radiation, while further out a more complete energy equation comprising the terms due to

the kinetic energy flux, enthalpy energy flux, gravitational potential energy flux, Alfvén wave energy flux and the radiation losses was used. The Alfvén waves were assumed to dissipated with a constant damping length, starting at the base of the wind, therefore damping was always present. The radiative losses had the same functional form as the analytical fit of Rosner et al. (1978), namely, $N_e N_H \Lambda(T)$, where $\Lambda(T)$ was tabulated by the authors for the temperature range $3.70 < \log T < 5.4$. Thermal conduction was ignored in this stellar wind model, mainly due to the low temperature[7] achieved by the plasma.

Some examples of application of their stellar wind model were presented. Two common characteristics of those examples are the high stellar surface magnetic field strength, with B_0 of a few hundred Gauss, and the very high base Alfvén wave energy flux, ranging from 3.8×10^9 to $4.2 \times 10^{10}\,\mathrm{erg\,cm^{-2}\,s^{-1}}$. These values can be compared with the typical solar values of 1 G and $10^5\,\mathrm{erg\,cm^{-2}\,s^{-1}}$, respectively. The initial acceleration of the wind was very high, as the plasma attains a velocity exceeding $100\,\mathrm{km\,s^{-1}}$ within 2 stellar radii. The terminal velocity was assumed to be around $200\,\mathrm{km\,s^{-1}}$. These wind models could not explain either the X-ray emission from the TTS.

Two later articles (Hartmann et al., 1990; Calvet et al., 1992) used one of the velocity profiles resulting from the stellar wind model of Hartmann et al. (1982) to compute several line profiles and compare them with observed line profiles. The main result from these studies was that it is difficult to explain simultaneously all line profiles with a single wind model. This may result from the poor knowledge of the physical and geometrical conditions in the line emission region, as well as from the difficulties in the atomic structure computations and the approximations made to overcome them.

Lago (1984) followed the solar wind model developed by Belcher (1971) and applied it to the TTS RU Lupi. This was a one-fluid, steady state, spherically symmetric, non-rotating wind model. The temperature was assumed to be constant and equal to 10^4 K, and the Alfvén waves were assumed to propagate in the WKB limit. The Alfvén waves propagate undamped near the stellar surface and were damped further out, when their amplitude became comparable to that of the ambient magnetic field.

Based on observations, the plasma velocity was required to reach $240\,\mathrm{km\,s^{-1}}$ at a distance of $0.4\,R_0$ above the reference level R_0. This implied a strong acceleration of the plasma, although, a visual inspection of Figures 4 and 7 in this work, seem to indicate that the plasma has already a high velocity at the reference level. This model does not explain the X-ray emission for the TTS, although this is not a major drawback for RU Lupi, since X-rays were not detected from this star (Lamzin et al., 1996, and references therein).

All previous stellar wind models have low plasma temperatures, not exceeding 10^5 K, and

[7]The computer code written by the authors to implement this stellar wind model could not handle wind temperature in excess of 10^5 K.

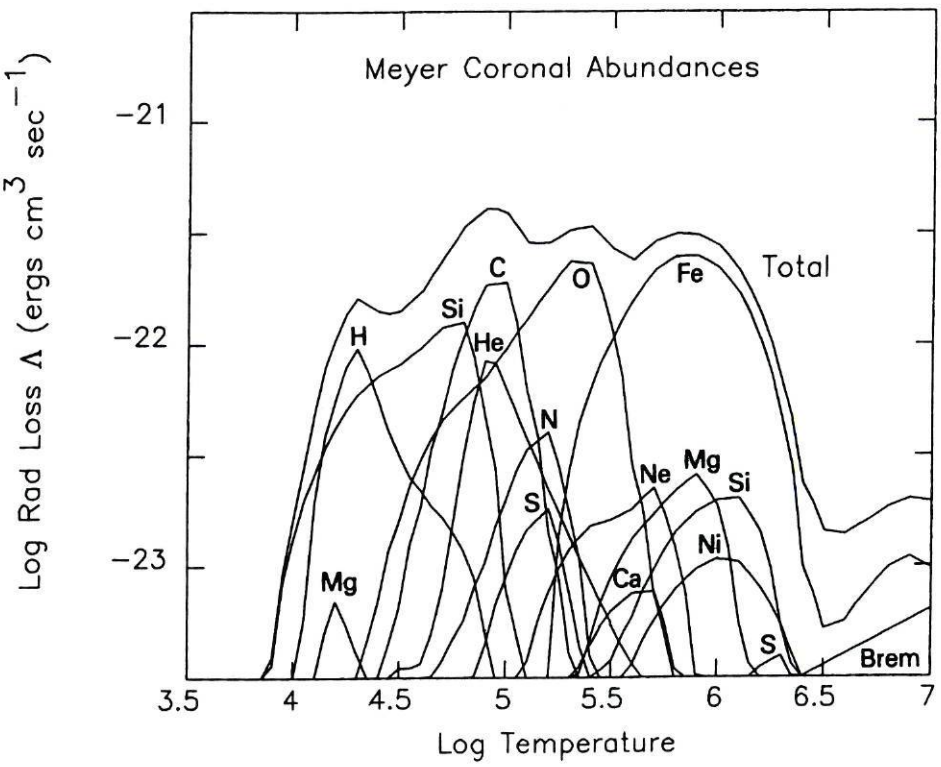

Figure 3.13: Contribution from several elements and from bremsstrahlung to the radiative loss function. This Figure is adapted from Cook et al. (1989).

consequently unable to account for the X-ray emission of TTS. In an attempt to explain the TTS X-ray emission through a high temperature stellar wind, Kiguchi et al. (1998) developed a stellar wind model with an energy equation. The chosen energy equation has terms due to the kinetic energy flux, enthalpy energy flux, gravitational energy flux and thermal conductivity flux, complemented by a mechanical heating law and the radiative losses. The mechanical heating law has the usual form of a negative exponential. The radiative losses included only the term due to bremsstrahlung, corresponding to a cooling rate per unit volume and time that is proportional to the square root of the plasma temperature, $\Lambda \propto T^{1/2}$. This radiative cooling is adequate for high plasma temperatures, although it misses the features due to the line and continuum emission from elements like H, C, O or Fe, as shown in Fig. 3.13.

Two of the examples shown by the authors are for a star with $M_\star = M_\odot$ and $R_\star = 2\,R_\odot$. From the values of Table 2 in Kiguchi et al. (1998) it is found that the number density at the base is approximately $10^{13}\,\mathrm{cm}^{-3}$, for $T_0 = 10^4\,\mathrm{K}$. The figures shown do not present directly the velocity profiles but rather the equivalent temperature (T_{eqv}) defined as

$$T^{\mathrm{v}}_{\mathrm{eqv}} = \frac{\mu m_{\mathrm{H}}}{K_{\mathrm{B}}} v^2 \qquad \text{and} \qquad T^{\mathrm{s}}_{\mathrm{eqv}} = \frac{\mu m_{\mathrm{H}}}{K_{\mathrm{B}}} c_{\mathrm{s}}^2 \tag{3.106}$$

where μ is the mean molecular weight, m_{H} is the mass of the hydrogen atom, K_{B} is the

$\log(T^{\rm v}_{\rm eqv})$	v (km s^{-1})
6.0	128.5
7.0	406.3
7.6	810.7
7.8	1021.
8.0	1285.

Table 3.2: Conversion between $\log(T^{\rm v}_{\rm eqv})$ and v for some values of $\log(T^{\rm v}_{\rm eqv})$, as defined in Kiguchi et al. (1998).

Boltzmann constant, v is the plasma velocity and $c_{\rm s}$ is the isothermal sound velocity, i.e.

$$c_{\rm s}^2 = \frac{K_{\rm B}T}{\mu m_{\rm H}} \tag{3.107}$$

where T is the plasma temperature. From these two equations it is readily seen that the plasma temperature and the equivalent temperature for the isothermal sound speed are the same. Analysis of Figure 6 in Kiguchi et al. (1998) shows that the plasma temperature increases from 10^4 K at the base of the wind to over 10^7 K within 0.05 $R_\star$ above the stellar surface. The conversion between $\log(T^{\rm v}_{\rm eqv})$ and v for some values of $\log(T^{\rm v}_{\rm eqv})$ is given in Table 3.2. Analysis of this Table and Figure 6 of the cited article shows that the plasma has been accelerated to a velocity exceeding 400 km s^{-1} within 0.05 $R_\star$ above the stellar surface, and to over 800 km s^{-1}, or even 1000 km s^{-1} for model 2, at 0.284 $R_\star$ above the stellar surface.

Both the very fast increase in the plasma temperature and its strong initial acceleration have the same cause, namely the form of the radiative losses. As already mentioned, the authors have only considered radiative losses due to bremsstrahlung, and these only dominate over other forms of radiation loss (in the optically thin regime) at high temperatures ($T > 10^7$ K), being a minor contributor at lower temperatures, as hinted in Fig. 3.13 and clearly seen in Fig. 3.14. Consequently the radiative losses are (severely) underestimated near the base of the wind, which results in more energy being available to heat and accelerate the plasma.

Neutral stellar wind models

This section presents the stellar wind models developed by Natta, Giovanardi and coworkers (Natta et al., 1988a; Natta et al., 1988b; Natta and Giovanardi, 1990). They developed neutral wind models, which are mostly neutral, and therefore low-temperature, where the gas temperature ($T_{\rm g}$) is below 10^4 K in their isothermal wind models.

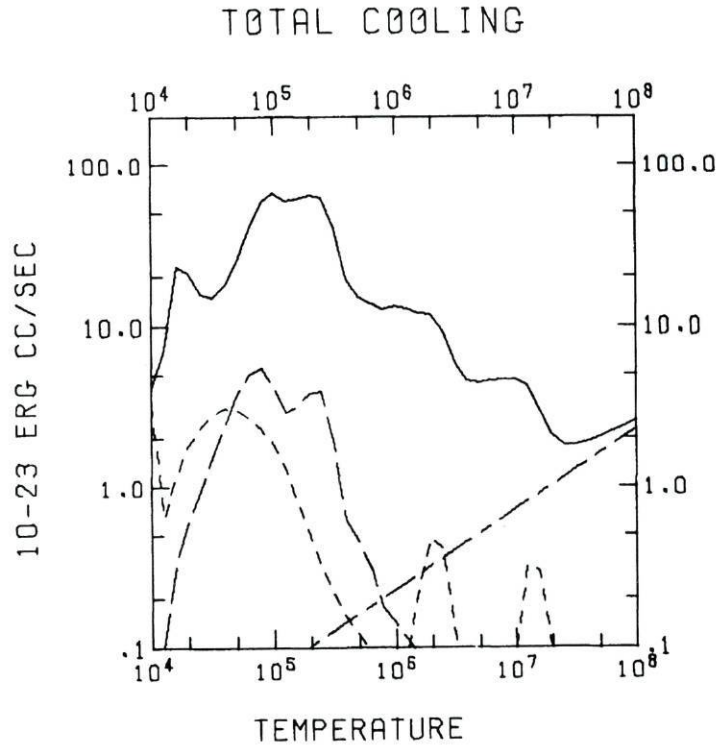

Figure 3.14: Radiative loss function. (——): total cooling; (- - -): forbidden line cooling; (— — —): semiforbidden line cooling; (- — - —): bremsstrahlung. This Figure is adapted from Raymond et al. (1976).

These models are peculiar, in the sense that the velocity profile is not an output of the model, but is rather prescribed as an input. Therefore a question arises: are these true stellar wind models or are they radiative transfer codes in a moving medium where both the velocity and temperature profiles are prescribed? The latter interpretation seems to be favoured by the authors themselves.

The velocity law is of the form

$$v = v_0 + v_1 \left(1 - r^{-\alpha}\right) \tag{3.108}$$

where v_0 is the velocity at the base of the wind, v_1 is the terminal velocity minus v_0, $r = R/R_0$ is the radial distance in units of the radial position of the base of the wind, and α is a parameter describing the initial acceleration of the gas: $\alpha = 0.5$ results in a slow initial acceleration, while $\alpha = 2$ results in a strong initial acceleration. These models assume a spherical symmetric geometry and a mass density given by the continuity equation ($R^2 \rho v = \text{const}$).

These models enabled Natta and co-workers (Natta et al., 1988a; Natta and Giovanardi, 1990) to compute the luminosity in the Br_α line, as well as to model the Na I D line profiles, and to infer values for T_g ranging from 5900 to 6500 K and $\dot{M}$ from $4{\times}10^{-8}$ to $3{\times}10^{-7}\, M_\odot\, \text{yr}^{-1}$, for a sample of five TTS.

Stochastic stellar wind models

Motivated by the complex line profiles of some TTS, and their interpretation, Grinin and Mitskevich (1991) have proposed stochastic stellar wind models. In these models the gas motion is along the radial direction, however, contrary to the usual assumption, the flow is not continuous but is rather constituted by a series of dense 'blobs' of gas, as shown in Fig. 3.15. To have a mathematically and numerically tractable problem the space between the blobs is considered empty.

They have considered a simplified version of the momentum equation to describe the dynamics of the gas, with a term due to the gravitational force and another one due to a prescribed accelerating force whose nature is not precise,

$$V \frac{\mathrm{d}V}{\mathrm{d}R} = -\frac{GM_\star}{R^2} + f(R_\star) \exp\left(-\frac{\frac{R}{R_\star} - 1}{L}\right) \quad , \tag{3.109}$$

$f(R_\star)$ is the value of the accelerating force at the stellar surface, L is the damping length, and the other symbols have their usual meaning. The non-inclusion of the term due to the thermal pressure gradient force in this momentum equation has two main consequences.

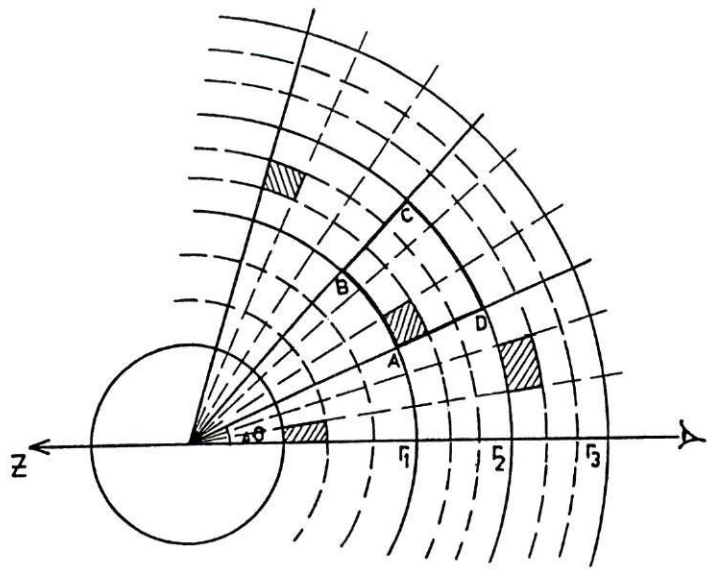

Figure 3.15: Geometry used for the stellar wind model of Grinin and Mitskevich. The 'blobs' are represented by the shaded areas. This Figure is adapted from Grinin and Mitskevich (1991).

First, Eq. (3.109) has not a critical point where regularity conditions are imposed, and second, it is possible to find an analytic solution for the equation, namely

$$V^2 - V_0^2 = V_{\rm esc}^2 \left(\frac{R}{R_\star} - 1 \right) - V_{\rm f}^2 \left[\exp\left(- \frac{\frac{R}{R_\star} - 1}{L} \right) - 1 \right] \quad , \tag{3.110}$$

where the escape speed is

$$V_{\rm esc}^2 = \frac{2GM_\star}{R_\star} \tag{3.111}$$

and $V_{\rm f}$ is

$$V_{\rm f}^2 = LR_\star f(R_\star) \quad , \tag{3.112}$$

V_0 being the gas velocity at the base of the wind, chosen to be equal to $30\,{\rm km\,s^{-1}}$, therefore allowing the use of the Sobolev method to compute the line profiles. The velocity profile defined by Eq. (3.110) is shown in Fig. 3.16. It starts with $V = V_0$ at the stellar surface, attains a maximum and decreases afterwards, with $V_\infty = 0$. This value for the terminal velocity is possible due to the inexistence of a critical point and its implied regularity conditions[8]. With their choice of terms in the momentum equation (Eq. (3.109)) the

[8]In next Chapter it will be seen that the 'wind' solution can have $V_\infty = 0$ when the momentum equation has two critical points

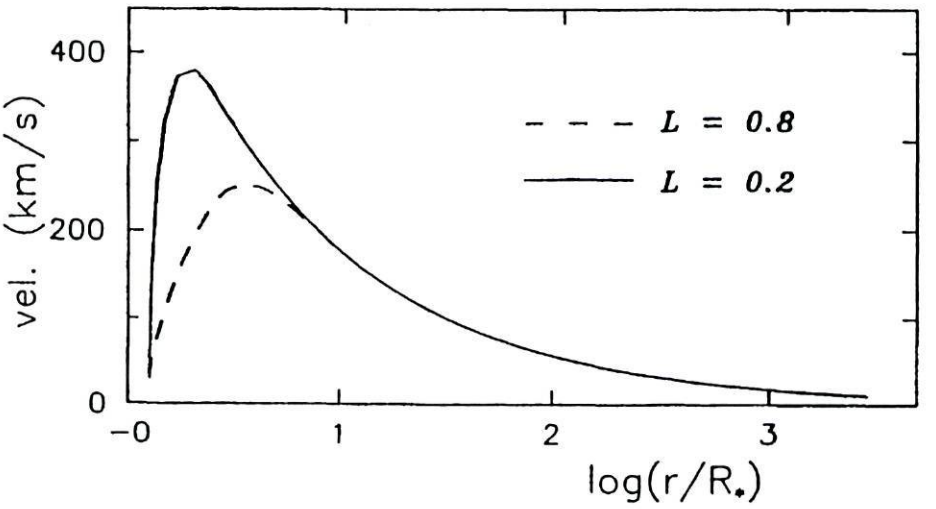

Figure 3.16: Velocity profiles for two values of the damping length L. This Figure is adapted from Grinin and Mitskevich (1991).

authors have effectively prescribed the velocity profile, consequently the remark about the neutral winds models being or not true stellar wind models also applies to these stochastic models.

By further assuming that the wind is isothermal, with $T_g = 8000$ K, Grinin and Mitskevich (1991) have computed many line profiles comparable to the observed line profiles. Some examples of the computed line profiles are shown in Fig. 3.17. They also speculate that some blobs may be 'expelled' with a velocity smaller than the escape velocity and consequently fall back on the stellar surface. This constitutes a possible explanation for the simultaneous inflow and outflow of matter inferred from the observed line profiles of some TTS (Calvet et al., 1992; Natta, 1992; Beristain et al., 2001).

Using the formalism developed by Lindsey and Jefferies (1990) for the radiative transfer computations, Mitskevich et al. (1993) have investigated the conditions for the formation of doubled line profiles, as sometimes seen in the H_α line. They computed line profiles for lines of high optical depth (like H_α) and also to lines of 'intermediate' optical depth (like the Ca II infrared triplet). These computations reinforce the conclusions already reached by Grinin and Mitskevich (1991), and are again comparable to the observations.

Mitskevich (1994; 1995a; 1995b) has further developed the theory of non-continuous winds, by adding an energy equation and dust 'clouds', in order to compute the UV and IR excess seen in the spectral energy distribution of the CTTS. With these models he was able to find correlations between different line and continuum diagnostics, comparable to the observed ones for the CTTS.

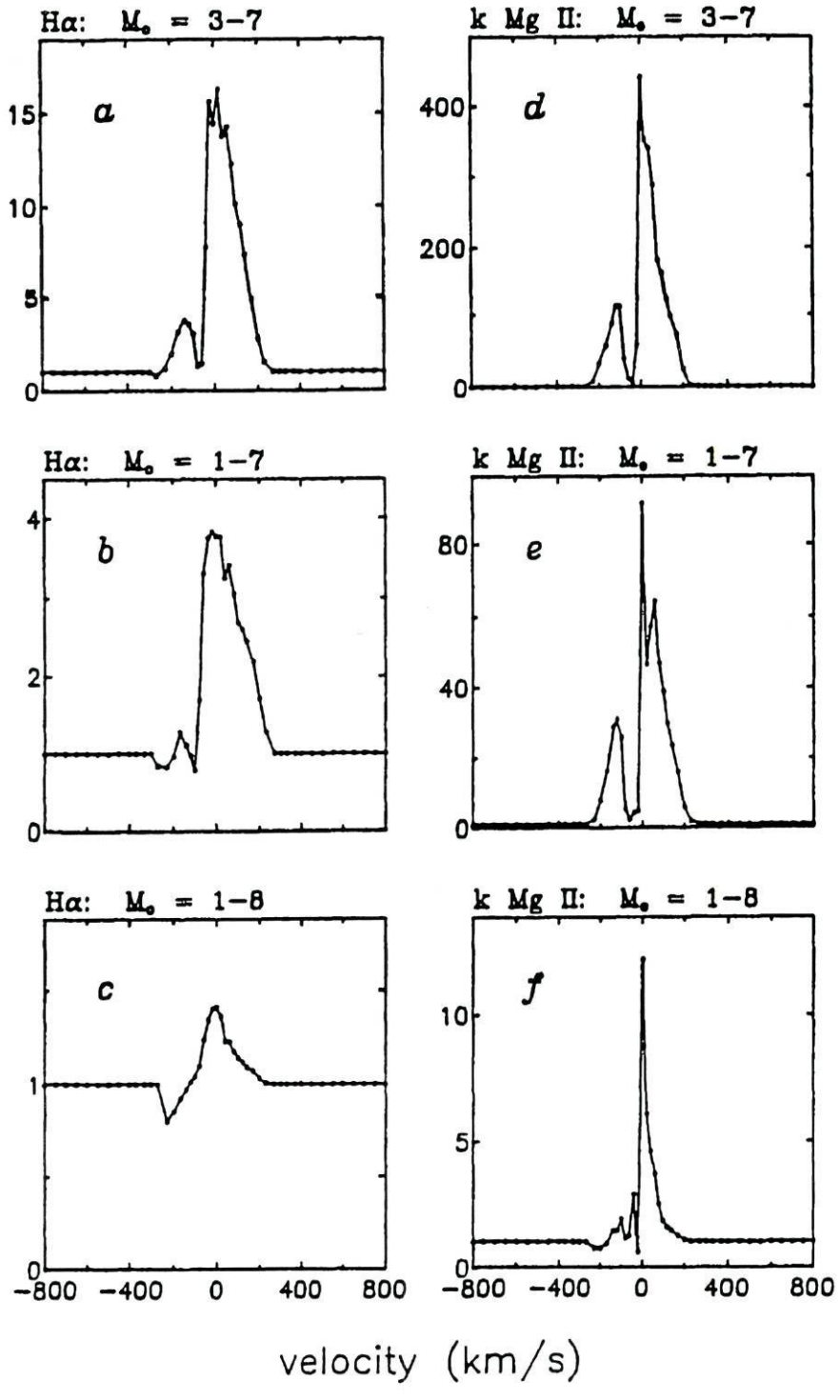

Figure 3.17: Examples of the line profiles obtained with the stochastic stellar wind model of Grinin and Mitskevich. This Figure is adapted from Grinin and Mitskevich (1991).

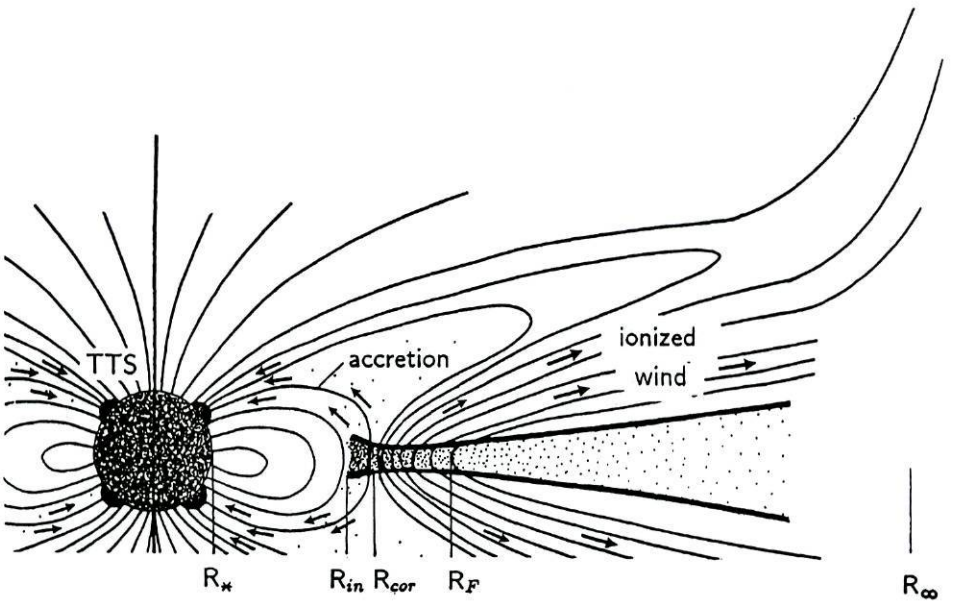

Figure 3.18: The star-disk system used in the model of Paatz and Camenzind. This Figure is adapted from Paatz and Camenzind (1996).

Winds and circumstellar disk models

Other stellar wind models proposed for the CTTS consider a star and a circumstellar disk. In these star-disk systems the wind can originate at the star and/or at the disk. An example of the geometry used for a star-disk system is shown in Fig. 3.18.

Both the star and the disk can generate their own magnetic field and the interaction the both magnetospheres is very complex. Many assumptions about the shape of the field lines, viscosity of the disk, magnetization and ionization of the disk, etc, need to be made for the problem to be mathematically tractable.

This type of wind models is far from the main goal of this thesis, namely the development of spherically symmetric stellar wind models with a detailed energy equation. Therefore they will not be reviewed in detail. Nevertheless, for completeness some references are given: Shu et al. (1994a; 1994b), Li (1996), Paatz and Camenzind (1996), Kudoh and Shibata (1997).

3.8 Conclusion

In this Chapter a review of stellar wind models proposed for TTS was made. This review focused on steady state hydrodynamical stellar (solar) wind models with a detailed energy equation. The main driving force in these models is the thermal pressure gradient, and

when included, the Alfvén wave pressure gradient. Of the different solar wind models analysed it can be concluded that those fitting better the observations at the base and at the earth's orbit are the ones with two energy sources. In particular those having a prescribed volumetric mechanical heating near the base of the wind, and the inclusion of Alfvén waves.

Most of the stellar wind models proposed for TTS have low temperatures, ranging from a few 10^3 to 10^5 K. The reason to select this temperature range is to explain the spectral lines of H_α, Na I D or Ca II H and K, that cannot exist in high temperature plasmas (with $T > 10^6$ K, for example). The stochastic wind model (Grinin and Mitskevich, 1991) was very successful in accounting for many aspects of the observed spectral line profiles. However, they are unable to explain the X-ray emission observed in a large fraction of the TTS. If the X-rays are thermal in origin then wind temperatures in excess of 10^6 K are required. The stellar wind model of Kiguchi et al. (1998) included a detailed energy equation, and was able to obtain the necessary temperatures to originate the X-ray emission. However, in the radiative losses only the effects of bremsstrahlung were considered, resulting in an underestimate of the radiative losses in the transition region and lower corona. Therefore the results obtained should only be considered qualitatively. The winds emanating from a star-disk system were also briefly mentioned.

A first application of a stellar wind model to TTS was made using the model of Tsinganos and Trussoni (1991). This stellar wind model could not be successfully applied to TTS since, for values of the stellar magnetic field and rotation rate adequate for them, the resulting temperature profile has very high values at large distances from the star.

Chapter 4

Stellar wind models with a prescribed temperature profile

This Chapter deals with the main objective of this Thesis, namely, the development of stellar wind models with a detailed energy equation. However, prior to that it is instructive to extend the work of Parker, and look for wind solutions where the form of the temperature profile is prescribed, while keeping the assumption of 'complete' spherical symmetry.

4.1 Equations

The stellar wind models follow the usual hydrodynamical equations of mass conservation and momentum

$$\nabla \cdot (\rho \vec{V}) = 0 \quad , \tag{4.1}$$

$$\rho \vec{V} \cdot \nabla \vec{V} = -\nabla P - \rho \frac{GM}{R^2} \hat{e}_{\rm r} \quad , \tag{4.2}$$

respectively, as well as the equation of perfect gas law[1]

$$P = A \rho T \quad , \qquad A = \frac{K_{\rm B}}{\mu m_H} \quad . \tag{4.3}$$

[1]The constant A is usually called R, the gas constant. To prevent confusion with the radial distance, the gas constant is labelled A in this Thesis

In this work 'complete' spherical symmetry is assumed[2], i.e., all quantities depend solely on the radial distance R, and the only non-vanishing component of the velocity is $V_{\rm R}$, therefore $\vec{V} = (V_{\rm R}\,,0\,,0) = (V\,,0\,,0)$. Consequently, the following expressions for Eqs. (4.1) and (4.2) arise

$$\frac{\mathrm{d}}{\mathrm{d}R}(R^2\rho V) = 0 \tag{4.4}$$

$$\rho V\frac{\mathrm{d}V}{\mathrm{d}R} = -\frac{\mathrm{d}P}{\mathrm{d}R} - \rho\frac{GM}{R^2} \quad . \tag{4.5}$$

Equation (4.4) can be integrated to give

$$R^2\rho V = Z \tag{4.6}$$

where Z is the mass flux per steradian, and the total mass loss rate is $4\pi Z$. Upon substitution of $\mathrm{d}P/\mathrm{d}R$, the following expression for the momentum equation arises

$$\frac{1}{V}\left(V^2 - AT\right)\frac{\mathrm{d}V}{\mathrm{d}R} = \frac{2AT}{R} - A\frac{\mathrm{d}T}{\mathrm{d}R} - \frac{GM}{R^2} \quad . \tag{4.7}$$

The momentum equation has a critical point, where

$$\frac{2AT_{\rm c}}{R_{\rm c}} - A\left.\frac{\mathrm{d}T}{\mathrm{d}R}\right|_{\rm c} - \frac{GM}{R_{\rm c}^2} = 0 \tag{4.8}$$

and

$$V_{\rm c}^2 = AT_{\rm c} \quad . \tag{4.9}$$

As already mentioned when discussing the Parker (1958) solar wind model, it is the presence of the critical point that filters out the wind solution from all the possible solutions to the momentum equation. Nevertheless, it is also possible that the vanishing of the right-hand side (Eq. (4.8)) is accompanied of a maximum or a minimum of the velocity profile, i.e.,

$$\frac{\mathrm{d}V}{\mathrm{d}R} = 0 \quad . \tag{4.10}$$

A classical example of this behaviour are the breeze-type solutions of Chamberlain (1961).

[2]A extension of Parker's solar wind model where $\vec{V} = (V_{\rm R}\,,V_\theta\,,V_\varphi)$ and $T(R) = T_0$ can be found on Machado (1995)

4.1.1 Reasons to specify the temperature profile

To solve the momentum equation (Eq. (4.7)) it is necessary to know the temperature profile and its derivative. These profiles can be retrieved from a more or less detailed energy equation. However, due to the complex mathematical nature of the energy equation and the poor knowledge of some of its terms, a first approach will be to follow the same line as in the original Parker solar wind model and prescribe the temperature profile.

Several prescribed temperature profiles will be used in this Chapter. Some of them can be applied to all space around the star, while others can only be applied near (a few stellar radii above) the stellar surface.

4.1.2 Normalization and linearization

To normalize the momentum equation we shall start by defining the normalized variables

$$a = \frac{R}{R_c} \ , \qquad u = \frac{V}{V_c} \qquad \text{and} \qquad \tau = \frac{T}{T_c} \tag{4.11}$$

where the subscript 'c' denotes the quantities evaluated at the critical point. Upon substitution on the momentum equation, it reads

$$\frac{1}{u}\left(u^2 - \tau\right)\frac{\mathrm{d}u}{\mathrm{d}a} = \frac{2\tau}{a} - \frac{\mathrm{d}\tau}{\mathrm{d}a} - \frac{GM}{R_c V_c^2 a^2} \tag{4.12}$$

where R_c is the radial distance of the critical point and V_c its velocity, cf. Eqs. (4.8) and (4.9).

At the critical point ($a = 1$, $u = 1$, $\tau = 1$) Eq. (4.12) has an indetermination of the form $0/0$. In this work the method chosen to overcome this indetermination is to linearize the momentum equation near the critical point. The basic theory is presented in Appendix A, and requires the first order Taylor's expansion of the normalized variables

$$a = 1 + \delta \ , \qquad u = 1 + \epsilon \ , \qquad \tau = 1 + \left.\frac{\mathrm{d}\tau}{\mathrm{d}a}\right|_c \delta \tag{4.13}$$

and, since the prescribed temperature profiles used in this Chapter are independent of the velocity, the derivative of the temperature is linearized as

$$\frac{\mathrm{d}\tau}{\mathrm{d}a} = \left.\frac{\mathrm{d}\tau}{\mathrm{d}a}\right|_c + \left.\frac{\mathrm{d}^2\tau}{\mathrm{d}a^2}\right|_c \delta \ . \tag{4.14}$$

Substituting Eqs. (4.13) and (4.14) in the normalized momentum equation (Eq. (4.12)), it reads, after linearization,

$$\left(-\left.\frac{\mathrm{d}\tau}{\mathrm{d}a}\right|_{\mathrm{c}}\delta+2\epsilon\right)\frac{\mathrm{d}\epsilon}{\mathrm{d}\delta}=\left(2-\left.\frac{\mathrm{d}^2\tau}{\mathrm{d}a^2}\right|_{\mathrm{c}}\right)\delta \tag{4.15}$$

that will be referred as the linearized momentum equation. From it, the linearized coefficients defined in Appendix A can be recovered

$$\begin{aligned} b &= -\left.\frac{\mathrm{d}\tau}{\mathrm{d}a}\right|_{\mathrm{c}} \\ c &= 2 \\ e &= 2-\left.\frac{\mathrm{d}^2\tau}{\mathrm{d}a^2}\right|_{\mathrm{c}} \\ f &= 0 \ . \end{aligned} \tag{4.16}$$

These coefficients are used to compute the λ's

$$\lambda_{\pm}=\frac{b\pm\sqrt{b^2+8e}}{2} \tag{4.17}$$

which allow the nature of the critical point to be determined. For an X-type critical point the slopes of the two critical solutions are

$$\left.\frac{\mathrm{d}u}{\mathrm{d}a}\right|_{\mathrm{c}}=\frac{\lambda_{\pm}-b}{2} \qquad \text{or} \qquad \left.\frac{\mathrm{d}u}{\mathrm{d}a}\right|_{\mathrm{c}}=\frac{e}{\lambda_{\pm}} \ . \tag{4.18}$$

The remaining sections of this Chapter address the study of stellar wind models with several prescribed temperature profiles.

4.2 Linear temperature profile

The first prescribed temperature profile will be a linear temperature profile of the form

$$T(R)=T_0+B(R-R_0) \tag{4.19}$$

where R_0 is the radial distance of the base of the wind, set equal to $R_\star$ in this work, and T_0 is the corresponding temperature. This temperature profile was chosen due to its simplicity. It cannot be applied to all space around the star, as at large distances from the star the temperature would be too high if $B > 0$, or too low and negative if $B < 0$. Nevertheless, it can be used as a crude approximation to the transition region.

The first derivative of the temperature is

$$\frac{\mathrm{d}T}{\mathrm{d}R} = B \tag{4.20}$$

while the second derivative is null everywhere.

The critical velocity is

$$V_\mathrm{c}^2 = AT_\mathrm{c} = A\left(Q + BR_\mathrm{c}\right) \tag{4.21}$$

where

$$Q = T_0 - BR_0 \tag{4.22}$$

and

$$R_\mathrm{c} = \frac{Q}{B}\left(-1 \pm \sqrt{1 + \frac{GMB}{AQ^2}}\right) \quad . \tag{4.23}$$

The sign is chosen in such a way that $R_\mathrm{c} > R_0$. If Q and B are both positive then the plus sign must be selected.

The derivative of the normalized temperature is

$$\frac{\mathrm{d}\tau}{\mathrm{d}a} = \frac{ABR_\mathrm{c}}{V_\mathrm{c}^2} \quad . \tag{4.24}$$

Consequently, the normalized momentum equation (Eq. (4.12)) becomes

$$\frac{1}{u}\left(u^2 - \tau\right)\frac{\mathrm{d}u}{\mathrm{d}a} = \frac{ABR_\mathrm{c}}{V_\mathrm{c}^2} + \frac{2AQ}{V_\mathrm{c}^2 a} - \frac{GM}{R_\mathrm{c} V_\mathrm{c}^2 a^2} \tag{4.25}$$

and the linearized momentum equation (Eq. (4.15)) is simplified to

$$\left(-\frac{ABR_\mathrm{c}}{V_\mathrm{c}^2}\delta + 2\epsilon\right)\frac{\mathrm{d}\epsilon}{\mathrm{d}\delta} = 2\delta \quad . \tag{4.26}$$

The linearized coefficients (Eqs. (4.16)) are

$$\begin{aligned} b &= -\frac{ABR_\mathrm{c}}{V_\mathrm{c}^2} \\ c &= 2 \\ e &= 2 \\ f &= 0 \quad . \end{aligned} \tag{4.27}$$

4.2.1 Applications of the stellar wind model

The profiles of temperature and velocity for three different values of B are shown in Fig. 4.1. In all the models the temperature at the base of the wind is $T_0 = 10^4$ K, therefore much higher than $T_{\rm eff}$ for the TTS, and the model star has $M_\star = M_\odot$ and $R_\star = 1.6\,R_\odot$. The model represented by the solid lines as a value of B suitable for a linear approximation to the first temperature points in Fig. 1 of Lago (1984). The corresponding velocity profile has a very slow initial acceleration, and the value of the velocity remains below $10\,{\rm km\,s^{-1}}$ at $R = 5\,R_0$.

The model represented by the dashed profiles has a value of B more suitable to represent the transition region, with its large increase of the temperature. The initial acceleration is faster than in the previous model, and reasonable values for the wind velocity are attained within few stellar radii above the base of the wind. The model represented by the dotted lines corresponds to a situation between the previous two.

All three wind models have a topology similar to that of Parker's solar wind model, with one X-type critical point. With increasing B, the pairs $(R_{\rm x}\,, V_{\rm x})$ are $(13.4\,R_\star, 97.9\,{\rm km\,s^{-1}})$, $(5.05\,R_\star, 177\,{\rm km\,s^{-1}})$ and $(3.03\,R_\star, 279\,{\rm km\,s^{-1}})$, respectively.

The stellar wind model with a prescribed linear temperature profile, makes it possible to attain high plasma velocities close to the stellar surface. However, selecting a value of the parameter B suitable for the high velocity regime implies that the temperature becomes rapidly above any reasonable coronal temperature. Furthermore, from the analysis of the dashed velocity profile in Fig. 4.1 it is found that the velocity remains below $10\,{\rm km\,s^{-1}}$ up to $R \sim 1.2$-$1.3\,R_0$. Consequently, it must be concluded that this stellar wind model is not adequate to explain the inferred properties of the TTS winds, namely the high initial acceleration and the high values of the velocity near the stellar surface.

4.3 Gaussian temperature profile

This section addresses the properties of an approximately Gaussian temperature profile, of the form

$$T(R) = T_1 \left(\frac{R}{R_1}\right)^2 \exp\left(-\frac{R - R_1}{\sigma}\right)^2 \quad . \tag{4.28}$$

If the parameters $R_0 (\equiv R_\star)$, T_0, R_1 and T_1 are specified then σ is fixed and is given by the expression

$$\sigma^2 = \frac{(R_1 - R_0)^2}{2\ln(R_1/R_0) - \ln(T_1/T_0)} \quad . \tag{4.29}$$

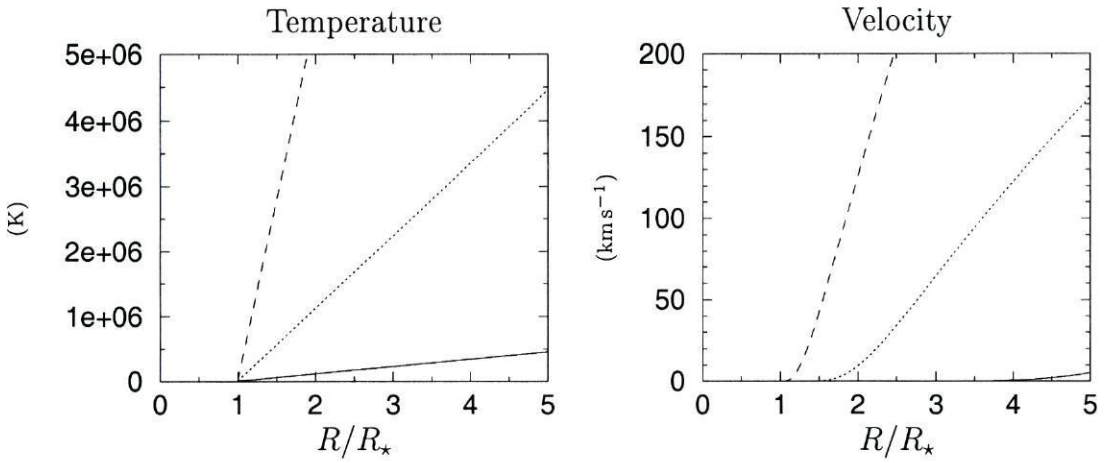

Figure 4.1: Effect in the temperature and velocity profiles when the parameter B of the linear temperature profile is changed. (—): $B = 10^{-6}\,\mathrm{K}\,R_0^{-1}$, $(\cdots)$: $B = 10^{-5}\,\mathrm{K}\,R_0^{-1}$, (- - -): $B = 5 \times 10^{-5}\,\mathrm{K}\,R_0^{-1}$.

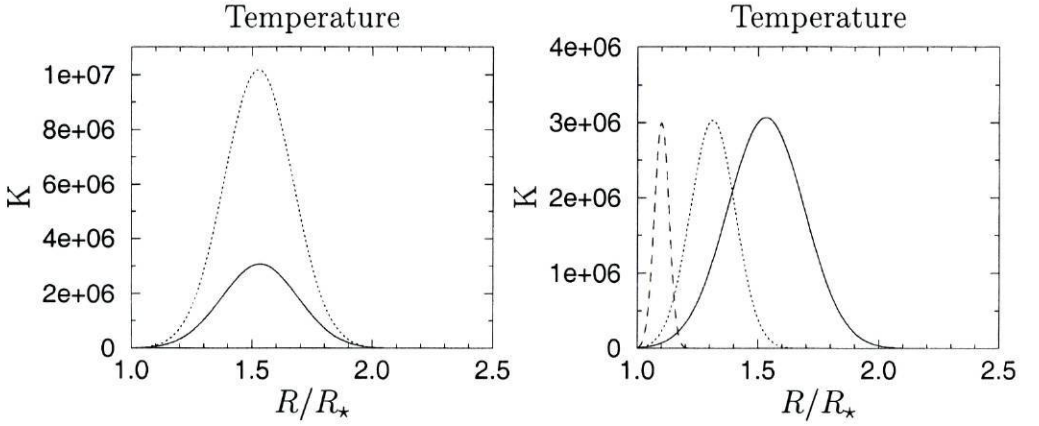

Figure 4.2: Examples of the gaussian temperature profile. Effect of the parameter T_1 (left plot), for $R_1 = 1.5\,R_\star$. (—): $T_1 = 3 \times 10^6\,\mathrm{K}$; $(\cdots)$: $T_1 = 10^7\,\mathrm{K}$. Effect of the parameter R_1 (right plot), for $T_1 = 3 \times 10^6\,\mathrm{K}$. (—): $R_1 = 1.5\,R_\star$; $(\cdots)$: $R_1 = 1.3\,R_\star$; (- -): $R_1 = 1.1\,R_\star$.

The effects of the parameters R_1 and T_1 on this temperature profile can be seen in Fig. 4.2.

The derivative of the temperature profile in Eq. (4.28) is

$$\frac{\mathrm{d}T}{\mathrm{d}R} = 2\left[1 - \frac{R}{\sigma^2}(R - R_1)\right]\frac{T}{R} \tag{4.30}$$

while the critical radius is located at the roots of the following transcendental equation

$$2A\frac{T_\mathrm{c}}{\sigma^2}(R_\mathrm{c} - R_1) - \frac{GM}{R_\mathrm{c}^2} = 0 \quad . \tag{4.31}$$

From the exploration of the space parameter it was found that this equation has two different roots.

The normalization and linearization of the momentum equation leads to the following expressions for the normalized temperature derivatives

$$\frac{\mathrm{d}\tau}{\mathrm{d}a} = 2\left[1 - \left(\frac{R_\mathrm{c}}{\sigma}\right)^2 a(a - a_1)\right]\frac{\tau}{a} \tag{4.32}$$

and

$$\frac{\mathrm{d}^2\tau}{\mathrm{d}a^2} = 2\left(\frac{R_\mathrm{c}}{\sigma}\right)^2 (a_1 - 2a)\frac{\tau}{a} - \frac{1}{a}\frac{\mathrm{d}\tau}{\mathrm{d}a} + \left(\frac{\mathrm{d}\tau}{\mathrm{d}a}\right)^2 \tag{4.33}$$

where $a_1 = R_1/R_\mathrm{c}$. At the critical point these derivatives reduce to

$$\left.\frac{\mathrm{d}\tau}{\mathrm{d}a}\right|_\mathrm{c} = 2\left[1 - \left(\frac{R_\mathrm{c}}{\sigma}\right)^2 (1 - a_1)\right] \tag{4.34}$$

and

$$\left.\frac{\mathrm{d}^2\tau}{\mathrm{d}a^2}\right|_\mathrm{c} = 2\left(\frac{R_\mathrm{c}}{\sigma}\right)^2 (a_1 - 2) - \left.\frac{\mathrm{d}\tau}{\mathrm{d}a}\right|_\mathrm{c} + \left(\left.\frac{\mathrm{d}\tau}{\mathrm{d}a}\right|_\mathrm{c}\right)^2 \quad . \tag{4.35}$$

The normalized momentum equation (Eq. (4.12)) reads

$$\frac{1}{u}\left(u^2 - \tau\right)\frac{\mathrm{d}u}{\mathrm{d}a} = 2\left(\frac{R_\mathrm{c}}{\sigma}\right)^2 (a - a_1)\tau - \frac{GM}{R_\mathrm{c}V_\mathrm{c}^2} \tag{4.36}$$

and the linearized coefficients (Eqs. (4.16)) are

$$\begin{aligned} b &= 2\left[\left(\frac{R_\mathrm{c}}{\sigma}\right)^2 (1 - a_1) - 1\right] \\ c &= 2 \\ e &= 2 - 2\left(\frac{R_\mathrm{c}}{\sigma}\right)^2 (a_1 - 2) + \left.\frac{\mathrm{d}\tau}{\mathrm{d}a}\right|_\mathrm{c} - \left(\left.\frac{\mathrm{d}\tau}{\mathrm{d}a}\right|_\mathrm{c}\right)^2 \\ f &= 0 \quad . \end{aligned} \tag{4.37}$$

4.3.1 Applications of the stellar wind model

As already mentioned, Eq. (4.31) has two different roots. From the results of the parameter space exploration it was found that the critical point closest to the stellar surface is an X-type point, with parameters R_x, V_x and T_x, while the one further out is a spiral critical point, with parameters R_s, V_s and T_s. Some velocity profiles representative of the topology

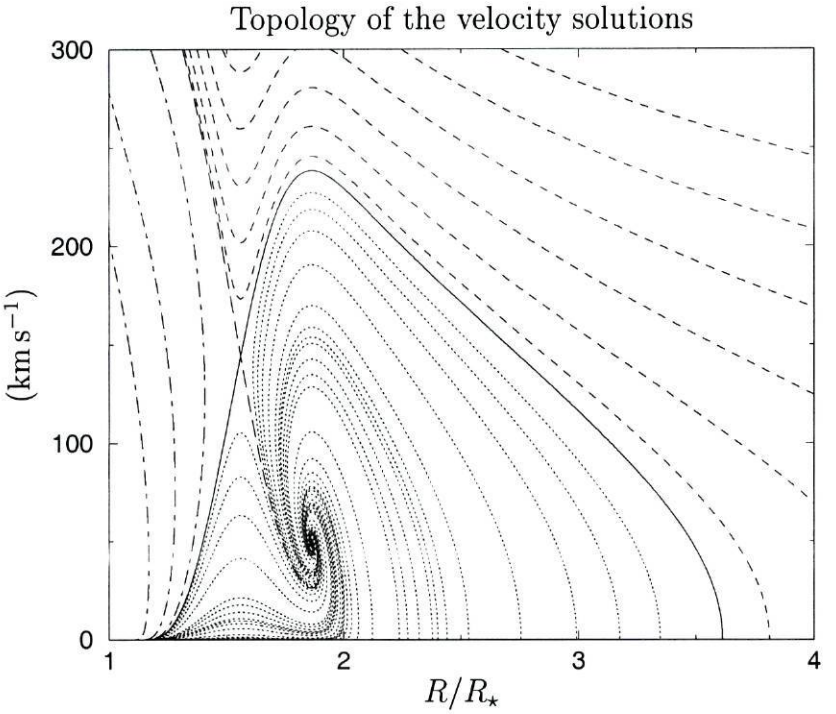

Figure 4.3: Topology of the velocity solutions for the stellar wind model with prescribed gaussian temperature profile. The input parameters are: $M_\star = M_\odot$, $R_\star = 1.6\,R_\odot$, $\mu = 1.2$, $T_0 = 10^4\,\mathrm{K}$, $R_1 = 1.50\,R_\star$ and $T_1 = 3 \times 10^6\,\mathrm{K}$.

of the solutions are shown in Fig. 4.3, where the location of both the X-type and the spiral critical points are clearly seen.

The wind profile, i.e., the solution that crosses the X-type critical point with positive slope, shown in Fig. 4.3 is peculiar, in the sense that the velocity increases, reaches a maximum and decreases afterwards. The maximum occurs at the distance of the spiral critical point, R_s. This wind solution obeys Eqs. (4.8) and (4.9) at the X-type critical point, and Eqs. (4.8) and (4.10) at $R = R_\mathrm{s}$, while $V(R_\mathrm{s}) > V_\mathrm{s}$. This wind profile resembles the velocity profile proposed by Grinin and Mitskevich (1991) for the stochastic winds. The assumptions made to obtain the wind profile shown in Fig. 4.3 are different from the assumptions made by Grinin and Mitskevich, and in particular, the topology of the solutions of Eq. (4.36) has two critical points, while the momentum equation used by Grinin and Mitskevich does not have any critical point.

The 'accretion' solution, i.e., that crossing the X-type critical point with negative slope, is also peculiar. This solution is only defined between the stellar surface and the spiral critical point, where it starts. Analysis of the wind solution shown in Fig. 4.3 reveals that it also does not extend to infinity, but rather finishes at a finite distance, where the value of the velocity vanishes.

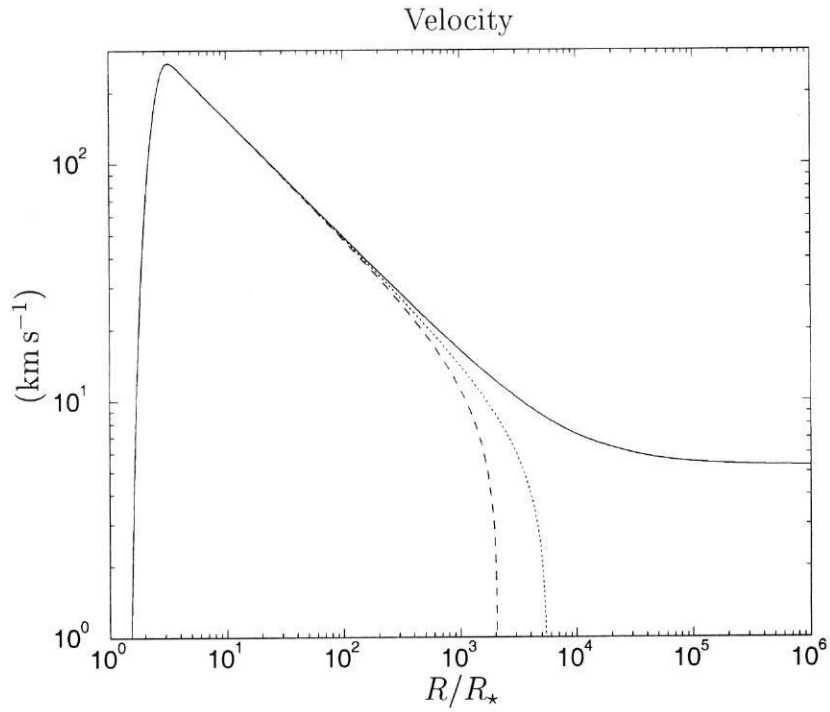

Figure 4.4: Effects induced in the 'wind' velocity profile by changing the parameter R_1 of the gaussian temperature profile. (---): $R_1 = 2.177\,R_\star$; $(\cdots)$: $R_1 = 2.178\,R_\star$; (—): $R_1 = 2.179\,R_\star$.

For the wind solution to extend to infinity with finite values it is necessary to increase one (or both) of the parameters R_1 and T_1, resulting in the availability of more energy to power the wind. Or to decrease the mean molecular weight μ, resulting in a less dense wind. An example of this effect can be seen in Fig. 4.4, where the value of the parameter R_1 has been increased until the solution extended to infinity with finite values. This figure also shows that the behaviour of the solution is very sensitive to small changes of the parameter, when the parameter is close to its 'critical' value. In this case changing R_1 from 2.178 to $2.179\,R_\star$ is enough for the solution to extend to infinity.

However, as it is evident from Fig. 4.4, even when the solution extends to infinity, the terminal value of the velocity is very low. Another drawback of the stellar wind model is the temperature profile itself. The analysis of Fig. 4.2 shows that the temperature profile has high values only within a few stellar radii above the stellar surface, depending on the value of R_1. The values of the temperature rapidly become vanishingly small due to the exponential decrease of the temperature profile (Eq. (4.28)). These facts motivate the specification of another temperature profile.

Exponential temperature profile

The remaining of this Chapter addresses the different aspects of a stellar wind model with a prescribed 'exponential' temperature profile. This temperature profile can mimic the solar transition region and corona, being therefore more realistic than the previous temperature profiles. The topology of the velocity solutions is very rich and varied.

4.4 Equations and profiles

The temperature profile has the form (del Zanna, 1998)

$$T(R) = T_{\rm p} \left(\frac{\exp(B(x-1)/x)}{x} \right)^{\eta} \quad , \qquad x(R) = 1 + (B-1) \frac{R^{\nu/\eta} - 1}{R_{\rm max}^{\nu/\eta} - 1} \tag{4.38}$$

and will be referred to as the exponential temperature profile. Some examples of the curves that can be obtained from Eq. (4.38) are shown in Fig. 4.5. The derivative of Eq. (4.38) is

$$\frac{{\rm d}T}{{\rm d}R} = \frac{\nu(B-1)}{R_{\rm max}^{\nu/\eta} - 1} \frac{(B-x)}{x^2} R^{\nu/\eta} \frac{T}{R} \quad . \tag{4.39}$$

After using these two expressions in the momentum equation (Eq. (4.7)), results the following transcendental equation for the critical radius

$$2 - \frac{\nu(B-1)}{R_{\rm max}^{\nu/\eta} - 1} \frac{(B-x_{\rm c})}{x_{\rm c}^2} R_{\rm c}^{\nu/\eta} - \frac{GM}{AT_{\rm c}R_{\rm c}} = 0 \quad . \tag{4.40}$$

The derivatives of the normalized temperature τ

$$\frac{{\rm d}\tau}{{\rm d}a} = \frac{\nu(B-1)}{R_{\rm c}^{\nu/\eta} a_{\rm max}^{\nu/\eta} - 1} \frac{(B-x)}{x^2} R_{\rm c}^{\nu/\eta} a^{\nu/\eta} \frac{\tau}{a} \tag{4.41}$$

and

$$\frac{{\rm d}^2\tau}{{\rm d}a^2} = \frac{1}{\eta} \frac{{\rm d}\tau}{{\rm d}a} \left(\frac{B^2 - 4Bx + 2x^2}{\tau(B-x)^2} \frac{{\rm d}\tau}{{\rm d}a} + \frac{\nu - \eta}{a} \right) \tag{4.42}$$

are needed to write the normalized momentum equation and the linearized coefficients. At the critical point the derivatives simplify to

$$\left. \frac{{\rm d}\tau}{{\rm d}a} \right|_{\rm c} = \frac{\nu(B-1)}{R_{\rm c}^{\nu/\eta} a_{\rm max}^{\nu/\eta} - 1} \frac{(B-x_{\rm c})}{x_{\rm c}^2} R_{\rm c}^{\nu/\eta} \tag{4.43}$$

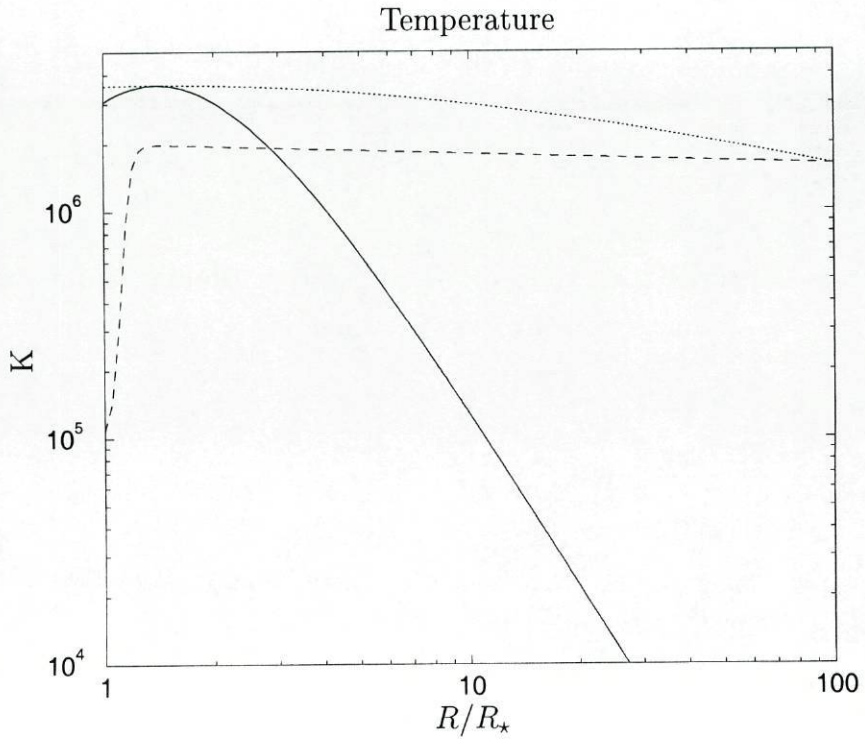

Figure 4.5: Three examples of the exponential temperature profile. All profiles have in common the following values of the input parameters $T_{\rm p} = 10^5\,{\rm K}$ and $R_{\rm max} = 1.4\,R_0$. The other parameters are: (—): $B = 5$, $\eta = 1.5$, $\nu = 2.6$; $(\cdots)$: $B = 5$, $\eta = 1.5$, $\nu = 0.5$; (---): $B = 2000$, $\eta = 0.0015$, $\nu = 0.05$.

and

$$\left.\frac{\mathrm{d}^2\tau}{\mathrm{d}a^2}\right|_{\mathrm{c}} = \frac{1}{\eta}\left.\frac{\mathrm{d}\tau}{\mathrm{d}a}\right|_{\mathrm{c}}\left(\frac{B^2-4Bx_{\mathrm{c}}+2x_{\mathrm{c}}^2}{(B-x_{\mathrm{c}})^2}\left.\frac{\mathrm{d}\tau}{\mathrm{d}a}\right|_{\mathrm{c}}+\nu-\eta\right) \quad . \tag{4.44}$$

The normalized momentum equation (Eq. (4.12)) becomes

$$\frac{1}{u}\left(u^2-\tau\right)\frac{\mathrm{d}u}{\mathrm{d}a} = \left(2-\frac{\nu(B-1)}{R_{\mathrm{c}}^{\nu/\eta}a_{\max}^{\nu/\eta}-1}\frac{(B-x)}{x^2}R_{\mathrm{c}}^{\nu/\eta}a^{\nu/\eta}\right)\frac{\tau}{a}-\frac{GM}{R_{\mathrm{c}}V_{\mathrm{c}}^2} \tag{4.45}$$

and the linearized coefficients (Eqs. (4.16)) are

$$\begin{aligned} b &= -\frac{\nu(B-1)}{R_{\mathrm{c}}^{\nu/\eta}a_{\max}^{\nu/\eta}-1}\frac{(B-x_{\mathrm{c}})}{x_{\mathrm{c}}^2}R_{\mathrm{c}}^{\nu/\eta} \\ c &= 2 \\ e &= 2-\frac{1}{\eta}\left.\frac{\mathrm{d}\tau}{\mathrm{d}a}\right|_{\mathrm{c}}\left(\frac{B^2-4Bx_{\mathrm{c}}+2x_{\mathrm{c}}^2}{(B-x_{\mathrm{c}})^2}\left.\frac{\mathrm{d}\tau}{\mathrm{d}a}\right|_{\mathrm{c}}+\nu-\eta\right) \\ f &= 0 \quad . \end{aligned} \tag{4.46}$$

In the next sections the effects of the parameter on the nature and position of the critical points are addressed, as well as the effects on the temperature and velocity profiles. Some applications of this stellar wind model to the TTS are also given.

4.5 Effect of the parameters on the critical point(s)

The exploration of the space parameter has proved to be very fruitful. It was found that for some values of the parameters (T_{p}, $R_{\max}$, B, ν, η) there were no critical points outside the star. For other values there was one critical point, that could be either an X-type critical point or a spiral critical point, being the later of no interest for the wind solutions. For other set of parameters there were two critical points, an X-type critical point closer to the star and a spiral critical point farther out. When the critical point was of type X, the two critical slopes were computed using Eq. (4.18). These results are summarized in Table 4.1, which also gives some examples of the input parameters.

Before proceeding with the exploration of the parameter space, and the effects of the input parameters on the critical points, it is adequate to present some examples of the velocity profiles obtained with this stellar wind model. The velocity profiles corresponding to the temperature profiles shown in Fig. 4.5 are displayed in Fig. 4.6. The profile represented by solid lines corresponds to a case with two critical points in the momentum equation, while the other two examples have only one critical point.

T_p	B	η	ν	R_c (R_0)	V_c (km s^{-1})	Nature of critical point	$T(R_0)$ (K)	$T(R_{max})$ (K)
1×10^5	2	1.5	2.6	—	—	none	1.5×10^5	1.6×10^5
2×10^6	2	1.5	1.01	2.7	145	X-type	3.1×10^6	3.2×10^6
1×10^5	2000	0.0015	0.1	4.7	110	spiral	1×10^5	2×10^6
1×10^5	5	1.5	2.6	1.9	146	X-type	3.1×10^6	3.6×10^6
				3.8	89	spiral		

Table 4.1: Some examples of the nature of the critical points of the momentum equation, when an exponential temperature profile is used. In these examples $R_{max} = 1.4\,R_0$, and T_p is in Kelvin.

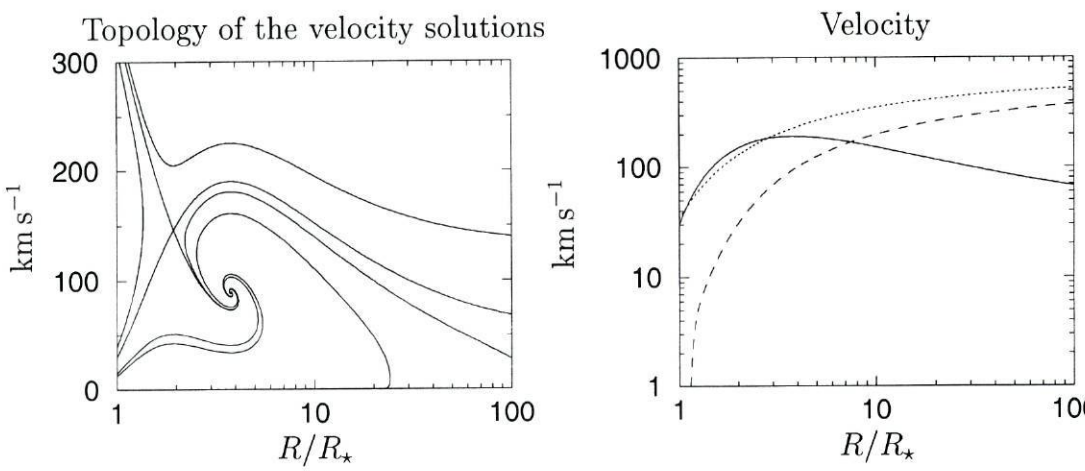

Figure 4.6: Velocity profiles corresponding to the temperature profiles of Fig. 4.5. **left:** velocity profiles representative of the topology of the velocity solutions, for the wind model with the solid line temperature profile. **right:** wind solutions for the three wind models with the temperature profiles of the cited Figure. The same line style scheme has been used in both Figures.

Input Parameter Changed:	Position of the Critical Points: X-type		Spiral	
ν	R_x ($R_\star$)	V_x ($\mathrm{km\,s^{-1}}$)	R_s ($R_\star$)	V_s ($\mathrm{km\,s^{-1}}$)
10	1.448	155.7	1.863	80.35
4	1.690	148.7	2.463	100.5
3	1.856	146.6	3.098	46.17
2.6	**1.942**	**146.4**	**3.788**	**89.16**
1.5	2.193	150.4	48.39	26.78
1.05	2.286	153.3	$> 10^{10}$	—
1.01	2.293	153.5	$\gg 10^{10}$	—
0.5	2.372	156.4	—	—

Table 4.2: Effect on the position of the critical points when the parameter ν is changed. The bold data row corresponds to the comparison model.

Returning now to the exploration of the parameter space, the first situation to be presented is when the momentum equation has two critical points.

4.5.1 Two critical points in the momentum equation

The model used for comparison has for input parameters:

$$T_p = 10^5\,\mathrm{K}\ ;\ R_{max} = 1.4\,R_0\ ;\ B = 5\ ;\ \eta = 1.5\ ;\ \nu = 2.6\ .$$

The effects on the critical points of changing these values will be studied in detail.

Parameter ν

The position and nature of the critical points for some other values of the parameter ν are shown in Table 4.2, where the other input parameters were kept constant.

In this case the comparison model has two critical points, the innermost of type X, and the outermost of type spiral. A similar situation arose while studying the topology of the velocity solutions for the stellar wind model with a prescribed Gaussian temperature profile. The 'wind' solution of the Gaussian temperature profile did not increase always with R, but rather reached a maximum at the radial position of the spiral critical point, and decreased afterwards. To have a 'wind' solution similar to the usual wind solutions, where the inequality $\mathrm{d}V/\mathrm{d}R > 0$ is always fulfilled, it is required that the spiral critical

point is as far away as possible from the X-type critical point, and consequently, from the stellar surface. The better agreement between the topology of this wind model with two critical points and the topology of the Parker model with only an X-type critical point occurs when $R_s \to \infty$.

Analysis of Table 4.2 shows that the value of the parameter ν must be decreased from its comparison value ($\nu = 2.6$) for the radial position of the spiral critical point to move towards infinity. For the values of the other input parameters used in the comparison model, the value of ν should be near or below 1 to have R_s so large that the spiral critical point has a minor role on the topology of the solutions.

Parameters η, B and T_p

The effects induced by changes on the parameters η, B and T_p on the positions of the critical points are shown in Table 4.3. The analysis of this Table shows that the effects resulting from changes on these input parameters are all similar. When one of the parameters η, B or T_p is increased, the radial position of the spiral critical point moves outwards, as wanted, in view of the previous discussion. However, at the same time the radial position of the X-type critical point approaches the stellar surface. Eventually, further increments on the parameters cause the X-type critical point to be located inside the star, preventing the 'wind' solution to exist.

On the contrary, decreasing the input parameters η, B or T_p causes the two critical points to move closer together, and eventually to disappear. Again, this is not interesting for this work, since without critical points the topology of the solutions is unknown.

Parameter R_{max}

Table 4.4 shows the effects produced by changes on the input parameter R_{max}. Similarly to the decrease of the input parameters η, B or T_p, for small enough values of the parameter R_{max} there are no critical points in the momentum equation. On the contrary, when the value of the parameter R_{max} is increased, the behaviour of the position of the critical points is similar as in the case of decreasing the parameter ν, i.e., both the X-type and the spiral critical points move outward. However, in the case of incrementing the parameter R_{max} the radial position of the spiral critical point does not approach infinity fast enough, while the radial position of the X-type critical point is also moving to large distances from the star. This is a major drawback, since for the wind solution $V < V_c$ when $R < R_c$, therefore the velocity near the stellar surface will be too low for these wind models.

Input Parameter Changed:		Position of the Critical Points: X-type		Spiral	
		R_x	V_x	R_s	V_s
name	value	($R_\star$)	($\mathrm{km\,s^{-1}}$)	($R_\star$)	($\mathrm{km\,s^{-1}}$)
η	2.1	inside	—	18.55	38.03
η	2.0	1.085	276.4	14.63	42.95
η	1.7	1.440	200.0	6.941	63.38
$\boldsymbol{\eta}$	**1.5**	**1.942**	**146.4**	**3.788**	**89.16**
η	1.4	—	—	—	—
B	7	inside	—	23.29	33.45
B	6.5	1.015	364.9	15.60	41.0
B	6	1.139	281.1	10.37	50.62
$\boldsymbol{B}$	**5**	**1.942**	**146.4**	**3.788**	**89.16**
B	4.8	—	—	—	—
T_p	6×10^5	inside	—	15.76	40.82
T_p	5×10^5	1.024	327.8	13.96	43.42
T_p	2×10^5	1.320	222.2	7.320	60.95
$\boldsymbol{T_p}$	$\mathbf{1 \times 10^5}$	**1.942**	**146.4**	**3.788**	**89.16**
T_p	8×10^4	—	—	—	—

Table 4.3: Same as in Table 4.2, but for changes of the parameters η, B and T_p.

Input Parameter Changed:	Position of the Critical Points: X-type		Spiral	
	R_x	V_x	R_s	V_s
$\boldsymbol{R_{max}}$	($R_\star$)	($\mathrm{km\,s^{-1}}$)	($R_\star$)	($\mathrm{km\,s^{-1}}$)
100	49.80	112.0	5438	2.184
1.6	1.981	152.6	5.104	75.40
1.4	**1.942**	**146.4**	**3.788**	**89.16**
1.3	1.982	139.9	3.111	100.1
1.2	—	—	—	—

Table 4.4: Same as in Table 4.2, but for changes of the parameter R_{max}.

4.5.2 Changing the nature of the spiral critical point

The analysis of Tables 4.3 and 4.4 shows that when the values of the parameters η, B, $T_{\rm p}$, or $R_{\rm max}$ are sufficiently low there are no critical points in the momentum equation. The behaviour of the critical points, and in particular the spiral critical point, for values of the input parameters around the limiting value is the subject of this section.

It is found that when any of the four input parameters is close to its limiting value the spiral critical point changes its nature to an improper node. To better understand the reasons beyond this change of nature, Eq. (4.17) may be written in a compact form

$$\lambda_{\pm} = P \pm Q \quad . \tag{4.47}$$

The variables P and Q can be easily recovered from the values of λ_+ and λ_-, using the equalities

$$P = \frac{\lambda_+ + \lambda_-}{2} \qquad \text{and} \qquad Q = \frac{\lambda_+ - \lambda_-}{2} \quad . \tag{4.48}$$

From the results of Appendix A it is known that Q is imaginary for the spiral critical points. Consequently, the argument of the square root in Eq. (4.17) will be negative. However, when the parameters are changed accordingly to Table 4.5 the value of the argument becomes eventually positive, therefore Q becomes real. For the values of the input parameters used the absolute value of Q is smaller than that of P, implying that the λ's have both the same sign. Again referring to the Appendix A, this means that the nature of the critical point is of an improper node.

4.5.3 One critical point in the momentum equation

For the model used for comparison the input parameters are set to the following values:

$$T_{\rm p} = 1 \times 10^5 K \ ; \ R_{\rm max} = 1.4 R_0 \ ; \ B = 2000 \ ; \ \eta = 0.0015 \ ; \ \nu = 0.05$$

corresponding to an X-type critical point. An exploration of the space parameter will be made to study the changes induced in the critical point.

Parameter ν

When the parameter ν is increased the nature of the critical point changes from X-type to spiral, as shown in Table 4.6. In this case the value of the variable Q (Eqs. (4.47) and

Input Parameter Changed:		Position of the Critical Points: X-type			farther out critical point		
		R_x	V_x	nature	R_c	V_c	$\lambda_\pm$
name	value	($R_\star$)	($\mathrm{km\,s^{-1}}$)		($R_\star$)	($\mathrm{km\,s^{-1}}$)	
$\boldsymbol{\eta}$	**1.50**	**1.942**	**146.4**	**spiral**	**3.788**	**89.16**	$\mathbf{1.952 \pm 2.845\,i}$
η	1.45	2.358	123.6	imp. node	2.891	106.2	0.0767 ; 1.581
η	1.40	—	—	—	—	—	—
$\boldsymbol{B}$	**5.0**	**1.942**	**146.4**	**spiral**	**3.788**	**89.16**	$\mathbf{1.952 \pm 2.845\,i}$
B	4.9	2.355	124.5	imp. node	3.006	103.9	0.1546 ; 1.518
B	4.8	—	—	—	—	—	—
$\boldsymbol{T_p}$	$\mathbf{1 \times 10^5}$	**1.942**	**146.4**	**spiral**	**3.788**	**89.16**	$\mathbf{1.952 \pm 2.845\,i}$
T_p	9×10^4	2.267	128.2	imp. node	3.119	101.3	0.8439 ; 0.8849
T_p	8×10^4	—	—	—	—	—	—
$\boldsymbol{R_{max}}$	**1.40**	**1.942**	**146.4**	**spiral**	**3.788**	**89.16**	$\mathbf{1.952 \pm 2.845\,i}$
R_{max}	1.30	1.982	139.9	spiral	3.111	100.1	$1.821 \pm 1.779\,i$
R_{max}	1.25	2.065	133.5	imp. node	2.721	108.9	0.3322 ; 1.365
R_{max}	1.20	—	—	—	—	—	—

Table 4.5: Changing the nature of the critical point farther out from the stellar surface, when some of the parameters are changed. The bold data rows correspond to the comparison model.

Parameter Changed: ν	Critical point nature	R_c ($R_\star$)	V_c (km s^{-1})	$\lambda_\pm$
0.10	spiral	4.691	110.0	$0.100 \pm 6.174\,i$
0.08	spiral	4.617	111.4	$0.080 \pm 4.332\,i$
0.06	**spiral**	**4.547**	**112.8**	$\mathbf{0.060 \pm 1.917\,i}$
0.05	**X-type**	**4.514**	**113.5**	**-0.7282 ; 0.7782**
0.03	X-type	4.452	114.9	-1.640 ; 1.670
0.01	X-type	4.392	116.2	-1.956 ; 1.966

Table 4.6: Effect on the position and nature of the critical point when the parameter ν is changed.

(4.48)) changes from real to imaginary when ν increases, and therefore the critical point changes from X-type to spiral (please refer to the Appendix A).

It is adequate to use the two values 0.05 and 0.06 for the parameter ν when the other parameters are changed, since these values correspond, respectively (Table 4.6), to an X-type and a spiral critical points in the momentum equation.

The behaviour of the slopes around the X-type and the spiral critical points are displayed in Fig. 4.7. Plots a) and b) correspond to 'normal' X-type and spiral critical points, while plots c) and d) correspond to the X-type and spiral critical points for the wind models with $\nu = 0.05$ and $\nu = 0.06$, already analysed and shown in Table 4.6. The analysis of Fig. 4.7 shows that the difference between the slopes around the 'normal' X-type and spiral critical points is notorious. However, the difference between the slopes around the X-type and the spiral critical points for the two values of the input parameter ν under study is barely noticed.

Parameter η

Decreasing the parameter η changes the nature of the critical point from X-type to spiral, and vice-versa, for each of the two values of the parameter ν used. Please refer to Table 4.7 for some examples.

Parameters B and T_p

The effects in the nature of the critical point of the momentum equation induced by variations of the parameters B or T_p depend on the value of the parameter ν, as can be seen in Tables 4.8 and 4.9. When $\nu = 0.05$, increasing B or T_p from their comparison

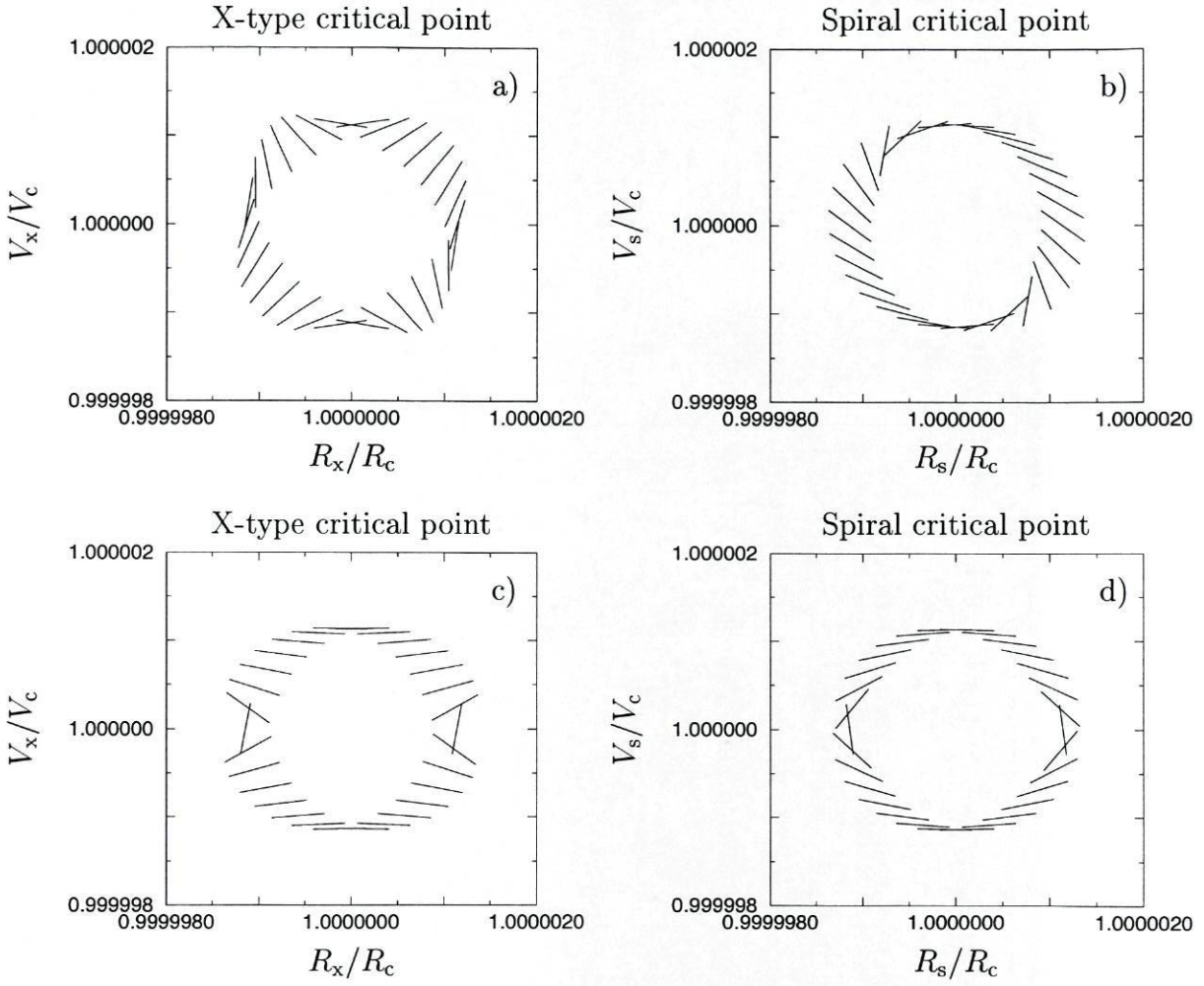

Figure 4.7: Slopes around the X-type and spiral critical points. **a)** and **b)**, X-type and spiral critical points, respectively, for the wind model with the input parameters: $T_p = 10^5\,\mathrm{K}$, $R_{max} = 1.4\,R_0$, $B = 5$, $\eta = 1.5$ and $\nu = 2.6$.

c) and **d)** X-type and spiral critical points for the wind models with the following input parameters in common: $T_p = 10^5\,\mathrm{K}$, $R_{max} = 1.4\,R_0$, $B = 2000$ and $\eta = 0.0015$. In **c)** $\nu = 0.05$, and in **d)** $\nu = 0.06$, refer to Table 4.6.

Parameter Changed:		Critical point			
		nature	R_c	V_c	$\lambda_\pm$
η	ν		($R_\star$)	(km s^{-1})	
0.0019		X-type	1.948	172.4	-0.2729 ; 0.3329
0.0018	0.06	spiral	2.408	155.0	$0.060 \pm 0.6902\,\mathrm{i}$
0.0015	**0.06**	**spiral**	**4.547**	**112.8**	$\mathbf{0.060 \pm 1.917\,i}$
0.0012		spiral	8.589	82.09	$0.060 \pm 2.911\,\mathrm{i}$
0.0016		X-type	3.660	126.1	-0.8557 ; 0.9057
0.0015	**0.05**	**X-type**	**4.514**	**113.5**	**-0.7282 ; 0.7782**
0.0013	0.05	X-type	6.867	92.03	-0.2084 ; 0.2584
0.0012		spiral	8.469	82.87	$0.050 \pm 1.032\,\mathrm{i}$

Table 4.7: Effect on the position and nature of the critical point when the parameter η was changed, for the two values of the parameter ν used for comparison.

values of 2000 and 10^5K, respectively, changes the nature of the critical point from X-type to spiral. However, when $\nu = 0.06$ changing any of the parameters above mentioned only affects the position of the critical point, and not its nature, which remains a spiral critical point.

Parameter $R_{\max}$

Increasing the value of the parameter $R_{\max}$ changes the nature of the critical point from spiral to X-type if $\nu = 0.06$, as for the increments of η. However, when $\nu = 0.05$ increasing $R_{\max}$ causes the nature of the critical point to change from X-type to spiral, contrary to the corresponding case for η shown in Table 4.7.

4.5.4 Asymptotic approximations

This section presents asymptotic approximate expressions for the temperature. The motivation beyond these approximations is a better understanding of the induced changes on the critical points studied in the previous sections.

If $R^{\nu/\eta} \gg 1$ and $x \gg 1$ as well as $x \gg B$ then the following approximate expressions for x, T and $\mathrm{d}T/\mathrm{d}R$ are found

$$x \sim \frac{B-1}{R_{\max}^{\nu/\eta} - 1} R^{\nu/\eta} \tag{4.49}$$

Parameter Changed:		Critical point			
		nature	R_c	V_c	$\lambda_\pm$
B	ν		($R_\star$)	(km s^{-1})	
4000		spiral	1.287	513.7	-1.649 ± 18.00 i
3000		spiral	1.323	246.0	-0.511 ± 34.51 i
2000	**0.06**	**spiral**	**4.547**	**112.8**	**0.060 ± 1.917 i**
1000		spiral	22.40	50.83	0.060 ± 1.917 i
100		spiral	93.85	24.83	0.060 ± 1.917 i
3000		spiral	1.304	245.8	-0.4862 ± 33.14 i
2820		spiral	1.353	215.8	-0.1072 ± 1.621 i
2810	**0.05**	X-type	1.358	214.2	-1.821 ; 1.734
2000		**X-type**	**4.514**	**113.5**	**-0.7282 ; 0.7782**
1000		X-type	21.87	51.57	-0.7282 ; 0.7782

Table 4.8: Same as Table 4.7, but for changes of the input parameter B.

Parameter Changed:		Critical point			
		nature	R_c	V_c	$\lambda_\pm$
T_p	ν		($R_\star$)	(km s^{-1})	
5×10^5		spiral	1.316	259.5	-0.6541 ± 45.10 i
$\mathbf{1 \times 10^5}$	**0.06**	**spiral**	**4.547**	**112.8**	**0.060 ± 1.917 i**
5×10^4		spiral	9.506	78.03	0.060 ± 1.917 i
5×10^5		spiral	1.294	259.2	-0.6286 ± 43.67 i
4×10^5		spiral	1.317	232.8	-0.3294 ± 21.44 i
3×10^5	**0.05**	X-type	1.437	202.2	-2.043 ; 2.072
$\mathbf{1 \times 10^5}$		**X-type**	**4.514**	**113.5**	**-0.7282 ; 0.7782**
5×10^4		X-type	9.364	78.81	-0.7282 ; 0.7782

Table 4.9: Same as Table 4.7, but for changes of the input parameter T_p.

Parameter Changed:		Critical point			
		nature	R_c	V_c	$\lambda_\pm$
$\boldsymbol{R_{max}}$	$\boldsymbol{\nu}$		$(R_\star)$	$(\mathrm{km\,s^{-1}})$	
4.0		X-type	4.263	116.6	-0.4017 ; 0.4570
3.9	**0.06**	spiral	4.263	116.6	$5.830 \pm 1.430\,\mathrm{i}$
1.4	**0.06**	**spiral**	**4.547**	**112.8**	$\mathbf{0.060 \pm 1.917\,i}$
1.2		spiral	53.19	32.99	$0.060 \pm 1.917\,\mathrm{i}$
4.8		spiral	4.634	116.7	$-0.1108 \pm 2.418\,\mathrm{i}$
4.7	**0.05**	X-type	4.564	116.7	-2.006 ; 1.923
1.4	**0.05**	**X-type**	**4.514**	**113.5**	**-0.7282 ; 0.7782**
1.2		X-type	4.551	113.0	-0.7282 ; 0.7782

Table 4.10: Same as Table 4.7, but for changes of the input parameter R_{max}.

$$T \sim T_p \frac{e^{\eta B}}{x^\eta} \sim T_p e^{\eta B} \left(\frac{R_{max}^{\nu/\eta} - 1}{B - 1} \right)^\eta \frac{1}{R^\nu} = \mathcal{T} \frac{1}{R^\nu} \tag{4.50}$$

and

$$\frac{dT}{dR} \sim -\nu \frac{T}{R} \tag{4.51}$$

where $\mathcal{T}$ in Eq. (4.50) is a constant. If the parameter ν is positive, then $T \to 0$ as $R \to \infty$ with a slope $-\nu$. At the critical point the normalized expressions corresponding to Eqs. (4.49) to (4.51) are

$$x_c \sim \frac{B - 1}{a_{max}^{\nu/\eta} - R_c^{-\nu/\eta}} \tag{4.52}$$

$$\tau_c \sim T_p e^{\eta B} \left(\frac{a_{max}^{\nu/\eta} - R_c^{-\nu/\eta}}{B - 1} \right)^\eta \tag{4.53}$$

and

$$\left. \frac{d\tau}{da} \right|_c \sim -\nu \quad . \tag{4.54}$$

The second derivative of the normalized temperature is also approximated by

$$\left. \frac{d^2\tau}{da^2} \right|_c \sim \frac{\nu}{\eta}(\nu + \eta) \quad . \tag{4.55}$$

From these expressions the linearized coefficients (Eqs. (4.16)) are

$$\begin{aligned} b &= \nu \\ c &= 2 \\ e &= 2\left(\frac{GM}{R_c V_c^2} - 1\right) - \left(2 + \frac{1}{\eta}(\nu + \eta)\right)\nu \\ f &= 0 \quad . \end{aligned} \tag{4.56}$$

Within the approximations the linearized coefficients depend only on the parameters ν and η. Their dependence on the parameters T_p, B and R_{max} comes through R_c and V_c, and is relatively weak. This is the reason why in Tables 4.8, 4.9 and 4.10 the values of the variables $\lambda_\pm$ do not change when the parameters T_p, B or R_{max} have small values, since in these cases the value of x is very large.

The limiting case $R \to \infty$

As long as the parameters ν and η verify $\nu/\eta > 0$ and $R \to \infty$ the approximate expressions (4.49) to (4.51) are valid. This section deals with the behaviour of the velocity and pressure when $R \to \infty$.

For convenience, the momentum equation (Eq. (4.7)) will be written again

$$\frac{1}{V}\left(V^2 - AT\right)\frac{\mathrm{d}V}{\mathrm{d}R} = \frac{2AT}{R} - A\frac{\mathrm{d}T}{\mathrm{d}R} - \frac{GM}{R^2} \quad .$$

In the limiting case $R \to \infty$ it can be written as

$$\frac{1}{V}\left(V^2 - AT\right)\frac{\mathrm{d}V}{\mathrm{d}R} = (2+\nu)\frac{AT}{R} - \frac{GM}{R^2}$$

or, substituting T by its approximation (Eq. (4.50)),

$$\frac{1}{V}\left(V^2 - AT\right)\frac{\mathrm{d}V}{\mathrm{d}R} = (2+\nu)A\mathcal{T}\frac{1}{R^{\nu+1}} - \frac{GM}{R^2} \quad .$$

The wind solution at very large values of R obbeys the inequality $V^2 \gg AT$. Therefore the approximate momentum equation becomes

$$V\frac{\mathrm{d}V}{\mathrm{d}R} = (2+\nu)A\mathcal{T}\frac{1}{R^{\nu+1}} - \frac{GM}{R^2} \quad . \tag{4.57}$$

Which of the two terms on the right-hand-side of the previous equation will be the dominant term depends on the value of the parameter ν. If $0 < \nu < 1$ then the first

term dominates and V is an increasing function of R, on the contrary, if $\nu > 1$ then the gravitational term is the leading one, and V is a decreasing function of R. To have the velocity of the wind solution decreasing with R demands the existence of a (spiral) critical point outwards from the X-type critical point, as in the case of the stellar wind model with a prescribed Gaussian temperature profile.

The following expressions for the behaviour of the velocity at very large values of R are found

$$V^2 = V_1^2 + 2A\mathcal{T}\frac{(2+\nu)}{\nu}\left(\frac{1}{R_1^\nu} - \frac{1}{R^\nu}\right) , \quad \text{when} \quad \nu < 1 \tag{4.58}$$

$$V^2 = V_1^2 - 2GM\left(\frac{1}{R_1} - \frac{1}{R}\right) , \quad \text{when} \quad \nu > 1 \tag{4.59}$$

where $R > R_1$ and R_1 is some large value of R used as a reference, being V_1 the corresponding value of the velocity. These two equations can also be written in a more compact form displaying the asymptotic approximation of V to the terminal velocity V_∞

$$V = \sqrt{V_\infty^2 - 2A\mathcal{T}\frac{(2+\nu)}{\nu}\frac{1}{R^\nu}} , \quad \text{when} \quad \nu < 1 \tag{4.60}$$

$$V = \sqrt{V_\infty^2 + 2GM\frac{1}{R}} , \quad \text{when} \quad \nu > 1 \ . \tag{4.61}$$

Therefore, V approaches V_∞ as

$$V \propto R^{-\nu} , \quad \text{when} \quad \nu < 1$$

and the approximation is from $V < V_\infty$, or

$$V \propto R^{-1} , \quad \text{when} \quad \nu > 1$$

and the approximation is from $V > V_\infty$.

Behaviour of the density

The density is recovered from Eq. (4.6)

$$\rho = \frac{Z}{R^2 V} \ .$$

From the asymptotic behaviour of the velocity already studied, it is found that the leading term is R^2, since V is approaching V_∞ at a slower rate. Therefore ρ decreases with R, as it should.

Looking at the approximations for $R \to \infty$ already studied, the most significant parameter is ν, as it determines the behaviour of the temperature ($T \propto R^{-\nu}$), therefore ν should be constrained to be positive.

4.6 Effect of the parameters on the temperature and velocity profiles

It is now appropriate to address the effects of the parameters on the temperature and velocity profiles. In all examples shown, the momentum equation has only an X-type critical point.

4.6.1 Parameters ν and η

The effects on the temperature and velocity profiles induced by changes of the input parameters ν and η are displayed in Fig. 4.8. Analysis of this Figure shows that the slope of the temperature profile changes with ν, in agreement with the previous discussion of the asymptotic approximations, Eqs. (4.50) and (4.51). The other main effect of this parameter is on the value of T_0, and has little effect on the value of $T_{\max}$. Increasing the value of ν decreases the value of T_0, and also the value of T for $R > R_{\max}$. Recalling that the stellar wind model under study is thermally driven, it is no surprise that the value of V_0 decreases with increasing ν. However, the value of the velocity at $R > R_{\max}$ is not very sensitive to changes of ν. The reason beyond this behaviour is the larger initial acceleration of the plasma when ν increases, due to the corresponding steeper temperature profile. The increase of the initial acceleration with ν compensates the strong decrease of V_0, and by $R \sim R_{\max}$ the three wind models shown for the changes of ν have $V \sim 200\,\mathrm{km\,s^{-1}}$.

The main effect of increasing the input parameter η is to increase the value of $T(R)$ at any R. Graphically, this corresponds to a vertical shift of the temperature profile, as shown in Fig. 4.8. This shift is not followed by significant alterations of the temperature slope. Consequently, increasing η also causes an increase of $V(R)$ at any R.

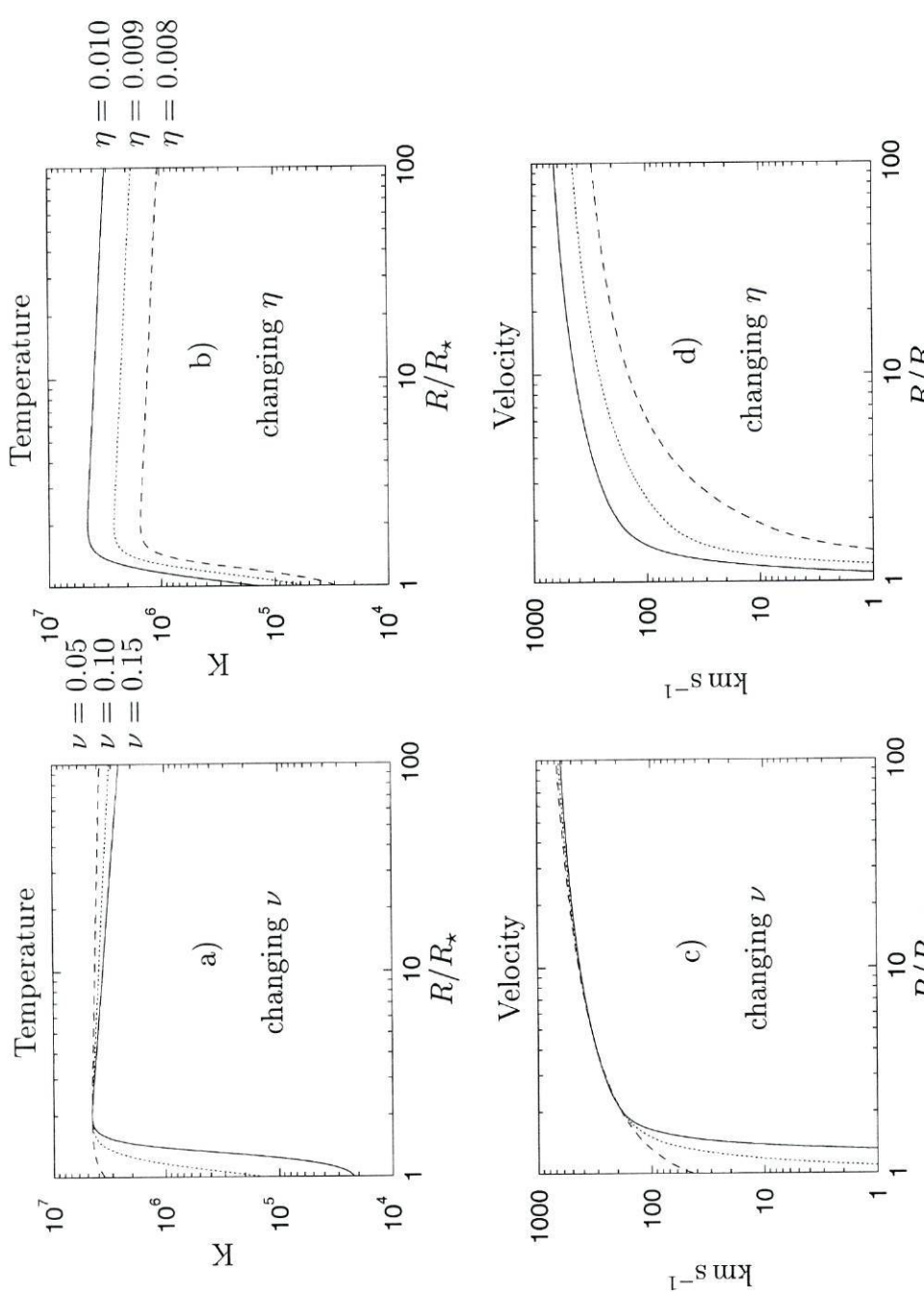

Figure 4.8: Effect on the temperature (top plots) and velocity (bottom plots) profiles of changing the parameters ν (left) and η (right). **a)** and **c)**, temperature and velocity profiles, respectively, for the wind model with: $T_{\rm p} = 2 \times 10^4$K, $R_{\rm max} = 2.0R_0$, $B = 550$, $\eta = 0.01$ and ν has the following values: solid (—) $\nu = 0.15$, dotted $(\cdots)$ $\nu = 0.10$, dashed (- - -) $\nu = 0.05$. **b)** and **d)**, temperature and velocity profiles, respectively, for the wind model with parameters: $T_{\rm p} = 2 \times 10^4$K, $R_{\rm max} = 2.0R_0$, $B = 550$, $\nu = 0.1$ and η has the following values: solid (—) $\eta = 0.010$, dotted $(\cdots)$ $\eta = 0.009$, dashed (- - -) $\eta = 0.008$.

4.6.2 Parameters B and $T_{\rm p}$

Figure 4.9 displays the effects induced on the temperature and velocity profiles by changes of the input parameters B and $T_{\rm p}$. The effects are similar to those of the parameter η, i.e., the values of $T(R)$ and $V(R)$ at any R increase when B or $T_{\rm p}$ increase.

4.6.3 Parameters $R_{\rm max}$ and μ

The effects induced by changes of the parameter $R_{\rm max}$ and of the mean molecular weight (μ) are displayed in Fig. 4.10. Graphically, changing $R_{\rm max}$ is consistent with a horizontal shift of the temperature profile, and therefore the larger effects occur between $R = R_0$ and $R = R_{\rm max}$. Increasing $R_{\rm max}$ decreases the value of T_0, and also that of V_0, due to the thermal nature of the wind model under study. For $R > R_{\rm max}$ the three wind models being studied have similar values of $V(R)$ at any R, since the acceleration due to the temperature gradient acts for a larger distance with increasing $R_{\rm max}$, and may compensate the smaller value of V_0.

The mean molecular weight has no effect on the temperature profile, while increasing μ decreases $V(R)$ at any R. This result is to be expected, since it is easier to drive a lighter wind.

4.7 Application to TTS

Of the three prescribed temperature profiles studied in this Chapter the one that is able to better fit the observations of the solar transition region and corona is the exponential temperature profile. For the thermally driven stellar winds, the temperature structure of the solar wind is used as a template for that of the TTS, therefore the stellar wind model with a prescribed exponential temperature profile will be applied to the TTS.

The first stellar parameter to change is the stellar radius, motivated by the fact that the TTS are still in the contracting phase towards the MS.

4.7.1 Increasing $R_\star$

The effects caused by the increase of the stellar radius on the profiles of temperature, number density, velocity and thermal pressure are shown in Fig. 4.11. The four examples displayed have $\nu = 2/7$, to ensure that the temperature slope far from the star follows one of the asymptotic laws of the conductive stellar wind models, namely the Parker value.

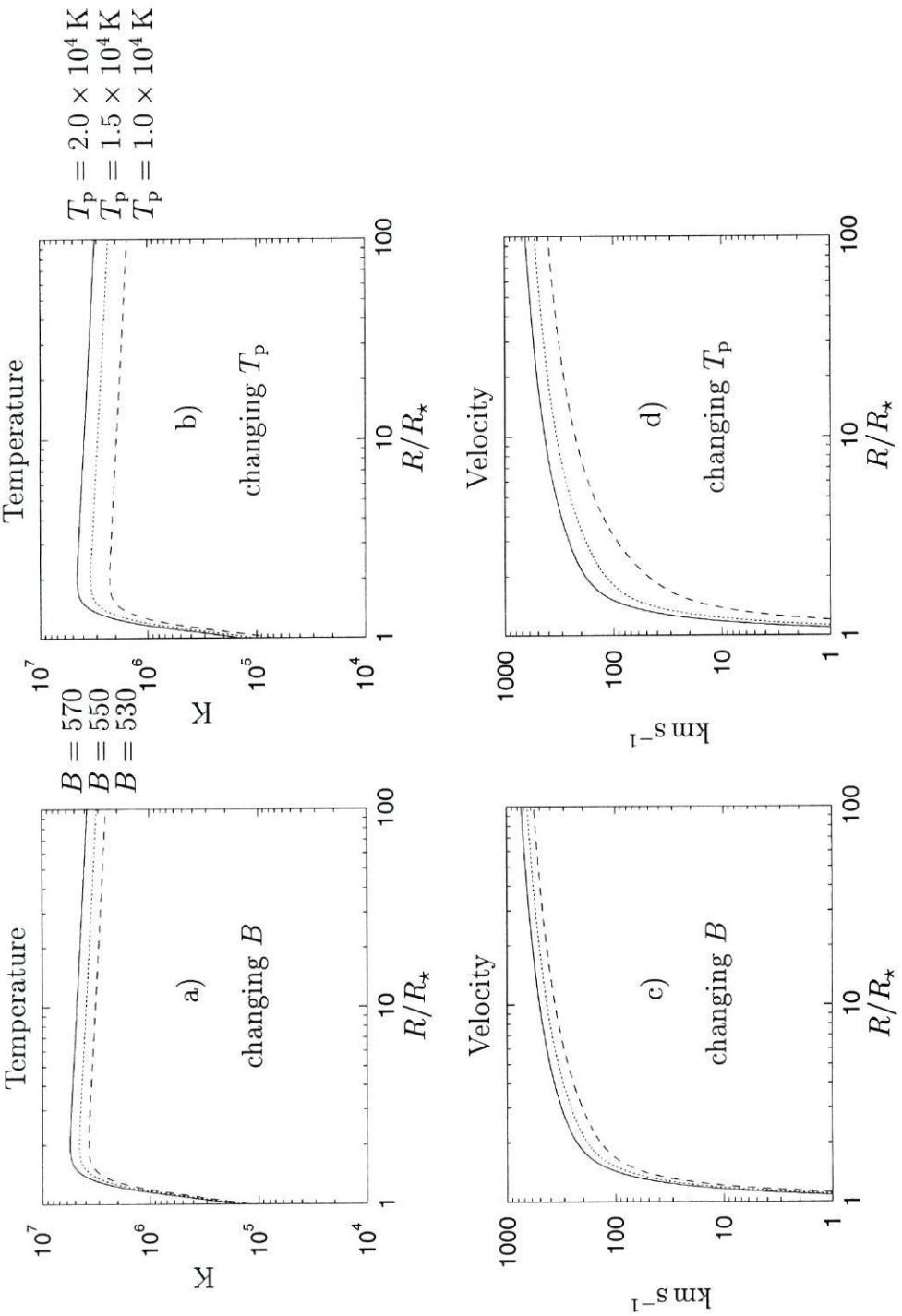

Figure 4.9: Effect of the parameters B (left) and T_p (right) on the temperature (top plots) and velocity (bottom plots) profiles. **a)** and **c)**, temperature and velocity profiles, respectively, for the wind model with: $T_\mathrm{p} = 2 \times 10^4$K, $R_\mathrm{max} = 2.0R_0$, $\nu = 0.1$, $\eta = 0.01$ and B has the following values: solid (—) $B = 570$, dotted $(\cdots)$ $B = 550$, dashed (- - -) $B = 530$. **b)** and **d)**, temperature and velocity profiles, respectively, for the wind model with parameters: $R_\mathrm{max} = 2.0R_0$, $B = 550$, $\nu = 0.1$, $\eta = 0.01$ and T_p has the following values: solid (—) $T_\mathrm{p} = 2 \times 10^4$K, dotted $(\cdots)$ $T_\mathrm{p} = 1.5 \times 10^4$K, dashed (- - -) $T_\mathrm{p} = 1 \times 10^4$K.

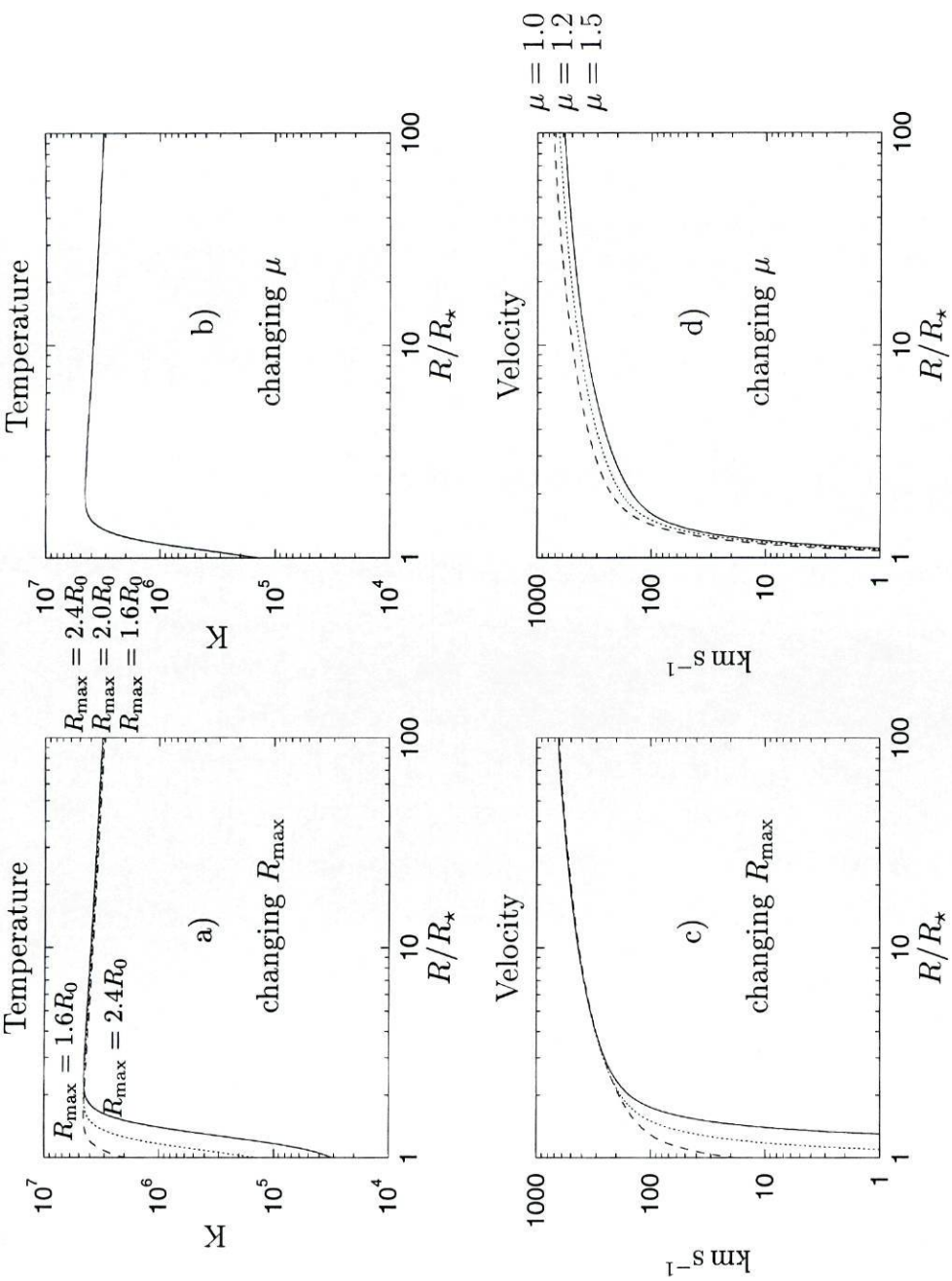

Figure 4.10: Effect of the parameters $R_{\rm max}$ (left) and the mean molecular weight - μ - (right) on the temperature (top plots) and velocity (bottom plots) profiles. **a)** and **c)**, temperature and velocity profiles, respectively, for the wind model with: $T_{\rm p} = 2 \times 10^4$K, $B = 550$, $\eta = 0.01$, $\nu = 0.1$ and $R_{\rm max}$ has the following values: solid (—) $R_{\rm max} = 2.0R_0$, dotted $(\cdots)$ $R_{\rm max} = 1.6R_0$, dashed (- - -) $R_{\rm max} = 2.4R_0$. **b)** and **d)**, temperature and velocity profiles, respectively, for the wind model where the temperature parameters are: $T_{\rm p} = 2 \times 10^4$K, $R_{\rm max} = 2.0R_0$, $B = 550$, $\nu = 0.1$, $\eta = 0.01$ and the mean molecular weight has the following values: solid (—) $\mu = 1.2$, dotted $(\cdots)$ $\mu = 1.0$, dashed (- - -) $\mu = 1.5$.

A search for a common temperature profile for all models was made, in an attempt to change only the stellar radius between models. However, it proved necessary to change also the value of η, otherwise the critical point could be of spiral nature, or there could be two critical points on the momentum equation.

Analysis of the models shown in Fig. 4.11 leads to the general conclusion that this stellar wind model can be applied successfully to stars with $M_\star \sim M_\odot$ and $R_\star > R_\odot$, as TTS are. The initial acceleration of the wind models shown is reasonably strong, the plasma attains $V \sim$ 100-200 km s^{-1} within one stellar radius. The terminal velocity decreases with increasing stellar radius, mainly due to the need to decrease η, for the reasons already mentioned, and consequently to 'lower' the temperature profile. The models with $R_\star = 3\,R_\odot$ and $R_\star = 4\,R_\odot$ do not seem to suffer from this limitation. The velocity profile of the larger star lies above the profile for the other star. However this effect is mainly due to the x-scale, as the radial distances are in units of the stellar radius.

4.7.2 Increasing n_0

The observations of the lines formed in the winds of the TTS also suggest that the number density near the star is of the order 10^{11}–10^{13} cm^{-3}. The effect of increasing the density at the base is shown in Fig. 4.12. Both the temperature and the velocity profiles are independent of the value of n_0. This result was expected, since the temperature profile (Eq. (4.38)) is independent of the density, and therefore the momentum equation (Eq. (4.7)) is also independent of the density. Consequently, changing n_0 does not affect the temperature or the velocity profiles.

4.7.3 Comparison with the coronal wind models

The results of the two previous sections allows the conclusion that this thermally driven stellar wind model can be successfully applied to the TTS. It is therefore appropriate to present models allowing the comparison with conductive stellar wind models. This is made through the adequate choice of the input parameter ν.

Figure 4.13 shows the effects induced when the temperature gradient at large distances ($-\nu$) is set equal to each of the three possible values for the one-fluid conductive stellar wind models, namely, -2/7, -2/5, -4/3. Since ν is the only parameter changing between the models, the results could already be anticipated from those of Fig. 4.8, namely, increasing ν does not change $T_{\max}$ and increases the absolute value of the temperature slopes both before and after $R_{\max}$. Changing only ν effectively means that the temperature profiles were not optimized for this comparison; in particular the -4/3 profile has a flat temperature

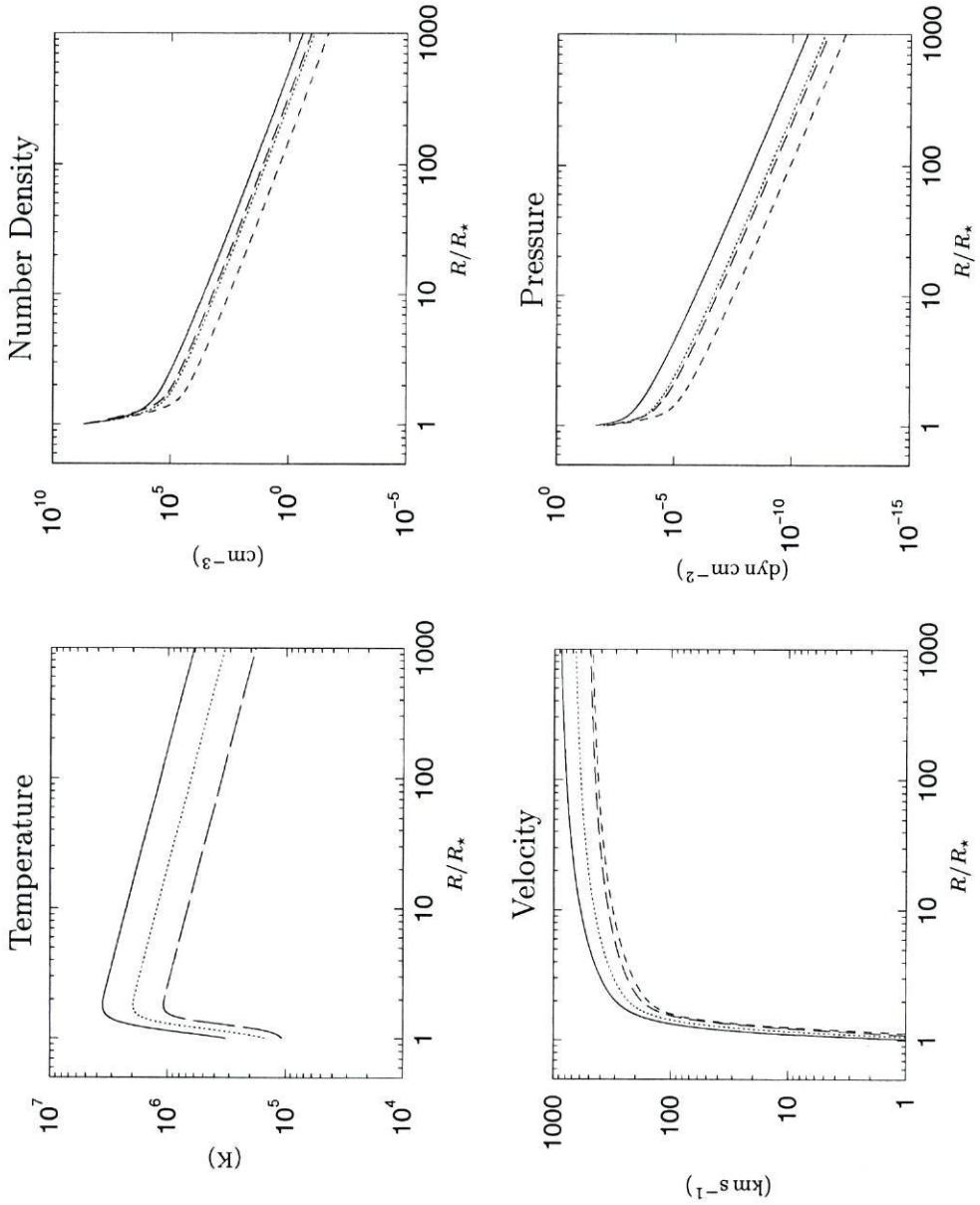

Figure 4.11: Effect on the different profiles of changing $R_\star$. All the profiles have in common the values of the parameters: $M_\star = M_\odot$, $\mu = 0.5$, $n_0 = 5 \times 10^8\,\mathrm{cm}^{-3}$, $T_\mathrm{p} = 10^5\,\mathrm{K}$, $R_\mathrm{max} = 1.8\,R_\star$, $B = 125$ and $\nu = 2/7$. (—): $R_\star = R_\odot$, $\eta = 0.030$; (···): $R_\star = 2\,R_\odot$, $\eta = 0.025$; (- - -): $R_\star = 3\,R_\odot$, $\eta = 0.020$; (– –): $R_\star = 4\,R_\odot$, $\eta = 0.020$.

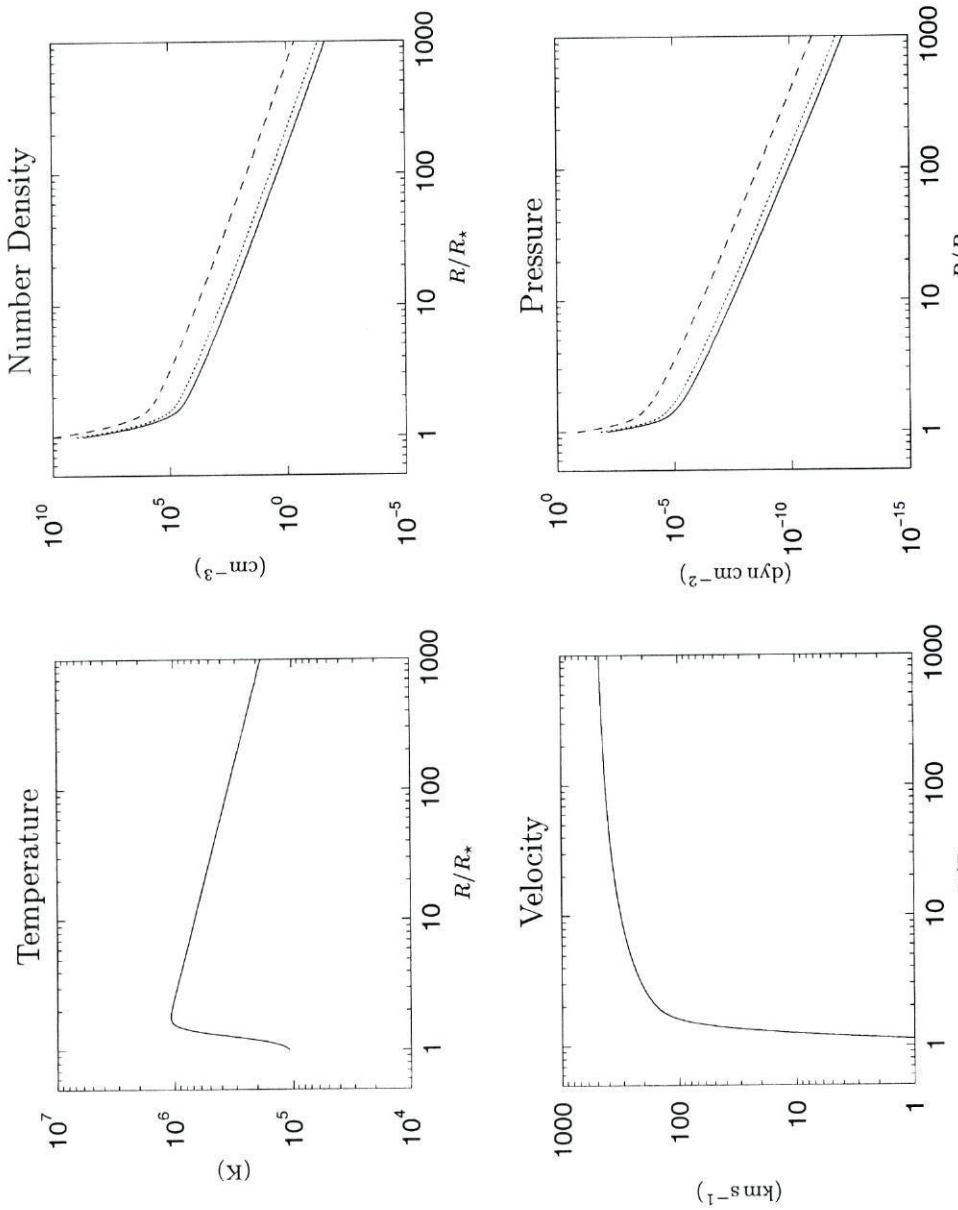

Figure 4.12: Effect on the different profiles of increments on n_0. All profiles have in common the values of the parameters: $M_\star = M_\odot$, $R_\star = 3\,R_\odot$, $\mu = 0.5$, $T_\mathrm{p} = 10^5\,\mathrm{K}$, $R_\mathrm{max} = 1.8\,R_\star$, $B = 125$, $\nu = 2/7$ and $\eta = 0.020$. (—): $n_0 = 5 \times 10^8\,\mathrm{cm}^{-3}$; (···):$n_0 = 10^9\,\mathrm{cm}^{-3}$; (- - -): $n_0 = 10^{10}\,\mathrm{cm}^{-3}$.

near the stellar surface, a steep rise (a 'transition region') followed by a fast decline after $R_{\rm max}$. This causes an abrupt increase of the velocity in the 'transition region', where the plasma accelerates from $V \ll 1\,{\rm km\,s^{-1}}$ to $V \sim 200\,{\rm km\,s^{-1}}$.

The momentum equation of the model with $\nu = 4/3$ has an X-type critical point at $(R_{\rm x}\,,\,V_{\rm x}) = (1.799\,,133.8)$ and a spiral critical point at $(R_{\rm s}\,,\,V_{\rm s}) = (9.214\,,45.50)$. The existence of the second critical point is not a surprise, in view of the discussion on the asymptotic form for the momentum equation, Eq. (4.57). The spiral critical point is located at a velocity of $V_{\rm s} \sim 45\,{\rm km\,s^{-1}}$, and the velocity of the 'wind' solution at $R = R_{\rm s}$ is $V_{\rm w} \sim 200\,{\rm km\,s^{-1}}$. Therefore the spiral critical point is far from the 'wind' solution, and consequently its effects are attenuated. Nevertheless, the velocity of the 'wind' solution reaches a maximum at $R = R_{\rm s}$, and decreases at a slow rate afterwards.

In summary, the stellar wind model with a prescribed exponential temperature profile can be used to qualitatively study the conductive wind models with asymptotic temperature slopes -2/7 and -2/5. However, it cannot be used to study the -4/3 case due to the existence of two critical points on the momentum equation. In any case, the study is only qualitative since the temperature profile is prescribed and is independent of the plasma density.

4.8 Conclusion

The basic stellar wind model is a one-fluid, hydrodynamic model, under steady state, spherically symmetric, thermally driven with a prescribed temperature profile. Three stellar wind models fulfilling this basic model were studied, differing on the prescribed temperature profile. The three different temperature profiles used were: a linear temperature profile, a Gaussian temperature profile and an exponential temperature profile. Due to the thermal nature of this stellar wind models the temperature must attain coronal values ($\sim 10^6\,{\rm K}$) to have wind velocities of a few hundred ${\rm km\,s^{-1}}$, as observed in the solar wind and inferred in the TTS winds.

The stellar wind model with a prescribed linear temperature profile could only be applied near the stellar surface, at best, as the temperature is always increasing. For moderate temperature slopes the initial acceleration of the plasma is not strong enough, and velocities above 100-200 ${\rm km\,s^{-1}}$ are only achieved far from the star. For higher temperature slopes the initial acceleration is stronger and velocities exceeding 100-200 ${\rm km\,s^{-1}}$ are reached close to the stellar surface. However, the temperature rises above any reasonable coronal value. It is therefore concluded that this stellar wind model is not a reliable one, even near the stellar surface.

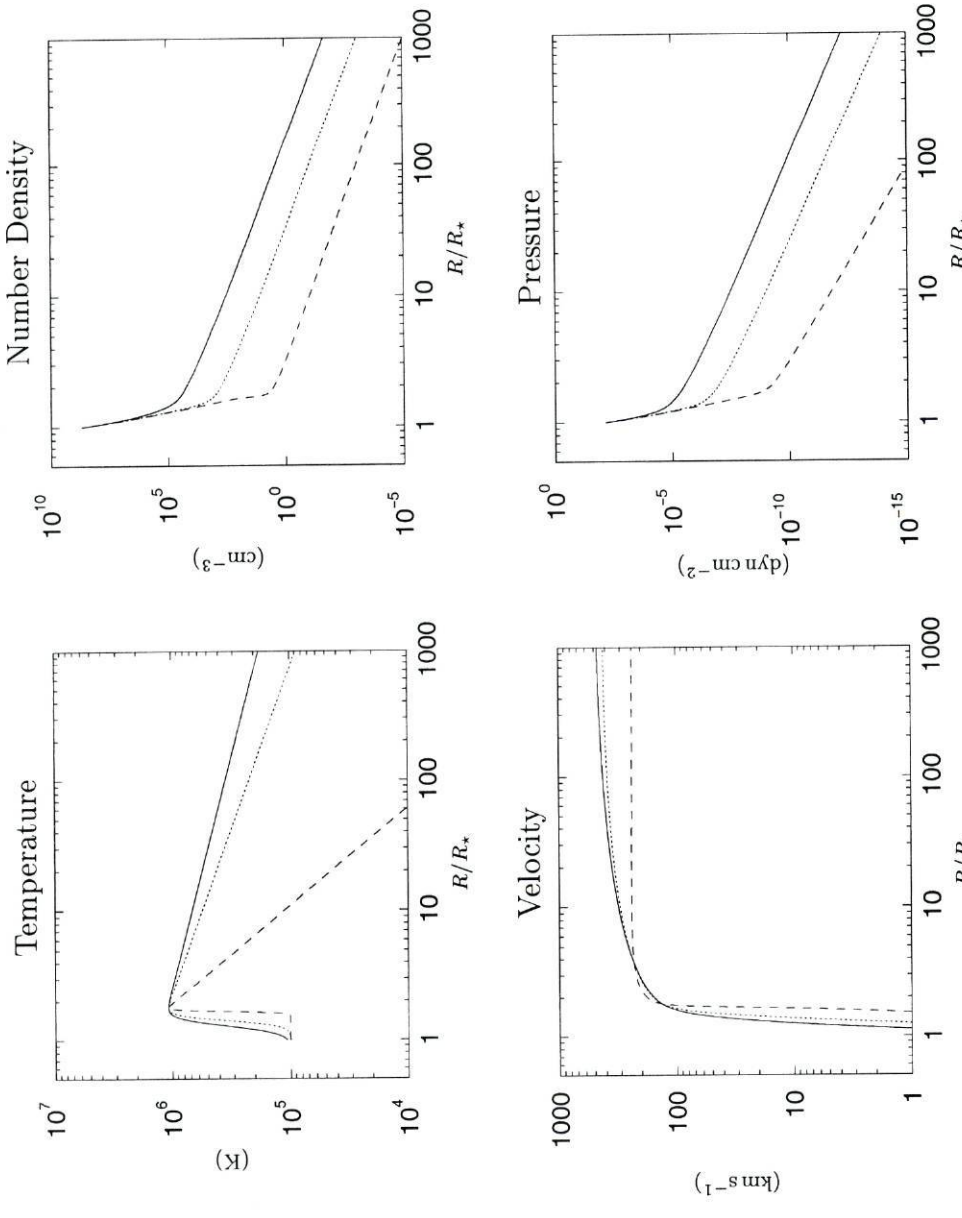

Figure 4.13: Possible temperature profiles with the three possible terminal values of the temperature gradient for the coronal wind model. All the profiles have in common the input parameters: $M_\star = M_\odot$, $R_\star = 3\,R_\odot$, $\mu = 0.5$, $n_0 = 5 \times 10^8\,\mathrm{cm}^{-3}$, $T_\mathrm{p} = 10^5\,\mathrm{K}$, $R_\mathrm{max} = 1.8\,R_\star$, $B = 125$ and $\eta = 0.020$. (—): $\nu = 2/7$; $(\cdots)$:$\nu = 2/5$; (– –): $\nu = 4/3$.

The stellar wind model with a prescribed Gaussian temperature profile could, in principle, be applied to a wider region as the temperature increases to a maximum and then decreases. Nevertheless, the decrease of the temperature after the maximum value is much faster then it is observed for the solar wind, for example. From the exploration of the parameter space it was found that the momentum equation has two critical points. One closer to the star of X-type, and the furthest a spiral critical point. This extra critical point causes the velocity of the 'wind' solution (the one crossing the X-type critical point with positive slope) to reach a maximum at $R = R_s$. For reasonable values of the parameters $V_{max} < 200\,\mathrm{km\,s^{-1}}$, contrary to the observations of TTS, where velocities in excess of $300\,\mathrm{km\,s^{-1}}$ are inferred. This low value of V_{max} and the slow initial acceleration of the plasma are the main reasons to discard this model. Another drawback is the vanishing of the velocity at a finite distance for some values of the parameters. For the velocity of the 'wind' solution to have finite values at infinity the parameters must reach, or exceed, some 'critical' values.

The velocity profile of the 'wind' solution resembles the velocity profile proposed by Grinin and Mitskevich (1991). However, in the present model it arises from the existence of two critical points in the momentum equation. In this work it is the temperature profile to be prescribed, not the velocity profile.

The third stellar wind model presented has a prescribed 'exponential' temperature profile, with a more complex parameterization, having five parameters. Depending on the value of the input parameters the resulting momentum equation could be without critical points, with one critical point (spiral or X-type), or even two critical points, an X-type closer to the stellar surface and a spiral or improper node critical point farther out from the stellar surface.

By carefully choosing the values of the input parameters a good fit to the solar wind temperature profile is possible. Without a detailed temperature profile for winds in TTS, the temperature profile of the solar wind is used as a template for the thermally driven wind models of the TTS. To have a strong initial acceleration, and for the velocity to increase up to $100\,\mathrm{km\,s^{-1}}$ within less than a stellar radius above the stellar surface, the value of T_0 must be a few 10^5 K. The 'transition region' must be narrow to rapidly achieve coronal temperatures, in excess of 10^6 K. A wind model with a temperature profile of this form is able to drive winds for stars with solar mass and larger radius, as are the TTS.

In these stellar wind models the temperature profile is independent of the plasma density, implying that the momentum equation is also independent of the plasma density. This allows building wind models with any value of the base density n_0, and any value for the mass loss rate. Therefore, the stellar wind model with a prescribed exponential temperature profile can be successfully applied to the TTS. Nevertheless, the values of the

velocity very close to the stellar surface are much lower than suggested by the observations.

Finally, wind models with an asymptotic slope for the exponential temperature profile equal to -2/7, -2/5 and -4/3 were presented to allow comparison with the conductive stellar wind models. This comparison can only be qualitative since the temperature profile is prescribed and independent of the plasma density, while the temperature profile of the conductive stellar wind models is not prescribed and depends on the plasma density. The comparison of the -4/3 case is not possible due to the existence of two critical points on the momentum equation, and consequent velocity profile with a maximum.

Chapter 5

A stellar wind model with a detailed energy equation

This Chapter proceeds with the development of stellar wind models for T Tauri stars. The model to be built will again be hydrodynamic and assume complete spherical symmetry. To close the system of equations an energy equation will be used. This energy equation includes terms due to the thermal conductivity flux, radiative losses and a prescribed mechanical heating function. The classical expression for the thermal conductivity flux will be used, and the radiative losses are those for an optically thin plasma.

5.1 Equations

The stellar wind model presented in this Chapter is a natural development of the models of the previous Chapter. The equations for the ideal gas law, mass and momentum conservation are still Eqs. (4.3), (4.6) and (4.7), respectively. In the previous Chapter this system of equations was closed by prescribing the form of the temperature profile. However, in this Chapter an energy equation will be used for that purpose. The following Section addresses the form of the energy equation and its different terms.

5.2 The energy equation and its terms

Following Priest (1982), the energy equation may be written in the form

$$\rho T \frac{\mathrm{D}s}{\mathrm{D}t} = -\nabla \cdot \vec{q} - L_{\mathrm{r}} + H \tag{5.1}$$

where s is the entropy per unit mass, $\vec{q}$ the thermal conductivity flux, L_r the radiative losses, H is the mechanical heating function and

$$\frac{D}{Dt} \equiv \frac{\partial}{\partial t} + \vec{V} \cdot \nabla \tag{5.2}$$

is the material derivative.

The physical meaning of Eq. (5.1) is that the rate of heat changes for a unit volume of gas as it moves in space are due to the thermal heat conduction, the radiation losses and the volumetric heat additions.

The left-hand side of Eq. (5.1) can be written in a more suitable form by using the first law of thermodynamics

$$de = T ds - P\, d\left(\frac{1}{\rho}\right) \tag{5.3}$$

where e is the internal energy per unit mass. For an ideal gas

$$e = \frac{P}{(\gamma - 1)\rho} \quad , \tag{5.4}$$

where $\gamma = c_p/c_v$ is the ratio of the specific heats[1]. Therefore

$$\rho T \frac{Ds}{Dt} = \frac{1}{\gamma - 1}\left(\frac{DP}{Dt} - \gamma \frac{P}{\rho}\frac{D\rho}{Dt}\right) \tag{5.5}$$

or, in a compact form:

$$\rho T \frac{Ds}{Dt} = \frac{\rho^\gamma}{\gamma - 1}\frac{D}{Dt}\left(\frac{P}{\rho^\gamma}\right) \quad . \tag{5.6}$$

Substitution of this Equation in Eq. (5.1) results in the expression

$$\frac{\rho^\gamma}{\gamma - 1}\frac{D}{Dt}\left(\frac{P}{\rho^\gamma}\right) = -\nabla \cdot \vec{q} - L_r + H \quad . \tag{5.7}$$

This is the form of the energy equation adopted here. In a steady state under complete spherical symmetry the left-hand side simplifies to

$$\frac{V}{\gamma - 1}\left(\frac{dP}{dR} - \gamma \frac{P}{\rho}\frac{d\rho}{dR}\right) \quad . \tag{5.8}$$

[1]For a perfect monoatomic gas $\gamma = 5/3$

Temperature (K) \ electron density (cm^{-3})	1	10^3	10^6	10^9	10^{12}
10^3	19.7	16.3	12.8	9.43	5.97
10^4	**23.2**	**19.7**	16.3	12.8	9.43
10^5	26.7	**23.2**	**19.7**	**16.3**	12.8
10^6	29.7	26.3	**22.8**	**19.3**	15.9
10^7	32.0	28.5	25.1	21.6	18.1

Table 5.1: Coulomb logarithm. Table adapted from Spitzer (1956; 1962).

5.2.1 Thermal conductivity

The thermal conductivity flux can be written as

$$\begin{aligned} \vec{q} &= -\vec{\boldsymbol{\kappa}} \cdot \nabla T \quad , \text{ or, under spherical symmetry,} \\ \vec{q} &= -\kappa \frac{\mathrm{d}T}{\mathrm{d}R} \hat{e}_\mathrm{r} \end{aligned} \tag{5.9}$$

where $\vec{\boldsymbol{\kappa}}$ is the heat conduction tensor, and κ is the heat conduction.

The expression for κ parallel to the magnetic field is (Spitzer, 1956; Spitzer, 1962)

$$\kappa \simeq \kappa_\mathrm{e} \propto \frac{T_\mathrm{e}^{5/2}}{\sqrt{m_\mathrm{e}} \cdot \ln \Lambda} \tag{5.10}$$

where m_e is the electron mass, and $\ln \Lambda$ is the Coulomb logarithm; the global heat conduction is mostly due to the electrons, as they are lighter, and Table 5.1 (reproducing Table 5.1 of Spitzer (1956; 1962)) shows the most suited values for the model being typed in boldface. From inspection of these values it is seen that $\ln \Lambda$ is nearly constant, with a value around 20. In this work $\ln \Lambda$ will be considered constant, therefore the heat flux is written as

$$\kappa = \kappa_0 T^{5/2} \tag{5.11}$$

where κ_0 is the proportionality constant, with the value proposed by Hollweg (1986), namely $\kappa_0 = 8.4 \times 10^{-7}\,\mathrm{erg\,s^{-1}\,K^{-1}\,cm^{-1}}$, and $\ln \Lambda \sim 20$ in Eq. (5.10).

Equation (5.11) for the thermal conductivity assumes that the plasma has many collisions per unit time. However, the mean time between collisions (or self-collision time) is inversely proportional to the density (Spitzer, 1956; Spitzer, 1962)

$$t_\mathrm{ce} \propto \frac{\sqrt{m_\mathrm{e}} \cdot T_\mathrm{e}^{3/2}}{n_\mathrm{e} \cdot \ln \Lambda} \quad . \tag{5.12}$$

Far from the star the density is very low and the assumption of many collisions is not valid, although in a magnetized plasma, under the frozen-in approximation, there are more collisions in the direction perpendicular to the ambient magnetic field than for a non-magnetized plasma, as was discussed in Chapter 3. Having realized this break down of the theory several authors proposed expressions for the so called collisionless electron heat conduction (Hollweg, 1974; Hollweg, 1976; Canullo et al., 1996). However, the use of expressions for the collisionless electron heat conduction will result in an increased complexity of the equations to be solved.

It must also be recognized that this is not the only cause of uncertainty in the model, there are other causes, namely:

- the form of the radiative loss function, in particular its dependence on the coronal elemental abundances (Cook et al., 1989);
- the use of spherical symmetry;
- the neglect of the magnetic field;
- the use of a one-fluid model.

Taking into account these simplifications the classical expression for the electron heat conduction with constant κ_0 will be used in this work.

5.2.2 Radiative losses

The radiative losses for a low density and optically thin plasma in equilibrium can be approximated by the expression

$$L_{\mathrm{r}} = n_{\mathrm{e}} n_{\mathrm{p}} Q(T) \tag{5.13}$$

where $Q(T)$ is the radiative loss function, whose units are $\mathrm{erg\,s^{-1}\,cm^3}$. This function has been computed by several authors (Cox and Tucker, 1969; Raymond et al., 1976; Cook et al., 1989) using the radiative emission in resonance lines and continuum (radiative and dielectric recombination). The general characteristics of the various computed radiative loss functions are the increase of its value from $T \sim 10^4$K up to $T \sim 10^5$K, a small plateau and its decrease up to $T \sim 10^7$K. The particular form of the radiative loss function depends on the coronal elemental abundances (Cook et al., 1989), as well as on the atomic parameters used.

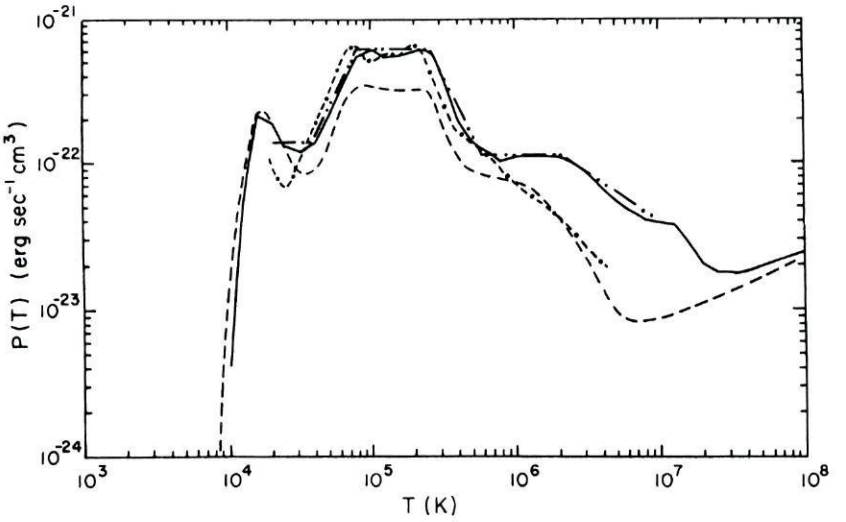

Figure 5.1: Analytical fit (·—·) to the radiative loss function (—). Other proposed radiative loss functions are displayed by the curves (- - -) and (· - - ·): . This Figure is adapted from Rosner et al. (1978).

The analytical fit for $Q(T)$ given by Rosner et al. (1978) is one of the most widely used (Hollweg, 1986; Withbroe, 1988; Hollweg and Johnson, 1988; Sandbæk and Leer, 1995; Cuseri et al., 1999, amongst others) and will be used in this work. Its functional form is:

$$
\begin{aligned}
Q(T) &= 10^{-21.85} && \text{for } 10^{4.3} < T < 10^{4.6} \text{ K} \\
&= 10^{-31} T^2 && \text{for } 10^{4.6} < T < 10^{4.9} \text{ K} \\
&= 10^{-21.2} && \text{for } 10^{4.9} < T < 10^{5.4} \text{ K} \\
&= 10^{-10.4} T^{-2} && \text{for } 10^{5.4} < T < 10^{5.75} \text{ K} \\
&= 10^{-21.94} && \text{for } 10^{5.75} < T < 10^{6.3} \text{ K} \\
&= 10^{-17.73} T^{-2/3} && \text{for } 10^{6.3} < T < 10^{7} \text{ K}
\end{aligned}
$$

and is displayed in Fig. 5.1. Sometimes $Q(T)$ is replaced by χT^{α} to stress the fact that this analytical fit to the radiative loss function is a piecewise continuous function of temperature.

For a completely ionized hydrogen plasma, $n_{\rm e} = n_{\rm p} = n$, $n = \rho/\mu m_{\rm H}$, $\mu = 1/2$, and replacing $Q(T)$ by χT^{α}, Eq. (5.13) becomes:

$$
L_{\rm r} = \left(\frac{\rho}{\mu m_{\rm H}} \right)^2 \chi T^{\alpha} \quad . \tag{5.14}
$$

5.2.3 Mechanical heating

There are several proposed mechanisms of coronal heating, like the phase mixing of Alfvén waves (Heyvaerts and Priest, 1983), resonant absorption of waves (Ionson, 1978), acoustic shock waves, gravitational damping of Alfvén waves (Khabibrakhmanov and Mullan, 1994), nanoflares (Parker, 1988). Some of them have been used with relative success in a tentative to solve simultaneously the problems of coronal heating and solar wind driving. As an example, the gravitational damping of Alfvén waves was investigated by Cuseri et al. (1999) as the source of coronal heating and solar wind driving mechanism, and yet it was still necessary to use an extra prescribed mechanical heating function that deposits energy close to the stellar surface to bring the models in closer agreement with observations. This points out that there is not just one mechanism of coronal heating/wind driving operating, but several simultaneously, some of them more effective very near the stellar surface, others farther out.

Again taking the sun as an analogue, it is known that the corona begins well within one solar radius above the solar surface. To achieve this increase in the temperature from surface values to coronal values, as well as to give the initial acceleration of the plasma, there must be a large deposition of mechanical energy within one solar radius.

Instead of using a particular mechanism for the mechanical energy deposition it was decided to start with a simple negative exponential to characterize the volumetric heating function of the stellar wind model under study

$$H = h_0 e^{-\frac{R-R_\star}{\sigma}} \tag{5.15}$$

where the units of h_0 are $\mathrm{erg\,s^{-1}\,cm^{-3}}$ and σ is a measure of the extent of the mechanical heating deposition. For the particular case of phase mixing of Alfvén waves in a cartesian coordinate system, Hood et al. (1997) find the rate of ohmic heating to be given by a negative exponential, although of more complex parameterization than Eq. (5.15). This adds more support to the use of Eq. (5.15) as the volumetric heating rate, at least in a first approach.

5.2.4 Adding all terms

Joining the relevant expressions in accordance with the energy equation (Eq. (5.7)), results in

$$\frac{V}{\gamma-1}\left(\frac{\mathrm{d}P}{\mathrm{d}R}-\gamma AT\frac{\mathrm{d}\rho}{\mathrm{d}R}\right)=\frac{1}{R^2}\frac{\mathrm{d}}{\mathrm{d}R}\left(R^2\kappa_0 T^{5/2}\frac{\mathrm{d}T}{\mathrm{d}R}\right)-\left(\frac{\rho}{\mu m_{\mathrm{H}}}\right)^2\chi T^\alpha+h_0 e^{-\frac{R-R_\star}{\sigma}} \tag{5.16}$$

rearranging terms and expanding ρ, $\mathrm{d}\rho/\mathrm{d}R$ and $\mathrm{d}P/\mathrm{d}R$ gives

$$\frac{\mathrm{d}}{\mathrm{d}R}\left(R^2\kappa_0 T^{5/2}\frac{\mathrm{d}T}{\mathrm{d}R}\right) = AZ\left[\frac{1}{\gamma-1}\frac{\mathrm{d}T}{\mathrm{d}R} + T\left(\frac{2}{R}+\frac{1}{V}\frac{\mathrm{d}V}{\mathrm{d}R}\right)\right] + \left(\frac{Z}{\mu m_{\mathrm{H}}}\right)^2\frac{\chi T^{\alpha}}{R^2V^2} - R^2 h_0 e^{-\frac{R-R_\star}{\sigma}} \quad . \tag{5.17}$$

This is a second order differential equation for T. As usual, it is transformed in two first order differential equations by defining

$$F = R^2\kappa_0 T^{5/2}\frac{\mathrm{d}T}{\mathrm{d}R} \tag{5.18}$$

and this system of equations becomes

$$\frac{\mathrm{d}T}{\mathrm{d}R} = \frac{F}{R^2\kappa_0 T^{5/2}} \tag{5.19}$$

$$\frac{\mathrm{d}F}{\mathrm{d}R} = AZ\left[\frac{1}{\gamma-1}\frac{\mathrm{d}T}{\mathrm{d}R} + T\left(\frac{2}{R}+\frac{1}{V}\frac{\mathrm{d}V}{\mathrm{d}R}\right)\right] + \left(\frac{Z}{\mu m_{\mathrm{H}}}\right)^2\frac{\chi T^{\alpha}}{R^2V^2} - R^2 h_0 e^{-\frac{R-R_\star}{\sigma}} \quad . \tag{5.20}$$

These two equations together with the momentum equation (Eq. (4.7)) form the system of equations to be integrated. It is opportune to express the relation between F and q

$$F = -R^2 q \quad . \tag{5.21}$$

5.3 Comparison with conductive wind models

Multiplying the momentum equation (Eq. (4.7)) by $\rho V R^2$, adding to Eq. (5.20) and using Eq. (5.21), results in

$$\frac{\mathrm{d}}{\mathrm{d}R}\left\{R^2\left[\rho V\left(\frac{1}{2}V^2 + \frac{A\gamma}{\gamma-1}T - \frac{GM}{R}\right) + q\right]\right\} = R^2 h_0 e^{-\frac{R-R_\star}{\sigma}} - \left(\frac{Z}{\mu m_{\mathrm{H}}}\right)^2\frac{\chi T^{\alpha}}{R^2V^2} \quad . \tag{5.22}$$

When the right-hand side of this Equation is identically zero it reduces to the energy equation of the coronal stellar wind models, Eq. (3.71). It is opportune to recall the asymptotic behaviour of the temperature for these stellar wind models, namely: $T \propto R^{-2/7}$, Parker (1965), $T \propto R^{-2/5}$, Wang and Chang (1965), and $T \propto R^{-4/3}$, Durney (1971). Another result relevant for this work is the existence of upward and downward divergent solutions.

The wind model under study has some similarities with coronal wind models, namely the right-hand side of Eq. (5.22) becomes vanishingly small at large distances from the stellar surface. Consequently, the asymptotic behaviour near infinity for this particular wind model tends to be similar to that of coronal wind models. The other similarity is the use of the classic expression for the thermal conductivity flux, that results in the existence of upward and downward divergent solutions, as will be seen later.

5.3.1 The energy fluxes

From Eq. (5.22) the energy fluxes may be written as

$$f_{\rm k} = \frac{1}{2}\rho V^3 \tag{5.23}$$

$$f_{\rm e} = \rho V \frac{A\gamma}{\gamma - 1} T \tag{5.24}$$

$$f_{\rm g} = \rho V \frac{GM}{R} \tag{5.25}$$

$$q = -\kappa_0 T^{5/2} \frac{{\rm d}T}{{\rm d}R} \tag{5.26}$$

$$f_{\rm m} = \sigma h_0 \left[1 + 2\frac{\sigma}{R} + 2\left(\frac{\sigma}{R}\right)^2\right] e^{-\frac{R-R_\star}{\sigma}} \tag{5.27}$$

$$\Delta f_{\rm r} = \frac{1}{R^2}\left(\frac{Z}{\mu m_{\rm H}}\right)^2 \int_{R_\star}^{R} \frac{\chi T^\alpha}{R^2 V^2} {\rm d}R \tag{5.28}$$

where $f_{\rm k}$ is the kinetic energy flux, $f_{\rm e}$ the enthalpy flux, $f_{\rm g}$ the gravitational potential energy flux, q the thermal conductivity flux, $f_{\rm m}$ the mechanical heating energy flux and $\Delta f_{\rm r}$ the radiation flux emitted between the stellar surface and the radial distance R.

5.4 Indetermination at the critical point

Raising the indetermination at the critical point of the momentum equation is the subject of this Section.

By defining the normalized variables

$$a = \frac{R}{R_{\rm c}} \ , \qquad u = \frac{v}{V_{\rm c}} \ , \qquad \tau = \frac{T}{T_{\rm c}} \ , \qquad \phi = \frac{F}{F_{\rm c}} \tag{5.29}$$

where the values of $T_{\rm c}$ and $F_{\rm c}$ are computed from the expressions

$$T_{\rm c} = \frac{V_{\rm c}^2}{A} \qquad \text{and} \qquad F_{\rm c} = R_{\rm c}\kappa_0 T_{\rm c}^{7/2}\left(2 - \frac{GM}{R_{\rm c}V_{\rm c}^2}\right) \ , \tag{5.30}$$

the derivatives in Eqs. (4.7), (5.19) and (5.20) become

$$\left(u^2-\tau\right)\frac{1}{u}\frac{\mathrm{d}u}{\mathrm{d}a}=2\frac{\tau}{a}-\frac{\mathrm{d}\tau}{\mathrm{d}a}-\frac{GM}{R_{\mathrm{c}}V_{\mathrm{c}}^2a^2} \tag{5.31}$$

$$\frac{\mathrm{d}\tau}{\mathrm{d}a}=\frac{F_{\mathrm{c}}}{\kappa_0 R_{\mathrm{c}}T_{\mathrm{c}}^{7/2}}\frac{\phi}{a^2\tau^{5/2}} \tag{5.32}$$

$$\begin{aligned}\frac{\mathrm{d}\phi}{\mathrm{d}a}=&\frac{V_{\mathrm{c}}^2Z}{F_{\mathrm{c}}}\left[\frac{1}{(\gamma-1)}\frac{\mathrm{d}\tau}{\mathrm{d}a}+\tau\left(\frac{2}{a}+\frac{1}{u}\frac{\mathrm{d}u}{\mathrm{d}a}\right)\right]\\&+\left(\frac{Z}{\mu m_{\mathrm{H}}}\right)^2\frac{\chi T^{\alpha}}{F_{\mathrm{c}}R_{\mathrm{c}}V_{\mathrm{c}}^2a^2u^2}-\frac{R_{\mathrm{c}}^3h_0}{F_{\mathrm{c}}}a^2e^{-\frac{R-R_\star}{\sigma}}\quad,\end{aligned} \tag{5.33}$$

respectively.

To overcome the indetermination of the momentum equation at the critical point it is necessary to linearize the system of equations defined by Eqs. (5.31) to (5.33). Using the methods described in Appendix A, the starting point is the expansion to first order of the normalized variables

$$a=1+\delta\ ,\qquad u=1+\epsilon\ ,\qquad \tau=1+\left.\frac{\mathrm{d}\tau}{\mathrm{d}a}\right|_{\mathrm{c}}\delta \tag{5.34}$$

and

$$\frac{\mathrm{d}\tau}{\mathrm{d}a}=\left.\frac{\mathrm{d}\tau}{\mathrm{d}a}\right|_{\mathrm{c}}+\frac{\partial}{\partial a}\left(\frac{\mathrm{d}\tau}{\mathrm{d}a}\right)\bigg|_{\mathrm{c}}\delta+\frac{\partial}{\partial u}\left(\frac{\mathrm{d}\tau}{\mathrm{d}a}\right)\bigg|_{\mathrm{c}}\epsilon\quad. \tag{5.35}$$

The partial derivatives of second order of the normalized temperature are

$$\frac{\partial}{\partial a}\left(\frac{\mathrm{d}\tau}{\mathrm{d}a}\right)=\left.\frac{\mathrm{d}\tau}{\mathrm{d}a}\right|_{\mathrm{c}}\frac{1}{a^2\tau^{5/2}}\left(\frac{\partial\phi}{\partial a}-\frac{2\phi}{a}-\frac{5\phi}{2\tau}\frac{\mathrm{d}\tau}{\mathrm{d}a}\right) \tag{5.36}$$

and

$$\frac{\partial}{\partial u}\left(\frac{\mathrm{d}\tau}{\mathrm{d}a}\right)=\left.\frac{\mathrm{d}\tau}{\mathrm{d}a}\right|_{\mathrm{c}}\frac{1}{a^2\tau^{5/2}}\frac{\partial\phi}{\partial u} \tag{5.37}$$

where

$$\frac{\partial\phi}{\partial a}=\frac{V_{\mathrm{c}}^2Z}{F_{\mathrm{c}}}\left(\frac{1}{(\gamma-1)}\frac{\mathrm{d}\tau}{\mathrm{d}a}+2\frac{\tau}{a}\right)+\left(\frac{Z}{\mu m_{\mathrm{H}}}\right)^2\frac{\chi T^{\alpha}}{F_{\mathrm{c}}R_{\mathrm{c}}V_{\mathrm{c}}^2a^2u^2}-\frac{R_{\mathrm{c}}^3h_0}{F_{\mathrm{c}}}a^2e^{-\frac{R-R_\star}{\sigma}} \tag{5.38}$$

$$\frac{\partial \phi}{\partial u} = \frac{V_c^2 Z}{F_c u} \quad . \tag{5.39}$$

These derivatives at the critical point simplify to

$$\left.\frac{\mathrm{d}\tau}{\mathrm{d}a}\right|_c = \frac{F_c}{\kappa_0 R_c T_c^{7/2}} \tag{5.40}$$

$$\left.\frac{\partial}{\partial a}\left(\frac{\mathrm{d}\tau}{\mathrm{d}a}\right)\right|_c = \left.\frac{\mathrm{d}\tau}{\mathrm{d}a}\right|_c \left(\left.\frac{\partial \phi}{\partial a}\right|_c - 2 - \frac{5}{2}\left.\frac{\mathrm{d}\tau}{\mathrm{d}a}\right|_c\right) \tag{5.41}$$

$$\left.\frac{\partial}{\partial u}\left(\frac{\mathrm{d}\tau}{\mathrm{d}a}\right)\right|_c = \left.\frac{\mathrm{d}\tau}{\mathrm{d}a}\right|_c \left.\frac{\partial \phi}{\partial u}\right|_c \tag{5.42}$$

$$\left.\frac{\partial \phi}{\partial a}\right|_c = \frac{V_c^2 Z}{F_c}\left(\frac{1}{(\gamma-1)}\left.\frac{\mathrm{d}\tau}{\mathrm{d}a}\right|_c + 2\right) + \left(\frac{Z}{\mu m_{\mathrm{H}}}\right)^2 \frac{\chi T_c^{\alpha}}{F_c R_c V_c^2} - \frac{R_c^3 h_0}{F_c} e^{-\frac{R_c - R_\star}{\sigma}} \tag{5.43}$$

$$\left.\frac{\partial \phi}{\partial u}\right|_c = \frac{V_c^2 Z}{F_c} \quad . \tag{5.44}$$

Therefore, the linearized coefficients defined in Appendix A are

$$\begin{aligned} b &= -\left.\frac{\mathrm{d}\tau}{\mathrm{d}a}\right|_c \\ c &= 2 \\ e &= 2\left(1 - \left.\frac{\mathrm{d}\tau}{\mathrm{d}a}\right|_c\right) + \left.\frac{\mathrm{d}\tau}{\mathrm{d}a}\right|_c \left(\frac{5}{2}\left.\frac{\mathrm{d}\tau}{\mathrm{d}a}\right|_c - \left.\frac{\partial \phi}{\partial a}\right|_c\right) \\ f &= -\left.\frac{\partial \phi}{\partial u}\right|_c \quad . \end{aligned} \tag{5.45}$$

The derivatives of the velocity at an X-type critical point are

$$\left.\frac{\mathrm{d}u}{\mathrm{d}a}\right|_c = \frac{\lambda_\pm - b}{c} = \frac{e}{\lambda_\pm - f} \qquad \text{, where} \qquad \lambda_\pm = \frac{b + f \pm \sqrt{(b-f)^2 + 4ce}}{2} \tag{5.46}$$

the positive derivative corresponds to the wind solution, and is thus retained in this work, while the negative derivative corresponds to the accretion solution, and therefore is discarded.

To further increase the accuracy of the analytical solution near the critical point, a second order Taylor expansion was used. The second derivative of the temperature is obtained by joining the two partial derivatives of Eqs. (5.41) and (5.42), i.e.,

$$\left.\frac{\mathrm{d}^2\tau}{\mathrm{d}a^2}\right|_{\mathrm{c}} = \left.\frac{\partial}{\partial a}\left(\frac{\mathrm{d}\tau}{\mathrm{d}a}\right)\right|_{\mathrm{c}} + \left.\frac{\partial}{\partial u}\left(\frac{\mathrm{d}\tau}{\mathrm{d}a}\right)\right|_{\mathrm{c}} \left.\frac{\mathrm{d}u}{\mathrm{d}a}\right|_{\mathrm{c}} \quad . \tag{5.47}$$

To obtain the second derivative of the velocity at the critical point both members of the momentum equation (Eq. (5.31)) were derived twice

$$\frac{\mathrm{d}}{\mathrm{d}a}[\mathbf{left}] = \frac{1}{u}(u^2-\tau)\left[\frac{\mathrm{d}^2u}{\mathrm{d}a^2} - \frac{1}{u}\left(\frac{\mathrm{d}u}{\mathrm{d}a}\right)^2\right] + \frac{1}{u}\frac{\mathrm{d}u}{\mathrm{d}a}\left(2u\frac{\mathrm{d}u}{\mathrm{d}a} - \frac{\mathrm{d}\tau}{\mathrm{d}a}\right) \tag{5.48}$$

$$\begin{aligned}\frac{\mathrm{d}^2}{\mathrm{d}a^2}[\mathbf{left}] = {} & \frac{1}{u}(u^2-\tau)\left[\frac{\mathrm{d}^3u}{\mathrm{d}a^3} - \frac{3}{u}\frac{\mathrm{d}^2u}{\mathrm{d}a^2}\frac{\mathrm{d}u}{\mathrm{d}a} + \frac{2}{u^2}\left(\frac{\mathrm{d}u}{\mathrm{d}a}\right)^3\right] \\ & + \left(6\frac{\mathrm{d}u}{\mathrm{d}a} - \frac{2}{u}\frac{\mathrm{d}\tau}{\mathrm{d}a}\right)\frac{\mathrm{d}^2u}{\mathrm{d}a^2} + \frac{2}{u^2}\left(\frac{\mathrm{d}u}{\mathrm{d}a}\right)^2\left(\frac{\mathrm{d}\tau}{\mathrm{d}a} - 2u\frac{\mathrm{d}u}{\mathrm{d}a}\right) \\ & + \frac{1}{u}\frac{\mathrm{d}u}{\mathrm{d}a}\left[2\left(\frac{\mathrm{d}u}{\mathrm{d}a}\right)^2 - \frac{\mathrm{d}^2\tau}{\mathrm{d}a^2}\right]\end{aligned} \tag{5.49}$$

$$\frac{\mathrm{d}}{\mathrm{d}a}[\mathbf{right}] = \frac{2}{a}\frac{\mathrm{d}\tau}{\mathrm{d}a} - 2\frac{\tau}{a^2} - \frac{\mathrm{d}^2\tau}{\mathrm{d}a^2} + \frac{2GM}{R_{\mathrm{c}}V_{\mathrm{c}}^2a^3} \tag{5.50}$$

$$\frac{\mathrm{d}^2}{\mathrm{d}a^2}[\mathbf{right}] = 4\frac{\tau}{a^3} - \frac{4}{a^2}\frac{\mathrm{d}\tau}{\mathrm{d}a} + \frac{2}{a}\frac{\mathrm{d}^2\tau}{\mathrm{d}a^2} - \frac{\mathrm{d}^3\tau}{\mathrm{d}a^3} - \frac{6GM}{R_{\mathrm{c}}V_{\mathrm{c}}^2a^4} \tag{5.51}$$

where the third derivative of τ appearing in the previous equation is

$$\begin{aligned}\frac{\mathrm{d}^3\tau}{\mathrm{d}a^3} = {} & -\frac{\mathrm{d}^2\tau}{\mathrm{d}a^2}\left(\frac{2}{a} + \frac{5}{2\tau}\frac{\mathrm{d}\tau}{\mathrm{d}a}\right) \\ & + \frac{1}{a^2\tau^{5/2}}\left.\frac{\mathrm{d}\tau}{\mathrm{d}a}\right|_{\mathrm{c}}\left\{\frac{\mathrm{d}^2\phi}{\mathrm{d}a^2} - \frac{2}{a} - \frac{5}{2\tau}\frac{\mathrm{d}\tau}{\mathrm{d}a} + 2\left[\frac{1}{a^2} + \frac{5}{2\tau^2}\left(\frac{\mathrm{d}\tau}{\mathrm{d}a}\right)^2 - \frac{5}{2\tau}\frac{\mathrm{d}^2\tau}{\mathrm{d}a^2}\right]\phi\right\}\end{aligned} \tag{5.52}$$

while the second derivative of ϕ is

$$\begin{aligned}\frac{\mathrm{d}^2\phi}{\mathrm{d}a^2} = {} & \frac{V_{\mathrm{c}}^2Z}{F_{\mathrm{c}}}\left\{\frac{1}{(\gamma-1)}\frac{\mathrm{d}^2\tau}{\mathrm{d}a^2} + \frac{\mathrm{d}\tau}{\mathrm{d}a}\left(\frac{2}{a} + \frac{1}{u}\frac{\mathrm{d}u}{\mathrm{d}a}\right) + \tau\left[-\frac{2}{a^2} + \frac{1}{u}\left(\frac{\mathrm{d}^2u}{\mathrm{d}a^2} - \frac{1}{u}\left(\frac{\mathrm{d}u}{\mathrm{d}a}\right)^2\right)\right]\right\} \\ & + \left(\frac{Z}{\mu m_{\mathrm{H}}}\right)^2\frac{\chi T^\alpha}{F_{\mathrm{c}}R_{\mathrm{c}}V_{\mathrm{c}}^2}\left(\alpha\frac{\mathrm{d}\ln(\tau)}{\mathrm{d}a} - \frac{2}{a} - \frac{2}{u}\frac{\mathrm{d}u}{\mathrm{d}a}\right) - \frac{R_{\mathrm{c}}^3h_0}{F_{\mathrm{c}}}a\left(2 - \frac{R_{\mathrm{c}}a}{\sigma}\right)e^{-\frac{R-R_\star}{\sigma}}\end{aligned} \tag{5.53}$$

In order to obtain the second derivative of u at the critical point Eqs. (5.49), (5.51), (5.52) and (5.53) will be separated in a 'a'-part (without dependences on $\mathrm{d}^2u/\mathrm{d}a^2$) and a '$u$'-part (with dependences on $\mathrm{d}^2u/\mathrm{d}a^2$), after being computed at the critical point, denoted by $\cdots|_{\mathrm{c}}^{a}$ and $\cdots|_{\mathrm{c}}^{u}$ respectively, as follows:

$$\frac{\mathrm{d}^2}{\mathrm{d}a^2}\,[\mathbf{left}]\Big|_{\mathrm{c}}^{a} = 2\left(\frac{\mathrm{d}u}{\mathrm{d}a}\Big|_{\mathrm{c}}\right)^2\left(\frac{\mathrm{d}\tau}{\mathrm{d}a}\Big|_{\mathrm{c}} - 2\,\frac{\mathrm{d}u}{\mathrm{d}a}\Big|_{\mathrm{c}}\right) + \frac{\mathrm{d}u}{\mathrm{d}a}\Big|_{\mathrm{c}}\left[2\left(\frac{\mathrm{d}u}{\mathrm{d}a}\Big|_{\mathrm{c}}\right)^2 - \frac{\mathrm{d}^2\tau}{\mathrm{d}a^2}\Big|_{\mathrm{c}}\right] \tag{5.54}$$

$$\frac{\mathrm{d}^2}{\mathrm{d}a^2}\,[\mathbf{left}]\Big|_{\mathrm{c}}^{u} = \left(6\,\frac{\mathrm{d}u}{\mathrm{d}a}\Big|_{\mathrm{c}} - 2\,\frac{\mathrm{d}\tau}{\mathrm{d}a}\Big|_{\mathrm{c}}\right)\frac{\mathrm{d}^2u}{\mathrm{d}a^2}\Big|_{\mathrm{c}} \tag{5.55}$$

and

$$\frac{\mathrm{d}^2}{\mathrm{d}a^2}\,[\mathbf{right}]\Big|_{\mathrm{c}}^{a} = 4 - 4\,\frac{\mathrm{d}\tau}{\mathrm{d}a}\Big|_{\mathrm{c}} + 2\,\frac{\mathrm{d}^2\tau}{\mathrm{d}a^2}\Big|_{\mathrm{c}} - \frac{\mathrm{d}^3\tau}{\mathrm{d}a^3}\Big|_{\mathrm{c}}^{a} - \frac{6GM}{R_{\mathrm{c}}V_{\mathrm{c}}^2} \tag{5.56}$$

$$\frac{\mathrm{d}^2}{\mathrm{d}a^2}\,[\mathbf{right}]\Big|_{\mathrm{c}}^{u} = -\,\frac{\mathrm{d}^3\tau}{\mathrm{d}a^3}\Big|_{\mathrm{c}}^{u} \tag{5.57}$$

the third derivative of τ:

$$\begin{aligned}\frac{\mathrm{d}^3\tau}{\mathrm{d}a^3}\Big|_{\mathrm{c}}^{a} = &-\frac{\mathrm{d}^2\tau}{\mathrm{d}a^2}\Big|_{\mathrm{c}}\left(2+\frac{5}{2}\,\frac{\mathrm{d}\tau}{\mathrm{d}a}\Big|_{\mathrm{c}}\right)\\ &+\frac{\mathrm{d}\tau}{\mathrm{d}a}\Big|_{\mathrm{c}}\left\{\frac{\mathrm{d}^2\phi}{\mathrm{d}a^2}\Big|_{\mathrm{c}}^{a} - 2 - \frac{5}{2}\,\frac{\mathrm{d}\tau}{\mathrm{d}a}\Big|_{\mathrm{c}} + 2\left[1+\frac{5}{2}\left(\frac{\mathrm{d}\tau}{\mathrm{d}a}\Big|_{\mathrm{c}}\right)^2 - \frac{5}{2}\,\frac{\mathrm{d}^2\tau}{\mathrm{d}a^2}\Big|_{\mathrm{c}}\right]\right\}\end{aligned} \tag{5.58}$$

$$\frac{\mathrm{d}^3\tau}{\mathrm{d}a^3}\Big|_{\mathrm{c}}^{u} = \frac{\mathrm{d}\tau}{\mathrm{d}a}\Big|_{\mathrm{c}}\,\frac{\mathrm{d}^2\phi}{\mathrm{d}a^2}\Big|_{\mathrm{c}}^{u} \tag{5.59}$$

the second derivative of ϕ

$$\begin{aligned}\frac{\mathrm{d}^2\phi}{\mathrm{d}a^2}\Big|_{\mathrm{c}}^{a} = &\frac{V_{\mathrm{c}}^2 Z}{F_{\mathrm{c}}}\left[\frac{1}{(\gamma-1)}\,\frac{\mathrm{d}^2\tau}{\mathrm{d}a^2}\Big|_{\mathrm{c}} + \frac{\mathrm{d}\tau}{\mathrm{d}a}\Big|_{\mathrm{c}}\left(2+\frac{\mathrm{d}u}{\mathrm{d}a}\Big|_{\mathrm{c}}\right) - 2 - \left(\frac{\mathrm{d}u}{\mathrm{d}a}\Big|_{\mathrm{c}}\right)^2\right]\\ &+\left(\frac{Z}{\mu m_{\mathrm{H}}}\right)^2\frac{\chi T_{\mathrm{c}}^{\alpha}}{F_{\mathrm{c}}R_{\mathrm{c}}V_{\mathrm{c}}^2}\left(\alpha\,\frac{\mathrm{d}\ln(\tau)}{\mathrm{d}a}\Big|_{\mathrm{c}} - 2 - 2\,\frac{\mathrm{d}u}{\mathrm{d}a}\Big|_{\mathrm{c}}\right) - \frac{R_{\mathrm{c}}^3 h_0}{F_{\mathrm{c}}}\left(2-\frac{R_{\mathrm{c}}}{\sigma}\right)\end{aligned} \tag{5.60}$$

and

$$\frac{\mathrm{d}^2\phi}{\mathrm{d}a^2}\Big|_{\mathrm{c}}^{u} = \frac{V_{\mathrm{c}}^2 Z}{F_{\mathrm{c}}}\,\frac{\mathrm{d}^2u}{\mathrm{d}a^2}\Big|_{\mathrm{c}}\quad . \tag{5.61}$$

The second derivative of the velocity is obtained by equating Eqs. (5.55) and (5.57) to Eqs. (5.54) and (5.56), while the second derivative of ϕ is given by the addition of Eqs. (5.60) and (5.61).

5.5 Method of solution

To integrate the system of Eqs. (5.32) to (5.33) two different approaches (methods A and B) will be used

Method A:

1 – guess the velocity profile $u(a)$;

2 – integrate simultaneously Eqs. (5.32) and (5.33);

3 – make a Taylor's expansion around the critical point and integrate Eq. (5.31);

4 – go to §2 and iterate until convergence.

Method B

1 – make a Taylor's expansion around the critical point;

2 – integrate simultaneously Eqs. (5.32), (5.31) and (5.33);

3 – go to §1 and iterate until convergence.

After several experiments with both methods, method B showed to be the most appropriate. Therefore, this method was adopted in this work and its structure is now described with more detail.

1 – guess the position of the critical point (R_c, V_c) and compute the values for T_c and F_c;

2 – choose the parameters of the mechanical heating function (h_0 and σ);

3 – choose the base density (n_0);

4 – choose V_0;

5 – compute $Z = R_\star V_0 \rho_0$;

6 – make a second order Taylor's expansion and integrate Eqs. (5.31), (5.32) and (5.33) simultaneously;

7 – with the resulting profiles search for other critical points of Eq. (5.31):

- if more than one critical point stop;
- otherwise proceed;

8 – set $V_0 = V(R = R_\star)$,

9– compare actual and previous value for V_0:

- if relative difference less than 10^{-10} finish;
- otherwise compute new value for Z and go to §6.

The performance of the previous iterations results in profiles for the velocity, temperature and thermal conductivity flux. Paying particular attention to the temperature profile, it is known (Weber, 1970; Couturier, 1977, among others) that one of the consequences of using the classical expression for the thermal conductivity flux in the stellar wind models is the existence of upward and downward diverging solutions. For reasons that will be discussed in next Section, the convergence of the upward and downward solutions for these equations will be made by changing V_c and consequently perform new iterations for V_0.

5.5.1 Differentiating upward and downward diverging solutions

To numerically differentiate between the upward and downward diverging solutions the method of Couturier (1977) is used. This method starts with the assumption that the temperature follows a power law of the form

$$T \propto R^y \quad . \tag{5.62}$$

The value of the power index is obtained from an expression involving the first derivative

$$y = \frac{R}{T}\frac{\mathrm{d}T}{\mathrm{d}R} \quad , \tag{5.63}$$

from the second derivative the following expression results

$$\frac{R}{q}\frac{\mathrm{d}q}{\mathrm{d}R} - \frac{7R}{2T}\frac{\mathrm{d}T}{\mathrm{d}R} + 1 = 0 \tag{5.64}$$

where q is the thermal conductivity flux (Eq. (5.26)). The performance of the operations indicated in the left-hand side of the previous equation is called a *null test*, i.e.

$$\frac{R}{q}\frac{\mathrm{d}q}{\mathrm{d}R} - \frac{7R}{2T}\frac{\mathrm{d}T}{\mathrm{d}R} + 1 = \theta \tag{5.65}$$

where the result, θ, is not necessarily zero.

Applying Eq. (5.63) to the profiles of temperature and thermal conductivity flux obtained by the integration of the equations under study, results in an equivalent power index, as

if the temperature followed a power law. The quality of the power law assumption is ascertained by the result obtained from Eq. (5.65), i.e., when θ remains consistently close to zero the power law assumption for the temperature is a good approximation.

Figures 5.2 and 5.3 may help in the visualization of these ideas. The first of these Figures shows the temperature profiles of the models to be analysed in more detail in Section 5.6.1. The four models have the common input parameters: $R_c = 3.0\,R_\star$, $h_0 = 5.5 \times 10^{-7}\,\mathrm{erg\,cm^{-3}\,s^{-1}}$, $\sigma = 1.0\,R_\star$, and $n_0 = 10^7\,\mathrm{cm^{-3}}$, differing only in the input velocity at the critical point. The models with $V_c = 174.48$ (solid line) and $174.47\,\mathrm{km\,s^{-1}}$ (dotted line) are clearly differentiated in Fig. 5.2 while those with $V_c = 174.47682521$ (dashed line) and $174.47682520\,\mathrm{km\,s^{-1}}$ (long-dashed line) are not. In such situations Eqs. (5.63) and (5.65) are useful.

The resulting profiles for y and θ after application of Eqs. (5.63) and (5.65) to the profiles corresponding to the four models referred are shown in Fig. 5.3. The left-hand side plots display profiles for the models with $V_c = 174.48$ (solid line) and $174.47\,\mathrm{km\,s^{-1}}$ (dotted line) and the right-hand side plots those for the models with $V_c = 174.47682521$ (dashed line) and $174.47682520\,\mathrm{km\,s^{-1}}$ (long-dashed line). Although the temperature profiles of the two later models were indistinguishable in Fig. 5.2 they become clearly differentiated in the right-hand side plots of Fig. 5.3. In summary, if with increased R the value of y is increasing and simultaneously θ is less than zero and decreasing, the solution is diverging upward. On the contrary, if y is decreasing and at the same time θ is positive and increasing, then the solution is diverging downward.

As mentioned before, these wind models should approximate the behaviour of the coronal wind models at large distances from the star, since the right-hand side of Eq. (5.22) becomes vanishingly small. This is clearly shown in the top-right plot of Fig. 5.3, where the equivalent power index of both the upward and the downward solutions approach the value -2/7 indicated by the dashed line and at the same time the result of the null test remains very close to zero.

5.6 Effect of the parameters

The effect of changes in the velocity at the critical point (V_c) will be treated with some detail, in order to show how to improve the convergence of the upward and downward solutions of the system of equations describing the stellar wind model under study.

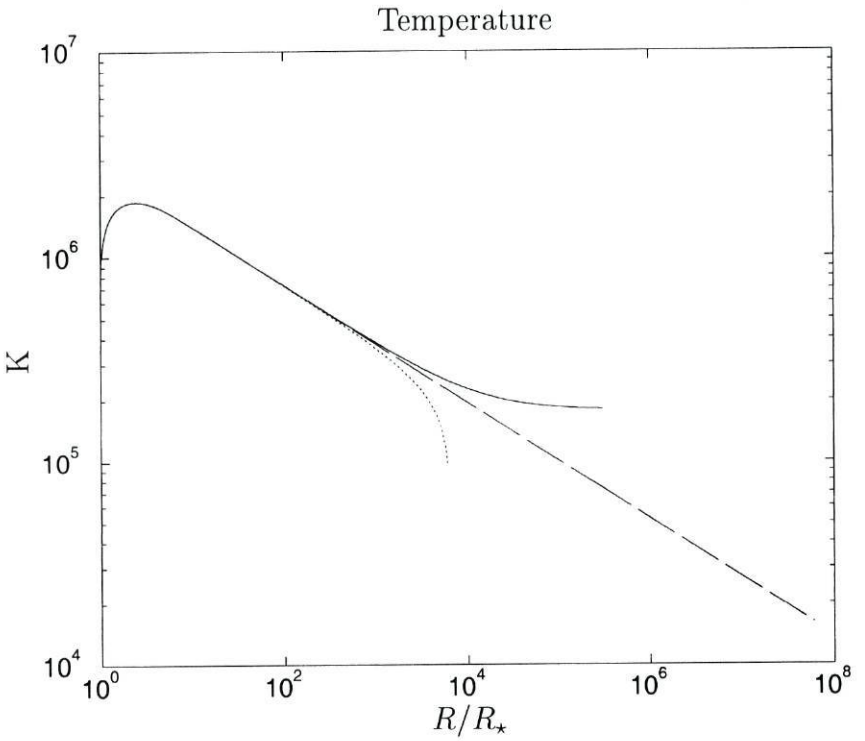

Figure 5.2: Upward and downward diverging solutions. The four curves have in common the input parameters: $R_c = 3.0\,R_\star$, $h_0 = 5.5 \times 10^{-7}\,\mathrm{erg\,cm^{-3}\,s^{-1}}$, $\sigma = 1.0\,R_\star$, and $n_0 = 10^7\,\mathrm{cm^{-3}}$, while V_c, the output value of V_0 and the type of solution are:

	type	V_c ($\mathrm{km\,s^{-1}}$)	V_0 ($\mathrm{km\,s^{-1}}$)
(—)	upward	174.48	2.48
(···)	downward	174.47	2.52
(---)	upward	174.47682521	2.496342148
(– –)	downward	174.47682520	2.496342197

The dashed and long-dashed profiles are indistinguishable in this Figure. The remaining profiles (V, n and q) corresponding to these temperature profiles will be shown in Fig. 5.4.

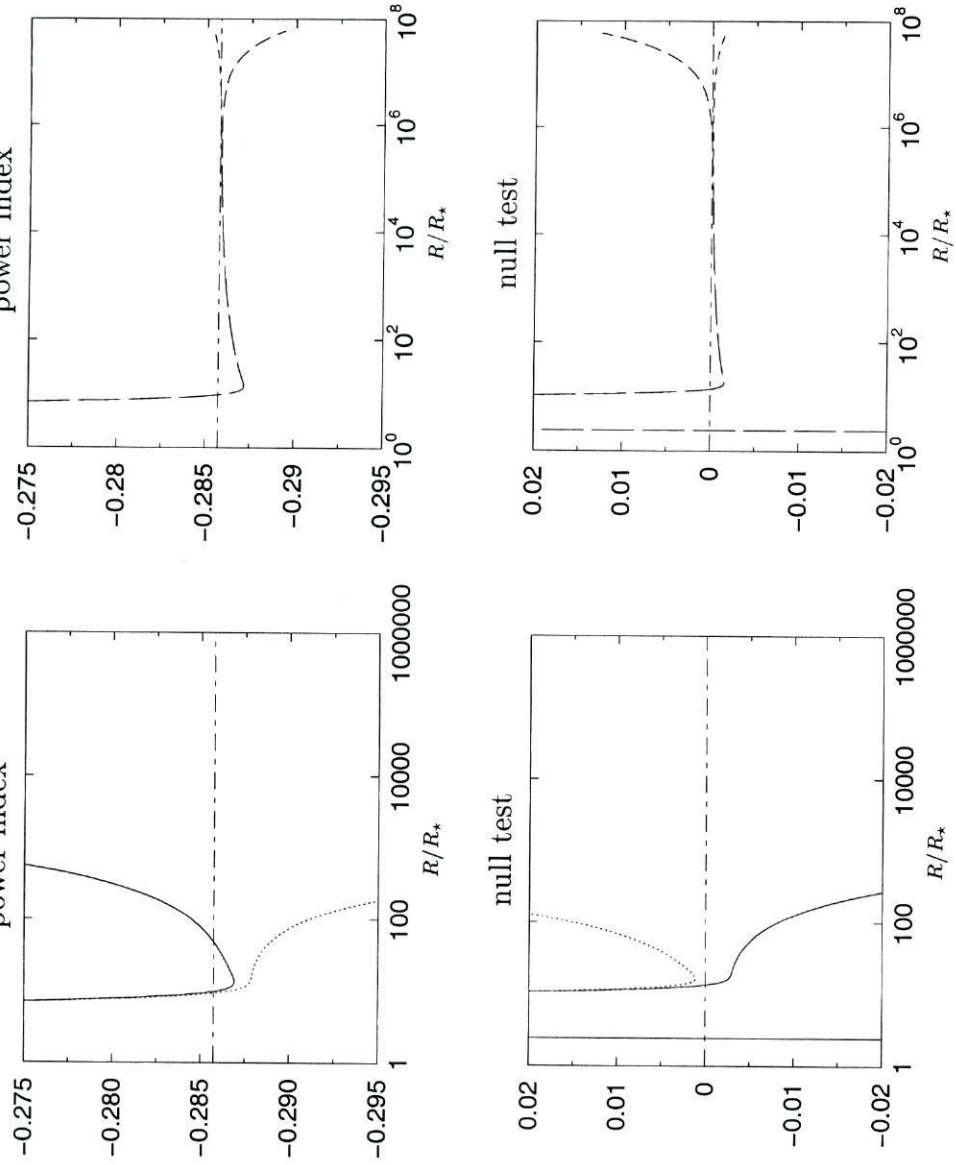

Figure 5.3: Results of applying Eq. (5.63) (top plots, titled 'power index') and Eq. (5.65) (lower plots, titled 'null test') to the profiles of temperature, thermal conductivity flux and velocity corresponding to the models shown in Fig. 5.4 and whose temperature profiles are shown in more detail in Fig. 5.2. The left plots show the results as solid lines when $V_c = 174.48\,\mathrm{km\,s^{-1}}$ (upward solution), and as dotted lines when $V_c = 174.47\,\mathrm{km\,s^{-1}}$ (downward solution). The right plots show the results as dashed lines when $V_c = 174.47682521\,\mathrm{km\,s^{-1}}$ (upward solution), and as long-dashed lines when $V_c = 174.47682520\,\mathrm{km\,s^{-1}}$ (downward solution).

5.6.1 Effect of changes on V_c or R_c

Figure 5.4 shows the effects of changes in V_c in several output quantities, namely the temperature, number density, velocity and thermal conductivity flux. In the four plots the solid lines are for the case when the upward solution has $V_c = 174.48\,\mathrm{km\,s^{-1}}$ and the downward $V_c = 174.47\,\mathrm{km\,s^{-1}}$. The differences in the temperature profiles of both solutions are clearly seen, while those of the other quantities are less apparent, nevertheless the relative difference of the various quantities is rather high, as shown in Fig. 5.5 (solid line in each plot).

To improve the convergence between the upward and the downward solutions it is necessary to increase the precision in the determination of V_c, as shown by the dotted lines in the four plots of Fig. 5.4. The profiles for the upward and the downward solutions are indistinguishable in Fig. 5.4, and their respective relative differences are less than 10^{-6} up to $10^4\,R_\odot$, at least (dotted lines of Fig. 5.5). In this particular case $V_c = 174.47682521\,\mathrm{km\,s^{-1}}$ for the upward solution and $V_c = 174.47682520\,\mathrm{km\,s^{-1}}$ for the downward solution.

In all the plots of this Chapter, when only one (usually the upward) of the solutions is presented it has been computed with enough precision to ensure that the various profiles (V, T, Q, n) have relative errors less than 10^{-6} up to $10^4\,R_\star$, distance that roughly corresponds to the orbit of Pluto, for the particular case of the solar system.

The effects of changing R_c are very similar to those of changing V_c as shown in Fig. 5.6. This was the main reason for choosing to fix R_c and iteratively search for the corresponding value of V_c that gives small enough relative differences for the various output quantities of the upward and the downward solutions, as mentioned previously.

As a conclusion, if the parameters V_c or R_c increase the values for the velocity and temperature at the base decrease, while their values far from the stellar surface increase. An explanation for the case when V_c is increased comes from the recognition that the plasma must attain this higher velocity while having the same mechanical heating energy available (recall that R_c, h_0 and σ are kept constant). Therefore it starts at a lower velocity at the base, resulting in a smaller mass flux, that in turn demands a smaller value for the base temperature. For the case of increased R_c the same value of V_c (and T_c) is attained at a larger distance R, therefore, in the range $R_\star < R < R_c$ the values reached by the velocity and the temperature at any R are smaller than the corresponding values for the comparison model.

This is shown quantitatively in Table 5.2 where particular values for the velocity and temperature profiles, namely V_0, T_0, V_c, T_c, $\mathrm{d}V/\mathrm{d}R|_c$, $\mathrm{d}T/\mathrm{d}R|_c$, $\mathrm{d}^2V/\mathrm{d}R^2|_c$, $\mathrm{d}^2T/\mathrm{d}R^2|_c$, for the upward and downward solutions shown in Fig. 5.4 (dotted lines), and for models with increased V_c, R_c, h_0, σ or n_0 are presented. The mentioned upward and downward

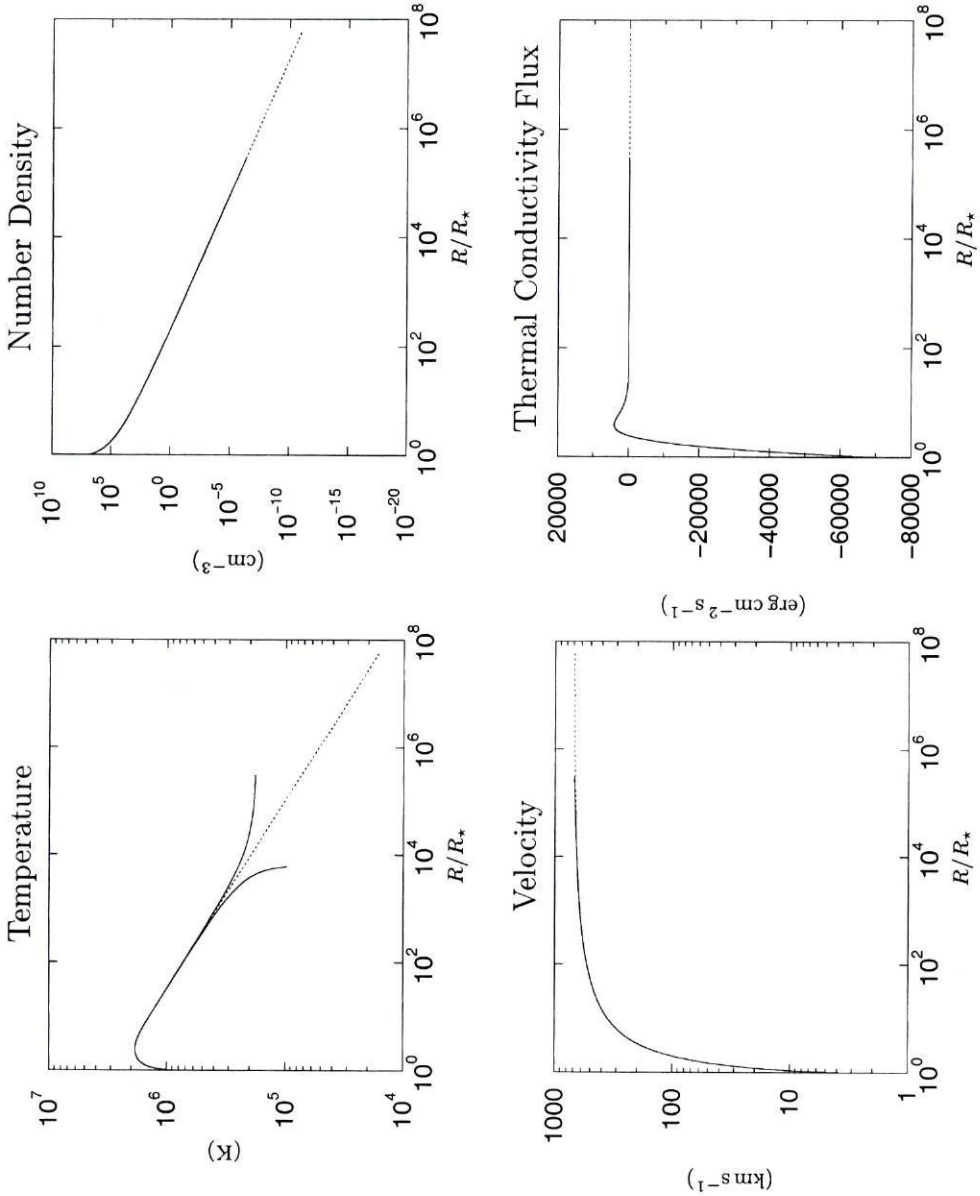

Figure 5.4: Upward and downward diverging solutions caused by changes on the input parameter V_c, and the induced effects in the profiles of temperature, number density, velocity and thermal conductivity flux. (—) upward: $V_c = 174.48\,\mathrm{km\,s^{-1}}$, $V_0 = 2.48\,\mathrm{km\,s^{-1}}$; downward: $V_c = 174.47\,\mathrm{km\,s^{-1}}$, $V_0 = 2.52\,\mathrm{km\,s^{-1}}$. $(\cdots)$ upward: $V_c = 174.47682521\,\mathrm{km\,s^{-1}}$, $V_0 = 2.496342148\,\mathrm{km\,s^{-1}}$; downward: $V_c = 174.47682520\,\mathrm{km\,s^{-1}}$, $V_0 = 2.496342197\,\mathrm{km\,s^{-1}}$. The common input parameters to the four models are: $R_c = 3.0\,R_\star$, $h_0 = 5.5 \times 10^{-7}\,\mathrm{erg\,cm^{-3}\,s^{-1}}$, $\sigma = 1.0\,R_\star$, and $n_0 = 10^7\,\mathrm{cm^{-3}}$.

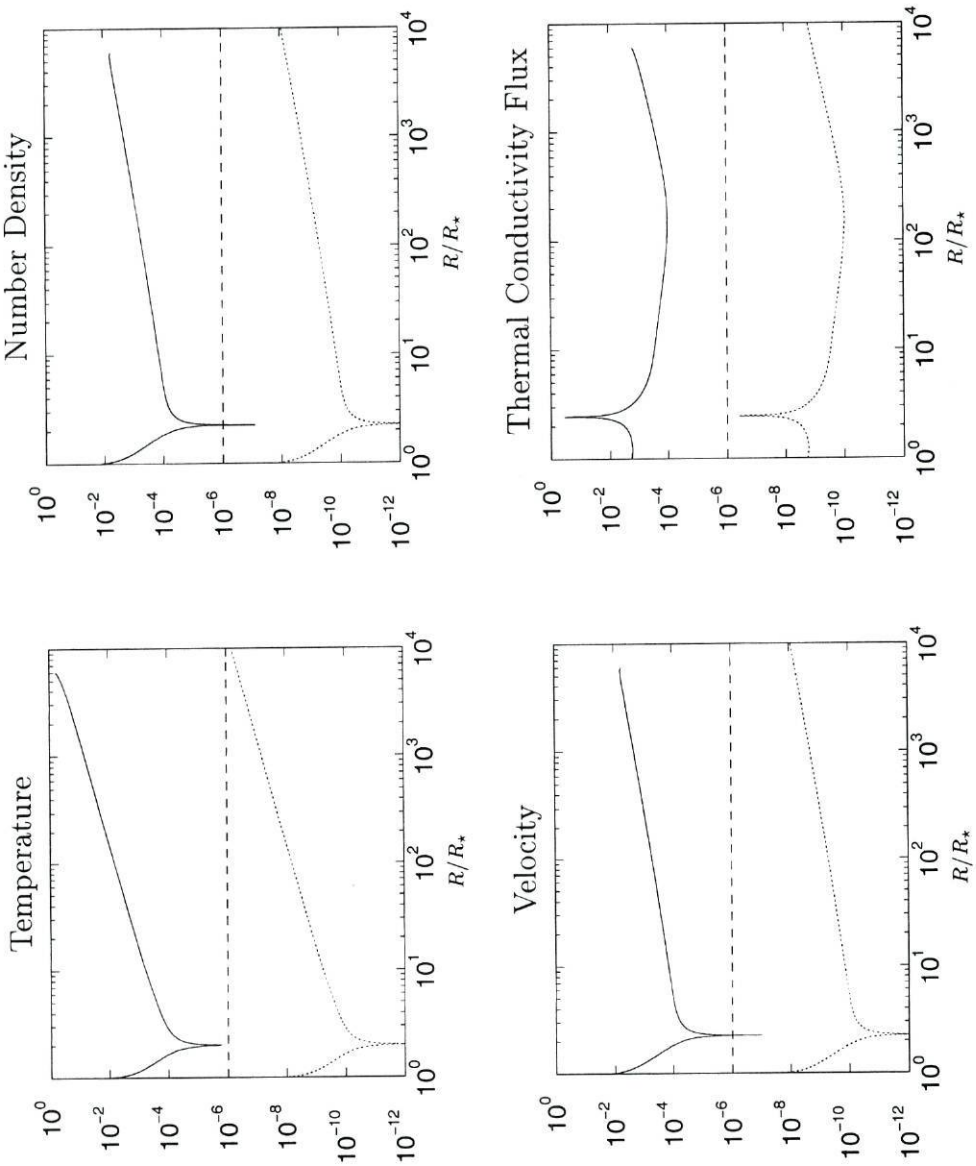

Figure 5.5: Relative difference of the upward and downward diverging solutions for the temperature, number density, velocity and thermal conductivity flux, for the two cases shown in Fig. 5.4. The same line scheme is used in both Figures.

solutions are used as comparison models, and the increments to the input parameters for the other models have been chosen large enough to allow differentiation between the models within the precision used.

It must be noted that in this Table the upward and the downward solutions of the comparison models at the level of precision used are undifferentiated. From the analysis of the column relative to increasing V_c, it is seen that both the velocity and the temperature at the base of the wind decrease, while at the critical point the derivative of the velocity increases. However, the derivative of the temperature decreases in absolute value. The outcome will be an increased velocity and temperature at large distances or, looking in a different angle, the higher temperature is powering a higher velocity wind. A similar analysis can be made for increased R_c.

5.6.2 Effect of changes on h_0 or σ

Figures 5.7 and 5.8 show the effects on the profiles due to changes of h_0 and σ, respectively. As for the case of increasing V_c or R_c, here too, when h_0 or σ are increased the values of the base temperature and velocity decrease. However, their values far from the stellar surface also decrease, contrary to the former case.

An explanation for this behaviour is that increases of h_0 or σ result in the availability of more mechanical energy to drive the wind. As the velocity at the critical point is kept fixed, the wind starts with a lower value of the base velocity, however at the critical point the extra mechanical energy has consequences contrary to what could be expected. To better understanding this behaviour, the two columns of Table 5.2 for the models with increased h_0 and σ will be analysed. Reading from this Table it is found that increasing h_0 or σ results in a decrease of both V_0 and T_0, as well as an increase of the derivative of the velocity at the critical point, as expected since the wind experiences a larger acceleration. Since the values of R_c and V_c are kept constant T_c and F_c have the same values as in the comparison model (refer to Eq. (5.30)), and from Eq. (5.19) the derivative of the temperature at the critical point remains the same. However the second derivative of the temperature depends on $\mathrm{d}F/\mathrm{d}R$ (see Eq. (5.47)) which depends explicitly on the mechanical heating, (see Eq. (5.41)), consequently this derivative is more negative than that of the comparison models. The implications of this are twofold: first, a more negative second derivative of the temperature implies a faster increase in absolute value of the temperature gradient, and second by making a Taylor's expansion at a distance δ ($\delta > 0$) of R_c, the value obtained for the temperature is below that of the comparison models. Therefore, what drives the faster wind is the faster decrease of the temperature, while in the previous cases (when V_c or R_c were increased) it was the slower decrease of the temperature.

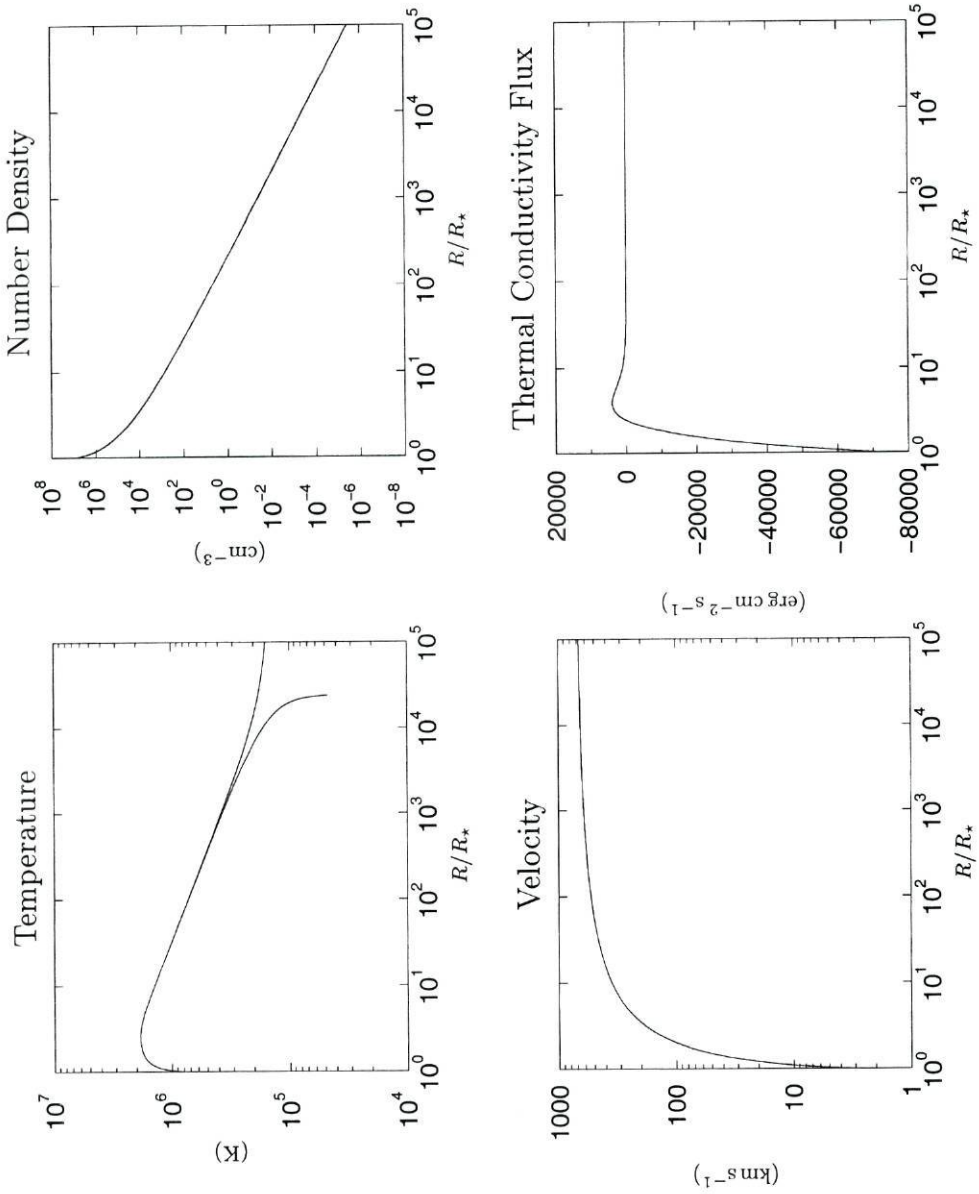

Figure 5.6: Same as Fig. 5.4, but for changes of R_c. Upward solution: $R_c = 3.0001\,R_\star$, $V_0 = 2.4687\,\mathrm{km\,s^{-1}}$; downward solution: $R_c = 2.9999\,R_\star$, $V_0 = 2.5235\,\mathrm{km\,s^{-1}}$. The input parameters common to both models are: $V_c = 174.47682521\,\mathrm{km\,s^{-1}}$, $h_0 = 5.5 \times 10^{-7}\,\mathrm{erg\,cm^{-3}\,s^{-1}}$, $\sigma = 1.0\,R_\star$, and $n_0 = 10^7\,\mathrm{cm^{-3}}$.

	comparison model		input parameter changed				
	upward	downward	V_c	R_c	h_0	σ	n_0
V_0 ($\mathrm{km\,s^{-1}}$)	2.4963	2.4963	2.3776	2.1860	2.3473	2.3982	2.6871
T_0 (K)	7.2348×10^5	7.2348×10^5	6.9919×10^5	6.5894×10^5	6.9287×10^5	7.0358×10^5	7.6130×10^5
V_c ($\mathrm{km\,s^{-1}}$)	174.47682521	174.47682520	174.50	174.48	174.48	174.48	174.48
T_c (K)	1.8439×10^6	1.8439×10^6	1.8444×10^6	1.8439×10^6	1.8439×10^6	1.8439×10^6	1.8439×10^6
$\left.\frac{dV}{dR}\right\|_c$ ($\mathrm{km\,s^{-1}}\,R_\star^{-1}$)	8.7627×10^{-5}	8.7627×10^{-5}	8.7665×10^{-5}	8.7645×10^{-5}	8.7650×10^{-5}	8.7650×10^{-5}	8.7606×10^{-5}
$\left.\frac{dT}{dR}\right\|_c$ ($\mathrm{K}\,R_\star^{-1}$)	-7.7575×10^{-7}	-7.7575×10^{-7}	-7.7106×10^{-7}	-7.6935×10^{-7}	-7.7575×10^{-7}	-7.7575×10^{-7}	-7.7575×10^{-7}
$\left.\frac{d^2V}{dR^2}\right\|_c$ ($\mathrm{km\,s^{-1}}\,R_\star^{-2}$)	-5.0016×10^{-16}	-5.0016×10^{-16}	-5.0041×10^{-16}	-5.0029×10^{-16}	-5.0047×10^{-16}	-5.0037×10^{-16}	-4.9983×10^{-16}
$\left.\frac{d^2T}{dR^2}\right\|_c$ ($\mathrm{K}\,R_\star^{-2}$)	-1.2323×10^{-17}	-1.2323×10^{-17}	-1.2357×10^{-17}	-1.2386×10^{-17}	-1.2373×10^{-17}	-1.2371×10^{-17}	-1.2276×10^{-17}

Table 5.2: Values of the velocity and temperature at the base and at the critical point and their derivatives at the critical point for the comparison models and five other models corresponding to increased input parameters. The comparison models (see Fig. 5.4, dotted curves) have in common the input parameters $R_c = 3.0\,R_\star$, $h_0 = 5.5\times10^{-7}\,\mathrm{erg\,cm^{-3}\,s^{-1}}$, $\sigma = 1.0\,R_\star$, and $n_0 = 10^7\,\mathrm{cm^{-3}}$, while $V_c = 174.47682521\,\mathrm{km\,s^{-1}}$ for the upward solution and $V_c = 174.47682520\,\mathrm{km\,s^{-1}}$ for the downward solution. For the other five models (one per column) the input parameters keep the same values as for the upward solution of the comparison model with the exception of the input parameter changed, namely $V_c = 174.5\,\mathrm{km\,s^{-1}}$, $R_c = 3.001\,R_\star$, $h_0 = 5.51\times10^{-7}\,\mathrm{erg\,cm^{-3}\,s^{-1}}$, $\sigma = 1.001\,R_\star$, $n_0 = 1.1\times10^7\,\mathrm{cm^{-3}}$. All numerical values shown were rounded, except the values of V_c for the comparison models.

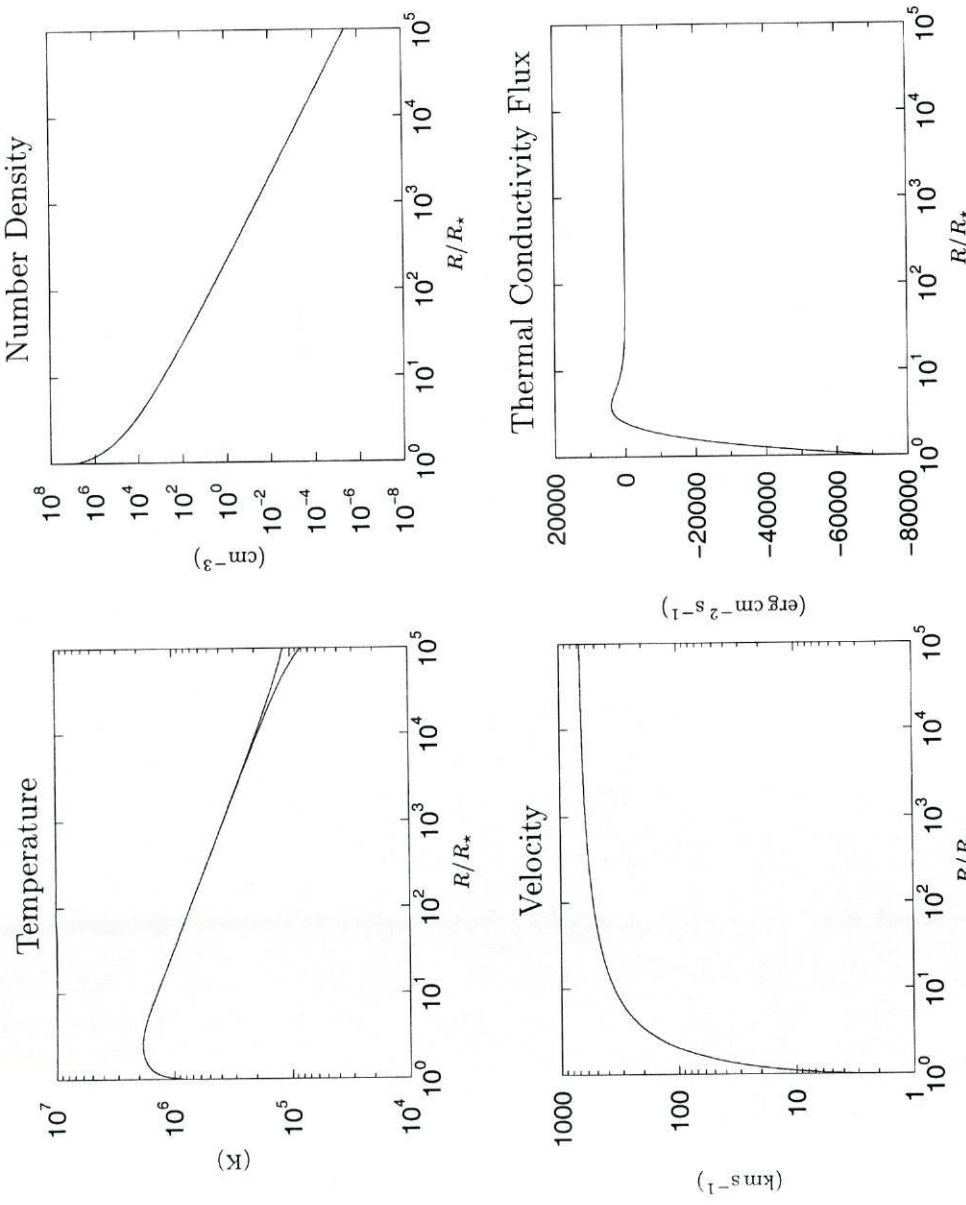

Figure 5.7: Same as Fig. 5.4, but for changes of h_0. Upward solution: $h_0 = 5.4999 \times 10^{-7}$ erg cm^{-3} s^{-1}, $V_0 = 2.4977$ km s^{-1}; downward solution: $h_0 = 5.5001 \times 10^{-7}$ erg cm^{-3} s^{-1}, $V_0 = 2.4949$ km s^{-1}. The common parameters are: $R_c = 3.0\,R_\star$, $V_c = 174.47682521$ km s^{-1}, $\sigma = 1.0\,R_\star$, and $n_0 = 10^7$ cm^{-3}.

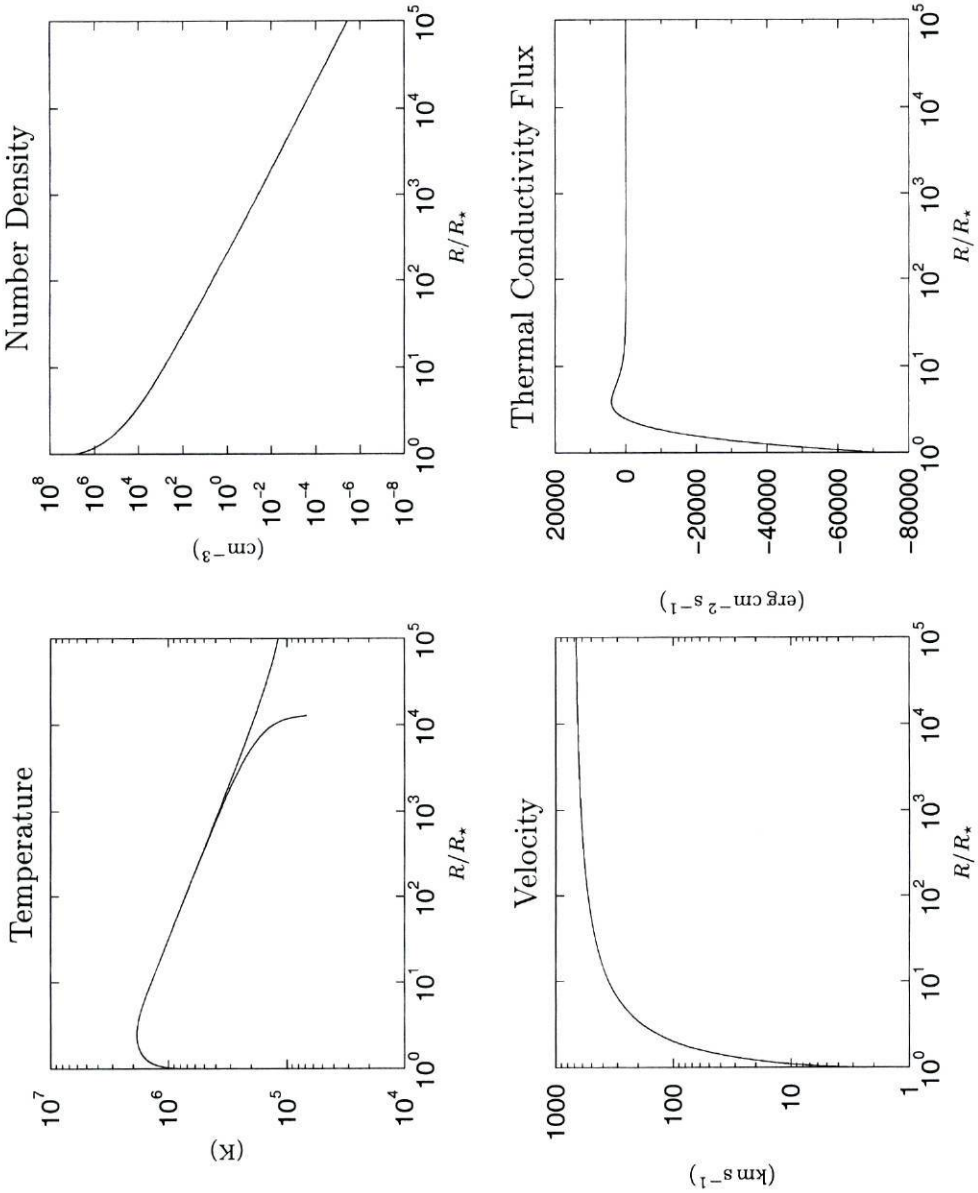

Figure 5.8: Same as Fig. 5.4, but for changes of σ. Upward solution: $\sigma = 0.99999\,R_\star$, $V_0 = 2.4973\,\mathrm{km\,s^{-1}}$; downward solution: $\sigma = 1.0001\,R_\star$, $V_0 = 2.4869\,\mathrm{km\,s^{-1}}$. The common parameters are: $R_\mathrm{c} = 3.0\,R_\star$, $V_\mathrm{c} = 174.47682521\,\mathrm{km\,s^{-1}}$, $h_0 = 5.5 \times 10^{-7}\,\mathrm{erg\,cm^{-3}\,s^{-1}}$, and $n_0 = 10^7\,\mathrm{cm^{-3}}$.

5.6.3 Effect of n_0

The effects of changes in the base density are shown in Fig. 5.9. As for the previous input parameters the change is in the fourth decimal place. However, the induced effects are smaller than with the previous parameters, even in the temperature profile. To graphically distinguish between the upward and downward solutions it was necessary to increase the upper limit on R from 10^5 to $10^7\,R_\star$.

Contrary to the situation in the previous subsections, increasing n_0 demands an increase of both V_0 and T_0. This is readily understood since a denser wind implies a larger mass flux. However, the mechanical heating input is kept constant and thus it is the higher base temperature that helps accelerating the plasma. This higher temperature results in an increased base velocity, and therefore the overall plasma acceleration is smaller up to the critical point. Referring to Table 5.2 (last column) it is seen that the velocity and the temperature at the base of the wind are higher than for the comparison model, while the velocity gradient at the critical point is smaller resulting in a slower wind at large distances from the star. The temperature gradient at the critical point has the same value as for the comparison models, however, its second derivative is smaller in absolute value and the temperature far from the star is higher than in the comparison model. This higher temperature is the responsible for driving the wind.

5.7 Application to T Tauri stars

In this Section some applications of the wind model under study will be presented. As this Section deals with the development of wind models for T Tauri stars (TTS) the parameters will be changed in order to be more suitable for the TTS. The examples presented so far have a rather low density at the base, even for the solar wind, therefore this will be the first parameter to be changed.

In the first application the mechanical heating and the radial position of the critical point will be kept constant, while iterations will be made on the velocity of the critical point to ensure agreement of the upward and downward solutions. The results for the wind models with base density equal to 1.0, 2.0 and $4.0 \times 10^7\,\mathrm{cm}^{-3}$ are presented in Fig. 5.10.

As discussed before the increase of the amount of plasma to accelerate demands more energy. However, since the mechanical heating is kept constant it is the increased base temperature that helps driving the wind. For the model with $n_0 = 1.0 \times 10^7\,\mathrm{cm}^{-3}$ the base temperature was already typical of the upper transition region ($7.2{\times}10^5\,\mathrm{K}$) while for the models with $n_0 = 2.0$ and $4.0 \times 10^7\,\mathrm{cm}^{-3}$ it further increases to coronal values ($1.2{\times}10^6\,\mathrm{K}$

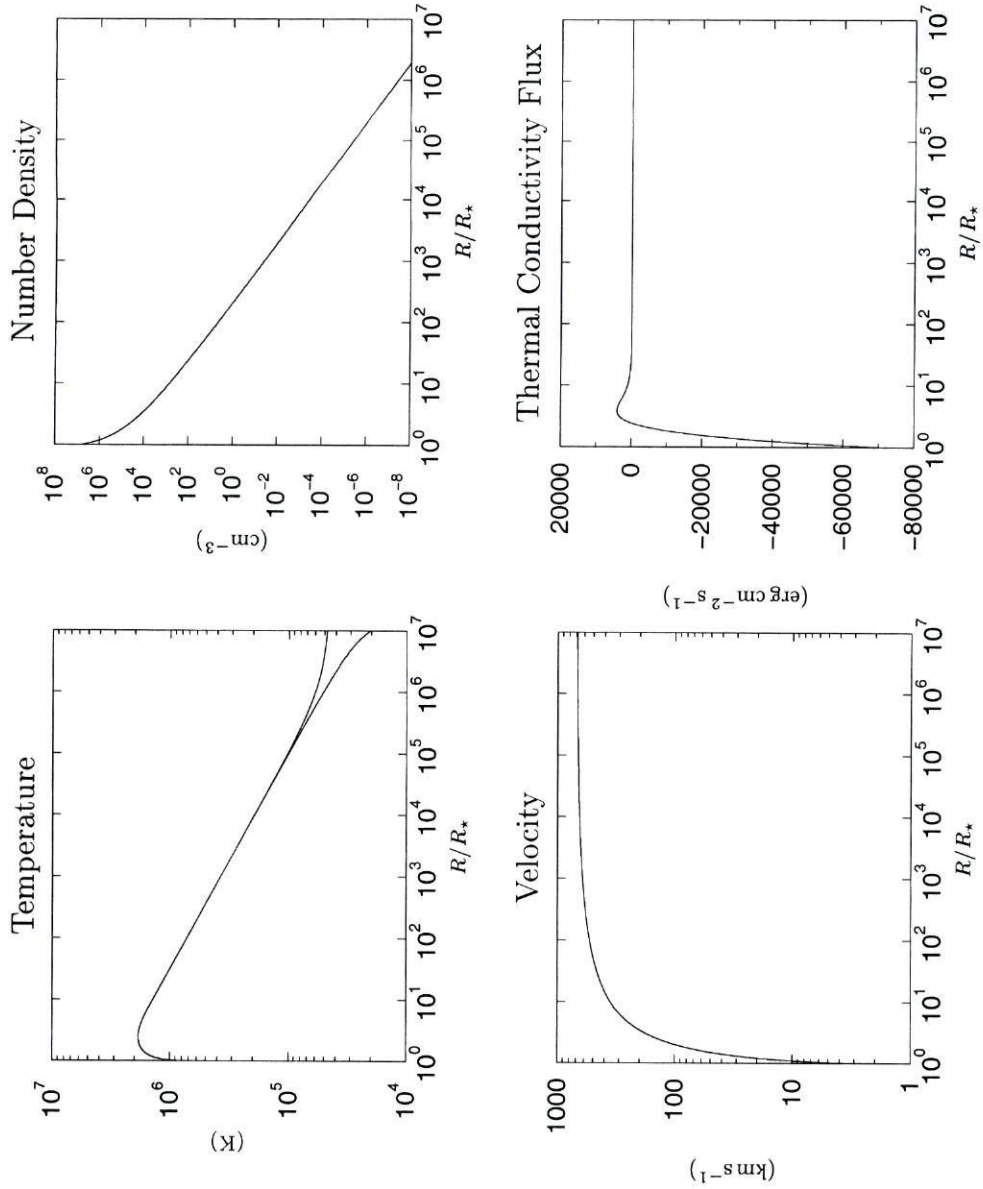

Figure 5.9: Same as Fig. 5.4 but for changes of n_0. Upward solution: $n_0 = 1.0001 \times 10^7\,\mathrm{cm}^{-3}$, $V_0 = 2.4965\,\mathrm{km\,s}^{-1}$; downward solution: $n_0 = 9.9999 \times 10^6\,\mathrm{cm}^{-3}$, $V_0 = 2.4963\,\mathrm{km\,s}^{-1}$. The common parameters are: $R_\mathrm{c} = 3.0\,R_\star$, $V_\mathrm{c} = 174.47682521\,\mathrm{km\,s}^{-1}$, $h_0 = 5.5 \times 10^{-7}\,\mathrm{erg\,cm}^{-3}\,\mathrm{s}^{-1}$, and $\sigma = 1.0\,R_\star$. Note the different abscissa scale.

and 2.0×10^6 K, respectively). Even worst, the model with the highest base density attains the maximum value of the temperature at the base, being in this aspect similar to the coronal wind models.

One of the aims of this work was to study the structure of the outer atmosphere and winds of TTS, including the profile of the temperature that, taking the sun as example, should start with a value as low as possible near the star, increase to coronal values and then decrease. The solar analogy should be valid for the two following reasons: first the TTS have spectral types between late-F to M which means that their effective temperatures are less than $\sim$ 6000 K, and second TTS are strong X-ray emitters (Neuhäuser et al., 1995; Neuhäuser, 1996; Alcalá et al., 1997; Neuhäuser et al., 1997; Preibisch, 1997; Gregorio-Hetem et al., 1998; Grosso et al., 2000; Wichmann et al., 2000, as examples of recent articles) hinting on the existence of plasma with temperatures in excess of 10^6 K. It is not yet known if the origin of the X-ray emission for the TTS is thermal or not. In particular for the CTTS the origin of the X-rays could be a hot corona or an accretion shock at the base of an accretion column, although for the WTTS it is commonly assumed that they originate in a hot corona (Guenther et al., 2000, and references therein). The observations made at several wavelength ranges by Guenther et al. (2000) for the WTTS V773 Tau led them to conclude that the X-ray emission of this TTS comes from a hot corona, larger than the solar corona.

These observations and the interpretation that has been made for them hint that at least some TTS have a temperature profile in their extended atmospheres similar to the solar one, i.e., the temperature starts in the photosphere with a value below 6000 K, rises in the transition region up to the coronal values in excess of 10^6 K, and declines afterwards. Even if this general structure for the extended atmospheres of some TTS is valid, the detailed structure is certainly different from that of the solar extended atmosphere. Compared to the sun, TTS have much larger surface fluxes in lines formed in different regions of their atmospheres and also in the X-ray flux (Costa, 2000).

Inspection of the temperature profiles shown in Fig. 5.10 leads to the conclusion that only the one corresponding to the model with $n_0 = 1.0 \times 10^7\,\mathrm{cm}^{-3}$ could be considered to meet the requirements of mimicking a transition region and a corona, while the other two profiles have a base temperature already typical of the corona. Since these very high temperatures at the base of the wind are an undesirable feature it is necessary to search other alternatives to drive the denser wind. This will be the subject of next Section.

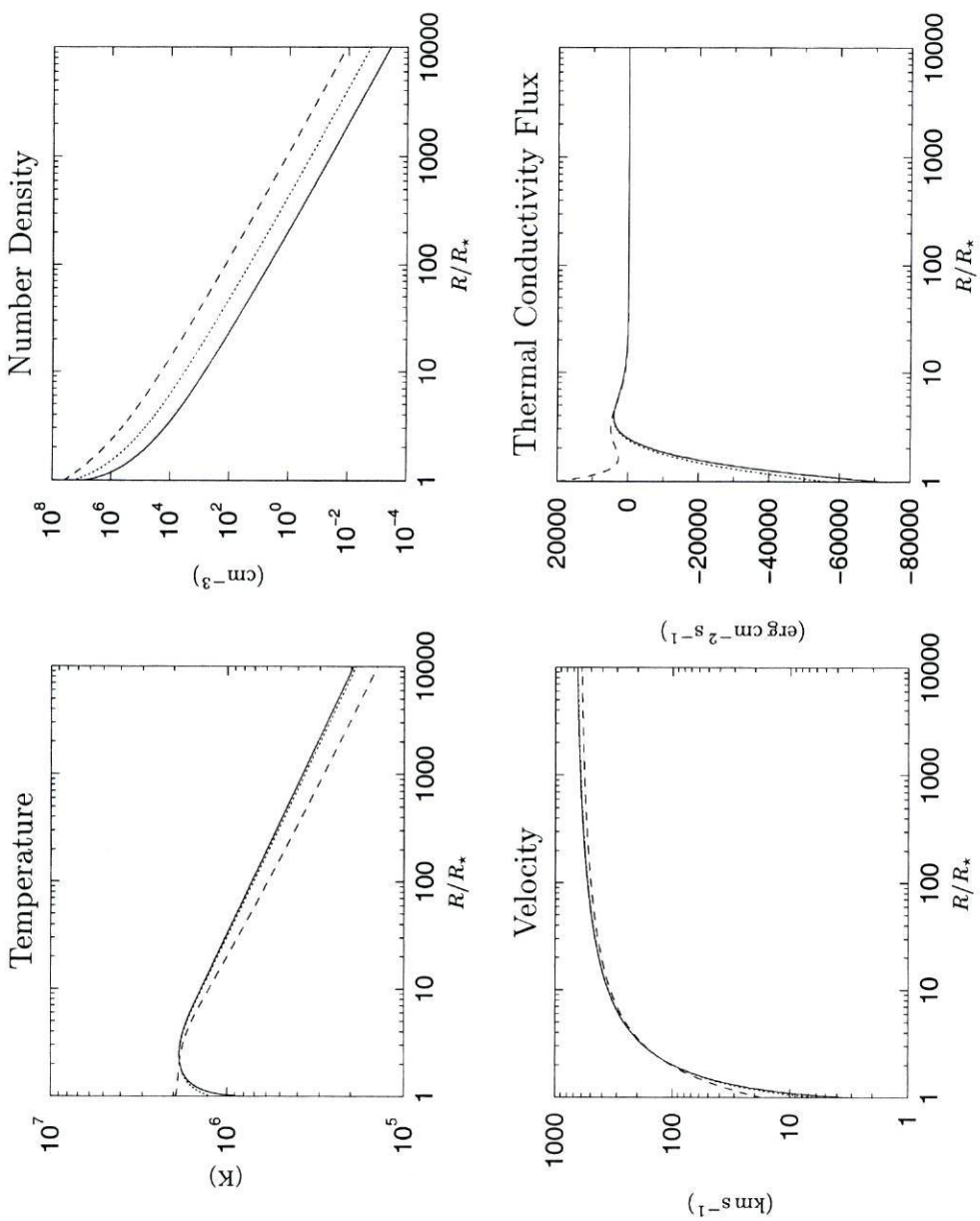

Figure 5.10: Effects induced by increasing the base density (n_0), while the the mechanical heating (both $h_0 = 5.50 \times 10^{-7}\,\mathrm{erg\,cm^{-3}\,s^{-1}}$ and $\sigma = 1.0\,R_\star$) and $R_\mathrm{c} = 3.0\,R_\star$ are kept constant.

	n_0 (cm^{-3})	V_c (km s^{-1})	V_0 (km s^{-1})	T_0 (K)
(—):	1.0×10^7	174.48	2.496	7.235×10^5
(···):	2.0×10^7	174.04	5.820	1.201×10^6
(- - -):	4.0×10^7	171.39	17.54	1.951×10^6

5.8 Driving a wind with $n_0 = 4.0 \times 10^7\,\mathrm{cm}^{-3}$

In this Section a search for alternatives to the very high temperature at the base needed to drive a wind with $n_0 = 4.0 \times 10^7\,\mathrm{cm}^{-3}$ is made. The first two subsections deal with the increase in the mechanical heating input, while the last subsection deals with changes on the position of the critical point.

5.8.1 Increasing h_0

As might be foreseen from the discussion in previous Sections, the increase in the 'amount' of the mechanical heating h_0 has the desirable effect of decreasing the temperature at the base of the wind, shown in Fig. 5.11. The increase of h_0 has also the effect of changing the position of the maximum temperature from the base of the wind to some distance above it.

It must however be stressed that the value of h_0 can not be increase without limits when the values of σ and R_c are kept fixed. This is displayed for the temperature profiles in Figure 5.12 where all the models have $R_c = 3.0\,R_\star$ and $\sigma = 1.0\,R_\star$, while the value of h_0 is equal to $6.0650 \times 10^{-7}\,\mathrm{erg\,cm^{-3}\,s^{-1}}$ for the comparison model (solid line) and is increased to $6.0651 \times 10^{-7}\,\mathrm{erg\,cm^{-3}\,s^{-1}}$ for the other models. The latter value for h_0 is above the limiting value possible to use in conjunction with the values of the remaining parameters. In this case there are only downward solutions, and it is not possible for the solution to go up to infinity. When $h_0 = 6.0651 \times 10^{-7}\,\mathrm{erg\,cm^{-3}\,s^{-1}}$ the increment of the velocity at the critical point from 173.96 to $173.97\,\mathrm{km\,s^{-1}}$ has the expected consequence of increasing the value of the radial distance where the temperature suddenly drops to zero. The maximum value for the mentioned radial distance occurs for $V_c \approx 173.97602\,\mathrm{km\,s^{-1}}$. Further increases of the value of V_c have the unexpected result of decreasing the value for the distance where the sudden temperature drop occurs.

After some tests it was concluded that having h_0 with three decimal places was the best choice in terms of the amount of work invested in its search and in the precision of the solution. It was verified that a larger accuracy has a very small effect in the profiles of velocity, temperature and thermal conductivity flux.

The results shown in Fig. 5.11 are the best that can be obtained with changes on the 'amount' of the mechanical heating alone. Since in all the models the temperature at the base remained above $10^6\,\mathrm{K}$ it is necessary to search for the solution of this problem in other parameters. This is done in the next subsection where the extent of the mechanical heating is changed, implying therefore changes on h_0 and V_c so that the upward and the downward diverging solutions converge within the desired precision.

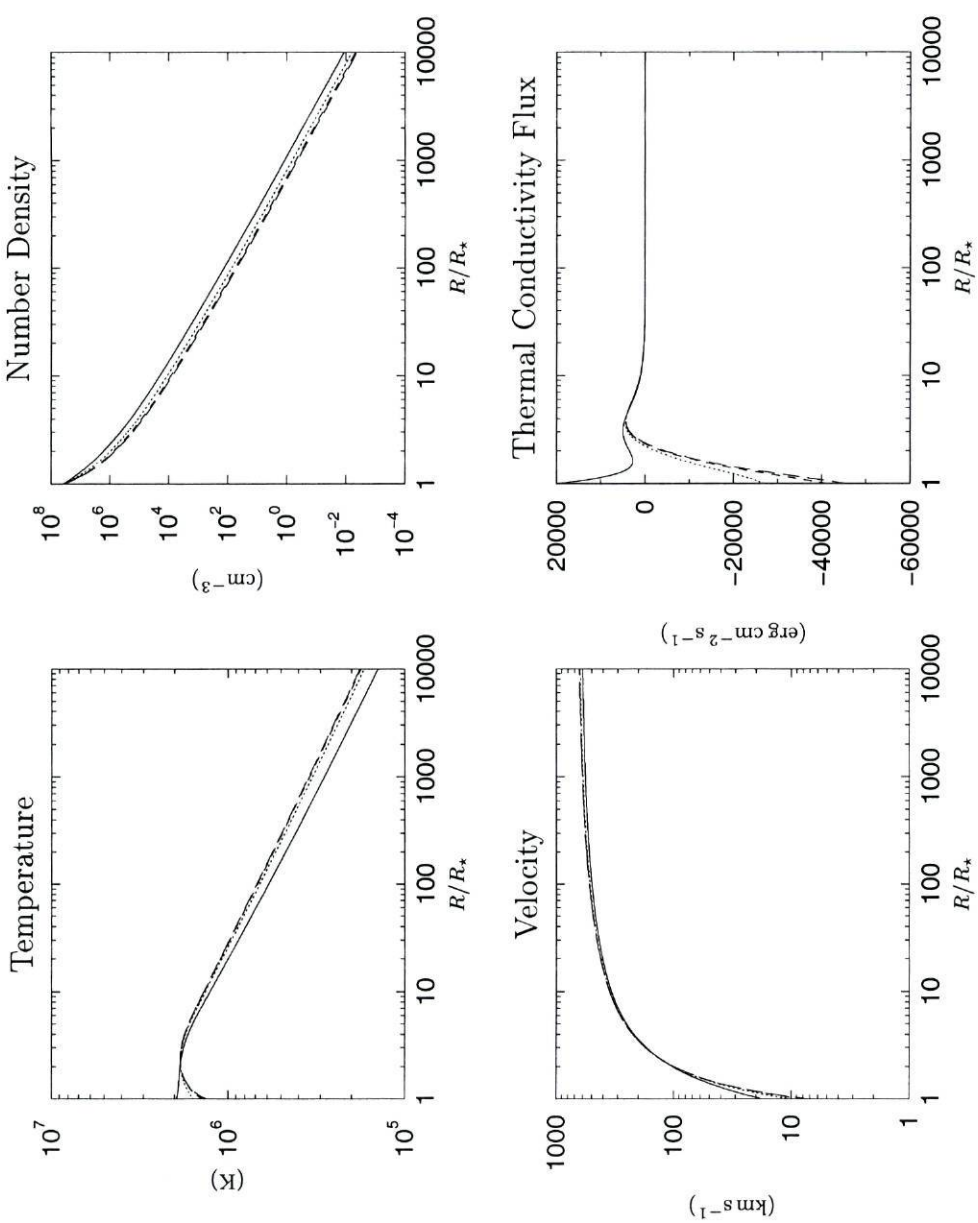

Figure 5.11: Effects induce by increasing the 'amount' of mechanical heating (h_0), while its extent ($\sigma = 1.0\,R_\star$) and $R_\mathrm{c} = 3.0\,R_\star$ are kept constant.

	h_0 ($\mathrm{erg\,cm^{-3}\,s^{-1}}$)	V_c ($\mathrm{km\,s^{-1}}$)	V_0 ($\mathrm{km\,s^{-1}}$)	T_0 (K)
(—):	5.50×10^{-7}	171.39	17.54	1.951×10^6
(···):	6.0×10^{-7}	173.31	10.07	1.564×10^6
(– –):	6.06×10^{-7}	173.81	7.666	1.386×10^6
(–·–):	6.065×10^{-7}	173.96	6.878	1.318×10^6

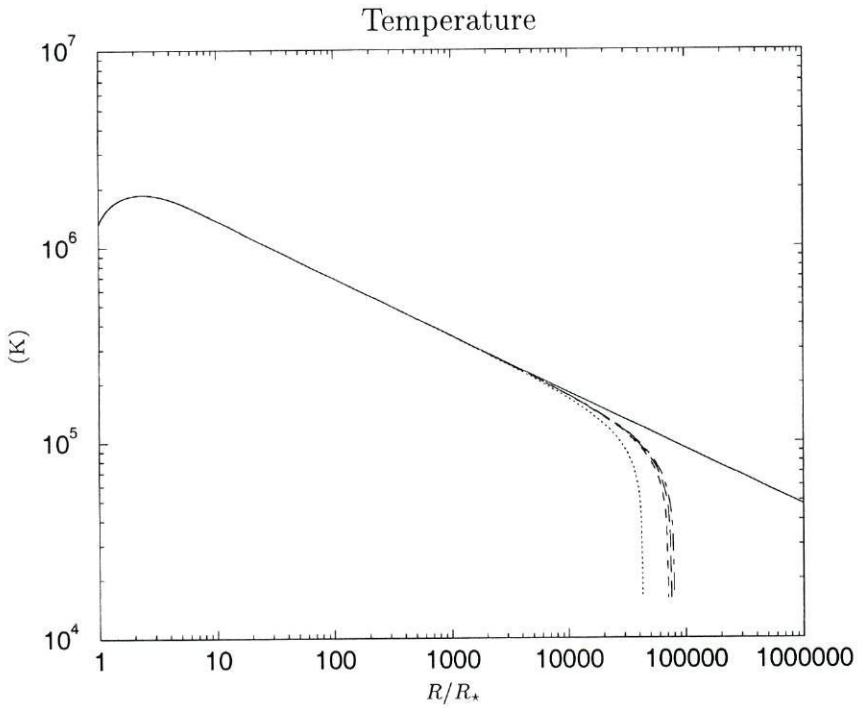

Figure 5.12: Effect of increasing the 'amount' of mechanical heating (h_0) for a too large value, while its extent ($\sigma = 1.0\,R_\star$) and $R_c = 3.0\,R_\star$ are kept constant.

	h_0 ($\mathrm{erg\,cm^{-3}\,s^{-1}}$)	V_c ($\mathrm{km\,s^{-1}}$)	V_0 ($\mathrm{km\,s^{-1}}$)
(—):	6.0650×10^{-7}	173.96279154	6.878
(···):	6.0651×10^{-7}	173.96	6.891
(---):	6.0651×10^{-7}	173.97	6.837
(– –):	6.0651×10^{-7}	173.98	6.782
(-·-):	6.0651×10^{-7}	173.97602	6.804

σ	h_0	mechanical heating rate ($\mathrm{erg\,cm^{-3}\,s^{-1}}$)			f_m ($\mathrm{erg\,cm^{-2}\,s^{-1}}$)
($R_\star$)	($\mathrm{erg\,cm^{-3}\,s^{-1}}$)	at $R = 2\,R_\star$	at $R = 3\,R_\star$	at $R = 4\,R_\star$	at base
0.6	1.592×10^{-6}	3.01×10^{-7}	5.68×10^{-8}	1.07×10^{-8}	1.95×10^{5}
0.8	9.102×10^{-7}	2.61×10^{-7}	7.47×10^{-8}	2.14×10^{-8}	1.97×10^{5}
1.0	6.065×10^{-7}	2.23×10^{-7}	8.08×10^{-8}	3.02×10^{-8}	2.11×10^{5}
1.2	4.407×10^{-7}	1.91×10^{-7}	8.32×10^{-8}	3.62×10^{-8}	2.31×10^{5}

Table 5.3: Volumetric mechanical heating rates for different values of σ, specified at $R = 2$, 3 and $4\,R_\star$, and the mechanical heating flux at the base of the wind.

5.8.2 Changing σ

The effects caused by the alteration of the extent of the mechanical heating deposition (σ) are shown in Fig. 5.13. From the stellar surface up to the critical point the changes induced by the alteration of σ are small, being clearly seen only on the plot of the thermal conductivity flux. On the contrary, the changes on the temperature and velocity profiles are most notorious at large distances from the stellar surface. This can be explained by analysing Table 5.3 where the registered values show that the models with larger σ have, at the critical point and beyond, more mechanical energy left to power a faster and hotter wind. It must also be mentioned that the mechanical heating flux at the base of the wind is approximately the same for all these models since the mass flux and V_c differ little from model to model, or in other words, the amount of plasma to accelerate and the velocity it must have at $R = R_\mathrm{c}$ are almost the same for all models.

One of the most prominent features of Fig. 5.13 was the almost constancy of the temperature and the velocity at the base of the wind while σ has its value doubled from 0.6 to $1.2\,R_\star$. From this statement and the conclusion of the previous subsection it must be concluded that changing only the mechanical heating input is not enough to lower the temperature at the base to values in agreement with those of the transition region ($\sim 10^5\,\mathrm{K}$). Consequently, the possible answer to this problem must be in the changes induced by the last input parameter: the radial position of the critical point, R_c. Since in the method of solution adopted R_c is guessed it is not known beforehand if it was the best choice, some trials are necessary to select the most adequate value for R_c.

5.8.3 Changing R_c

The changes on the profiles of temperature, velocity, thermal conductivity flux and number density induced by altering R_c are shown in Fig. 5.14. In this Figure the input parameter σ has the value $0.8\,R_\star$ in order to build some wind models with a value of the mechanical heating input different from that used in the majority of the previous figures ($1.0\,R_\star$).

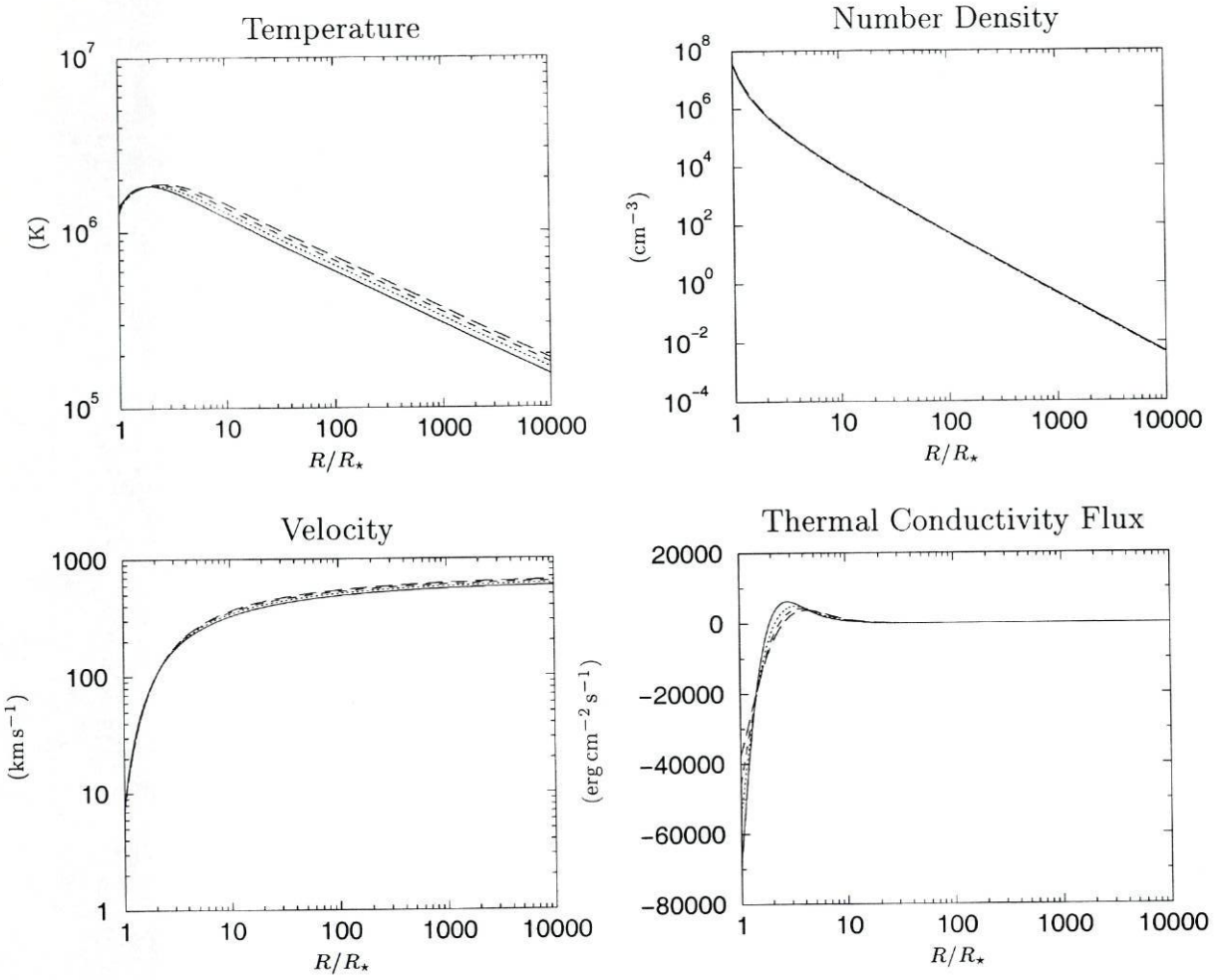

Figure 5.13: Effect of increasing the extent of mechanical heating deposition (σ), while $R_c = 3.0\,R_\star$ is kept constant.

	σ ($R_\star$)	h_0 ($\mathrm{erg\,cm^{-3}\,s^{-1}}$)	V_c ($\mathrm{km\,s^{-1}}$)	V_0 ($\mathrm{km\,s^{-1}}$)	T_0 (K)
(—):	0.60	1.592×10^{-6}	169.00	6.894	1.250×10^{6}
(···):	0.80	9.102×10^{-7}	171.76	6.587	1.269×10^{6}
(---):	1.00	6.065×10^{-7}	173.96	6.878	1.318×10^{6}
(– –):	1.20	4.407×10^{-7}	175.65	7.590	1.390×10^{6}

$R_c(R_\star)$	value of V ($km\,s^{-1}$)		
	100	200	300
	attained at $R/R_\star =$		
2.5	1.619	2.605	4.447
3.0	2.004	3.544	7.057
3.5	2.423	4.684	10.85
4.0	2.874	6.070	16.25

Table 5.4: Radial distance where the values of the velocity equal to 100, 200 and 300 $km\,s^{-1}$ are attained, as function of the position of the critical point.

The analysis of Fig. 5.14 shows that increasing the value of R_c has both good and bad effects on the various profiles. With values of R_c beyond $\sim 3.5\,R_\star$ the base temperature has its value decreased below one million Kelvin. The farther out is the position of R_c the lower is the temperature at the base. However, this decrease in T_0 is also followed by a decrease in V_0 and consequently on the mass loss rate (recall that $\dot{M} = 4\pi R_\star^2 V_0 \rho_0$, and $R_\star$ and ρ_0 are constant in the models of this Section).

The other major drawback of increasing R_c is the overall slower acceleration of the wind. This effect is quantified in Table 5.4 where it is worth noticing the very slow acceleration of the plasma for the wind model with $R_c = 4.0\,R_\star$. In this case a velocity of 300 $km\,s^{-1}$ is only attained at a radial distance of $16\,R_\star$.

5.8.4 Conclusion of this Section

The conclusion of this Section is that it is possible for the stellar wind model under study to drive denser winds while starting with a temperature at the base of a few 10^5 K. However, since this is a purely thermal wind, the lower temperature at the base is achieved by moving the position of the critical point (R_c) to larger distances from the stellar surface. The outcome of the lower base temperature and a farther out position of the critical point is an overall smaller acceleration of the plasma.

5.9 Application to TTS again

In the last Sections it was recognized that the stellar wind model under study has difficulties in driving dense winds for a star with solar radius and mass. Could the larger radius of TTS be helpful in this matter? The intuitive answer seems to be negative, since when T_0, V_0, $dT/dR|_c$ and $M_\star$ are held fixed and $R_\star$ is increased the initial acceleration of the

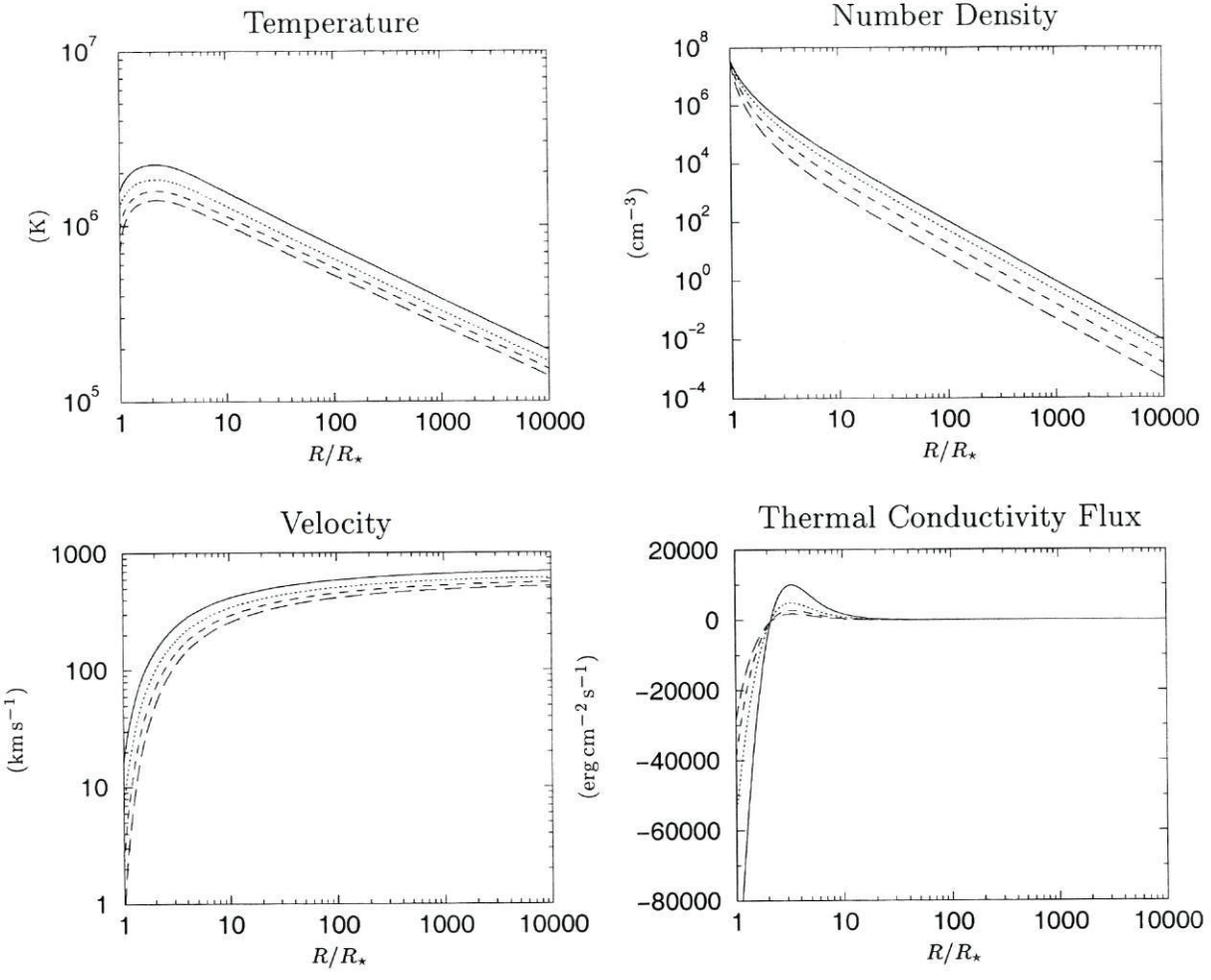

Figure 5.14: Effect of changing the position of the radial distance of the critical point (R_c) while $\sigma = 0.8\,R_\star$ is kept constant.

	R_c ($R_\star$)	h_0 ($\mathrm{erg\,cm^{-3}\,s^{-1}}$)	V_c ($\mathrm{km\,s^{-1}}$)	V_0 ($\mathrm{km\,s^{-1}}$)	T_0 (K)
(—):	2.50	1.953×10^{-6}	191.57	15.87	1.545×10^{6}
(···):	3.00	9.102×10^{-7}	171.76	6.587	1.269×10^{6}
(---):	3.50	5.061×10^{-7}	157.50	2.094	$= 9.407\times10^{5}$
(– –):	4.00	3.211×10^{-7}	146.39	0.5953	6.664×10^{5}

plasma is smaller, as an inspection of Eq. (4.7) shows.

5.9.1 Increasing the model $R_\star$

The plots of Fig. 5.15 confirm that the increment of the stellar radius worsens the profiles of temperature and velocity. It is seen that increasing the stellar radius results in an overall smaller acceleration of the plasma. This slower acceleration of the wind is followed by the undesirable increase of the temperature at the base. In this Figure the unit of measure for the radial distance used is the stellar radius, therefore the profiles will look even worst if a constant unit (for example $R_\odot$) is used instead.

The profiles in Fig. 5.15 recall those of Fig. 5.10. In both cases the solution to bring the temperature at the base to values of a few 10^5 K is to increase the radial distance of the critical point, which is done in Fig. 5.16. The curves for $R_c = 5.0\,R_\star$ and $\sigma = 1.2\,R_\star$ (dashed) are slightly better than those for $R_c = 5.0\,R_\star$ and $\sigma = 0.8\,R_\star$ in the sense that the acceleration of the plasma is a little higher. Nevertheless, the former model reaches $V = 300\,\mathrm{km\,s^{-1}}$ at $R = 47\,R_\star$, while for the latter this happens farther out at $R = 57\,R_\star$. These results help quantifying the very slow acceleration of the plasma.

As mentioned earlier one of the main drawbacks of increasing the value of R_c is the consequent decrease of V_0 and the mass loss rate.

5.9.2 Changing the model $M_\star$

TTS have masses up to $3\,M_\odot$, the majority of them having less than one solar mass. The results for models with $R_\star = 1.2\,R_\odot$ and stellar masses of 0.9, 1.0 and $1.1\,M_\odot$ are shown in Fig. 5.17. In all the three cases the velocity and temperature at the base of the wind are very similar. The largest changes induced by the higher stellar mass are found farther out in a larger acceleration of the wind, and also a higher plasma temperature.

5.10 Conclusion

From the results of the previous Sections it must be concluded that the stellar wind model that was the object of this Chapter is not suitable to drive the winds of TTS. Even for a rather low density at the base of the wind of only $4.0 \times 10^7\,\mathrm{cm^{-3}}$ the wind has major drawbacks, namely the very slow acceleration of the plasma. The densities inferred from TTS lines forming close to their stellar surfaces are in the range 10^{11}–$10^{12}\,\mathrm{cm^{-3}}$, about 4 orders of magnitude above the highest value used in this Chapter.

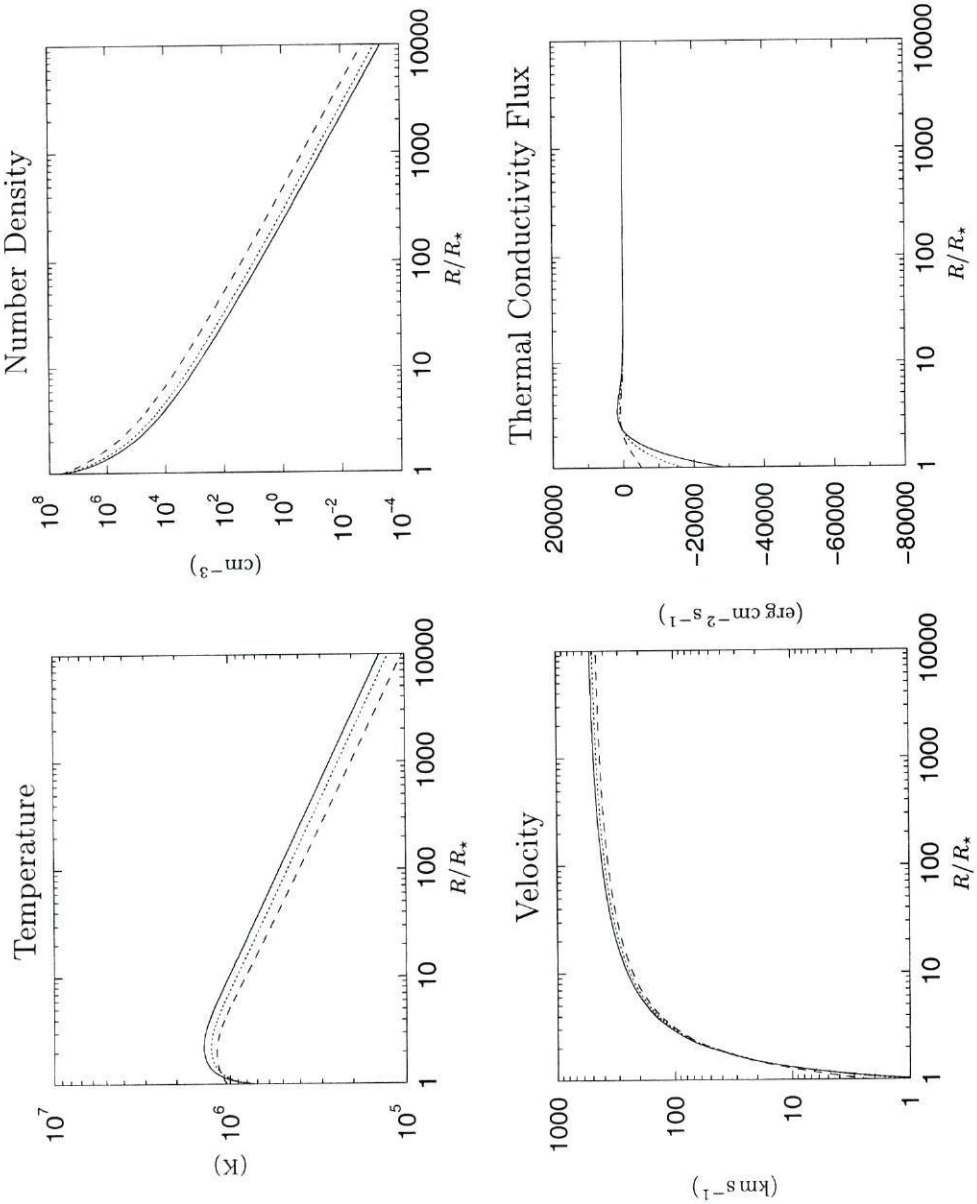

Figure 5.15: Effects induced by increasing the stellar radius. In all the models $R_c = 4.0\,R_\star$ and $\sigma = 0.8\,R_\star$.

	$R_\star$ ($R_\odot$)	h_0 (erg cm^{-3} s^{-1})	V_c (km s^{-1})	V_0 (km s^{-1})	T_0 (K)
(—):	1.0	3.211×10^{-7}	146.39	0.595	6.664×10^5
(···):	1.1	1.931×10^{-7}	139.42	0.898	7.697×10^5
(– –):	1.2	1.239×10^{-7}	132.79	2.197	1.035×10^6

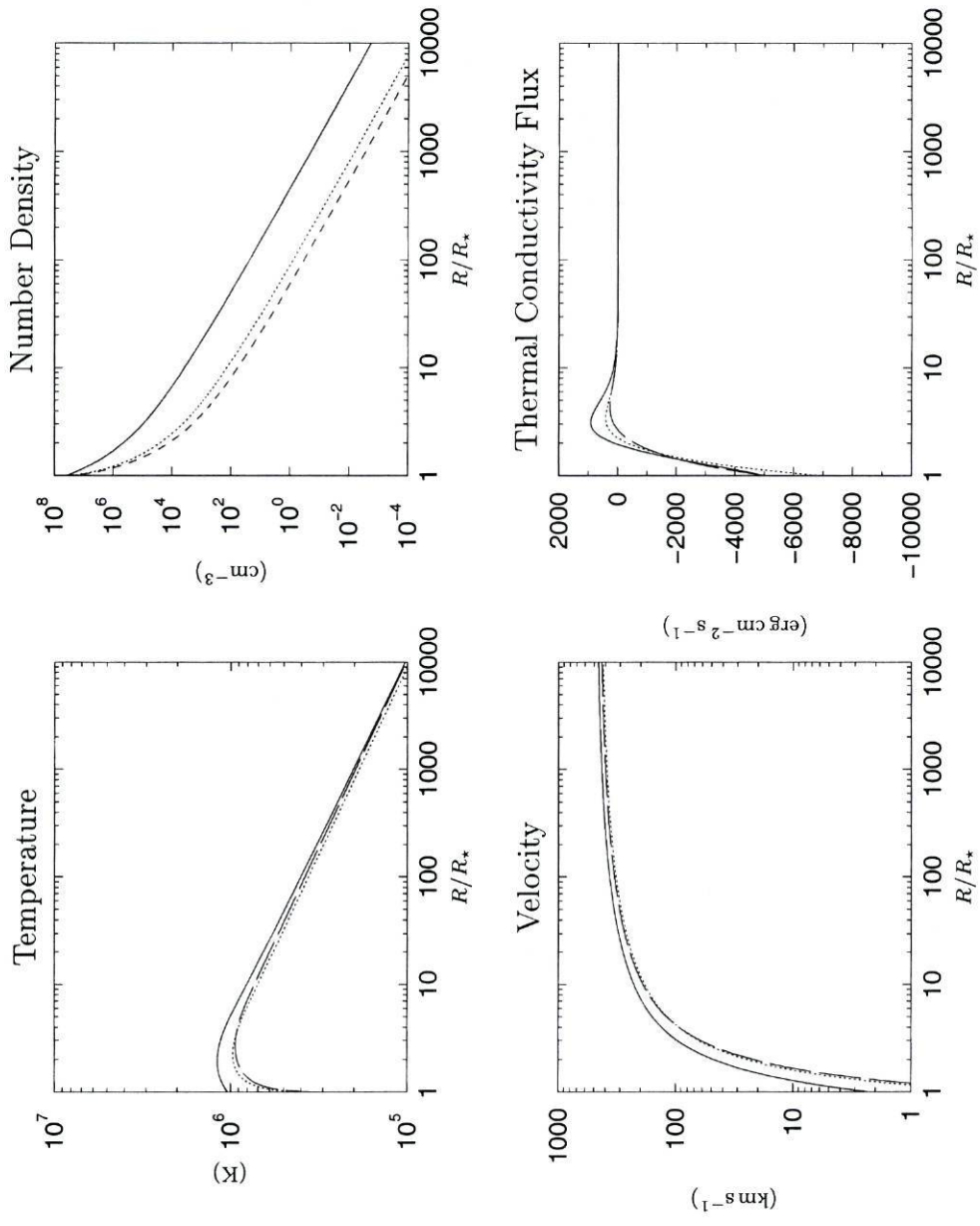

Figure 5.16: Improving the results for the model with $R_\star = 1.2\,R_\odot$.

	R_c ($R_\star$)	σ ($R_\star$)	h_0 (erg cm^{-3} s^{-1})	V_c (km s^{-1})	V_0 (km s^{-1})	T_0 (K)
(—):	4.0	0.80	1.239×10^{-7}	132.79	2.197	1.035×10^{6}
(···):	5.0	0.80	6.070×10^{-8}	118.59	0.064	3.399×10^{5}
(– – –):	5.0	1.20	2.390×10^{-8}	120.13	0.029	2.818×10^{5}

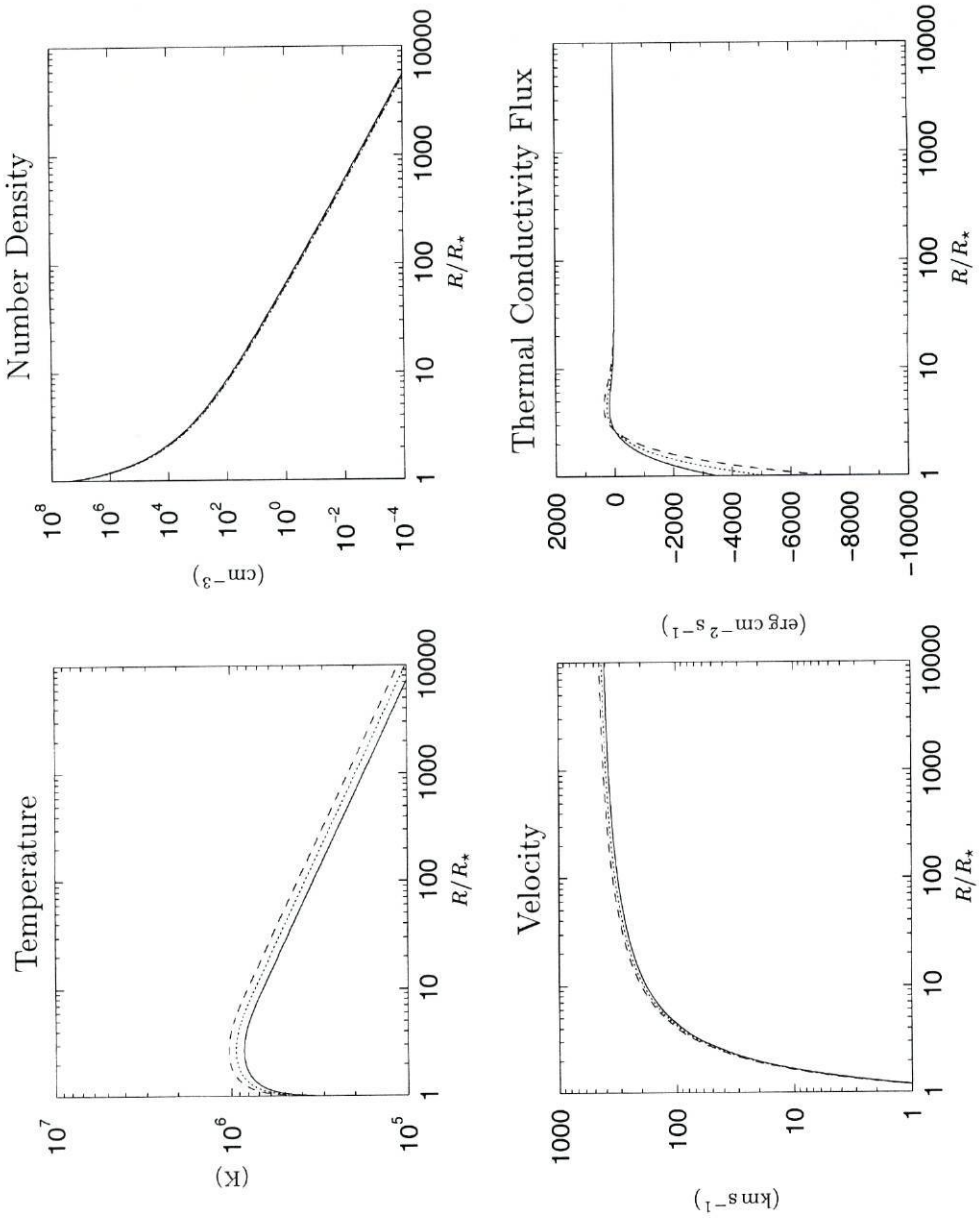

Figure 5.17: Changing the model stellar mass. For all the profiles $R_\star = 1.2\,R_\odot$, $R_\mathrm{c} = 5.0\,R_\star$, $\sigma = 1.2\,R_\star$.

	$M_\star$ ($M_\odot$)	h_0 (erg cm^{-3} s^{-1})	V_c (km s^{-1})	V_0 (km s^{-1})	T_0 (K)
(—):	0.9	1.656×10^{-8}	113.96	0.032	2.819×10^5
(· · ·):	1.0	2.390×10^{-8}	120.13	0.029	2.818×10^5
(– –):	1.1	3.331×10^{-8}	125.99	0.031	3.188×10^5

Chapter 6

A stellar wind model with Alfvén waves

A spherical symmetric and hydrodynamic stellar wind model powered by a simple volumetric heating rate of prescribed exponential form is not able to drive the dense and fast winds of TTS, as the examples of wind models in the previous Chapter have shown. Therefore it is necessary to add more ingredients to the model, and several possibilities arise:

- use for the mechanical heating two or more prescribed exponentials, with different h_0's and different σ's;
- include a momentum addition term;
- relax the assumption of spherical symmetry;
- include waves, in particular Alfvén waves.

In this work it was chosen to keep the assumption of spherical symmetry, use just one prescribed exponential for the mechanical heating and to develop the stellar wind model of the previous Chapter to include the effects of Alfvén waves.

Alfvén waves exert a force on the plasma due to the gradient of the magnetic pressure associated with them. Consequently there is a new term on the momentum equation. By the damping of Alfvén waves the plasma is heated and therefore a new term on the energy equation appears. This Chapter addresses the consequences of these two extra terms on the stellar wind model.

6.1 Stellar wind model: the equations

The stellar wind model being developed in this Chapter is an extension of the model from the previous one including the effects due to the propagation of Alfvén waves. The assumption of complete spherical symmetry remains, and also the time independent character of the model. Under these assumptions the continuity equation is still

$$R^2 \rho V = Z \quad . \tag{6.1}$$

However, the momentum and energy equations are modified to include the terms due to the Alfvén waves. The momentum equation (Eq. (3.24)) in vectorial form is:

$$\rho\left(\vec{V}\cdot\nabla\right)\vec{V} + \rho\left(\delta\vec{V}\cdot\nabla\right)\delta\vec{V} = -\nabla P - \rho\frac{GM}{R^2}\,\hat{e}_{\rm r} + \frac{\left(\vec{B}\cdot\nabla\right)\vec{B}}{4\pi} - \nabla\left(\frac{B^2}{8\pi}\right) + \frac{\left(\delta\vec{B}\cdot\nabla\right)\delta\vec{B}}{4\pi} - \nabla\left(\frac{\delta B^2}{8\pi}\right) \quad . \tag{6.2}$$

The various terms are now expanded under complete spherical symmetry[1], starting with the magnetic tension:

$$\frac{\left(\vec{B}\cdot\nabla\right)\vec{B}}{4\pi} = \frac{B_{\rm r}}{4\pi}\frac{{\rm d}B_{\rm r}}{{\rm d}R} \tag{6.3}$$

proceeding with the magnetic pressure:

$$-\nabla\left(\frac{B^2}{8\pi}\right) = -\frac{\rm d}{{\rm d}R}\left(\frac{B_{\rm r}^2}{8\pi}\right) = -\frac{B_{\rm r}}{4\pi}\frac{{\rm d}B_{\rm r}}{{\rm d}R} \quad . \tag{6.4}$$

Therefore, under spherical symmetry, the magnetic tension and pressure cancel each other. Consequently the magnetic field has a passive role in the dynamics of the plasma.

The magnetic tension due to the Alfvén waves[2] is:

$$\frac{\left(\delta\vec{B}\cdot\nabla\right)\delta\vec{B}}{4\pi} = \frac{1}{4\pi}\left(-\frac{\delta B_\theta^2 + \delta B_\varphi^2}{R}\,\hat{e}_{\rm r} - \frac{\delta B_\varphi^2\cot\theta}{R}\,\hat{e}_\varphi + \frac{\delta B_\theta \delta B_\varphi \cot\theta}{R}\,\hat{e}_\theta\right) \tag{6.5}$$

and the equivalent term for the velocity perturbation is:

$$\rho\left(\delta\vec{V}\cdot\nabla\right)\delta\vec{V} = \rho\left(-\frac{\delta V_\theta^2 + \delta V_\varphi^2}{R}\,\hat{e}_{\rm r} - \frac{\delta V_\varphi^2\cot\theta}{R}\,\hat{e}_\varphi + \frac{\delta V_\theta \delta V_\varphi \cot\theta}{R}\,\hat{e}_\theta\right) \quad . \tag{6.6}$$

[1] Under this assumption the global magnetic field ($\vec{B}$) has the form of a monopole.

[2] Recall that Alfvén waves are transverse waves.

For Alfvén waves these two terms cancel each other. The remaining term due to the magnetic pressure of the Alfvén waves is:

$$-\nabla\left(\frac{\delta B^2}{8\pi}\right) = -\frac{\mathrm{d}}{\mathrm{d}R}\left(\frac{\delta B_\theta^2 + \delta B_\varphi^2}{8\pi}\right) \quad . \tag{6.7}$$

After averaging over all wave frequencies, wavenumbers and polarizations, the momentum equation becomes (Hollweg, 1973; Sandbæk et al., 1994):

$$\rho V\frac{\mathrm{d}V}{\mathrm{d}R} = -\frac{\mathrm{d}P}{\mathrm{d}R} - \rho\frac{GM}{R^2} - \frac{\mathrm{d}}{\mathrm{d}R}\left(\frac{\langle\delta B^2\rangle}{8\pi}\right) \tag{6.8}$$

and the energy equation includes a term, Q_w, due to the transfer of energy from the waves to the plasma in the form of heat:

$$\frac{V}{\gamma-1}\left(\frac{\mathrm{d}P}{\mathrm{d}R} - \gamma AT\frac{\mathrm{d}\rho}{\mathrm{d}R}\right) = \frac{1}{R^2}\frac{\mathrm{d}F}{\mathrm{d}R} - \left(\frac{\rho}{\mu m_\mathrm{H}}\right)^2 \chi T^\alpha + h_0 e^{-\frac{R-R_\star}{\sigma}} + Q_\mathrm{w} \quad . \tag{6.9}$$

The expression for Q_w is obtained after it is realized that the rate of change of the Alfvén wave energy flux is due to the rate of work done on the plasma by the magnetic pressure gradient force and by wave damping which results in the heating of the plasma. In symbolic language the rate of change of the energy flux is the divergence of the energy flux, the rate of work done is the product of the velocity by the force and the heating is Q_w, as follows:

$$\frac{1}{R^2}\frac{\mathrm{d}F_\mathrm{w}}{\mathrm{d}R} = V\frac{\mathrm{d}}{\mathrm{d}R}\left(\frac{\langle\delta B^2\rangle}{8\pi}\right) - Q_\mathrm{w} \quad . \tag{6.10}$$

F_w is related to the wave energy flux by

$$F_\mathrm{w} = R^2 f_\mathrm{w} = \frac{\langle\delta B^2\rangle}{8\pi}\frac{3M_\mathrm{A}+2}{M_\mathrm{A}}VR^2 \quad . \tag{6.11}$$

We will now turn our attention to the expression for the magnetic wave amplitude. When $\langle\delta B^2\rangle/B^2 < \varepsilon$, where ε is smaller than one, the waves are assumed to propagate as small amplitude WKB waves, i.e., there is no wave damping and $Q_\mathrm{w} = 0$. In this case (cf. Hollweg (1973), and Chapter 3):

$$\langle\delta B^2\rangle_1 = \frac{8\pi F_{\mathrm{w}_0}\rho}{Z}\frac{M_\mathrm{A}}{2+3M_{\mathrm{A}_0}}\left(\frac{1+M_{\mathrm{A}_0}}{1+M_\mathrm{A}}\right)^2 \quad . \tag{6.12}$$

It is further assumed that for large wave amplitudes damping mechanisms set in and effectively limit the wave amplitude to a fraction of the ambient magnetic field:

$$\langle\delta B^2\rangle_\mathrm{B} = \varepsilon B^2 \quad . \tag{6.13}$$

To ensure a smooth transition between the two regimes the geometrical mean of both expressions will be used (cf. (Jacques, 1978)):

$$\langle \delta B^2 \rangle = \frac{\langle \delta B^2 \rangle_1 \langle \delta B^2 \rangle_B}{\langle \delta B^2 \rangle_1 + \langle \delta B^2 \rangle_B} \quad . \tag{6.14}$$

From this expression it is found that $\langle \delta B^2 \rangle < \langle \delta B^2 \rangle_1$ and $\langle \delta B^2 \rangle < \langle \delta B^2 \rangle_B$, therefore the ratios

$$\frac{\langle \delta B^2 \rangle}{\langle \delta B^2 \rangle_1} = \frac{\langle \delta B^2 \rangle_B}{\langle \delta B^2 \rangle_1 + \langle \delta B^2 \rangle_B} \qquad \text{and} \qquad \frac{\langle \delta B^2 \rangle}{\langle \delta B^2 \rangle_B} = \frac{\langle \delta B^2 \rangle_1}{\langle \delta B^2 \rangle_1 + \langle \delta B^2 \rangle_B} \tag{6.15}$$

will be used to quantify the relative importance of $\langle \delta B^2 \rangle_1$ and $\langle \delta B^2 \rangle_B$ for the value of $\langle \delta B^2 \rangle$, respectively. This choice is based on the fact that

$$\frac{\langle \delta B^2 \rangle}{\langle \delta B^2 \rangle_1} + \frac{\langle \delta B^2 \rangle}{\langle \delta B^2 \rangle_B} = 1 \tag{6.16}$$

and on the following limiting cases:

$$\begin{aligned} &\text{if } \langle \delta B^2 \rangle_1 \ll \langle \delta B^2 \rangle_B \text{ then } \langle \delta B^2 \rangle \sim \langle \delta B^2 \rangle_1 \ , \ \tfrac{\langle \delta B^2 \rangle}{\langle \delta B^2 \rangle_1} \sim 1 \text{ and } \tfrac{\langle \delta B^2 \rangle}{\langle \delta B^2 \rangle_B} \sim 0 \\ &\text{if } \langle \delta B^2 \rangle_B \ll \langle \delta B^2 \rangle_1 \text{ then } \langle \delta B^2 \rangle \sim \langle \delta B^2 \rangle_B \ , \ \tfrac{\langle \delta B^2 \rangle}{\langle \delta B^2 \rangle_1} \sim 0 \text{ and } \tfrac{\langle \delta B^2 \rangle}{\langle \delta B^2 \rangle_B} \sim 1 \end{aligned}$$

The derivative of the wave amplitude (Eq. (6.14)) is:

$$\frac{\mathrm{d}\ln\left(\langle \delta B^2 \rangle\right)}{\mathrm{d}R} = \frac{\langle \delta B^2 \rangle}{\langle \delta B^2 \rangle_1} \frac{\mathrm{d}\ln\left(\langle \delta B^2 \rangle_1\right)}{\mathrm{d}R} + \frac{\langle \delta B^2 \rangle}{\langle \delta B^2 \rangle_B} \frac{\mathrm{d}\ln\left(\langle \delta B^2 \rangle_B\right)}{\mathrm{d}R} \tag{6.17}$$

the derivatives of $\langle \delta B^2 \rangle_1$ and $\langle \delta B^2 \rangle_B$ are:

$$\frac{\mathrm{d}\ln\left(\langle \delta B^2 \rangle_1\right)}{\mathrm{d}R} = \frac{1 + 3M_A}{2(1 + M_A)} \frac{\mathrm{d}\ln\rho}{\mathrm{d}R} \tag{6.18}$$

and

$$\frac{\mathrm{d}\ln\left(\langle \delta B^2 \rangle_B\right)}{\mathrm{d}R} = -\frac{4}{R} \tag{6.19}$$

where

$$\frac{\mathrm{d}\ln(\rho)}{\mathrm{d}R} = -\left(\frac{2}{R} + \frac{1}{V}\frac{\mathrm{d}V}{\mathrm{d}R}\right) \tag{6.20}$$

from the equation of continuity (Eq. (6.1)).

From Eq. (6.11) the derivative of $F_{\rm w}$ is

$$\frac{{\rm d}F_{\rm w}}{{\rm d}R} = \frac{Z\langle\delta B^2\rangle}{8\pi\rho M_{\rm A}}\left[(1+3M_{\rm A})\left(\frac{2+3M_{\rm A}}{2(1+M_{\rm A})}\frac{\langle\delta B^2\rangle}{\langle\delta B^2\rangle_1}-1\right)\frac{{\rm d}\ln\rho}{{\rm d}R} - (2+3M_{\rm A})\frac{\langle\delta B^2\rangle}{\langle\delta B^2\rangle_{\rm B}}\frac{4}{R}\right] \tag{6.21}$$

and the heat of the plasma due to the waves becomes:

$$Q_{\rm w} = \frac{V\langle\delta B^2\rangle}{\pi M_{\rm A}}\left[(1+3M_{\rm A})\frac{\langle\delta B^2\rangle_1-\langle\delta B^2\rangle}{8\langle\delta B^2\rangle_1}\frac{{\rm d}\ln\rho}{{\rm d}R}+\frac{1+M_{\rm A}}{R}\frac{\langle\delta B^2\rangle}{\langle\delta B^2\rangle_{\rm B}}\right] \quad . \tag{6.22}$$

This expression for $Q_{\rm w}$ has two limiting cases of interest:

$$\begin{array}{l}\text{if } \langle\delta B^2\rangle_1 \ll \langle\delta B^2\rangle_{\rm B} \text{ then } \langle\delta B^2\rangle \sim \langle\delta B^2\rangle_1 \text{ and } Q_{\rm w}\sim 0 \ , \\ \text{if } \langle\delta B^2\rangle_{\rm B} \ll \langle\delta B^2\rangle_1 \text{ then } \langle\delta B^2\rangle \sim \langle\delta B^2\rangle_{\rm B} \text{ and } Q_{\rm w}\sim \frac{V\langle\delta B^2\rangle_{\rm B}}{\pi M_{\rm A}}\left(\frac{1+3M_{\rm A}}{8}\frac{{\rm d}\ln\rho}{{\rm d}R}+\frac{1+M_{\rm A}}{R}\right)\end{array}$$

which show that when the undamped mode ($\langle\delta B^2\rangle_1$) dominates there is no plasma heating due to the waves.

Returning now to the momentum equation (Eq. (6.8)) by performing the substitution of ${\rm d}P/{\rm d}R$ and ${\rm d}\langle\delta B^2\rangle/{\rm d}R$ in it, arriving to

$$\left(V^2-AT-\frac{1}{16\pi\rho}\frac{1+3M_{\rm A}}{1+M_{\rm A}}\frac{\langle\delta B^2\rangle^2}{\langle\delta B^2\rangle_1}\right)\frac{1}{V}\frac{{\rm d}V}{{\rm d}R} = \left(AT+\frac{1}{16\pi\rho}\frac{1+3M_{\rm A}}{1+M_{\rm A}}\frac{\langle\delta B^2\rangle^2}{\langle\delta B^2\rangle_1}+\frac{1}{4\pi\rho}\frac{\langle\delta B^2\rangle^2}{\langle\delta B^2\rangle_{\rm B}}\right)\frac{2}{R}-A\frac{{\rm d}T}{{\rm d}R}-\frac{GM}{R^2} \quad . \tag{6.23}$$

This equation has a critical point, which is given by

$$V_{\rm c}^2 = AT_{\rm c}+\frac{1}{16\pi\rho_{\rm c}}\frac{1+3M_{\rm Ac}}{1+M_{\rm Ac}}\frac{\langle\delta B^2\rangle_{\rm c}^2}{\langle\delta B^2\rangle_{1{\rm c}}} \tag{6.24}$$

and

$$\left(V_{\rm c}^2+\frac{1}{4\pi\rho_{\rm c}}\frac{\langle\delta B^2\rangle_{\rm c}^2}{\langle\delta B^2\rangle_{\rm Bc}}\right)\frac{2}{R_{\rm c}}-A\left.\frac{{\rm d}T}{{\rm d}R}\right|_{\rm c}-\frac{GM}{R_{\rm c}^2}=0 \tag{6.25}$$

where the subscript 'c' denotes quantities evaluated at the critical point.

The energy equation can be written as a differential equation related to the thermal conductivity flux:

$$\frac{\mathrm{d}F}{\mathrm{d}R} = -\left(ATZ + \frac{Z}{8\pi\rho}\frac{1+3M_\mathrm{A}}{M_\mathrm{A}}\frac{\langle\delta B^2\rangle}{\langle\delta B^2\rangle_1}(\langle\delta B^2\rangle_1 - \langle\delta B^2\rangle)\right)\frac{\mathrm{d}\ln\rho}{\mathrm{d}R} + \frac{AZ}{\gamma-1}\frac{\mathrm{d}T}{\mathrm{d}R} - \frac{Z}{\pi\rho R}\frac{1+M_\mathrm{A}}{M_\mathrm{A}}\frac{\langle\delta B^2\rangle^2}{\langle\delta B^2\rangle_\mathrm{B}} + \left(\frac{Z}{\mu m_\mathrm{H}}\right)^2\frac{\chi T^\alpha}{R^2V^2} - R^2 h_0 e^{-\frac{R-R_\star}{\sigma}} \tag{6.26}$$

where, as before, F is the thermal conductivity flux multiplied by $(-R^2)$,

$$F = R^2\kappa_0 T^{5/2}\frac{\mathrm{d}T}{\mathrm{d}R} \quad . \tag{6.27}$$

From Eqs. (6.24) and (6.25) it is possible to relate T_c and F_c with R_c and V_c

$$T_\mathrm{c} = \frac{V_\mathrm{c}^2}{A} - \frac{1}{16\pi A\rho_\mathrm{c}}\frac{1+3M_\mathrm{Ac}}{1+M_\mathrm{Ac}}\frac{\langle\delta B^2\rangle_\mathrm{c}^2}{\langle\delta B^2\rangle_\mathrm{1c}} \tag{6.28}$$

$$F_\mathrm{c} = R_\mathrm{c}\kappa_0 T_\mathrm{c}^{5/2}\left[\left(V_\mathrm{c}^2 + \frac{1}{4\pi\rho_\mathrm{c}}\frac{\langle\delta B^2\rangle_\mathrm{c}^2}{\langle\delta B^2\rangle_\mathrm{Bc}}\right)\frac{2}{A} - \frac{GM}{R_\mathrm{c}}\right] \quad . \tag{6.29}$$

6.2 The energy fluxes

The energy fluxes are given by the same expressions as in the previous Chapter, Eqs. (5.23) to (5.28), together with the Alfvén wave energy flux:

$$f_\mathrm{w} = \frac{V\langle\delta B^2\rangle}{8\pi}\frac{2+3M_\mathrm{A}}{M_\mathrm{A}} \quad . \tag{6.30}$$

It is convenient to define f_v as

$$f_\mathrm{v} = f_\mathrm{k} + f_\mathrm{e} + f_\mathrm{g} = \left(\frac{1}{2}V^2 + \frac{A\gamma}{\gamma-1}T - \frac{GM}{R}\right)\rho V \tag{6.31}$$

therefore f_v is the sum of the energy fluxes associated with the plasma flow, advected with velocity V.

6.3 The indetermination at the critical point

A few more steps are needed to bring the equations into a suitable form for their numerical integration. These steps are the subject of this section.

6.3.1 Normalization

It is convenient to normalize all equations to quantities at the critical point. For that purpose the normalized variables introduced in the previous Chapter will be used again. These are:

$$a = \frac{R}{R_c} \ , \qquad u = \frac{V}{V_c} \ , \qquad \tau = \frac{T}{T_c} \ , \qquad \phi = \frac{F}{F_c} \ . \tag{6.32}$$

Consequently, after normalization, Eqs. (6.23), (6.27) and (6.26) become, respectively:

$$\begin{aligned}\left(u^2 - \frac{AT_c}{V_c^2}\tau - \frac{1}{16\pi V_c^2\rho}\frac{1+3M_A}{1+M_A}\frac{\langle\delta B^2\rangle^2}{\langle\delta B^2\rangle_1}\right)\frac{1}{u}\frac{\mathrm{d}u}{\mathrm{d}a} = \\ \left(\frac{AT_c}{V_c^2}\tau + \frac{1}{16\pi V_c^2\rho}\frac{1+3M_A}{1+M_A}\frac{\langle\delta B^2\rangle^2}{\langle\delta B^2\rangle_1} + \frac{1}{4\pi V_c^2\rho}\frac{\langle\delta B^2\rangle^2}{\langle\delta B^2\rangle_B}\right)\frac{2}{a} \\ - \frac{AT_c}{V_c^2}\frac{\mathrm{d}\tau}{\mathrm{d}a} - \frac{GM}{R_c V_c^2 a^2}\end{aligned} \tag{6.33}$$

$$\frac{\mathrm{d}\tau}{\mathrm{d}a} = \frac{F_c}{\kappa_0 R_c T_c^{7/2}}\frac{\phi}{a^2\tau^{5/2}} \tag{6.34}$$

$$\begin{aligned}\frac{\mathrm{d}\phi}{\mathrm{d}a} = \left(\frac{AT_cZ}{F_c}\tau + \frac{Z}{8\pi F_c\rho}\frac{1+3M_A}{M_A}\frac{\langle\delta B^2\rangle}{\langle\delta B^2\rangle_1}(\langle\delta B^2\rangle_1 - \langle\delta B^2\rangle)\right)\left(\frac{2}{a} + \frac{1}{u}\frac{\mathrm{d}u}{\mathrm{d}a}\right) \\ + \frac{AT_cZ}{F_c(\gamma-1)}\frac{\mathrm{d}\tau}{\mathrm{d}a} - \frac{Z}{\pi F_c\rho a}\frac{1+M_A}{M_A}\frac{\langle\delta B^2\rangle^2}{\langle\delta B^2\rangle_B} \\ + \left(\frac{Z}{\mu m_H}\right)^2\frac{\chi T^\alpha}{R_c V_c^2 F_c}\frac{1}{a^2u^2} - \frac{R_c^3 h_0}{F_c}a^2 e^{-\frac{R-R_\star}{\sigma}} \ .\end{aligned} \tag{6.35}$$

These three equations form the system of equations that will be numerically integrated.

Normalized accelerations

The normalized momentum equation, Eq. (6.8), is:

$$u\frac{\mathrm{d}u}{\mathrm{d}a} = -\frac{1}{V_c^2\rho}\frac{\mathrm{d}P}{\mathrm{d}a} - \frac{GM}{R_c V_c^2 a^2} - \frac{1}{V_c^2\rho}\frac{\mathrm{d}}{\mathrm{d}a}\left(\frac{\langle\delta B^2\rangle}{8\pi}\right) \ . \tag{6.36}$$

The term on the left-hand side is the plasma acceleration divided by V_c^2/R_c, that can be thought as a 'normalized acceleration', as a consequence all the terms in this equation will

be referred as 'normalized accelerations', namely:

$$\mathcal{A} = u\frac{\mathrm{d}u}{\mathrm{d}a} \tag{6.37}$$

$$\mathcal{A}_{\mathrm{P}} = -\frac{1}{V_{\mathrm{c}}^2\rho}\frac{\mathrm{d}P}{\mathrm{d}a} \tag{6.38}$$

$$\mathcal{A}_{\mathrm{g}} = -\frac{GM}{R_{\mathrm{c}}V_{\mathrm{c}}^2a^2} \tag{6.39}$$

$$\mathcal{A}_{\mathrm{w}} = -\frac{1}{V_{\mathrm{c}}^2\rho}\frac{\mathrm{d}}{\mathrm{d}R}\left(\frac{\langle\delta B^2\rangle}{8\pi}\right) \tag{6.40}$$

where $\mathcal{A}$ is the resulting normalized plasma acceleration, $\mathcal{A}_{\mathrm{P}}$, $\mathcal{A}_{\mathrm{g}}$ and $\mathcal{A}_{\mathrm{w}}$ are the normalized accelerations due to the thermal pressure gradient, the stellar gravity and the gradient of the wave pressure, respectively. Of these four normalized accelerations only $\mathcal{A}_{\mathrm{g}}$ is negative.

6.3.2 The critical slope

To overcome the indetermination of the momentum equation at the critical point is is necessary to linearize it. Using the methods of Appendix A, this requires starting by expanding the normalized variables to first order

$$a = 1+\delta\ , \qquad u = 1+\epsilon\ , \qquad \tau = 1+\left.\frac{\mathrm{d}\tau}{\mathrm{d}a}\right|_{\mathrm{c}}\delta \tag{6.41}$$

and

$$\frac{\mathrm{d}\tau}{\mathrm{d}a} = \left.\frac{\mathrm{d}\tau}{\mathrm{d}a}\right|_{\mathrm{c}} + \frac{\partial}{\partial a}\left(\frac{\mathrm{d}\tau}{\mathrm{d}a}\right)\bigg|_{\mathrm{c}}\delta + \frac{\partial}{\partial u}\left(\frac{\mathrm{d}\tau}{\mathrm{d}a}\right)\bigg|_{\mathrm{c}}\epsilon\ . \tag{6.42}$$

The derivative of the normalized temperature at the critical point is

$$\left.\frac{\mathrm{d}\tau}{\mathrm{d}a}\right|_{\mathrm{c}} = \frac{F_{\mathrm{c}}}{\kappa_0 R_{\mathrm{c}}T_{\mathrm{c}}^{7/2}}\ . \tag{6.43}$$

The second derivative of the normalized temperature is split in two:

$$\frac{\partial}{\partial a}\left(\frac{\mathrm{d}\tau}{\mathrm{d}a}\right) = \left.\frac{\mathrm{d}\tau}{\mathrm{d}a}\right|_{\mathrm{c}}\frac{1}{a^2\tau^{5/2}}\left(\frac{\partial\phi}{\partial a} - \frac{2\phi}{a} - \frac{5\phi}{2\tau}\frac{\mathrm{d}\tau}{\mathrm{d}a}\right) \tag{6.44}$$

and

$$\frac{\partial}{\partial u}\left(\frac{\mathrm{d}\tau}{\mathrm{d}a}\right) = \left.\frac{\mathrm{d}\tau}{\mathrm{d}a}\right|_{\mathrm{c}}\frac{1}{a^2\tau^{5/2}}\frac{\partial\phi}{\partial u} \tag{6.45}$$

where

$$\frac{\partial\phi}{\partial a} = \left(\frac{AT_cZ}{F_c}\tau + \frac{Z}{8\pi F_c\rho}\frac{1+3M_A}{M_A}\frac{\langle\delta B^2\rangle}{\langle\delta B^2\rangle_1}(\langle\delta B^2\rangle_1 - \langle\delta B^2\rangle)\right)\frac{2}{a} + \frac{AT_cZ}{F_c(\gamma-1)}\frac{d\tau}{da} - \frac{Z}{\pi F_c\rho a}\frac{1+M_A}{M_A}\frac{\langle\delta B^2\rangle^2}{\langle\delta B^2\rangle_B} + \left(\frac{Z}{\mu m_H}\right)^2\frac{\chi T^\alpha}{R_cV_c^2F_c}\frac{1}{a^2u^2} - \frac{R_c^3h_0}{F_c}a^2e^{-\frac{R-R_\star}{\sigma}} \tag{6.46}$$

and

$$\frac{\partial\phi}{\partial u} = \left(\frac{AT_cZ}{F_c}\tau + \frac{Z}{8\pi F_c\rho}\frac{1+3M_A}{M_A}\frac{\langle\delta B^2\rangle}{\langle\delta B^2\rangle_1}(\langle\delta B^2\rangle_1 - \langle\delta B^2\rangle)\right)\frac{1}{u}\frac{du}{da} \quad . \tag{6.47}$$

At the critical point the previous expressions simplify to

$$\frac{\partial}{\partial a}\left(\frac{d\tau}{da}\right)\bigg|_c = \frac{d\tau}{da}\bigg|_c\left(\frac{\partial\phi}{\partial a}\bigg|_c - 2 - \frac{5}{2}\frac{d\tau}{da}\bigg|_c\right) \tag{6.48}$$

and

$$\frac{\partial}{\partial u}\left(\frac{d\tau}{da}\right)\bigg|_c = \frac{d\tau}{da}\bigg|_c\frac{\partial\phi}{\partial u}\bigg|_c \tag{6.49}$$

where

$$\frac{\partial\phi}{\partial a}\bigg|_c = 2\left(\frac{AT_cZ}{F_c} + \frac{Z}{8\pi F_c\rho_c}\frac{1+3M_{Ac}}{M_{Ac}}\frac{\langle\delta B^2\rangle_c}{\langle\delta B^2\rangle_{1c}}(\langle\delta B^2\rangle_{1c} - \langle\delta B^2\rangle_c)\right) + \frac{AT_cZ}{F_c(\gamma-1)}\frac{d\tau}{da}\bigg|_c - \frac{Z}{\pi F_c\rho_c}\frac{1+M_{Ac}}{M_{Ac}}\frac{\langle\delta B^2\rangle_c^2}{\langle\delta B^2\rangle_{Bc}} + \left(\frac{Z}{\mu m_H}\right)^2\frac{\chi T_c^\alpha}{R_cV_c^2F_c} - \frac{R_c^3h_0}{F_c}e^{-\frac{R_c-R_\star}{\sigma}} \tag{6.50}$$

and

$$\frac{\partial\phi}{\partial u}\bigg|_c = \left(\frac{AT_cZ}{F_c} + \frac{Z}{8\pi F_c\rho_c}\frac{1+3M_{Ac}}{M_{Ac}}\frac{\langle\delta B^2\rangle_c}{\langle\delta B^2\rangle_{1c}}(\langle\delta B^2\rangle_{1c} - \langle\delta B^2\rangle_c)\right)\frac{du}{da}\bigg|_c \quad . \tag{6.51}$$

The quantities ρ, M_A, $\langle\delta B^2\rangle$, $\langle\delta B^2\rangle_1$, $\langle\delta B^2\rangle_B$ are linearized as follows:

$$\rho = \rho_c(1 - 2\delta - \epsilon) \tag{6.52}$$

$$M_A = M_{Ac}(1 + \delta + \epsilon/2) \tag{6.53}$$

$$\langle \delta B^2 \rangle_1 = \langle \delta B^2 \rangle_{1c} \left[1 - \frac{1 + 3M_{Ac}}{1 + M_{Ac}} (\delta + \epsilon/2) \right] \tag{6.54}$$

$$\langle \delta B^2 \rangle_B = \langle \delta B^2 \rangle_{Bc} (1 - 4\delta) \tag{6.55}$$

$$\langle \delta B^2 \rangle = \langle \delta B^2 \rangle_c \left[1 - \frac{\langle \delta B^2 \rangle_c}{\langle \delta B^2 \rangle_{1c}} \frac{1 + 3M_{Ac}}{1 + M_{Ac}} (\delta + \epsilon/2) - 4 \frac{\langle \delta B^2 \rangle_c}{\langle \delta B^2 \rangle_{Bc}} \delta \right] \quad . \tag{6.56}$$

The two expressions involving these quantities and appearing in the momentum equation (Eq. (6.33)) are also linearized

$$\begin{aligned} \frac{1}{16\pi V_c^2 \rho} \frac{1 + 3M_A}{1 + M_A} \frac{\langle \delta B^2 \rangle^2}{\langle \delta B^2 \rangle_1} = \\ \frac{1}{16\pi V_c^2 \rho_c} \frac{1 + 3M_{Ac}}{1 + M_{Ac}} \frac{\langle \delta B^2 \rangle_c^2}{\langle \delta B^2 \rangle_{1c}} \times \left[1 - \frac{8 \langle \delta B^2 \rangle_c}{\langle \delta B^2 \rangle_{Bc}} \delta \right. \\ \left. + \left(\frac{3M_{Ac}}{1 + 3M_{Ac}} - 2 \frac{\langle \delta B^2 \rangle_c}{\langle \delta B^2 \rangle_{1c}} \frac{1 + 3M_{Ac}}{1 + M_{Ac}} + \frac{3 + 4M_{Ac}}{1 + M_{Ac}} \right) (\delta + \epsilon/2) \right] \end{aligned} \tag{6.57}$$

$$\begin{aligned} \frac{1}{4\pi V_c^2 \rho} \frac{\langle \delta B^2 \rangle^2}{\langle \delta B^2 \rangle_B} = \\ \frac{1}{4\pi V_c^2 \rho_c} \frac{\langle \delta B^2 \rangle_c^2}{\langle \delta B^2 \rangle_{Bc}} \times \left[1 + \left(1 - \frac{\langle \delta B^2 \rangle_c}{\langle \delta B^2 \rangle_{1c}} \frac{1 + 3M_{Ac}}{1 + M_{Ac}} \right) \epsilon \right. \\ \left. + \left(6 - \frac{8 \langle \delta B^2 \rangle_c}{\langle \delta B^2 \rangle_{Bc}} - 2 \frac{\langle \delta B^2 \rangle_c}{\langle \delta B^2 \rangle_{1c}} \frac{1 + 3M_{Ac}}{1 + M_{Ac}} \right) \delta \right] \quad . \end{aligned} \tag{6.58}$$

After having established all necessary auxiliary linearizations, it is now possible to write the coefficients of the linearized momentum equation, defined in Appendix A. They are (cf. Eq. (A.1))

$$\begin{aligned} b = -\frac{A T_c}{V_c^2} \left. \frac{\mathrm{d}\tau}{\mathrm{d}a} \right|_c - \frac{1}{16\pi V_c^2 \rho_c} \frac{1 + 3M_{Ac}}{1 + M_{Ac}} \frac{\langle \delta B^2 \rangle_c^2}{\langle \delta B^2 \rangle_{1c}} \left[-\frac{8 \langle \delta B^2 \rangle_c}{\langle \delta B^2 \rangle_{Bc}} + \right. \\ \left. + \frac{3M_{Ac}}{1 + 3M_{Ac}} - 2 \frac{\langle \delta B^2 \rangle_c}{\langle \delta B^2 \rangle_{1c}} \frac{1 + 3M_{Ac}}{1 + M_{Ac}} + \frac{3 + 4M_{Ac}}{1 + M_{Ac}} \right] \end{aligned} \tag{6.59}$$

$$\begin{aligned} c = 1 - \frac{1}{8\pi V_c^2 \rho_c} \frac{1 + 3M_{Ac}}{1 + M_{Ac}} \frac{\langle \delta B^2 \rangle_c^2}{\langle \delta B^2 \rangle_{1c}} \times \\ \times \left[\frac{3M_{Ac}}{1 + 3M_{Ac}} - 2 \frac{\langle \delta B^2 \rangle_c}{\langle \delta B^2 \rangle_{1c}} \frac{1 + 3M_{Ac}}{1 + M_{Ac}} + \frac{3 + 4M_{Ac}}{1 + M_{Ac}} \right] \end{aligned} \tag{6.60}$$

$$e = 2\left\{2\frac{AT_\mathrm{c}}{V_\mathrm{c}^2}\left.\frac{\mathrm{d}\tau}{\mathrm{d}a}\right|_\mathrm{c} + \frac{1}{16\pi V_\mathrm{c}^2\rho_\mathrm{c}}\frac{1+3M_\mathrm{Ac}}{1+M_\mathrm{Ac}}\frac{\langle\delta B^2\rangle_\mathrm{c}^2}{\langle\delta B^2\rangle_\mathrm{1c}}\left[-\frac{8\langle\delta B^2\rangle_\mathrm{c}}{\langle\delta B^2\rangle_\mathrm{Bc}} + \right.\right.$$
$$\left. + \frac{3M_\mathrm{Ac}}{1+3M_\mathrm{Ac}} - 2\frac{\langle\delta B^2\rangle_\mathrm{c}}{\langle\delta B^2\rangle_\mathrm{1c}}\frac{1+3M_\mathrm{Ac}}{1+M_\mathrm{Ac}} + \frac{3+4M_\mathrm{Ac}}{1+M_\mathrm{Ac}}\right] +$$
$$\left. + \frac{1}{4\pi V_\mathrm{c}^2\rho_\mathrm{c}}\frac{\langle\delta B^2\rangle_\mathrm{c}^2}{\langle\delta B^2\rangle_\mathrm{Bc}}\left(5 - \frac{8\langle\delta B^2\rangle_\mathrm{c}}{\langle\delta B^2\rangle_\mathrm{Bc}} - 2\frac{\langle\delta B^2\rangle_\mathrm{c}}{\langle\delta B^2\rangle_\mathrm{1c}}\frac{1+3M_\mathrm{Ac}}{1+M_\mathrm{Ac}}\right) - 1 + \frac{GM}{R_\mathrm{c}V_\mathrm{c}^2}\right\}$$
$$+ \frac{AT_\mathrm{c}}{V_\mathrm{c}^2}\left.\frac{\mathrm{d}\tau}{\mathrm{d}a}\right|_\mathrm{c}\left(\frac{5}{2}\left.\frac{\mathrm{d}\tau}{\mathrm{d}a}\right|_\mathrm{c} - \left.\frac{\partial\phi}{\partial a}\right|_\mathrm{c}\right) \tag{6.61}$$

$$f = \frac{1}{16\pi V_\mathrm{c}^2\rho_\mathrm{c}}\frac{1+3M_\mathrm{Ac}}{1+M_\mathrm{Ac}}\frac{\langle\delta B^2\rangle_\mathrm{c}^2}{\langle\delta B^2\rangle_\mathrm{1c}}\left[\frac{3M_\mathrm{Ac}}{1+3M_\mathrm{Ac}} - 2\frac{\langle\delta B^2\rangle_\mathrm{c}}{\langle\delta B^2\rangle_\mathrm{1c}}\frac{1+3M_\mathrm{Ac}}{1+M_\mathrm{Ac}} + \frac{3+4M_\mathrm{Ac}}{1+M_\mathrm{Ac}}\right]$$
$$+ \frac{1}{2\pi V_\mathrm{c}^2\rho_\mathrm{c}}\frac{\langle\delta B^2\rangle_\mathrm{c}^2}{\langle\delta B^2\rangle_\mathrm{Bc}}\left(1 - 2\frac{\langle\delta B^2\rangle_\mathrm{c}}{\langle\delta B^2\rangle_\mathrm{1c}}\frac{1+3M_\mathrm{Ac}}{1+M_\mathrm{Ac}}\right) - \frac{AT_\mathrm{c}}{V_\mathrm{c}^2}\left.\frac{\mathrm{d}\tau}{\mathrm{d}a}\right|_\mathrm{c}\left.\frac{\partial\phi}{\partial u}\right|_\mathrm{c} \quad . \tag{6.62}$$

With these coefficients it is now possible to obtain the two derivatives of the velocity at the critical point:

$$\left.\frac{\mathrm{d}u}{\mathrm{d}a}\right|_\mathrm{c} = \frac{\lambda_\pm - b}{c} = \frac{e}{\lambda_\pm - f} \qquad \text{, where} \qquad \lambda_\pm = \frac{b+f \pm \sqrt{(b-f)^2+4ce}}{2} \quad . \tag{6.63}$$

The positive derivative corresponds to the wind solution, and is thus retained, while the negative derivative corresponds to the accretion solution, and is therefore discarded. The first derivatives of u, τ and ϕ at the critical point are all known, and are given by Eqs. (6.63), (6.43) and by the sum of the two partial derivatives ((6.50) + (6.51)), respectively.

6.3.3 Second derivatives

To increase the precision of the analytical approximation near the critical point a Taylor series expansion of second order was used. The first derivatives were already computed, this Section deals with the second derivatives.

To obtain the second derivative of the velocity it is necessary to derive the momentum equation, which results in long expressions for the derivatives. Consequently, each of the derivatives occupies its own page. The first derivatives of the momentum equation are shown in Eqs. (6.64) and (6.66), respectively, and it is evident that the coefficient of the second derivative of u in Eq. (6.64) vanishes at the critical point. Therefore it is necessary to obtain the second derivatives of the momentum equation shown in Eqs. (6.65) and (6.67). At the critical point the second derivatives simplify to the expressions shown in Eqs. (6.68) and (6.69).

$$\frac{\mathrm{d}}{\mathrm{d}a}\left[\mathbf{left}\right] = \frac{1}{u}\left(u^2 - \frac{AT_\mathrm{c}}{V_\mathrm{c}^2}\tau - \frac{1}{16\pi V_\mathrm{c}^2\rho}\frac{1+3M_\mathrm{A}}{1+M_\mathrm{A}}\frac{\langle\delta B^2\rangle^2}{\langle\delta B^2\rangle_1}\right)\left[\frac{\mathrm{d}^2u}{\mathrm{d}a^2} - \frac{1}{u}\left(\frac{\mathrm{d}u}{\mathrm{d}a}\right)^2\right]$$
$$+ \frac{1}{u}\frac{\mathrm{d}u}{\mathrm{d}a}\left\{2u\frac{\mathrm{d}u}{\mathrm{d}a} - \frac{AT_\mathrm{c}}{V_\mathrm{c}^2}\frac{\mathrm{d}\tau}{\mathrm{d}a}\right.$$
$$\left. - \frac{1}{16\pi V_\mathrm{c}^2\rho}\frac{\langle\delta B^2\rangle^2}{\langle\delta B^2\rangle_1(1+M_\mathrm{A})}\left[(1+3M_\mathrm{A})\left(2\frac{\mathrm{d}\ln\left(\langle\delta B^2\rangle\right)}{\mathrm{d}a} - \frac{\mathrm{d}\ln\left(\langle\delta B^2\rangle_1\right)}{\mathrm{d}a}\right) - \frac{1+5M_\mathrm{A}+3M_\mathrm{A}^2}{1+M_\mathrm{A}}\frac{\mathrm{d}\ln(\rho)}{\mathrm{d}a}\right]\right\} \quad (6.64)$$

$$\frac{\mathrm{d}^2}{\mathrm{d}a^2}\left[\mathbf{left}\right] = \frac{1}{u}\left(u^2 - \frac{AT_\mathrm{c}}{V_\mathrm{c}^2}\tau - \frac{1}{16\pi V_\mathrm{c}^2\rho}\frac{1+3M_\mathrm{A}}{1+M_\mathrm{A}}\frac{\langle\delta B^2\rangle^2}{\langle\delta B^2\rangle_1}\right)\left[\frac{\mathrm{d}^3u}{\mathrm{d}a^3} - \frac{3}{u}\frac{\mathrm{d}u}{\mathrm{d}a}\frac{\mathrm{d}^2u}{\mathrm{d}a^2} + \frac{2}{u^2}\left(\frac{\mathrm{d}u}{\mathrm{d}a}\right)^3\right]$$
$$+ \frac{2}{u}\left[\frac{\mathrm{d}^2u}{\mathrm{d}a^2} - \frac{1}{u}\left(\frac{\mathrm{d}u}{\mathrm{d}a}\right)^2\right]\left\{2u\frac{\mathrm{d}u}{\mathrm{d}a} - \frac{AT_\mathrm{c}}{V_\mathrm{c}^2}\frac{\mathrm{d}\tau}{\mathrm{d}a}\right.$$
$$\left. - \frac{1}{16\pi V_\mathrm{c}^2\rho}\frac{\langle\delta B^2\rangle^2}{\langle\delta B^2\rangle_1(1+M_\mathrm{A})}\left[(1+3M_\mathrm{A})\left(2\frac{\mathrm{d}\ln\left(\langle\delta B^2\rangle\right)}{\mathrm{d}a} - \frac{\mathrm{d}\ln\left(\langle\delta B^2\rangle_1\right)}{\mathrm{d}a}\right) - \frac{1+5M_\mathrm{A}+3M_\mathrm{A}^2}{1+M_\mathrm{A}}\frac{\mathrm{d}\ln(\rho)}{\mathrm{d}a}\right]\right\}$$
$$+ \frac{1}{u}\frac{\mathrm{d}u}{\mathrm{d}a}\left\{2\left(\frac{\mathrm{d}u}{\mathrm{d}a}\right)^2 + 2u\frac{\mathrm{d}^2u}{\mathrm{d}a^2} - \frac{AT_\mathrm{c}}{V_\mathrm{c}^2}\frac{\mathrm{d}^2\tau}{\mathrm{d}a^2}\right.$$
$$- \frac{1}{16\pi V_\mathrm{c}^2\rho}\frac{\langle\delta B^2\rangle^2}{\langle\delta B^2\rangle_1(1+M_\mathrm{A})}\left[\frac{M_\mathrm{A}(4+6M_\mathrm{A}+3M_\mathrm{A}^2)}{2(1+M_\mathrm{A})^2}\left(\frac{\mathrm{d}\ln}{\mathrm{d}a}(\rho)\right)^2 - \frac{1+5M_\mathrm{A}+3M_\mathrm{A}^2}{1+M_\mathrm{A}}\frac{\mathrm{d}^2\ln}{\mathrm{d}a^2}(\rho)\right.$$
$$\left. + \frac{3M_\mathrm{A}}{2}\frac{\mathrm{d}\ln}{\mathrm{d}a}(\rho)\left(\frac{\mathrm{d}\ln\left(\langle\delta B^2\rangle_1\right)}{\mathrm{d}a} - 2\frac{\mathrm{d}\ln\left(\langle\delta B^2\rangle\right)}{\mathrm{d}a}\right) + (1+3M_\mathrm{A})\left(2\frac{\mathrm{d}^2\ln\left(\langle\delta B^2\rangle\right)}{\mathrm{d}a^2} - \frac{\mathrm{d}^2\ln\left(\langle\delta B^2\rangle_1\right)}{\mathrm{d}a^2}\right)\right]$$
$$- \frac{1}{16\pi V_\mathrm{c}^2\rho}\frac{\langle\delta B^2\rangle^2}{\langle\delta B^2\rangle_1(1+M_\mathrm{A})}\left[(1+3M_\mathrm{A})\left(2\frac{\mathrm{d}\ln\left(\langle\delta B^2\rangle\right)}{\mathrm{d}a} - \frac{\mathrm{d}\ln\left(\langle\delta B^2\rangle_1\right)}{\mathrm{d}a}\right) - \frac{1+5M_\mathrm{A}+3M_\mathrm{A}^2}{1+M_\mathrm{A}}\frac{\mathrm{d}\ln}{\mathrm{d}a}(\rho)\right]\times$$
$$\left.\times\left(2\frac{\mathrm{d}\ln\left(\langle\delta B^2\rangle\right)}{\mathrm{d}a} - \frac{\mathrm{d}\ln\left(\langle\delta B^2\rangle_1\right)}{\mathrm{d}a} - \frac{2+M_\mathrm{A}}{2+2M_\mathrm{A}}\frac{\mathrm{d}\ln}{\mathrm{d}a}(\rho)\right)\right\} \quad (6.65)$$

$$\frac{\mathrm{d}}{\mathrm{d}a}[\mathbf{right}] = \frac{2}{a}\left\{\frac{AT_\mathrm{c}}{V_\mathrm{c}^2}\frac{\mathrm{d}\tau}{\mathrm{d}a} + \frac{1}{16\pi V_\mathrm{c}^2\rho}\frac{\langle\delta B^2\rangle^2}{\langle\delta B^2\rangle_1(1+M_\mathrm{A})}\left[(1+3M_\mathrm{A})\left(2\frac{\mathrm{d}\ln}{\mathrm{d}a}\left(\langle\delta B^2\rangle\right) - \frac{\mathrm{d}\ln}{\mathrm{d}a}\left(\langle\delta B^2\rangle_1\right)\right) - \frac{1+5M_\mathrm{A}+3M_\mathrm{A}^2}{1+M_\mathrm{A}}\frac{\mathrm{d}\ln}{\mathrm{d}a}(\rho)\right]\right.$$
$$\left. + \frac{1}{4\pi V_\mathrm{c}^2\rho}\frac{\langle\delta B^2\rangle^2}{\langle\delta B^2\rangle_\mathrm{B}}\left(2\frac{\mathrm{d}\ln}{\mathrm{d}a}\left(\langle\delta B^2\rangle\right) - \frac{\mathrm{d}\ln}{\mathrm{d}a}\left(\langle\delta B^2\rangle_\mathrm{B}\right) - \frac{\mathrm{d}\ln}{\mathrm{d}a}(\rho)\right)\right\}$$
$$- \frac{2}{a^2}\left(\frac{AT_\mathrm{c}}{V_\mathrm{c}^2}\tau + \frac{1}{16\pi V_\mathrm{c}^2\rho}\frac{1+3M_\mathrm{A}}{1+M_\mathrm{A}}\frac{\langle\delta B^2\rangle^2}{\langle\delta B^2\rangle_1} + \frac{1}{4\pi V_\mathrm{c}^2\rho}\frac{\langle\delta B^2\rangle^2}{\langle\delta B^2\rangle_\mathrm{B}}\right) - \frac{AT_\mathrm{c}}{V_\mathrm{c}^2}\frac{\mathrm{d}^2\tau}{\mathrm{d}a^2} + \frac{2GM}{R_\mathrm{c}V_\mathrm{c}^2a^3} \tag{6.66}$$

$$\frac{\mathrm{d}^2}{\mathrm{d}a^2}[\mathbf{right}] = \frac{2}{a}\left\{\frac{AT_\mathrm{c}}{V_\mathrm{c}^2}\frac{\mathrm{d}^2\tau}{\mathrm{d}a^2} + \frac{1}{16\pi V_\mathrm{c}^2\rho}\frac{\langle\delta B^2\rangle^2}{\langle\delta B^2\rangle_1(1+M_\mathrm{A})}\left[(1+3M_\mathrm{A})\left(2\frac{\mathrm{d}\ln}{\mathrm{d}a}\left(\langle\delta B^2\rangle\right) - \frac{\mathrm{d}\ln}{\mathrm{d}a}\left(\langle\delta B^2\rangle_1\right)\right) - \frac{1+5M_\mathrm{A}+3M_\mathrm{A}^2}{1+M_\mathrm{A}}\frac{\mathrm{d}\ln}{\mathrm{d}a}(\rho)\right]\times\right.$$
$$\left.\times\left(2\frac{\mathrm{d}\ln}{\mathrm{d}a}\left(\langle\delta B^2\rangle\right) - \frac{\mathrm{d}\ln}{\mathrm{d}a}\left(\langle\delta B^2\rangle_1\right) - \frac{2+M_\mathrm{A}}{2+2M_\mathrm{A}}\frac{\mathrm{d}\ln}{\mathrm{d}a}(\rho)\right)\right.$$
$$+ \frac{1}{16\pi V_\mathrm{c}^2\rho}\frac{\langle\delta B^2\rangle^2}{\langle\delta B^2\rangle_1(1+M_\mathrm{A})}\left[\frac{M_\mathrm{A}(4+6M_\mathrm{A}+3M_\mathrm{A}^2)}{2(1+M_\mathrm{A})^2}\left(\frac{\mathrm{d}\ln}{\mathrm{d}a}(\rho)\right)^2 - \frac{1+5M_\mathrm{A}+3M_\mathrm{A}^2}{1+M_\mathrm{A}}\frac{\mathrm{d}^2\ln}{\mathrm{d}a^2}(\rho)\right.$$
$$\left. + \frac{3M_\mathrm{A}}{2}\frac{\mathrm{d}\ln}{\mathrm{d}a}(\rho)\left(\frac{\mathrm{d}\ln}{\mathrm{d}a}\left(\langle\delta B^2\rangle_1\right) - 2\frac{\mathrm{d}\ln}{\mathrm{d}a}\left(\langle\delta B^2\rangle\right)\right) + (1+3M_\mathrm{A})\left(2\frac{\mathrm{d}^2\ln}{\mathrm{d}a^2}\left(\langle\delta B^2\rangle\right) - \frac{\mathrm{d}^2\ln}{\mathrm{d}a^2}\left(\langle\delta B^2\rangle_1\right)\right)\right]$$
$$\left. + \frac{1}{4\pi V_\mathrm{c}^2\rho}\frac{\langle\delta B^2\rangle^2}{\langle\delta B^2\rangle_\mathrm{B}}\left[\left(2\frac{\mathrm{d}\ln}{\mathrm{d}a}\left(\langle\delta B^2\rangle\right) - \frac{\mathrm{d}\ln}{\mathrm{d}a}\left(\langle\delta B^2\rangle_\mathrm{B}\right) - \frac{\mathrm{d}\ln}{\mathrm{d}a}(\rho)\right)^2 + 2\frac{\mathrm{d}^2\ln}{\mathrm{d}a^2}\left(\langle\delta B^2\rangle\right) - \frac{\mathrm{d}^2\ln}{\mathrm{d}a^2}\left(\langle\delta B^2\rangle_\mathrm{B}\right) - \frac{\mathrm{d}^2\ln}{\mathrm{d}a^2}(\rho)\right]\right\}$$
$$- \frac{4}{a^2}\left\{\frac{AT_\mathrm{c}}{V_\mathrm{c}^2}\frac{\mathrm{d}\tau}{\mathrm{d}a} + \frac{1}{16\pi V_\mathrm{c}^2\rho}\frac{\langle\delta B^2\rangle^2}{\langle\delta B^2\rangle_1(1+M_\mathrm{A})}\left[(1+3M_\mathrm{A})\left(2\frac{\mathrm{d}\ln}{\mathrm{d}a}\left(\langle\delta B^2\rangle\right) - \frac{\mathrm{d}\ln}{\mathrm{d}a}\left(\langle\delta B^2\rangle_1\right)\right) - \frac{1+5M_\mathrm{A}+3M_\mathrm{A}^2}{1+M_\mathrm{A}}\frac{\mathrm{d}\ln}{\mathrm{d}a}(\rho)\right]\right.$$
$$\left. + \frac{1}{4\pi V_\mathrm{c}^2\rho}\frac{\langle\delta B^2\rangle^2}{\langle\delta B^2\rangle_\mathrm{B}}\left(2\frac{\mathrm{d}\ln}{\mathrm{d}a}\left(\langle\delta B^2\rangle\right) - \frac{\mathrm{d}\ln}{\mathrm{d}a}\left(\langle\delta B^2\rangle_\mathrm{B}\right) - \frac{\mathrm{d}\ln}{\mathrm{d}a}(\rho)\right)\right\}$$
$$+ \frac{4}{a^3}\left(\frac{AT_\mathrm{c}}{V_\mathrm{c}^2}\tau + \frac{1}{16\pi V_\mathrm{c}^2\rho}\frac{1+3M_\mathrm{A}}{1+M_\mathrm{A}}\frac{\langle\delta B^2\rangle^2}{\langle\delta B^2\rangle_1} + \frac{1}{4\pi V_\mathrm{c}^2\rho}\frac{\langle\delta B^2\rangle^2}{\langle\delta B^2\rangle_\mathrm{B}}\right) - \frac{AT_\mathrm{c}}{V_\mathrm{c}^2}\frac{\mathrm{d}^3\tau}{\mathrm{d}a^3} - \frac{6GM}{R_\mathrm{c}V_\mathrm{c}^2a^4} \tag{6.67}$$

$$
\begin{aligned}
\frac{\mathrm{d}^2}{\mathrm{d}a^2}\left[\mathbf{left}\right]\Big|_{\mathrm{c}} = {} & 2\left[\frac{\mathrm{d}^2u}{\mathrm{d}a^2}\Big|_{\mathrm{c}} - \left(\frac{\mathrm{d}u}{\mathrm{d}a}\Big|_{\mathrm{c}}\right)^2\right]\left\{2\,\frac{\mathrm{d}u}{\mathrm{d}a}\Big|_{\mathrm{c}} - \frac{AT_{\mathrm{c}}}{V_{\mathrm{c}}^2}\,\frac{\mathrm{d}\tau}{\mathrm{d}a}\Big|_{\mathrm{c}} - \frac{1}{16\pi V_{\mathrm{c}}^2\rho_{\mathrm{c}}}\frac{\langle\delta B^2\rangle_{\mathrm{c}}^2}{\langle\delta B^2\rangle_{1\mathrm{c}}(1+M_{\mathrm{Ac}})}\times\right.\\
& \left.\times\left[(1+3M_{\mathrm{Ac}})\left(2\,\frac{\mathrm{d}\ln\left(\langle\delta B^2\rangle\right)}{\mathrm{d}a}\Big|_{\mathrm{c}} - \frac{\mathrm{d}\ln\left(\langle\delta B^2\rangle_1\right)}{\mathrm{d}a}\Big|_{\mathrm{c}}\right) - \frac{1+5M_{\mathrm{Ac}}+3M_{\mathrm{Ac}}^2}{1+M_{\mathrm{Ac}}}\,\frac{\mathrm{d}\ln}{\mathrm{d}a}(\rho)\Big|_{\mathrm{c}}\right]\right\}\\
& + \frac{\mathrm{d}u}{\mathrm{d}a}\Big|_{\mathrm{c}}\left\{2\left(\frac{\mathrm{d}u}{\mathrm{d}a}\Big|_{\mathrm{c}}\right)^2 + 2\,\frac{\mathrm{d}^2u}{\mathrm{d}a^2}\Big|_{\mathrm{c}} - \frac{AT_{\mathrm{c}}}{V_{\mathrm{c}}^2}\,\frac{\mathrm{d}^2\tau}{\mathrm{d}a^2}\Big|_{\mathrm{c}}\right.\\
& \quad - \frac{1}{16\pi V_{\mathrm{c}}^2\rho_{\mathrm{c}}}\frac{\langle\delta B^2\rangle_{\mathrm{c}}^2}{\langle\delta B^2\rangle_{1\mathrm{c}}(1+M_{\mathrm{Ac}})}\left(2\frac{\mathrm{d}\ln\left(\langle\delta B^2\rangle\right)}{\mathrm{d}a}\Big|_{\mathrm{c}} - \frac{\mathrm{d}\ln\left(\langle\delta B^2\rangle_1\right)}{\mathrm{d}a}\Big|_{\mathrm{c}} - \frac{2+M_{\mathrm{Ac}}}{2+2M_{\mathrm{Ac}}}\,\frac{\mathrm{d}\ln}{\mathrm{d}a}(\rho)\Big|_{\mathrm{c}}\right)\times\\
& \qquad \times\left[(1+3M_{\mathrm{Ac}})\left(2\,\frac{\mathrm{d}\ln\left(\langle\delta B^2\rangle\right)}{\mathrm{d}a}\Big|_{\mathrm{c}} - \frac{\mathrm{d}\ln\left(\langle\delta B^2\rangle_1\right)}{\mathrm{d}a}\Big|_{\mathrm{c}}\right) - \frac{1+5M_{\mathrm{Ac}}+3M_{\mathrm{Ac}}^2}{1+M_{\mathrm{Ac}}}\,\frac{\mathrm{d}\ln}{\mathrm{d}a}(\rho)\Big|_{\mathrm{c}}\right]\\
& \quad - \frac{1}{16\pi V_{\mathrm{c}}^2\rho_{\mathrm{c}}}\frac{\langle\delta B^2\rangle_{\mathrm{c}}^2}{\langle\delta B^2\rangle_{1\mathrm{c}}(1+M_{\mathrm{Ac}})}\left[\frac{M_{\mathrm{Ac}}(4+6M_{\mathrm{Ac}}+3M_{\mathrm{Ac}}^2)}{2(1+M_{\mathrm{Ac}})^2}\left(\frac{\mathrm{d}\ln}{\mathrm{d}a}(\rho)\Big|_{\mathrm{c}}\right)^2 - \frac{1+5M_{\mathrm{Ac}}+3M_{\mathrm{Ac}}^2}{1+M_{\mathrm{Ac}}}\,\frac{\mathrm{d}^2\ln}{\mathrm{d}a^2}(\rho)\Big|_{\mathrm{c}}\right.\\
& \qquad + \frac{3M_{\mathrm{Ac}}}{2}\,\frac{\mathrm{d}\ln}{\mathrm{d}a}(\rho)\Big|_{\mathrm{c}}\left(\frac{\mathrm{d}\ln\left(\langle\delta B^2\rangle_1\right)}{\mathrm{d}a}\Big|_{\mathrm{c}} - 2\,\frac{\mathrm{d}\ln\left(\langle\delta B^2\rangle\right)}{\mathrm{d}a}\Big|_{\mathrm{c}}\right)\\
& \qquad \left.\left. + (1+3M_{\mathrm{Ac}})\left(2\,\frac{\mathrm{d}^2\ln\left(\langle\delta B^2\rangle\right)}{\mathrm{d}a^2}\Big|_{\mathrm{c}} - \frac{\mathrm{d}^2\ln\left(\langle\delta B^2\rangle_1\right)}{\mathrm{d}a^2}\Big|_{\mathrm{c}}\right)\right]\right\}
\end{aligned}
\tag{6.68}
$$

$$
\begin{aligned}
\frac{\mathrm{d}^2}{\mathrm{d}a^2}\,[\mathbf{right}]\bigg|_{\mathrm{c}} = 2\Bigg\{ & \frac{AT_{\mathrm{c}}}{V_{\mathrm{c}}^2}\,\frac{\mathrm{d}^2\tau}{\mathrm{d}a^2}\bigg|_{\mathrm{c}} + \frac{1}{16\pi V_{\mathrm{c}}^2\rho_{\mathrm{c}}}\frac{\langle\delta B^2\rangle_{\mathrm{c}}^2}{\langle\delta B^2\rangle_{1\mathrm{c}}(1+M_{\mathrm{Ac}})}\left(2\,\frac{\mathrm{d}\ln\left(\langle\delta B^2\rangle\right)}{\mathrm{d}a}\bigg|_{\mathrm{c}} - \frac{\mathrm{d}\ln\left(\langle\delta B^2\rangle_1\right)}{\mathrm{d}a}\bigg|_{\mathrm{c}} - \frac{2+M_{\mathrm{Ac}}}{2+2M_{\mathrm{Ac}}}\,\frac{\mathrm{d}\ln(\rho)}{\mathrm{d}a}\bigg|_{\mathrm{c}}\right)\times \\
& \times\left[(1+3M_{\mathrm{Ac}})\left(2\,\frac{\mathrm{d}\ln\left(\langle\delta B^2\rangle\right)}{\mathrm{d}a}\bigg|_{\mathrm{c}} - \frac{\mathrm{d}\ln\left(\langle\delta B^2\rangle_1\right)}{\mathrm{d}a}\bigg|_{\mathrm{c}}\right) - \frac{1+5M_{\mathrm{Ac}}+3M_{\mathrm{Ac}}^2}{1+M_{\mathrm{Ac}}}\,\frac{\mathrm{d}\ln(\rho)}{\mathrm{d}a}\bigg|_{\mathrm{c}}\right] \\
& + \frac{1}{16\pi V_{\mathrm{c}}^2\rho_{\mathrm{c}}}\frac{\langle\delta B^2\rangle_{\mathrm{c}}^2}{\langle\delta B^2\rangle_{1\mathrm{c}}(1+M_{\mathrm{Ac}})}\left[\frac{M_{\mathrm{Ac}}(4+6M_{\mathrm{Ac}}+3M_{\mathrm{Ac}}^2)}{2(1+M_{\mathrm{Ac}})^2}\left(\frac{\mathrm{d}\ln(\rho)}{\mathrm{d}a}\bigg|_{\mathrm{c}}\right)^2 - \frac{1+5M_{\mathrm{Ac}}+3M_{\mathrm{Ac}}^2}{1+M_{\mathrm{Ac}}}\,\frac{\mathrm{d}^2\ln(\rho)}{\mathrm{d}a^2}\bigg|_{\mathrm{c}}\right. \\
& \quad + \frac{3M_{\mathrm{Ac}}}{2}\,\frac{\mathrm{d}\ln(\rho)}{\mathrm{d}a}\bigg|_{\mathrm{c}}\left(\frac{\mathrm{d}\ln\left(\langle\delta B^2\rangle_1\right)}{\mathrm{d}a}\bigg|_{\mathrm{c}} - 2\,\frac{\mathrm{d}\ln\left(\langle\delta B^2\rangle\right)}{\mathrm{d}a}\bigg|_{\mathrm{c}}\right) \\
& \quad \left. + (1+3M_{\mathrm{Ac}})\left(2\,\frac{\mathrm{d}^2\ln\left(\langle\delta B^2\rangle\right)}{\mathrm{d}a^2}\bigg|_{\mathrm{c}} - \frac{\mathrm{d}^2\ln\left(\langle\delta B^2\rangle_1\right)}{\mathrm{d}a^2}\bigg|_{\mathrm{c}}\right)\right] \\
& + \frac{1}{4\pi V_{\mathrm{c}}^2\rho_{\mathrm{c}}}\frac{\langle\delta B^2\rangle_{\mathrm{c}}^2}{\langle\delta B^2\rangle_{\mathrm{Bc}}}\left[\left(2\,\frac{\mathrm{d}\ln\left(\langle\delta B^2\rangle\right)}{\mathrm{d}a}\bigg|_{\mathrm{c}} - \frac{\mathrm{d}\ln\left(\langle\delta B^2\rangle_{\mathrm{B}}\right)}{\mathrm{d}a}\bigg|_{\mathrm{c}} - \frac{\mathrm{d}\ln(\rho)}{\mathrm{d}a}\bigg|_{\mathrm{c}}\right)^2\right. \\
& \quad \left. + 2\,\frac{\mathrm{d}^2\ln\left(\langle\delta B^2\rangle\right)}{\mathrm{d}a^2}\bigg|_{\mathrm{c}} - \frac{\mathrm{d}^2\ln\left(\langle\delta B^2\rangle_{\mathrm{B}}\right)}{\mathrm{d}a^2}\bigg|_{\mathrm{c}} - \frac{\mathrm{d}^2\ln(\rho)}{\mathrm{d}a^2}\bigg|_{\mathrm{c}}\right]\Bigg\} \\
- 4\Bigg\{ & \frac{AT_{\mathrm{c}}}{V_{\mathrm{c}}^2}\,\frac{\mathrm{d}\tau}{\mathrm{d}a}\bigg|_{\mathrm{c}} + \frac{1}{16\pi V_{\mathrm{c}}^2\rho_{\mathrm{c}}}\frac{\langle\delta B^2\rangle_{\mathrm{c}}^2}{\langle\delta B^2\rangle_{1\mathrm{c}}(1+M_{\mathrm{Ac}})}\times \\
& \times\left[(1+3M_{\mathrm{Ac}})\left(2\,\frac{\mathrm{d}\ln\left(\langle\delta B^2\rangle\right)}{\mathrm{d}a}\bigg|_{\mathrm{c}} - \frac{\mathrm{d}\ln\left(\langle\delta B^2\rangle_1\right)}{\mathrm{d}a}\bigg|_{\mathrm{c}}\right) - \frac{1+5M_{\mathrm{Ac}}+3M_{\mathrm{Ac}}^2}{1+M_{\mathrm{Ac}}}\,\frac{\mathrm{d}\ln(\rho)}{\mathrm{d}a}\bigg|_{\mathrm{c}}\right] \\
& + \frac{1}{4\pi V_{\mathrm{c}}^2\rho_{\mathrm{c}}}\frac{\langle\delta B^2\rangle_{\mathrm{c}}^2}{\langle\delta B^2\rangle_{\mathrm{Bc}}}\left(2\,\frac{\mathrm{d}\ln\left(\langle\delta B^2\rangle\right)}{\mathrm{d}a}\bigg|_{\mathrm{c}} - \frac{\mathrm{d}\ln\left(\langle\delta B^2\rangle_{\mathrm{B}}\right)}{\mathrm{d}a}\bigg|_{\mathrm{c}} - \frac{\mathrm{d}\ln(\rho)}{\mathrm{d}a}\bigg|_{\mathrm{c}}\right)\Bigg\} \\
& + \frac{AT_{\mathrm{c}}}{V_{\mathrm{c}}^2}\left(\frac{\mathrm{d}\tau}{\mathrm{d}a}\bigg|_{\mathrm{c}} - \frac{\mathrm{d}^3\tau}{\mathrm{d}a^3}\bigg|_{\mathrm{c}}\right) - \frac{4GM}{R_{\mathrm{c}}V_{\mathrm{c}}^2}
\end{aligned}
\tag{6.69}
$$

The auxiliary derivatives are:

$$\frac{\mathrm{d}\ln(\rho)}{\mathrm{d}a} = -\frac{2}{a} - \frac{1}{u}\frac{\mathrm{d}u}{\mathrm{d}a} \tag{6.70}$$

$$\frac{\mathrm{d}^2\ln(\rho)}{\mathrm{d}a^2} = \frac{2}{a^2} + \frac{1}{u^2}\left(\frac{\mathrm{d}u}{\mathrm{d}a}\right)^2 - \frac{1}{u}\frac{\mathrm{d}^2u}{\mathrm{d}a^2} \tag{6.71}$$

$$\frac{\mathrm{d}\ln\left(\langle\delta B^2\rangle_1\right)}{\mathrm{d}a} = \frac{1+3M_\mathrm{A}}{2(1+M_\mathrm{A})}\frac{\mathrm{d}\ln(\rho)}{\mathrm{d}a} \tag{6.72}$$

$$\frac{\mathrm{d}^2\ln\left(\langle\delta B^2\rangle_1\right)}{\mathrm{d}a^2} = \frac{1}{2(1+M_\mathrm{A})}\left[\frac{\mathrm{d}^2\ln(\rho)}{\mathrm{d}a^2} - \frac{M_\mathrm{A}}{1+M_\mathrm{A}}\left(\frac{\mathrm{d}\ln(\rho)}{\mathrm{d}a}\right)\right] \tag{6.73}$$

$$\frac{\mathrm{d}\ln\left(\langle\delta B^2\rangle_\mathrm{B}\right)}{\mathrm{d}a} = -\frac{4}{a} \tag{6.74}$$

$$\frac{\mathrm{d}^2\ln\left(\langle\delta B^2\rangle_\mathrm{B}\right)}{\mathrm{d}a^2} = \frac{4}{a^2} \tag{6.75}$$

$$\frac{\mathrm{d}\ln\left(\langle\delta B^2\rangle\right)}{\mathrm{d}a} = \frac{\langle\delta B^2\rangle}{\langle\delta B^2\rangle_1}\frac{\mathrm{d}\ln\left(\langle\delta B^2\rangle_1\right)}{\mathrm{d}a} + \frac{\langle\delta B^2\rangle}{\langle\delta B^2\rangle_\mathrm{B}}\frac{\mathrm{d}\ln\left(\langle\delta B^2\rangle_\mathrm{B}\right)}{\mathrm{d}a} \tag{6.76}$$

$$\begin{aligned}\frac{\mathrm{d}^2\ln\left(\langle\delta B^2\rangle\right)}{\mathrm{d}a^2} = {} & \left(\frac{\mathrm{d}\ln\left(\langle\delta B^2\rangle\right)}{\mathrm{d}a}\right)^2 + \frac{\langle\delta B^2\rangle}{\langle\delta B^2\rangle_1}\frac{\mathrm{d}^2\ln\left(\langle\delta B^2\rangle_1\right)}{\mathrm{d}a^2} + \frac{\langle\delta B^2\rangle}{\langle\delta B^2\rangle_\mathrm{B}}\frac{\mathrm{d}^2\ln\left(\langle\delta B^2\rangle_\mathrm{B}\right)}{\mathrm{d}a^2} \\ & - \frac{\langle\delta B^2\rangle}{\langle\delta B^2\rangle_1}\left(\frac{\mathrm{d}\ln\left(\langle\delta B^2\rangle_1\right)}{\mathrm{d}a}\right)^2 - \frac{\langle\delta B^2\rangle}{\langle\delta B^2\rangle_\mathrm{B}}\left(\frac{\mathrm{d}\ln\left(\langle\delta B^2\rangle_\mathrm{B}\right)}{\mathrm{d}a}\right)^2\end{aligned} \tag{6.77}$$

The second derivative of τ is

$$\frac{\mathrm{d}^2\tau}{\mathrm{d}a^2} = \frac{F_\mathrm{c}}{\kappa_0 R_\mathrm{c} T_\mathrm{c}^{7/2}}\frac{1}{a^2\tau^{5/2}}\left(\frac{\mathrm{d}\phi}{\mathrm{d}a} - 2\frac{\phi}{a} - \frac{5\phi}{2\tau}\frac{\mathrm{d}\tau}{\mathrm{d}a}\right) = \frac{\mathrm{d}\tau}{\mathrm{d}a}\left(\frac{\mathrm{d}\ln(\phi)}{\mathrm{d}a} - \frac{2}{a} - \frac{5}{2}\frac{\mathrm{d}\ln(\tau)}{\mathrm{d}a}\right) \tag{6.78}$$

simplifying to

$$\left.\frac{\mathrm{d}^2\tau}{\mathrm{d}a^2}\right|_\mathrm{c} = \left.\frac{\mathrm{d}\tau}{\mathrm{d}a}\right|_\mathrm{c}\left(\left.\frac{\mathrm{d}\phi}{\mathrm{d}a}\right|_\mathrm{c} - 2 - \frac{5}{2}\left.\frac{\mathrm{d}\tau}{\mathrm{d}a}\right|_\mathrm{c}\right) \quad , \tag{6.79}$$

at the critical point.

$$\begin{aligned}\frac{\mathrm{d}^2\phi}{\mathrm{d}a^2} = &-\left(\frac{AT_cZ}{F_c}\tau + \frac{Z}{8\pi F_c\rho}\frac{1+3M_A}{M_A}\frac{\langle\delta B^2\rangle}{\langle\delta B^2\rangle_1}\left(\langle\delta B^2\rangle_1 - \langle\delta B^2\rangle\right)\right)\frac{\mathrm{d}^2\ln}{\mathrm{d}a^2}(\rho)\\
&+\frac{\mathrm{d}\ln}{\mathrm{d}a}(\rho)\left\{\frac{AT_cZ}{F_c}\frac{\mathrm{d}\tau}{\mathrm{d}a} + \frac{Z}{8\pi F_c\rho M_A}\left[(1+3M_A)\left(\langle\delta B^2\rangle_1 - \langle\delta B^2\rangle\right)\left(\frac{\mathrm{d}\ln\left(\langle\delta B^2\rangle\right)}{\mathrm{d}a} - \frac{\mathrm{d}\ln\left(\langle\delta B^2\rangle_1\right)}{\mathrm{d}a}\right)\right.\right.\\
&\qquad\left.\left.+(1+3M_A)\left(\frac{\mathrm{d}\langle\delta B^2\rangle_1}{\mathrm{d}a} - \frac{\mathrm{d}\langle\delta B^2\rangle}{\mathrm{d}a}\right) - \frac{1+6M_A}{2}\left(\langle\delta B^2\rangle_1 - \langle\delta B^2\rangle\right)\frac{\mathrm{d}\ln}{\mathrm{d}a}(\rho)\right]\right\}\\
&-\frac{Z}{\pi F_c\rho a}\frac{\langle\delta B^2\rangle^2}{M_A\langle\delta B^2\rangle_B}\left[(1+M_A)\left(2\frac{\mathrm{d}\ln\left(\langle\delta B^2\rangle\right)}{\mathrm{d}a} - \frac{\mathrm{d}\ln\left(\langle\delta B^2\rangle_B\right)}{\mathrm{d}a} - \frac{1}{a}\right) - \frac{1+2M_A}{2}\frac{\mathrm{d}\ln}{\mathrm{d}a}(\rho)\right]\\
&+\frac{AT_cZ}{F_c(\gamma-1)}\frac{\mathrm{d}\tau}{\mathrm{d}a} + \left(\frac{Z}{\mu m_H}\right)^2\frac{\chi T^\alpha}{R_cV_c^2F_c}\left(\alpha\frac{\mathrm{d}\ln}{\mathrm{d}a}(\tau) - \frac{2}{a} - \frac{2}{u}\frac{\mathrm{d}u}{\mathrm{d}a}\right) - \frac{R_c^3h_0}{F_c}ae^{-\frac{R-R_\star}{\sigma}}\left(2 - \frac{R_ca}{\sigma}\right)\end{aligned} \tag{6.80}$$

$$\begin{aligned}\left.\frac{\mathrm{d}^2\phi}{\mathrm{d}a^2}\right|_c = &-\left(\frac{AT_cZ}{F_c} + \frac{Z}{8\pi F_c\rho_c}\frac{1+3M_{Ac}}{M_{Ac}}\frac{\langle\delta B^2\rangle_c}{\langle\delta B^2\rangle_{1c}}\left(\langle\delta B^2\rangle_{1c} - \langle\delta B^2\rangle_c\right)\right)\left.\frac{\mathrm{d}^2\ln}{\mathrm{d}a^2}(\rho)\right|_c\\
&+\left.\frac{\mathrm{d}\ln}{\mathrm{d}a}(\rho)\right|_c\left\{\left.\frac{AT_cZ}{F_c}\frac{\mathrm{d}\tau}{\mathrm{d}a}\right|_c + \frac{Z}{8\pi F_c\rho_cM_{Ac}}\left[(1+3M_{Ac})\left(\langle\delta B^2\rangle_{1c} - \langle\delta B^2\rangle_c\right)\left(\left.\frac{\mathrm{d}\ln\left(\langle\delta B^2\rangle\right)}{\mathrm{d}a}\right|_c - \left.\frac{\mathrm{d}\ln\left(\langle\delta B^2\rangle_1\right)}{\mathrm{d}a}\right|_c\right)\right.\right.\\
&\qquad\left.\left.+(1+3M_{Ac})\left(\left.\frac{\mathrm{d}\langle\delta B^2\rangle_1}{\mathrm{d}a}\right|_c - \left.\frac{\mathrm{d}\langle\delta B^2\rangle}{\mathrm{d}a}\right|_c\right) - \frac{1+6M_{Ac}}{2}\left(\langle\delta B^2\rangle_{1c} - \langle\delta B^2\rangle_c\right)\left.\frac{\mathrm{d}\ln}{\mathrm{d}a}(\rho)\right|_c\right]\right\}\\
&-\frac{Z}{\pi F_c\rho_c}\frac{\langle\delta B^2\rangle_c^2}{M_{Ac}\langle\delta B^2\rangle_{Bc}}\left[(1+M_{Ac})\left(2\left.\frac{\mathrm{d}\ln\left(\langle\delta B^2\rangle\right)}{\mathrm{d}a}\right|_c - \left.\frac{\mathrm{d}\ln\left(\langle\delta B^2\rangle_B\right)}{\mathrm{d}a}\right|_c - 1\right) - \frac{1+2M_{Ac}}{2}\left.\frac{\mathrm{d}\ln}{\mathrm{d}a}(\rho)\right|_c\right]\\
&+\frac{AT_cZ}{F_c(\gamma-1)}\left.\frac{\mathrm{d}\tau}{\mathrm{d}a}\right|_c + \left(\frac{Z}{\mu m_H}\right)^2\frac{\chi T_c^\alpha}{R_cV_c^2F_c}\left(\alpha\left.\frac{\mathrm{d}\ln}{\mathrm{d}a}(\tau)\right|_c - 2 - 2\left.\frac{\mathrm{d}u}{\mathrm{d}a}\right|_c\right) - \frac{R_c^3h_0}{F_c}e^{-\frac{R_c-R_\star}{\sigma}}\left(2 - \frac{R_c}{\sigma}\right)\end{aligned} \tag{6.81}$$

The third derivative of τ, used in the second derivative of ϕ, is

$$\frac{\mathrm{d}^3\tau}{\mathrm{d}a^3} = \frac{\mathrm{d}^2\tau}{\mathrm{d}a^2}\left(\frac{\mathrm{d}\ln}{\mathrm{d}a}(\phi) - \frac{2}{a} - \frac{5}{2}\frac{\mathrm{d}\ln}{\mathrm{d}a}(\tau)\right) + \frac{\mathrm{d}\tau}{\mathrm{d}a}\left(\frac{\mathrm{d}^2\ln}{\mathrm{d}a^2}(\phi) + \frac{2}{a^2} - \frac{5}{2}\frac{\mathrm{d}^2\ln}{\mathrm{d}a^2}(\tau)\right) \tag{6.82}$$

which, at the critical point, simplifies to

$$\left.\frac{\mathrm{d}^3\tau}{\mathrm{d}a^3}\right|_{\mathrm{c}} = \left.\frac{\mathrm{d}^2\tau}{\mathrm{d}a^2}\right|_{\mathrm{c}}\left(\left.\frac{\mathrm{d}\phi}{\mathrm{d}a}\right|_{\mathrm{c}} - 2 - \frac{5}{2}\left.\frac{\mathrm{d}\tau}{\mathrm{d}a}\right|_{\mathrm{c}}\right) + \left.\frac{\mathrm{d}\tau}{\mathrm{d}a}\right|_{\mathrm{c}}\left(\left.\frac{\mathrm{d}^2\ln}{\mathrm{d}a^2}(\phi)\right|_{\mathrm{c}} + 2 - \frac{5}{2}\left.\frac{\mathrm{d}^2\ln}{\mathrm{d}a^2}(\tau)\right|_{\mathrm{c}}\right) \tag{6.83}$$

As in the previous Chapter, to obtain the second derivative of the velocity at the critical point, it is necessary to separate all the equations into an a-part without explicit dependences on the second derivative of u, and an u-part with the explicit dependences on the second derivative of u. After having done this, Eqs. (6.68) and (6.69) are equated and $\mathrm{d}^2u/\mathrm{d}a^2|_{\mathrm{c}}$ is obtained. The equations used for these steps are not presented here in view of their large size, and because they will duplicate the equations already shown.

Having found the second derivative of u at the critical point, those for τ and ϕ are given by Eqs. (6.79) and (6.81), respectively, being therefore possible to make a second order Taylor's expansion around the critical point.

6.4 Method of solution

Two iterative methods of solution were used to reach convergence of the solution of the equations describing the stellar wind model developed in this Chapter (Eqs. (6.33) to (6.35)). The first was already used in the previous Chapter, the other is introduced here.

Method I:

1- fix the input parameters R_{c}, h_0, σ, n_0, $f_{\mathrm{w}0}$, B_0 and ε;

2- choose V_{c};

3- choose V_0 and compute $Z = R_\star^2 V_0 \rho_0$;

4- make a second order Taylor's expansion around the critical point and integrate the three equations simultaneously;

5– compute relative difference between actual and previous V_0:

- if convergence proceed;
- otherwise compute new Z and go to §4;

6– integrate towards infinity:

- if upward and downward diverging solutions have converged within numerical tolerance finish;
- otherwise choose new V_c accordingly and go to §4.

Method II:

1– fix the input parameters R_c, h_0, σ, n_0, V_0^{in}, B_0 and ε; compute $Z = R_\star^2 V_0^{in} \rho_0$;

2– fix the numerical tolerances tol_1 and tol_2, such that $tol_1 > tol_2$;

3– choose f_{w_0};

4– choose V_c;

5– make a second order Taylor's expansion around the critical point and integrate the three equations simultaneously;

6– compute relative difference between actual and previous V_0:

- if less than tol_2 proceed to §7;
- if less than tol_1 compute new Z and go to §5;
- if larger than tol_1 compare the value of actual and previous V_0 and select new value for V_c accordingly, set $V_0 = V_0^{in}$, compute new Z and go to §5;

7– integrate towards infinity:

- if upward and downward diverging solutions have converged within numerical tolerance finish;
- otherwise choose new f_{w_0} accordingly and go to §5.

6.5 First applications of this stellar wind model

Figure 6.1 shows the profiles of temperature, velocity, thermal conductivity flux and number density for three different wind models. In the Table shown in the caption of this and following Figures the vertical line separates the input parameters, on the left, from the output values, to the right. Represented by the solid lines is the wind model already shown in the previous Chapter, with the input parameters: $R_c = 4.0\,R_\star$, $V_c = 132.79867717\,\mathrm{km\,s^{-1}}$, $n_0 = 4.0 \times 10^7\,\mathrm{cm^{-3}}$, $h_0 = 1.239 \times 10^{-7}\,\mathrm{erg\,cm^{-3}\,s^{-1}}$ and $\sigma = 0.80\,R_\star$. Two of the output values are: $V_0 = 2.20\,\mathrm{km\,s^{-1}}$ and $T_0 = 1.04 \times 10^6\,\mathrm{K}$. The other two wind models have also the addition of some Alfvén wave flux at the base. The model displayed by the dotted lines has $f_{w_0} = 10.0\,\mathrm{erg\,cm^{-2}\,s^{-1}}$, $B_0 = 2.0\,\mathrm{G}$, $\varepsilon = 0.5$, $V_c = 132.92\,\mathrm{km\,s^{-1}}$, while the other input quantities conserve their values. The values of V_0 and T_0 are $1.93\,\mathrm{km\,s^{-1}}$ and $9.88{\times}10^5\,\mathrm{K}$, respectively. The velocity and temperature increase at large distances from the star, and decrease near the stellar surface, as wanted. Nevertheless, a further increase in the amount of the wave energy flux at the base leads to the known problem of too much energy for the wind, and consequent existence of only downward solutions, as exemplified by the model with dashed lines. This model has $f_{w_0} = 11.0\,\mathrm{erg\,cm^{-2}\,s^{-1}}$, $V_c \approx 133\,\mathrm{km\,s^{-1}}$, and the other input quantities have the same values as in the dotted model. The values of V_0 and T_0 are $1.88\,\mathrm{km\,s^{-1}}$ and $9.80{\times}10^5\,\mathrm{K}$, respectively.

From the study of these examples it is seen that the addition of a wave energy flux at the base of the wind has some benefits to improve the solutions of the wind models. Even with the very low input of $f_{w_0} = 10.0\,\mathrm{erg\,cm^{-2}\,s^{-1}}$ the temperature at the base of the wind decreases, and so does the velocity, while the velocity far from the star increases. The overall effect is a faster acceleration of the wind. However, with these values of the input parameters the plasma attains a velocity of $300\,\mathrm{km\,s^{-1}}$ at $25\,R_\star$, which is too far from the star.

In the models presented in Fig. 6.1 the main driving mechanism is the mechanical energy input. In order the Alfvén waves to play a more important role, the value of h_0 has to decrease, as discussed in Fig. 6.2 which presents some wind models.

When $h_0 = 1.235 \times 10^{-7}\,\mathrm{erg\,cm^{-3}\,s^{-1}}$ the wind model with $f_{w_0} = 11.0\,\mathrm{erg\,cm^{-2}\,s^{-1}}$ has both upward and downward solutions, being therefore possible to drive the wind up to infinity. However the value of the temperature at the base has increased to $1.12{\times}10^6\,\mathrm{K}$, while the overall acceleration of the plasma has decreased. The smaller value of the mechanical heat input allows the use of higher values for the Alfvén wave energy flux. This is shown by the model displayed with dotted lines, where the value of f_{w_0} has been increased to $50.0\,\mathrm{erg\,cm^{-2}\,s^{-1}}$. With the value of h_0 equal to $1.235 \times 10^{-7}\,\mathrm{erg\,cm^{-3}\,s^{-1}}$ it

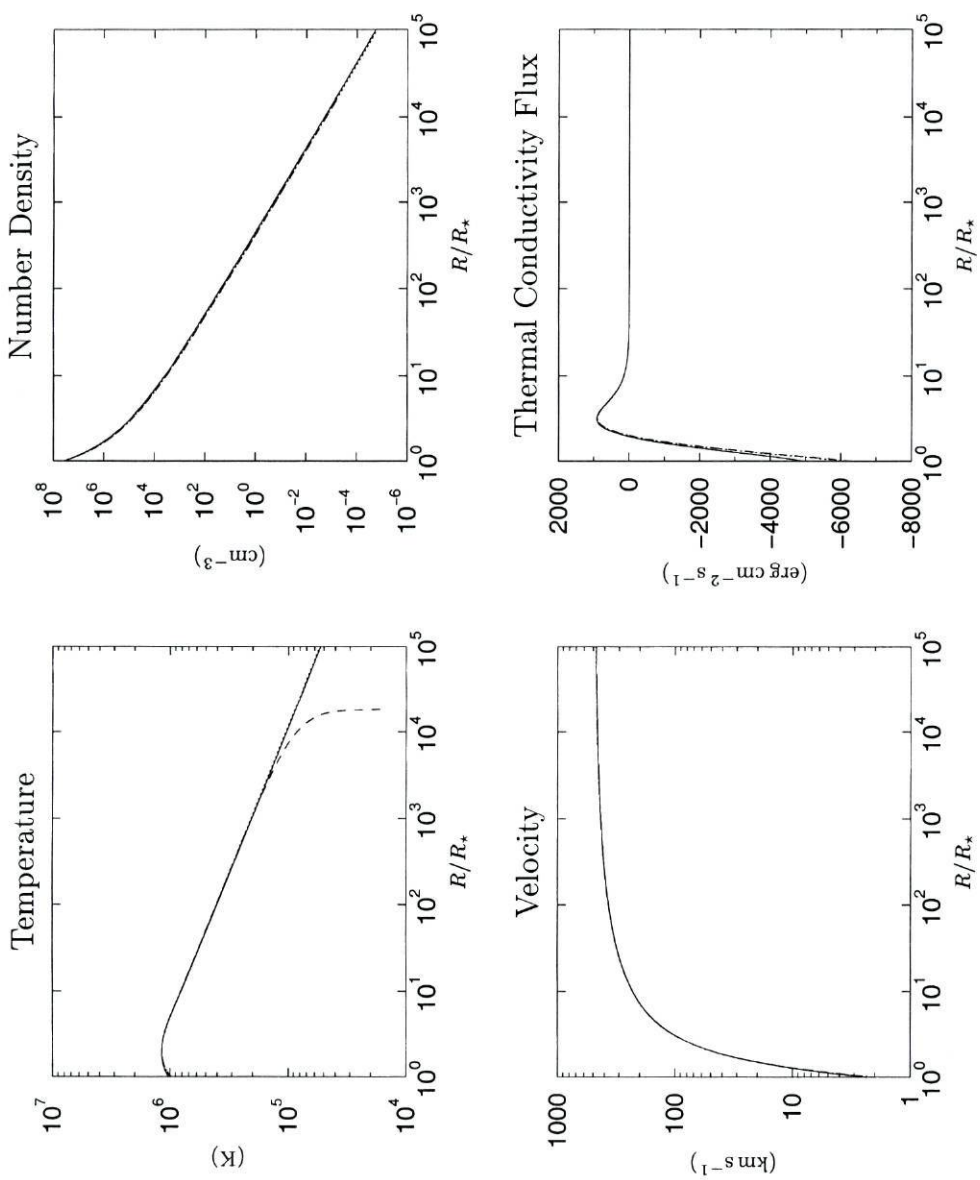

Figure 6.1: Effects induced in the profiles of temperature, number density, velocity and thermal conductivity flux when f_{w_0} is changed. The three models have in common the following input parameters: $R_c = 4.0\,R_\star$, $n_0 = 4.0 \times 10^7\,\mathrm{cm}^{-3}$, $h_0 = 1.239 \times 10^{-7}\,\mathrm{erg\,cm}^{-3}\,\mathrm{s}^{-1}$ and $\sigma = 0.80\,R_\star$.

	V_c (km s^{-1})	f_{w_0} (erg cm^{-2} s^{-1})	B_0 (G)	ε	V_0 (km s^{-1})	T_0 (K)
(—):	132.80	0	—	—	2.20	1.035×10^6
(· · ·):	132.92	10.0	2.0	0.50	1.93	9.877×10^5
(- - -):	132.94	11.0	2.0	0.50	1.88	9.796×10^5

f_{w_0} ($\mathrm{erg\,cm^{-2}\,s^{-1}}$)	h_0 ($\mathrm{erg\,cm^{-3}\,s^{-1}}$)	V_c ($\mathrm{km\,s^{-1}}$)	T_0 (K)	V_0 ($\mathrm{km\,s^{-1}}$)	$V = 300\,\mathrm{km\,s^{-1}}$ @ $R/R_\star =$
0	1.239×10^{-7}	132.79	1.035×10^{6}	2.197	25.75
10	1.239×10^{-7}	132.92	9.877×10^{5}	1.927	25.28
100	1.230×10^{-7}	132.51	1.122×10^{6}	2.770	26.36

Table 6.1: Comparison of tree wind models with the common input parameters: $R_c = 4.0\,R_\star$, $n_0 = 4.0 \times 10^7\,\mathrm{cm^{-3}}$, $\sigma = 0.80\,R_\star$, $B_0 = 2.0\,\mathrm{G}$ and $\varepsilon = 0.5$.

is not possible to increase much farther the value of f_{w_0}. Therefore, in Fig. 6.2 it is also shown a wind model with h_0 reduced to $1.230 \times 10^{-7}\,\mathrm{erg\,cm^{-3}\,s^{-1}}$ and f_{w_0} increased to $100.0\,\mathrm{erg\,cm^{-2}\,s^{-1}}$ (dashed lines).

There are not many differences between the three wind models of Fig. 6.2 and between them and the wind models of Fig. 6.1. All the wind models presented so far are mainly driven by the prescribed mechanical heat input, and therefore do not differ much from the thermal winds of the previous Chapter.

Three of the wind models already presented are compared in Table 6.1. As mentioned before, the addition of some Alfvén wave energy flux at the base of the wind causes an overall faster acceleration of the plasma, as seen in the rows for the wind model without Alfvén waves and that with $f_{w_0} = 10\,\mathrm{erg\,cm^{-2}\,s^{-1}}$. The last row presents a wind model where the amount of the Alfvén wave energy flux relative to the model in the middle row is increased by a factor of ten, while the amount of the mechanical heating input (h_0) is reduced by less than one percent. The analysis of these last two rows shows that the model with higher Alfvénic wave energy flux has a higher mass flux (V_0 is higher) However, the plasma experiences a smaller acceleration, with an asymptotic velocity equal to $300\,\mathrm{km\,s^{-1}}$.

Even in the wind model with $f_{w_0} = 100.0\,\mathrm{erg\,cm^{-2}\,s^{-1}}$ the Alfvén waves play a minor role in the dynamics. This is clearly shown in Fig. 6.3. The wave energy flux is much smaller than the mechanical heating flux, and the acceleration due to the wave pressure gradient is negligible when compared to that due to the thermal pressure gradient.

Is it possible to drive a faster wind within the framework of the stellar wind model developed in this Chapter? To answer this question more changes in the input parameters are needed. From the experience gained with the stellar wind model presented in the previous Chapter, higher velocities at the critical point are obtained by moving its radial position closer to the stellar surface. This is shown in Fig. 6.4, where the wind models presented have $R_c = 3.5\,R_\star$ (dotted and dashed lines) and are compared with the wind model without Alfvénic wave energy flux already shown in Fig. 6.1 (solid lines in both Figures). The comparison of the output profiles for the three models shows that the temperature profiles are very similar (the maximum temperature is 1.18×10^6 for the model

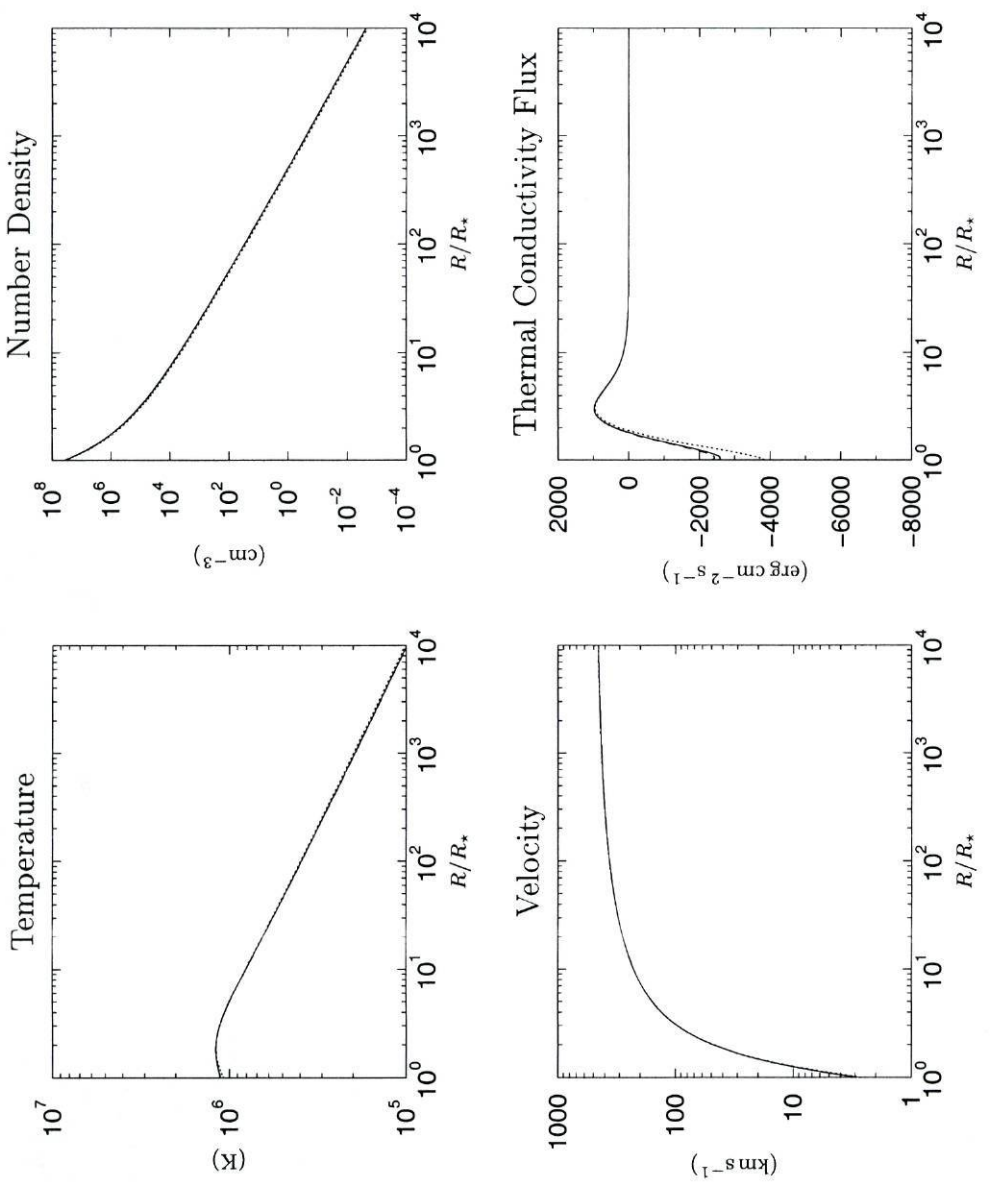

Figure 6.2: Effects in the profiles of temperature, number density, velocity and thermal conductivity flux when f_{w0} is further increased. All the three models have $R_c = 4.0\,R_\star$, $n_0 = 4.0 \times 10^7\,\mathrm{cm}^{-3}$, $\sigma = 0.80\,R_\star$, $B_0 = 2.0\,\mathrm{G}$ and $\varepsilon = 0.5$.

	V_c (km s^{-1})	h_0 (erg cm^{-3} s^{-1})	f_{w0} (erg cm^{-2} s^{-1})	V_0 (km s^{-1})	T_0 (K)
(—):	132.52	1.235×10^{-7}	11.0	2.74	1.117×10^6
(···):	132.67	1.235×10^{-7}	50.0	2.44	1.074×10^6
(– – –):	132.51	1.230×10^{-7}	100.0	2.77	1.122×10^6

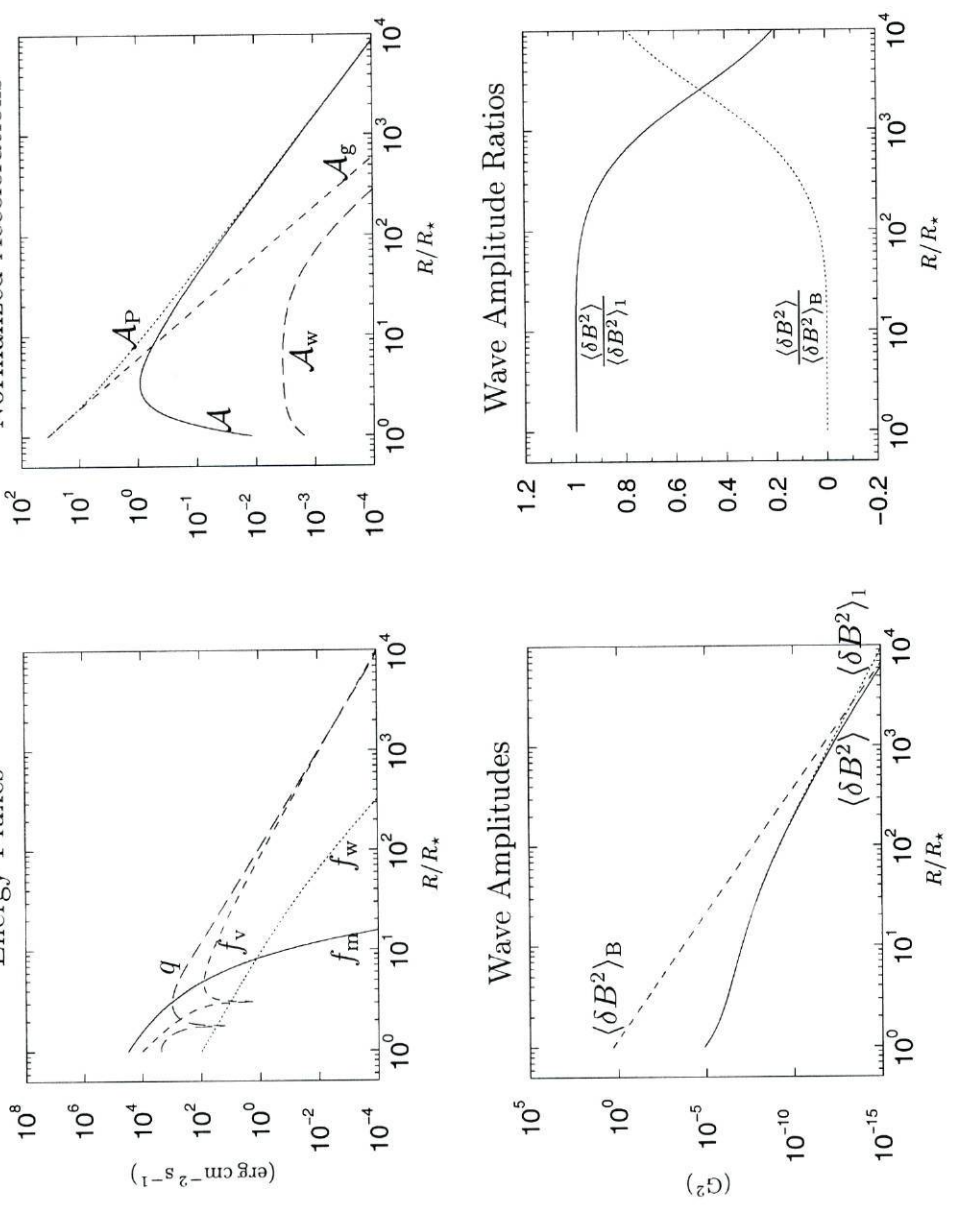

Figure 6.3: Profiles of the energy fluxes, normalized accelerations and wave amplitudes for a wind model with the following input parameters: $R_\star = 1.2\,R_\odot$, $R_c = 4.0\,R_\star$, $V_c = 132.51\,\mathrm{km\,s^{-1}}$, $n_0 = 4.0 \times 10^7\,\mathrm{cm^{-3}}$, $h_0 = 1.230 \times 10^{-7}\,\mathrm{erg\,cm^{-3}\,s^{-1}}$, $\sigma = 0.80\,R_\star$, $f_{w0} = 100.0\,\mathrm{erg\,cm^{-2}\,s^{-1}}$, $B_0 = 2.0\,\mathrm{G}$ and $\varepsilon = 0.5$, and corresponding to the dashed profiles of Fig. 6.2. For details about the symbols please refer to Section 6.2 for the energy fluxes, to Eqs. (6.37) to (6.40) for the normalized accelerations, and to Eqs. (6.12) to (6.15) for the symbols in the bottom plots.

without Alfvén waves and 1.28×10^6 K for the two models with Alfvén waves). However, the models with Alfvén waves have a velocity profile above that of the other model, and achieve this overall higher velocity with a larger mass flux.

The profile for the thermal conductivity flux of the model with $f_{w_0} = 3.44\times10^3\,\mathrm{erg\,cm^{-2}\,s^{-1}}$ attains its minimum value at some distance above the stellar surface, unlike the other two models that have the minimum at the base of the wind. This occurs because the Alfvén waves and the mechanical heating are not providing enough energy near the base to drive the wind, therefore some energy must be taken from the thermal conductivity flux arriving from the region of maximum temperature. One way to overcome this is to increase h_0, for example to $1.850\times10^{-7}\,\mathrm{erg\,cm^{-3}\,s^{-1}}$, shown by the dotted line profiles in Fig. 6.4. In this case the value of the velocity at the base was decreased, since a lower mass flux demands less energy to be driven.

6.6 Application to TTS: increasing n_0

In this Section a solution for the problem of driving a stellar wind with increased base density is searched. To start, some wind models with $n_0 = 10^8\,\mathrm{cm^{-3}}$ are shown in Fig. 6.5. Looking at the different temperature profiles it is seen that, with one exception (solid lines), they have in common the feature of having the maximum value of the temperature at the base. Therefore none of the later models fulfils the requirement of mimicking a transition region between the stellar surface and the corona. Nevertheless the wind models are presented since they can be used to learn more about the stellar wind model developed in this Chapter.

Both the upward and the downward diverging solutions are shown for the model with $R_c = 3.5\,R_\star$ (dot-dashed lines). This model and the one displayed by the long-dashed lines have a rather peculiar temperature profile for the upward diverging solution: it attains a minimum (near $R = 10^4\,R_\star$ in both cases) and increases afterwards. In the examples shown in the previous Chapter the upward diverging solutions have a temperature profile that keeps on decreasing after the 'diverging point', although at an ever smaller rate, or sometimes increased at a very small rate. In the two examples of Fig. 6.5 the temperature is decreasing at a very high rate before the 'diverging point', consequently, there are two possibilities: there are only downward diverging solutions, or the upward diverging solution must seek a high enough value of the temperature to drive the wind. Recall that in the upward diverging solutions of the purely thermal winds it is the high value of the temperature that is driving the wind. Although these are not purely thermal winds nevertheless, at distances beyond $10^3\,R_\star$, the energy flux due to the Alfvén waves is much less than the enthalpy flux. Therefore, at these large distances the wind behaves as a

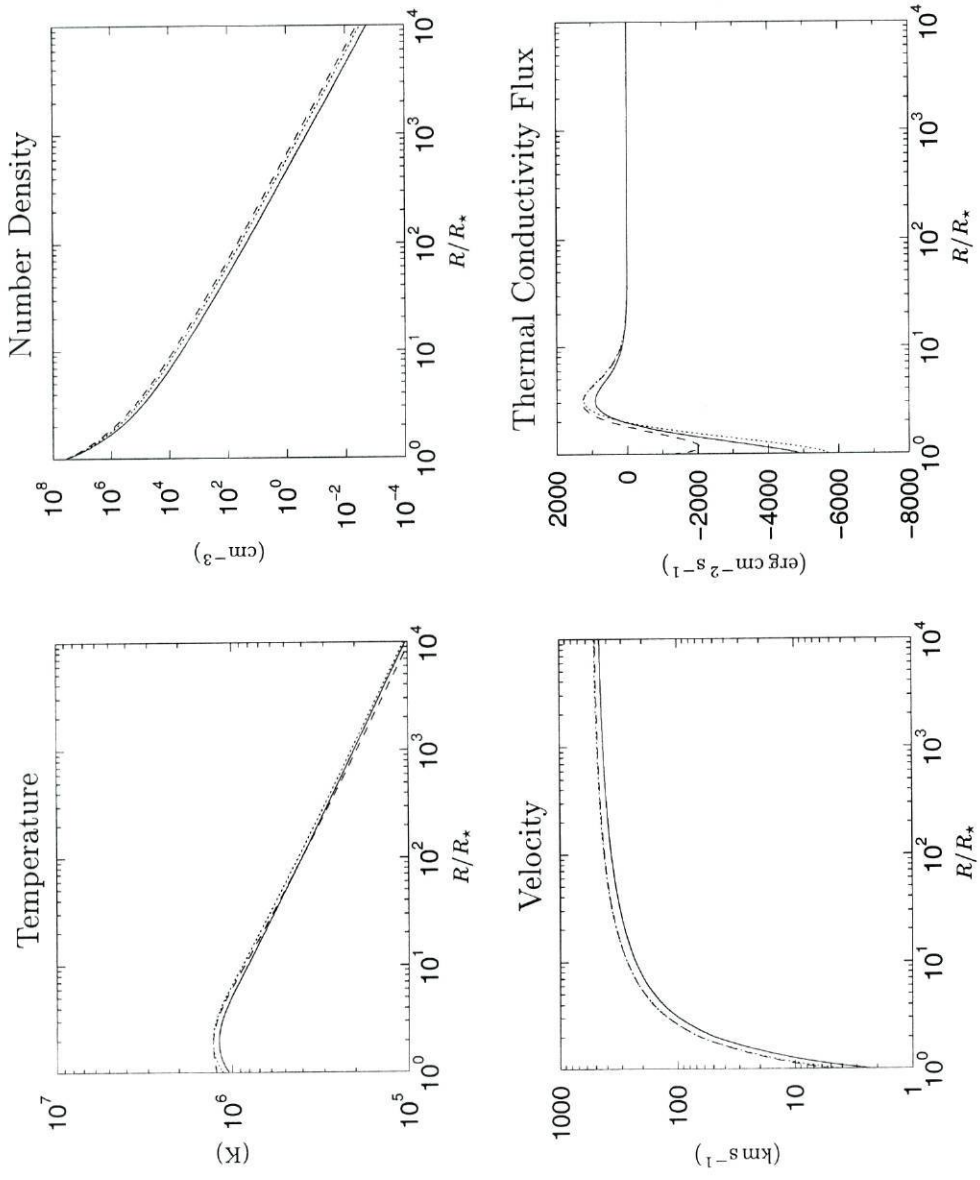

Figure 6.4: Comparison of a purely thermal wind model and two wind models including Alfvén wave flux. The three wind models have in common the input parameters: $n_0 = 4.0 \times 10^7$ cm^{-3} and $\sigma = 0.80\,R_\star$.

	R_c ($R_\star$)	V_c (km s^{-1})	h_0 (erg cm^{-3} s^{-1})	f_{w0} (erg cm^{-2} s^{-1})	B_0 (G)	ε	V_0 (km s^{-1})	T_0 (K)
(—):	4.0	132.79	1.239×10^{-7}	0	—	—	2.20	1.035×10^6
(···):	3.5	143.03	1.850×10^{-7}	2.40×10^3	1.0	0.5	4.00	1.124×10^6
(– – –):	3.5	142.64	1.800×10^{-7}	3.44×10^3	1.0	0.5	5.00	1.224×10^6

thermal wind.

The model with $R_c = 3.50\,R_\star$ (dot-dashed lines) will be used as a comparison model. The comparison model has a bad profile of temperature that needs to be improved. The first change is to decrease R_c to $3.00\,R_\star$, exemplified by the dotted profiles. With this value of R_c the value of V_c is increased, therefore more energy is needed, and both h_0 and f_{w_0} were increased. The profile of the temperature improves, however not enough, since it starts with $T_0 = 1.18 \times 10^6\,K$, decreases to $1.08{\times}10^6$ K, increases to $1.11{\times}10^6$ K and decreases afterwards.

The dashed profiles correspond to a model with $R_c = 3.00\,R_\star$ and a value of V_0 decreased to $2.00\,\mathrm{km\,s^{-1}}$. The decrease of the temperature profile at large distances ($R > 100\,R_\star$) is smooth, and with a slope comparable to the slope of the model displayed by the solid lines. However, near the star the behaviour of the temperature profile is the same as that of the model displayed by the dotted profiles.

Finally, the model shown by the long-dashed profiles has $R_c = 3.00\,R_\star$ and a mechanical heating input more concentrated near the base, with $\sigma = 0.50\,R_\star$. In this case the mechanical heating is too concentrated near the base, resulting in a fast decrease of the temperature after the point where most of the wave energy is being converted into thermal energy of the plasma ($\langle \delta B^2 \rangle_1 \approx \langle \delta B^2 \rangle_B$ for $R \sim 10\,R_\star$: at this point the Alfvén wave energy flux is comparable to the enthalpy flux, but it becomes rapidly negligible for larger distances). The purpose of this model is for the mechanical energy flux to give the initial push on the plasma and the Alfvén waves to take over and drive it to infinity. However, the value of σ used was too small for a successful model.

A better model for this value of the base density ($10^8\,\mathrm{cm^{-3}}$) is one with all these ingredients. A model with R_c decreased to $3.00\,R_\star$, V_0 decreased to $3.00\,\mathrm{km\,s^{-1}}$ and σ decreased to $0.70\,R_\star$ is displayed by the solid line profiles in Fig. 6.5. This model starts with a temperature below 10^6 K, that increases a little and then decreases approximately as a power law with exponent close to -2/7. Nevertheless this is not the best model that can be done with the stellar wind model being developed in this Chapter. The temperature at the base is still too high, and some energy is taken from the thermal conductivity flux arriving from the region of maximum temperature to help in the initial push of the plasma.

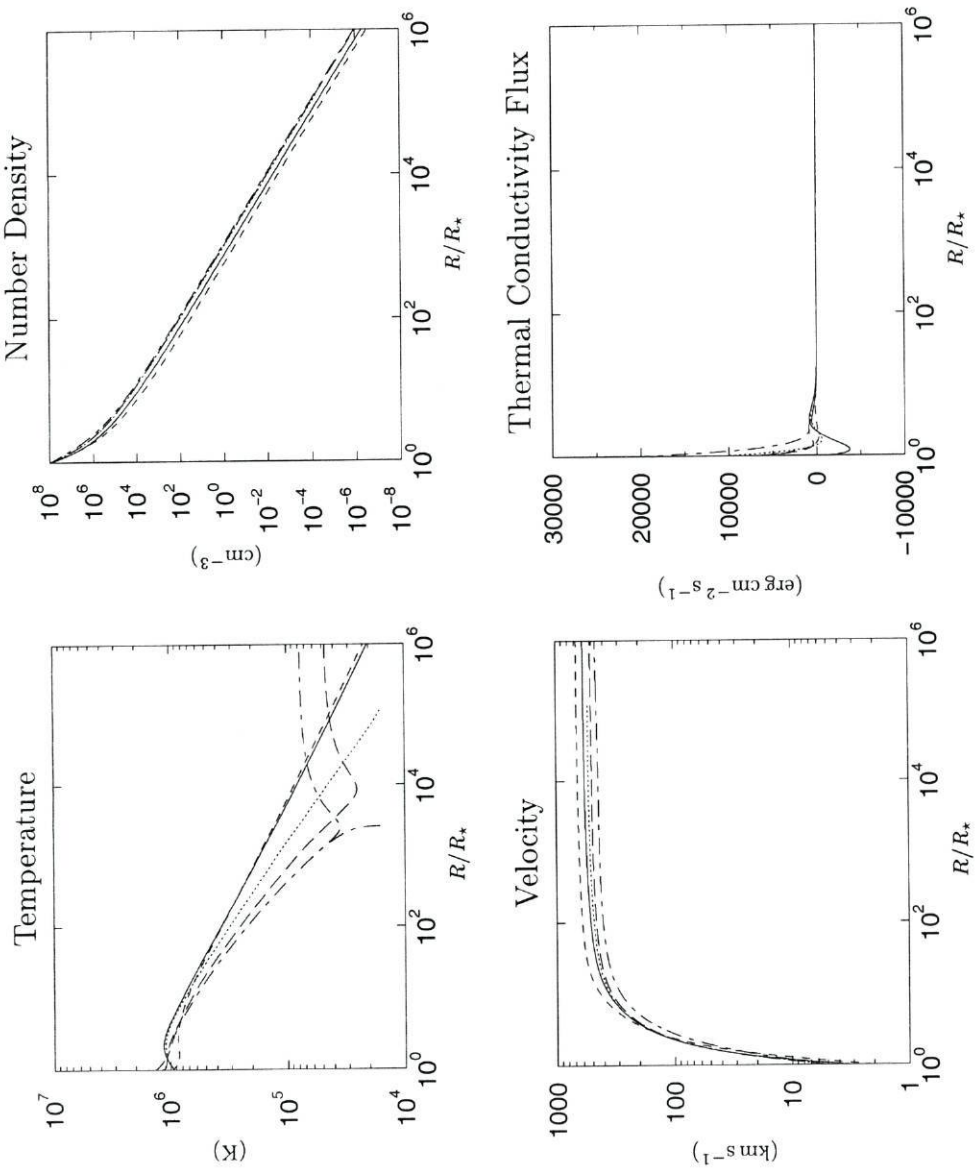

Figure 6.5: Effects in the profiles of temperature, number density, velocity and thermal conductivity flux for five wind models with $n_0 = 10^8\,\mathrm{cm}^{-3}$, $B_0 = 1.0\,\mathrm{G}$ and $\varepsilon = 0.5$.

	R_c ($R_\star$)	V_c (km s^{-1})	h_0 (erg cm^{-3} s^{-1})	σ ($R_\star$)	f_{w0} (erg cm^{-2} s^{-1})	V_0 (km s^{-1})	T_0 (K)
(—):	3.0	154.40	2.5×10^{-7}	0.70	3.10×10^{4}	3.00	9.5×10^{5}
(···):	3.0	152.98	2.0×10^{-7}	0.80	4.65×10^{4}	5.00	1.1×10^{6}
(– –):	3.0	154.21	5.0×10^{-8}	0.80	4.44×10^{4}	2.00	9.7×10^{5}
(– –):	3.0	148.11	4.0×10^{-7}	0.50	5.28×10^{4}	5.00	1.1×10^{6}
(–·–):	3.5	138.23	1.2×10^{-7}	0.80	3.41×10^{4}	5.00	1.3×10^{6}

6.6.1 The positive feedback near the base

Before starting with the study of the positive feedback at the base of the wind, the expression for the Alfvén wave energy flux at the base is displayed

$$f_{w_0} = \frac{\langle \delta B^2 \rangle_0}{4\pi} \left(V_{A_0} + \frac{3}{2} V_0 \right) \tag{6.84}$$

where the value of the base Alfvén velocity is given by

$$V_{A_0} = \frac{B_0}{\sqrt{4\pi \rho_0}} \tag{6.85}$$

and is also displayed the expression for $\langle \delta B^2 \rangle_{B_0}$

$$\langle \delta B^2 \rangle_{B_0} = \varepsilon B_0^2 \ . \tag{6.86}$$

In both methods of solution the values of B_0 and ρ_0 are fixed at the start, therefore V_{A_0} and $\langle \delta B^2 \rangle_{B_0}$ are constant. The value of f_{w_0} is changed only in the outer iterative cycle of method II, and its value is constant in the inner iterative cycles that will be analysed in the following paragraphs. In summary, the quantities f_{w_0}, V_{A_0} and $\langle \delta B^2 \rangle_{B_0}$ are constant in the iterations, while the other quantities have the values V_0^i, $\langle \delta B^2 \rangle_0^i$ and $\langle \delta B^2 \rangle_{1_0}^i$, at iteration i and the new values V_0^{ii}, $\langle \delta B^2 \rangle_0^{ii}$ and $\langle \delta B^2 \rangle_{1_0}^{ii}$, at iteration ii=i+1, and similarly at iteration iii=ii+1.

If $V_0^{ii} < V_0^i$ then $\langle \delta B^2 \rangle_0^{ii} > \langle \delta B^2 \rangle_0^i$, since f_{w_0} must be kept constant. The value of $\langle \delta B^2 \rangle_0$ changes due to changes in $\langle \delta B^2 \rangle_{1_0}$, since $\langle \delta B^2 \rangle_{B_0}$ is constant, therefore in this case the inequality is also $\langle \delta B^2 \rangle_{1_0}^{ii} > \langle \delta B^2 \rangle_{1_0}^i$. These inequalities have implications on the ratios defined in Eq. (6.15), and consequently on the relative importance of the two forms of Alfvén wave propagation on the value of $\langle \delta B^2 \rangle_0$.

The following inequalities arise:

$$\frac{\langle \delta B^2 \rangle_0^{ii}}{\langle \delta B^2 \rangle_{1_0}^{ii}} = \frac{\langle \delta B^2 \rangle_{B_0}}{\langle \delta B^2 \rangle_{1_0}^{ii} + \langle \delta B^2 \rangle_{B_0}} < \frac{\langle \delta B^2 \rangle_{B_0}}{\langle \delta B^2 \rangle_{1_0}^{i} + \langle \delta B^2 \rangle_{B_0}} = \frac{\langle \delta B^2 \rangle_0^i}{\langle \delta B^2 \rangle_{1_0}^i} \tag{6.87}$$

$$\frac{\langle \delta B^2 \rangle_0^{ii}}{\langle \delta B^2 \rangle_B} > \frac{\langle \delta B^2 \rangle_0^i}{\langle \delta B^2 \rangle_B} \ . \tag{6.88}$$

From the analysis of these inequalities it is seen that the damping of Alfvénic wave energy has its relative importance increased, which results in the availability of more energy at the base to heat the plasma and drive the wind. Having more energy at the base and

keeping the position of the critical fixed (both R_c and V_c) implies that the plasma starts at a lower velocity, therefore the value of the velocity at iteration *iii* will decrease further. This is a characteristic of a positive feedback: in successive iterations the values of V_0 are always ever smaller, i.e., $V_0^{\rm i} > V_0^{\rm ii} > V_0^{\rm iii}$ and $\left|V_0^{\rm iii} - V_0^{\rm ii}\right| > \left|V_0^{\rm ii} - V_0^{\rm i}\right|$. The value of T_0 is also decreased since the mass flux decreases, demanding therefore a lower temperature to be driven, and since the available energy to heat the plasma at the base increases, therefore allowing the existence of a larger temperature gradient. The process of positive feedback continues until the temperature at, or near, the base decreases to less than the minimum allowed for the fit to the radiative loss function to be valid, $T_{\rm min} \sim 2 \times 10^4$ K.

A similar reasoning could be done for an increased value of V_0, reaching the same conclusion of positive feedback. This time the velocity and temperature at the base keep on increasing until it is not possible to build a solution or extra critical points appear.

The positive feedback on the velocity at the base appears for high enough values of $f_{\rm w_0}$. In this case the iterative procedure of solution called 'Method II' in Section 6.4 must be used to search for the solution. In the cases where there is not positive feedback both methods of solution can be used to iteratively search for the solution.

Examples of positive feedback are shown in Figs. 6.6 and 6.7 for a decreasing and increasing V_0, respectively. The only input parameter change from one Figure to the other is the value of V_c, that changed from 154.3959 to 154.3955 km s^{-1}, while the value for convergence is 154.39572029 km s^{-1}, as displayed by the solid lines in the plots of Fig. 6.5. Since the difference from the values of V_c to the value of convergence is small in the first few iterations the profiles change very little from the 'converged' profiles. However, when the accumulated changes are appreciable, the changes in the profiles from iteration to iteration are very large, until the solution is no longer possible as mentioned before.

Analysing the profiles of Fig. 6.6 the most peculiar is the one of iteration 8 (dashed line). The value of V_0 has decreased from the initial 3.0 km s^{-1} to less than 1.0 km s^{-1}, however the temperature at the base has increased. Somehow it was possible to numerically find a temperature profile that starts at a high value, decreases steeply and immediately increases steeply, and then follows a 'normal' decrease. The relative contribution of the undamped propagation of the Alfvén waves to the wave amplitude shows a large decrease near the base, while the thermal conductivity flux changes from negative to positive by a large amount. With all these large changes the next iteration is not possible to be complete, as the temperature decreases below the permitted values.

In Fig. 6.6 the relative contribution of $\langle \delta B^2 \rangle_{\rm B}$ for the wave amplitude near the base is increasing from iteration to iteration. On the contrary, its relative contribution further out from the stellar surface is decreasing with the iterations. The reason for this behaviour is that from iteration to iteration the Alfvén waves have a larger role in the initial pushing

of the wind, and therefore less wave energy is left for the intermediate and outer regions of the wind. The opposite behaviour is found in Fig. 6.7.

6.7 Towards a better model

The model displayed in Fig. 6.8 mimics very well the transition region where the temperature has a steep increment from $T \sim 10^5$ to $T > 10^6$ K. The x-axis starts at $R = 0.5\,R_\star$ for better visualization of the steep gradients near the stellar surface. The plasma experiences a fast acceleration, from 1.0 km s^{-1} at the base of the wind up to 100 km s^{-1} at $R = 1.73\,R_\star$. To power all this acceleration and heating the energy input due to the mechanical heating and the Alfvén waves at the base are not enough and some energy must be taken from the thermal conductivity flux arriving from the region of maximum temperature.

Since the gradient of the velocity near the stellar surface is very high, the numerical tolerance for the value of the relative difference of V_0 between two successive iterations needed to be increased to $5{\times}10^{-6}$, otherwise it was not possible to achieve convergence. However, it must be stressed that the numerical tolerance used in the integration routines was kept equal to 10^{-11}.

6.8 Application to TTS: increasing the model $R_\star$

In Fig. 6.9 are displayed some wind models for stars with radius of 1.3, 1.4 and 1.5 $R_\odot$. All models have a transition region with very steep gradients of temperature and velocity, therefore the numerical tolerance for the relative difference of the values of V_0 between two successive iterations has the value of $5{\times}10^{-6}$. The value of V_0 have to be increased a little, otherwise the very steep gradients near the stellar surface would demand a temperature at the base below the minimum value possible for the use of the radiative cooling function ($T_{\rm min} \sim 2 \times 10^4$ K).

The temperature profile for the model with $R_\star = 1.5\,R_\odot$ has two local maxima. One closer to the star, is due to the mechanical heat input, while the other is due to the dissipation of the Alfvén waves. For the values of the input parameters of this model, in particular the large value of the base magnetic field, most of the wave damping occurs at $R > 10\,R_\star$, therefore re-heating the plasma. The transition from decreasing T to increasing T is smooth, thanks to the form chosen for the amplitude of wave fluctuations, where the wave damping increases its importance gradually. Other authors have chosen to have a region between the star and the point where $\langle \delta B^2 \rangle_{\rm I} = \langle \delta B^2 \rangle_{\rm B}$ without wave damping, i.e. $\langle \delta B^2 \rangle = \langle \delta B^2 \rangle_{\rm I}$, and wave damping afterwards, i.e. $\langle \delta B^2 \rangle = \langle \delta B^2 \rangle_{\rm B}$. As a

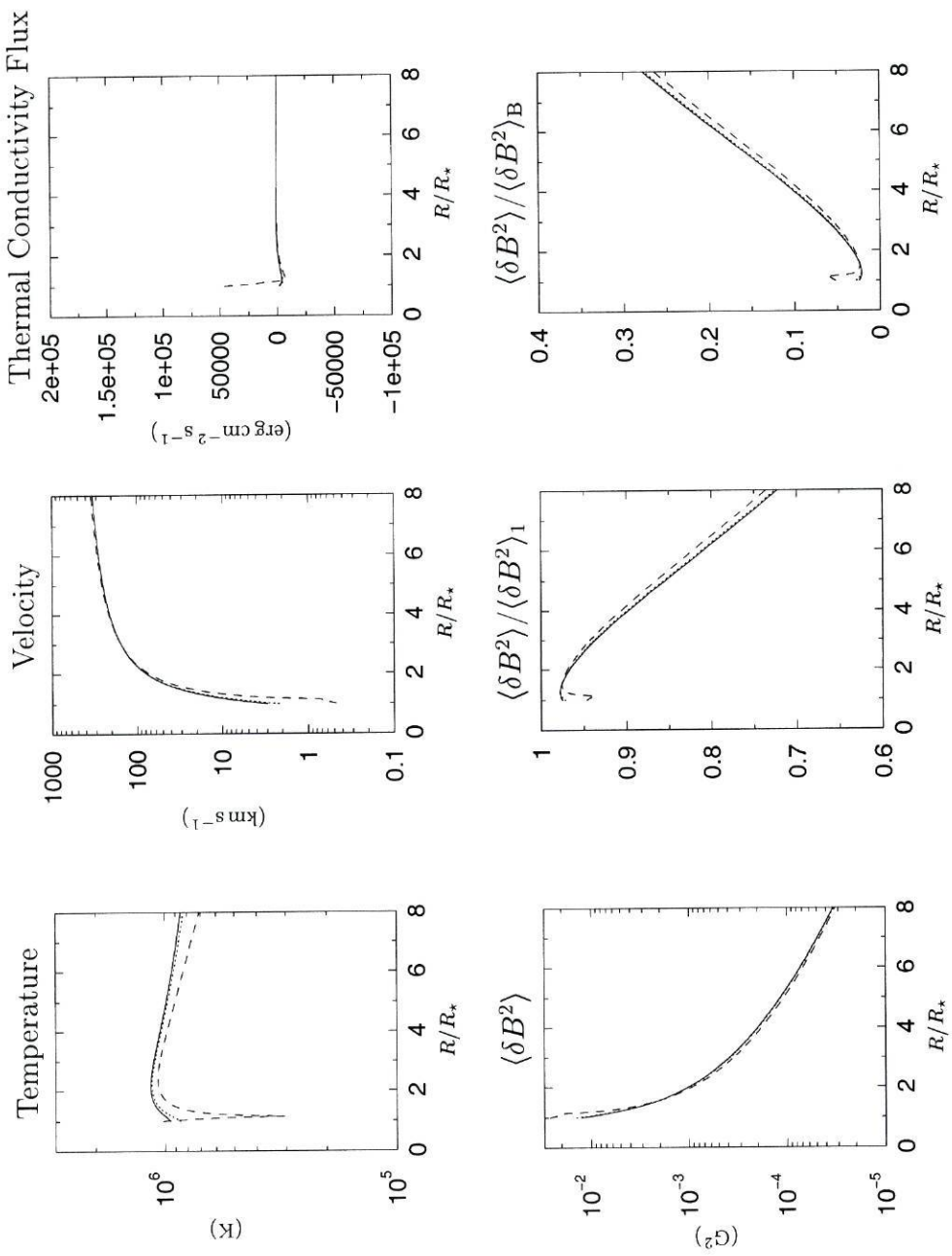

Figure 6.6: Profiles of temperature, velocity, thermal conductivity flux, average wave magnetic field amplitude $\langle \delta B^2 \rangle$, and relative importance of the undamped propagation of Alfvén waves ($\langle \delta B^2 \rangle / \langle \delta B^2 \rangle_1$) and of the damped propagation ($\langle \delta B^2 \rangle / \langle \delta B^2 \rangle_B$) for the total wave amplitude, for a wind model with $n_0 = 10^8\,\mathrm{cm}^{-3}$, $R_c = 3.00\,R_\star$, $V_c = 154.3959\,\mathrm{km\,s}^{-1}$, $h_0 = 2.50 \times 10^{-7}\,\mathrm{erg\,cm}^{-3}\,\mathrm{s}^{-1}$, $\sigma = 0.70\,R_\star$, $f_{w0} = 3.1014 \times 10^4\,\mathrm{erg\,cm}^{-2}\,\mathrm{s}^{-1}$, $B_0 = 1.0\,\mathrm{G}$ and $\varepsilon = 0.5$. The star has a radius of $1.2\,R_\odot$ and one solar mass. The various profiles are displayed for iterations 1 (—), 7 ($\cdots$) and 8 (– – –).

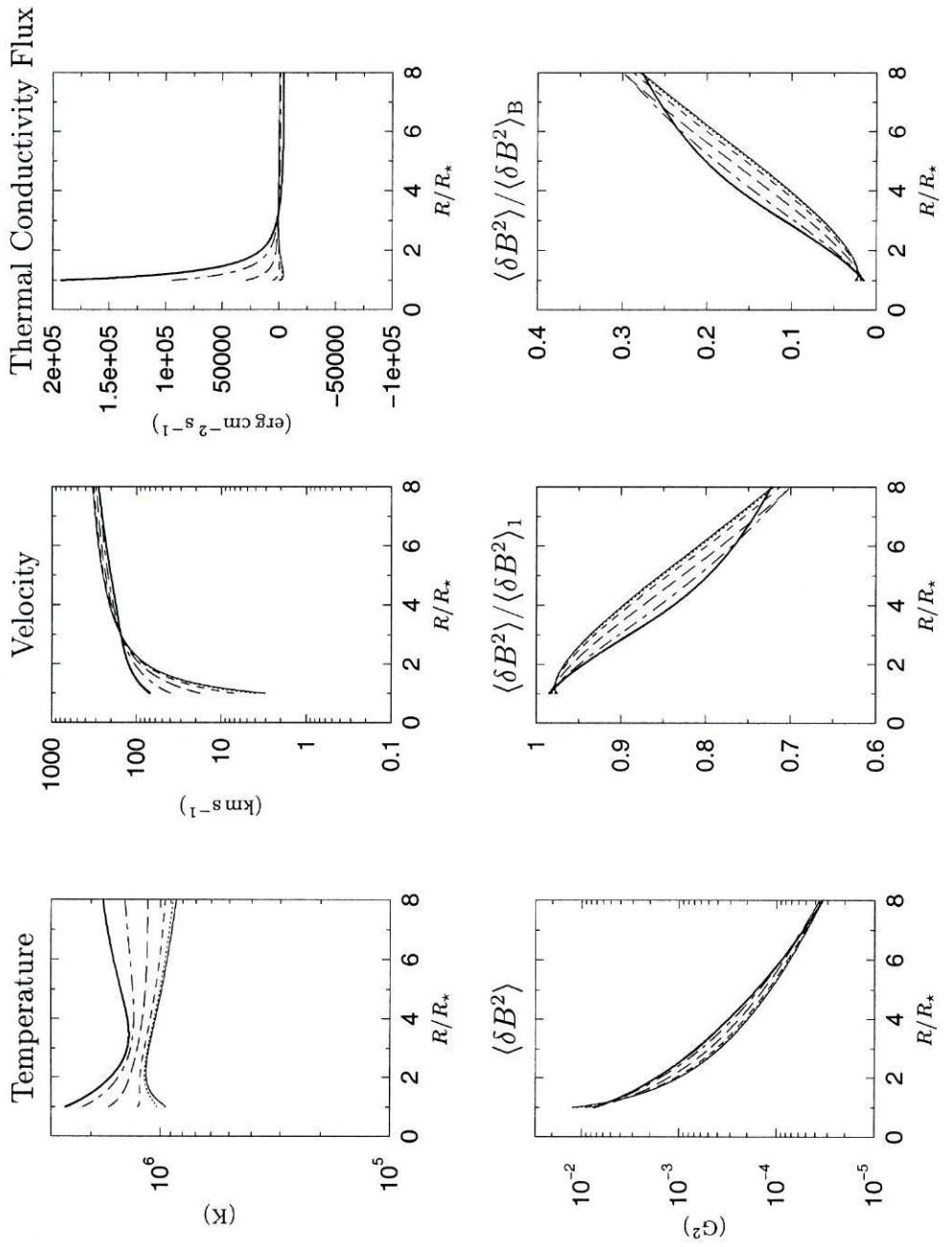

Figure 6.7: Profiles of temperature, velocity, thermal conductivity flux, average wave magnetic field amplitude $\langle \delta B^2 \rangle$, and relative importance of the undamped propagation of Alfvén waves ($\langle \delta B^2 \rangle / \langle \delta B^2 \rangle_1$) and of the damped propagation ($\langle \delta B^2 \rangle / \langle \delta B^2 \rangle_B$) for the total wave amplitude, for a wind model with the same input parameters as the model of Fig. 6.6, except $V_c = 154.3955\,\mathrm{km\,s^{-1}}$. The various profiles are displayed for iterations 1 (—; thin), 7 ($\cdots$), 8 (– –), 9 (– –), 10 (–·–) and 11 (—; thick).

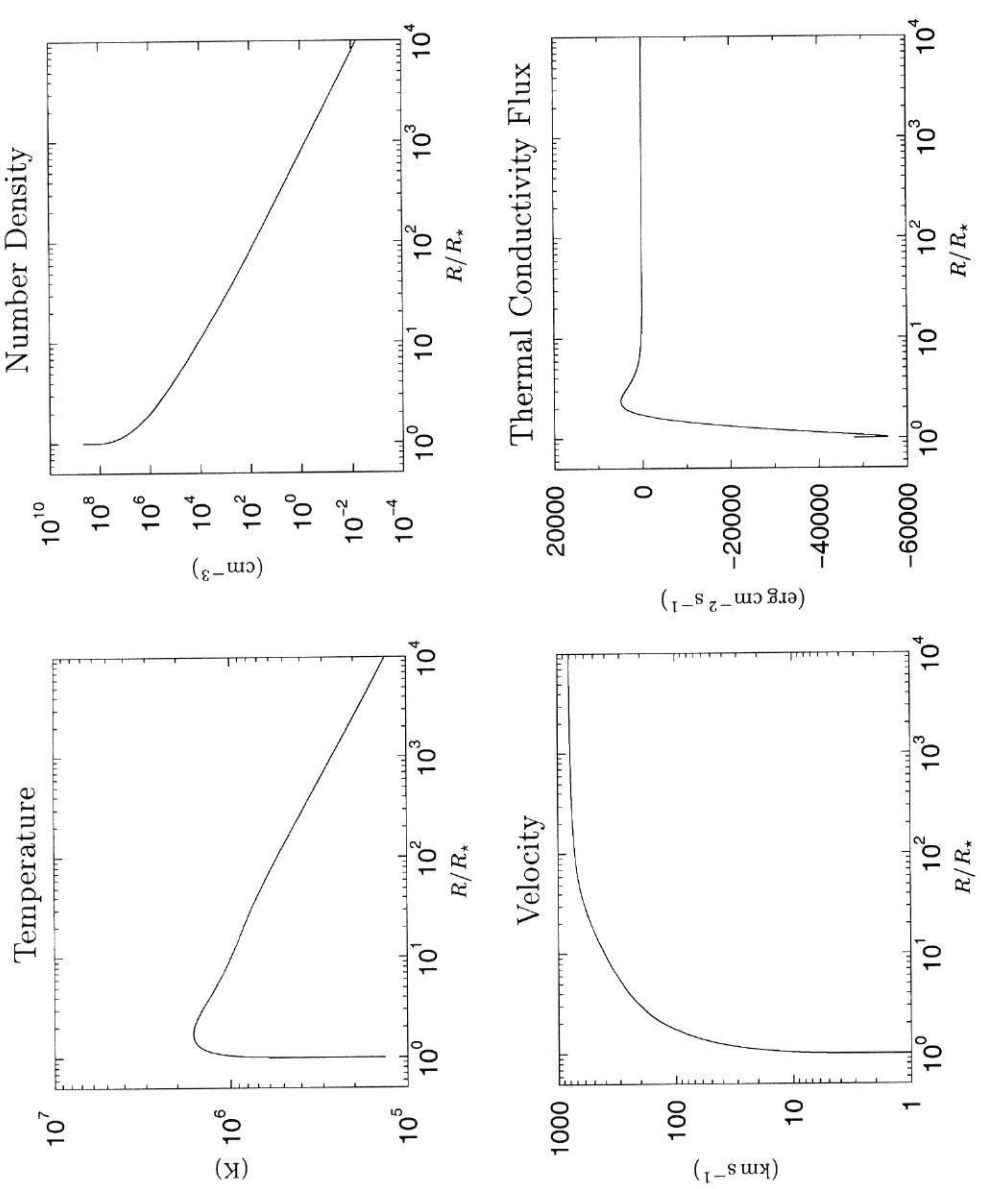

Figure 6.8: Profiles of temperature, number density, velocity and thermal conductivity flux for a wind model with $n_0 = 5.0 \times 10^8\,\mathrm{cm}^{-3}$, $V_0 = 1.00\,\mathrm{km\,s}^{-1}$, $R_\mathrm{c} = 2.50\,R_\star$, $V_\mathrm{c} = 168.10\,\mathrm{km\,s}^{-1}$, $h_0 = 2.30 \times 10^{-6}\,\mathrm{erg\,cm}^{-3}\,\mathrm{s}^{-1}$, $\sigma = 0.40\,R_\star$, $f_{\mathrm{w}_0} = 1.146 \times 10^5\,\mathrm{erg\,cm}^{-2}\,\mathrm{s}^{-1}$, $B_0 = 5.0\,\mathrm{G}$ and $\varepsilon = 0.5$. The star has a radius of $1.2\,R_\odot$ and one solar mass.

consequence, the temperature suffers an abrupt increase at the point where wave damping starts, contrary to the present stellar wind model in which the transition is gradual.

Although in this wind model the equality of $\langle \delta B^2 \rangle_1$ and $\langle \delta B^2 \rangle_B$ occurs at $R = 123.2\, R_\star$ the wave energy flux there is only $5.70\,\mathrm{erg\,cm^{-2}\,s^{-1}}$, having therefore little influence on the plasma. However, at the region of transition from decreasing to increasing T the wave energy flux is almost one thousand times higher, $f_w \sim 3500\,\mathrm{erg\,cm^{-2}\,s^{-1}}$, and even a relative contribution of the wave damping to the wave amplitude of about 0.4% is able to generate enough heat to start re-heating the plasma. At the position of the second maximum of temperature the value of the wave energy flux has decreased more than 10 times to about $160\,\mathrm{erg\,cm^{-2}\,s^{-1}}$, while the relative contribution of the wave damping to the wave amplitude has increased to more than 11%.

The wind models for the stars with 1.3 and $1.5\,R_\odot$ have a value for h_0 of the order of $2.3 \times 10^{-6}\,\mathrm{erg\,cm^{-3}\,s^{-1}}$, the mechanical heating input being more concentrated near the the star for the larger one. This is curious, since both models were independently achieved. The starting point for the $1.3\,R_\odot$ wind model was the model studied in the previous Section, with $R_\star = 1.2\,R_\odot$ and $n_0 = 5 \times 10^8\,\mathrm{cm^{-3}}$, while the model for the larger star was started from a model already with $R_\star = 1.5\,R_\odot$, but with a lower value for the base density, n_0. The input parameters for model with $1.4\,R_\odot$ were 'interpolated' from the corresponding input parameters for the 1.3 and $1.5\,R_\odot$ models.

From the analysis of these models it is found that with increasing $R_\star$ the position of the critical point (R_c) should decrease to have a value of V_c high enough, and to have a transition region with steep gradients. The value of the base velocity must increase, otherwise, due to the steep gradients, the base temperature will be less than the minimum value possible. For this particular case the value of h_0 is of the same order, while the value of σ must be decreased. With increasing $R_\star$ the values of f_{w_0} and B_0 must also be increased.

The final result of the changes in h_0, σ, f_{w_0} and B_0 is a stronger initial push of the plasma by the mechanical heating input, that manages to compensate for the weaker gravitational field, and the take over by the Alfvén waves at larger distances. The Alfvén waves exert a force due to the wave pressure gradient and heat the plasma by wave dissipation.

6.8.1 Effect of B_0

This Section addresses the effects induced on the solutions by increasing the value of the base magnetic field. The mechanical heating is kept constant (both h_0 and σ), as is the value of R_c, while V_c and f_{w_0} are allowed to change.

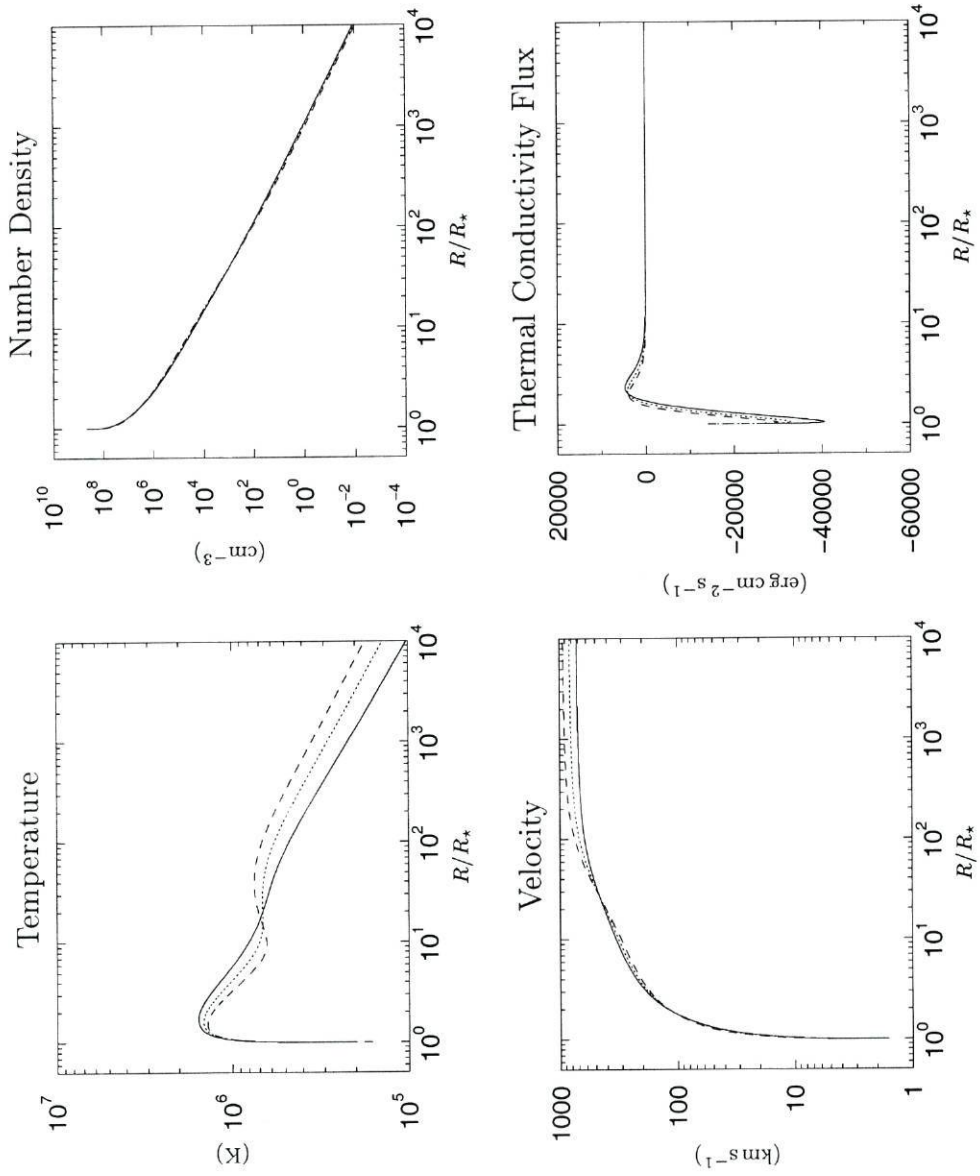

Figure 6.9: Effects induced in the profiles of temperature, number density, velocity and thermal conductivity flux for three wind models with $n_0 = 5.0 \times 10^8$ cm^{-3}, $\varepsilon = 0.5$ and increasing $R_\star$.

	$R_\star$ ($R_\odot$)	R_c ($R_\star$)	V_c (km s^{-1})	h_0 (erg cm^{-3} s^{-1})	σ ($R_\star$)	f_{w_0} (erg cm^{-2} s^{-1})	B_0 (G)	V_0 (km s^{-1})	T_0 (K)
(—):	1.3	2.50	158.74	2.300×10^{-6}	0.400	1.336×10^{5}	10.0	1.60	2.172×10^{5}
(···):	1.4	2.45	152.21	2.300×10^{-6}	0.350	2.363×10^{5}	15.0	1.70	1.983×10^{5}
(– – –):	1.5	2.40	146.19	2.374×10^{-6}	0.300	3.458×10^{5}	20.0	1.70	1.616×10^{5}

The profiles of temperature, number density, velocity and thermal conductivity flux corresponding to wind models with $B_0 = 20$, 40, 100 and 200 G , are shown in Fig. 6.10. In all the models the star has $R_\star = 1.5\,R_\odot$, $M_\star = M_\odot$, the critical point is at $R = 2.40\,R_\star$, and the mechanical heating is characterized by $h_0 = 2.374 \times 10^{-6}\,\mathrm{erg\,cm^{-3}\,s^{-1}}$ and $\sigma = 0.30\,R_\star$.

It is seen that between the stellar surface and the critical point the effects of a larger B_0 (and $f_{\mathrm{w}0}$) are very small, while at larger distances they are notorious. The most prominent effect is to increase the distance of the second temperature maximum and of its maximum value with increasing B_0. For the model with $B_0 = 200$ G the temperature at the second maximum is almost equal to that of the first maximum, and occurs at $R > 100\,R_\star$. This does not seem to be physically meaningful. With these high temperatures and Alfvén wave fluxes the velocity at large distances increases to values above $2000\,\mathrm{km\,s^{-1}}$.

The relative importance of the Alfvén wave flux and acceleration are shown in Figs. 6.11 and 6.12. From the analysis of these Figures it is concluded that the Alfvén waves play the leading role in both these models.

6.9 Conclusion

In this Chapter we developed a stellar wind model with the inclusion of Alfvén waves. The Alfvén wave flux has two distinct effects on the plasma: by damping, the waves heat the plasma, and they directly accelerate the plasma by the force due to their magnetic pressure gradient. From the study of the examples shown it is inferred that, within the framework adopted, the waves play a major role after the critical point, while the initial acceleration and heating of the plasma is mainly due to the prescribed mechanical heating. The particular form chosen for the magnetic amplitude of the Alfvén waves leads to a smooth transition between the undamped regime near the star to the damped regime at large distances. This smooth transition causes the temperature profile to be smooth, even in the cases of strong re-heating of the plasma.

Since within this formalism the Alfvén waves take over the mechanical heating at a certain distance above the stellar surface, it was possible to choose values of h_0 and σ for the mechanical heating law such that the temperature started at $1\text{–}3\times10^5$ K and steeply increased to over 10^6 K, therefore mimicking the solar transition region. This is a good feature of the model if the analogy with the solar outer atmosphere/corona is applicable.

The main purpose of this work is to study stellar wind models that could be applied to TTS. The model developed in the previous Chapter was not able to fulfil this purpose. The stellar wind model developed in this Chapter goes one step further in reproducing winds in TTS, as it was possible to build reasonable models for stars with $R_\star = 1.5\,R_\odot$

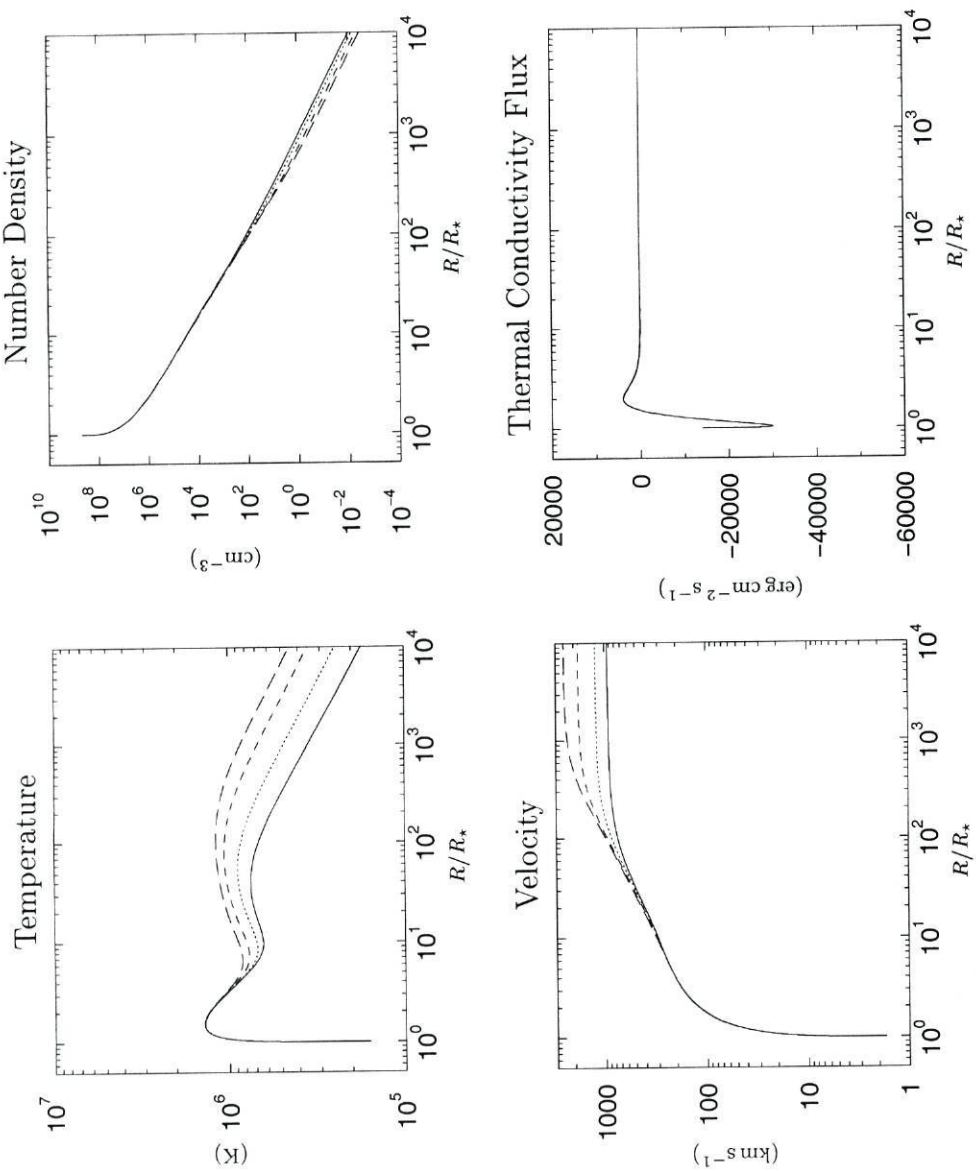

Figure 6.10: Effects induced in the profiles of temperature, number density, velocity and thermal conductivity flux for four wind models with increased B_0. All the models have in common the input parameters: $R_c = 2.40\,R_\star$, $n_0 = 5.0 \times 10^8\,\mathrm{cm}^{-3}$ $h_0 = 2.374 \times 10^{-6}\,\mathrm{erg\,cm}^{-3}\,\mathrm{s}^{-1}$, $\sigma = 0.30\,R_\star$ and $\varepsilon = 0.5$.

	V_c (km s^{-1})	f_{w_0} (erg cm^{-2} s^{-1})	B_0 (G^2)	V_0 (km s^{-1})	T_0 (K)
(—):	146.19	3.458×10^5	20.0	1.70	1.616×10^5
(···):	146.29	6.952×10^5	40.0	1.70	1.613×10^5
(- - -):	146.63	1.763×10^6	100.0	1.70	1.606×10^5
(– –):	147.13	3.590×10^6	200.0	1.70	1.597×10^5

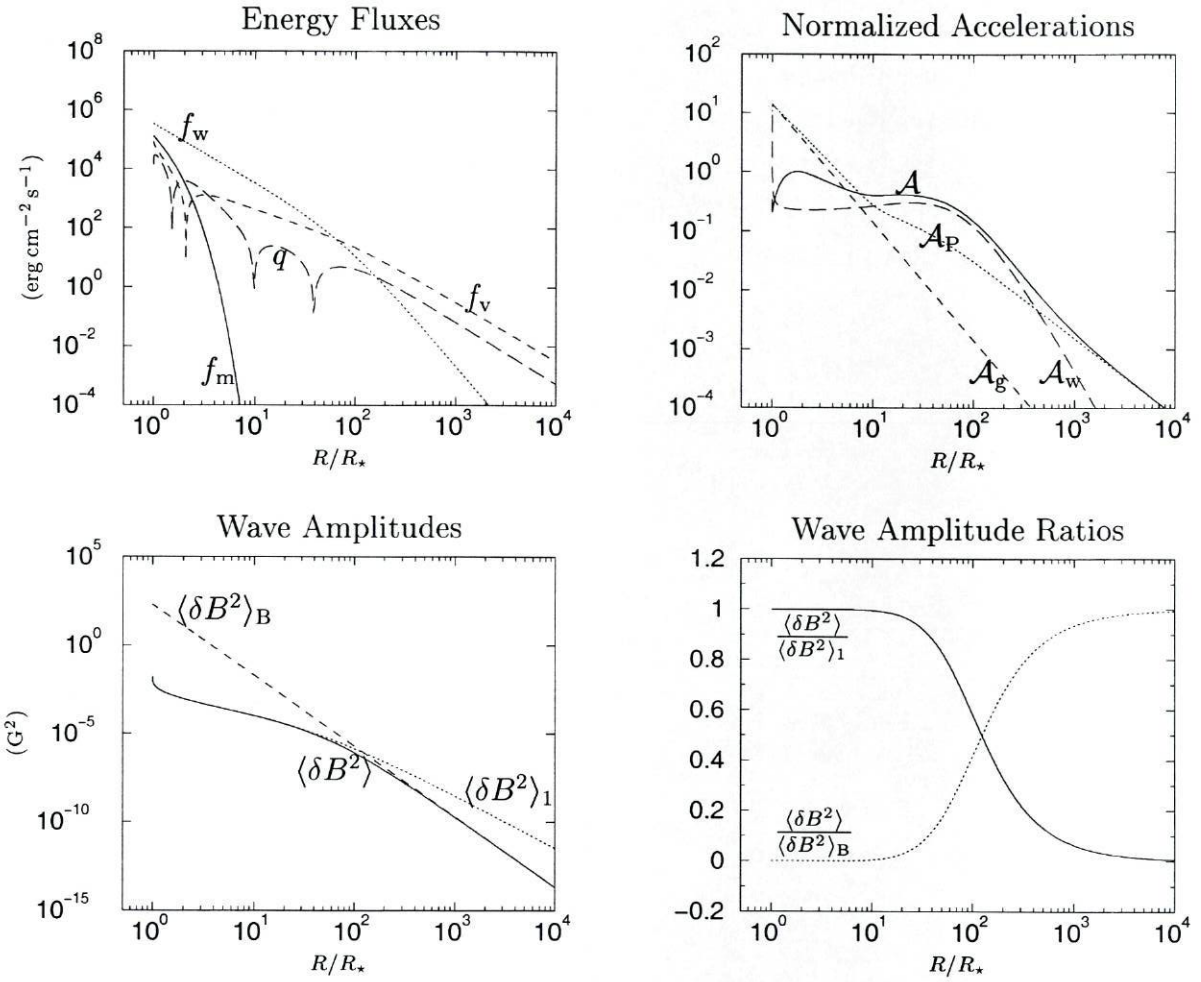

Figure 6.11: Profiles of the energy fluxes, normalized accelerations and wave amplitudes for a wind model with the input parameters: $R_\star = 1.5\,R_\odot$, $R_c = 2.40\,R_\star$, $V_c = 146.19\,\mathrm{km\,s^{-1}}$, $n_0 = 5.0 \times 10^8\,\mathrm{cm^{-3}}$, $h_0 = 2.374 \times 10^{-6}\,\mathrm{erg\,cm^{-3}\,s^{-1}}$, $\sigma = 0.30\,R_\star$, $f_{w0} = 3.458 \times 10^5\,\mathrm{erg\,cm^{-2}\,s^{-1}}$, $B_0 = 20.0\,\mathrm{G}$ and $\varepsilon = 0.5$. In the plot for the energy fluxes, $f_v = f_k + f_g + f_e$. For details about the symbols please refer to: Section 6.2 for the energy fluxes, Eqs. (6.37) to (6.40) for the normalized accelerations and Eqs. (6.12) to (6.14) for the wave amplitudes.

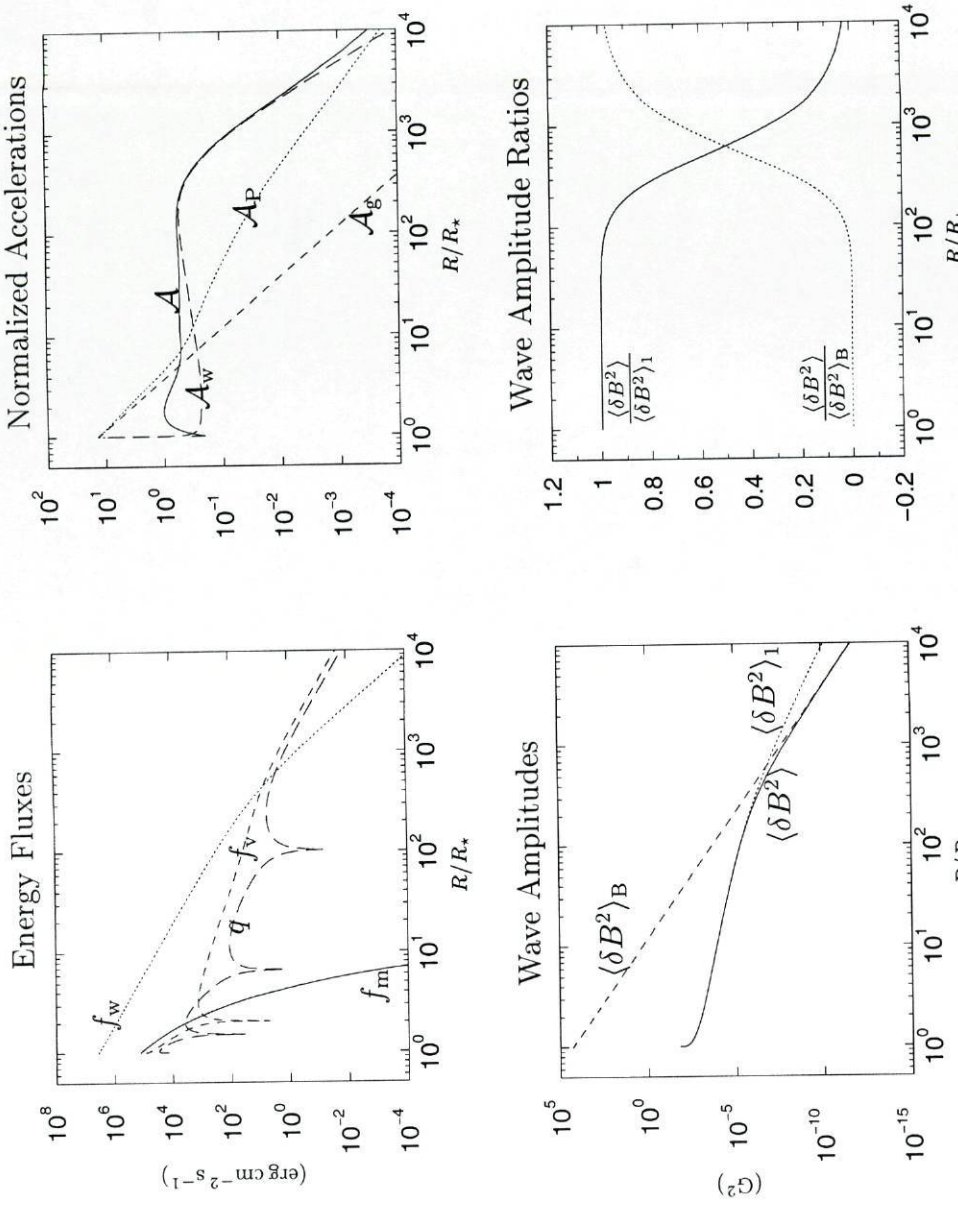

Figure 6.12: Profiles of the energy fluxes, normalized accelerations and wave amplitudes for a wind model with the input parameters: $R_\star = 1.5\,R_\odot$, $R_c = 2.40\,R_\star$, $V_c = 147.13\,\mathrm{km\,s^{-1}}$, $n_0 = 5.0 \times 10^8\,\mathrm{cm^{-3}}$, $h_0 = 2.374 \times 10^{-6}\,\mathrm{erg\,cm^{-3}\,s^{-1}}$, $\sigma = 0.30\,R_\star$, $f_{w0} = 3.590 \times 10^6\,\mathrm{erg\,cm^{-2}\,s^{-1}}$, $B_0 = 200.0\,\mathrm{G}$ and $\varepsilon = 0.5$. In the plot for the energy fluxes, $f_v = f_k + f_g + f_e$. For details about the symbols please refer to: Section 6.2 for the energy fluxes, Eqs. (6.37) to (6.40) for the normalized accelerations and Eqs. (6.12) to (6.14) for the wave amplitudes.

and densities at the base equal to $5 \times 10^8\,\mathrm{cm}^{-3}$. Analysis of the different examples shown seems to indicate that it is possible to go to higher values of both the stellar radius and the base density. However it is very difficult to find the 'good' parameters for a star with given radius and base density for the wind. Sometimes it takes several hours of systematic trials until a set of parameters is found that allows the computer program to automatically iterate until convergence. This was true even for the star with $R_\star = 1.4\,R_\odot$: although the input parameters were 'interpolated', as mentioned, it was not a fast process. The 'good' model for a star with $R_\star = 1.2\,R_\odot$ with its very steep gradients near the base took many hours of difficult iterations, with the author often helping the computer by choosing a narrower range for the limits of the input parameters.

With all these difficulties it is left to future work to proceed towards reproducing the real TTS powerful winds. Namely, to accommodate the much higher densities at the base given by the observations.

Chapter 7

Conclusion and future work

This final Chapter presents the general conclusions of this work and the foreseen directions of possible future work.

7.1 Conclusion

This work begun with a brief review of the main characteristics of T Tauri stars. The largest fraction of this review was devoted to their rotation rates and their winds to clarify the role of the centrifugal force on the acceleration of the wind. On very general terms it could be concluded that the TTS are mostly slow rotators, therefore, in a first approach, the centrifugal force can be neglected in the momentum equation. Another result from this bibliographic survey is the independency of the TTS rotation rate on the stellar mass or age, as inferred from its location on the HR-diagram, the effective temperature, or the classification of CTTS or WTTS. Whatever the subsample of TTS being considered, there are always slow and fast rotators in the group.

The following Chapter started by a review on the theory of magnetized plasmas, on the MHD equations used to describe the phenomena occurring in these plasmas, and on MHD wave theory. This Chapter continued with a review on stellar wind models for solar-like stars, where TTS are also included. The main emphasis was given to those models with a detailed energy equation, starting with the conductive solar wind models. Another class of stellar wind models are those focusing on the MHD equations and treating the wind energetics as a second order contributor. Amongst these MHD stellar wind models that of Tsinganos and Trussoni (1991) was studied in more detail. It was selected since it includes a measure of the stellar rotation rate as an input parameter. Although the majority of TTS are slow rotators, there are some fast rotating TTS also. However, this stellar wind

model could not be applied to TTS since for values of the rotation rate and/or surface magnetic field adequate for TTS the resulting temperature profile was not reasonable. In particular, the temperature far from the star was too high.

A review of the observational characteristics pointing to the existence of winds around the TTS was made, and of the stellar wind models proposed to TTS. Some of these models can be considered as solar-like, and most of them include the effects of Alfvén waves. Two other classes of wind models proposed to TTS can be classified as neutral winds and stochastic winds. However, in both classes of models the velocity law is prescribed, and it must therefore be questioned whether these are true stellar wind models. Winds arising from the interaction of a star and a circumstellar disk have also been proposed to the CTTS.

The first hydrodynamical stellar wind models developed in this work had a prescribed temperature profile and was presented in Chapter 4. It was concluded that neither the model with a prescribed linear temperature profile nor with a prescribed Gaussian temperature profile could be successfully applied to TTS winds. Another model with a prescribed exponential temperature profile can represent, in a reasonable way, the temperature structure of the solar transition region and corona. Further, it can also be successfully applied to TTS winds, in terms of stellar mass, radius and plasma density at the base of the wind.

Following that, Chapter 5 presented stellar wind models with a detailed energy equation including terms due to kinetic energy, enthalpy, potential gravitational energy, thermal conductivity, a term for the radiation losses in the optically thin regime and a term for the rate of volumetric mechanical heating with a prescribed functional form. These models could not be successfully applied to TTS, as the temperature at the base of the wind was too high, while the corresponding plasma velocity and density were too low. The initial plasma acceleration was neither strong enough. Comparison of the stellar wind model with a prescribed exponential temperature profile to the models with a detailed energy equation shows that both models use the same momentum equation, Eq. (4.7). However, the former ones have a prescribed temperature, independent of the plasma density, Eq. (4.38), while in the later ones the temperature is obtained from a detailed energy equation dependent on the plasma density, Eq. (5.16). In particular, the radiation losses are proportional to ρ^2, Eq. (5.14). This implies that the temperature and velocity profiles of the wind model with a detailed energy equation are affected by changes on the density structure, while those of the wind model with a prescribed temperature profile are not. Consequently, it was possible to apply successfully the later stellar wind model to TTS winds, and not the former.

Finally, in Chapter 6 a stellar wind model with a detailed energy equation including Alfvén

waves was constructed. The waves exert a force on the plasma, due to the gradient of their wave pressure, and when they damp while propagating the plasma is directly heated.

It was possible to build wind models with reasonable temperature and velocity profiles for stars with $M_\star = M_\odot$ and for $R_\star$ in the range 1-1.5 $R_\odot$. However, the number density at the base of the wind was still much lower than that inferred from the TTS, $n_0 = 5.0 \times 10^8\,\mathrm{cm}^{-3}$ compared to 10^{11}-$10^{13}\,\mathrm{cm}^{-3}$. Due to the difficulty of finding the 'good' input parameters for any given model, no further exploration of the space parameters in the direction of TTS winds was made.

And yet, these models are not too far from the initial goal, and the results so far hint that it will be possible to successfully apply this later model to TTS. Nevertheless, this has been left as future work. The temperature profiles shown for this wind model have in common a coronal-like region, with $T > 10^6\,\mathrm{K}$, being therefore able to explain the observed X-ray emission from some TTS, at least in a qualitative way.

7.2 Future work

Besides the space parameter exploration for the stellar wind model with Alfvén waves, other objectives are foreseen, such as to improve the energy equation in the stellar wind model. Namely, the inclusion of the effects of gravitational damping of the Alfvén waves (Khabibrakhmanov and Mullan, 1994; Cuseri et al., 1999). This form of wave damping gives extra terms on both the momentum and the energy equations. The waves accelerate the plasma due to their gravitational damping, and also heat the plasma. Therefore, this seems to be promising for driving the TTS powerful winds.

The effects of the low plasma density far from the star, in an almost collisionless state should also be included. This affects in particular the thermal conduction, and the form proposed by Canullo et al. (1996) can be used for that purpose.

One other improvement is the use of a multi-fluid model, starting with a two-fluid model with protons and electrons. However, the multi-fluid models have the drawback of needing the coefficients for the interaction between the various plasma components, and these coefficients are not well known, in particular for the collisionless regime.

The ultimate goal is to relax the assumption of spherical symmetry, and include the effects of the magnetic field in a self-consistent way. The first step could be the solution of a stellar wind model restricted to the equatorial plane, as the Weber and Davis (1967) model, but with a detailed energy equation. When the exploration of the parameter space for this stellar wind model is completed, the next objective could be a 2-dimensional MHD model

with an assumed geometry and a detailed energy equation, and with the equations for the force balance in the three coordinates self-consistently solved. This is a long term project.

Of course, this theoretical effort should be complemented by a similar observational effort. From the careful modelling of spectral lines at high spectral resolution, with new and improved atomic data, it will be possible to obtain several data points with values for the electronic temperature and number density, as well as the corresponding wind velocity. These data points can eventually be used to constrain the input parameters of the stellar wind models to be built.

Another alternative to confront with theory and observations is to compute the X-ray flux/luminosity from the radiative losses and compare them with the corresponding observations from TTS.

Appendix A

The critical points of the momentum equation

This Appendix deals with the study of the critical points. A method will be presented to linearize the momentum equation in order to classify the critical points, and in the case of an X-type critical point a method to determine the slopes of the solutions that cross the critical point will be given.

A.1 The critical points

A first order differential equation of the form

$$\frac{\mathrm{d}y}{\mathrm{d}x} = \frac{ex + fy}{bx + cy} \tag{A.1}$$

can be written as a system of two linear differential equations

$$\frac{\mathrm{d}x}{\mathrm{d}t} = bx + cy \tag{A.2}$$

$$\frac{\mathrm{d}y}{\mathrm{d}t} = ex + fy \quad . \tag{A.3}$$

The point (0,0) satisfies simultaneously

$$\frac{\mathrm{d}x}{\mathrm{d}t} = 0 \qquad \text{and} \qquad \frac{\mathrm{d}y}{\mathrm{d}t} = 0 \tag{A.4}$$

and it is called a critical point of Eq. (A.1).

Case	Nature of eigenvalues	Nature of critical point
1	$\lambda_+ > \lambda_- > 0$ or $\lambda_- < \lambda_+ < 0$	improper node
2	$\lambda_- < 0 < \lambda_+$	saddle or X-type
3	$\lambda_+ = \lambda_-$	node (proper or improper)
4	$\lambda_+, \lambda_- = r \pm \mathrm{i}s$	spiral
5	$\lambda_+ = \mathrm{i}s, \lambda_- = -\mathrm{i}s$	center

Table A.1: Nature of the critical point of a first order differential equation. Table adapted from Boyce and DiPrima (1986)

The nature of the critical point is established when the roots of the characteristic equation of the linear system ((A.2) and (A.3)) are known. The characteristic equation is

$$\lambda^2 - (b+f)\lambda + (bf - ce) = 0 \quad , \tag{A.5}$$

with roots (eigenvalues of the system of linear differential equations ((A.2) and (A.3)))

$$\lambda_\pm = \frac{b+f \pm \sqrt{(b+f)^2 - 4(bf-ce)}}{2} \qquad \text{or,} \tag{A.6}$$

$$\lambda_\pm = \frac{b+f \pm \sqrt{(b-f)^2 + 4ce}}{2} \quad . \tag{A.7}$$

The nature of the critical point as function of the eigenvalues is given in Table A.1, while a brief description of the behaviour of the solutions in the vicinity of the critical point is as follows:

- a *saddle* or *X-type* critical point is crossed by two solutions, each with a different slope,

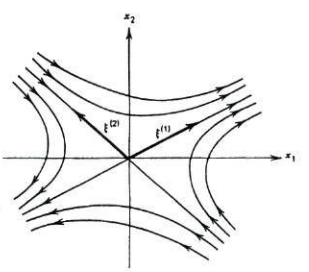

- a *node* is crossed by an infinite number of solutions. If it is a *proper node* then each solution has a different slope. If it is an *improper node* then only two slopes are allowed: an infinite number of solutions crosses the node with one of the slopes, and one solution crosses the node with the other slope,

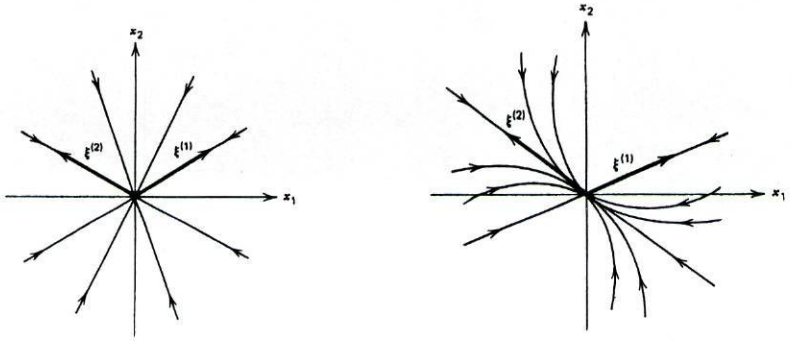

- a *spiral* critical point is not crossed by any solution, the trajectories around it being spirals,

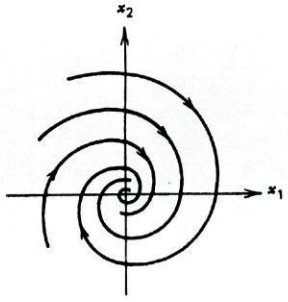

- a *center* critical point is not crossed by any solution, the trajectories around it being circles/ellipses.

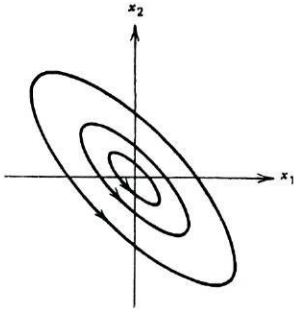

All the figures with the topology of the critical points shown were adapted from Boyce and DiPrima (1986).

In the case of an X-type critical point the slopes at the critical point of the two solutions that cross it can be computed from one of the following expressions

$$\left.\frac{\mathrm{d}y}{\mathrm{d}x}\right|_{\mathrm{c}} = \frac{\lambda - b}{c} \qquad \text{or} \qquad \left.\frac{\mathrm{d}y}{\mathrm{d}x}\right|_{\mathrm{c}} = \frac{e}{\lambda - f} \tag{A.8}$$

where λ is to be replaced by $\lambda_{\pm}$ given by Eq. (A.7).

A.2 The momentum equation

If spherical symmetry is assumed, then the relevant equations are:

-the perfect gas law

$$P = A\rho T \ , \qquad A = \frac{K_{\rm B}}{\mu m_H} \tag{A.9}$$

- the equation of mass continuity

$$\frac{\mathrm{d}}{\mathrm{d}R}(R^2 \rho V) = 0 \tag{A.10}$$

- the momentum equation

$$\rho V \frac{\mathrm{d}V}{\mathrm{d}R} = -\frac{\mathrm{d}P}{\mathrm{d}R} - \rho \frac{GM}{R^2} \tag{A.11}$$

After some algebra, the momentum equation can be written in the form:

$$\frac{1}{V}\left(V^2 - AT\right)\frac{\mathrm{d}V}{\mathrm{d}R} = \frac{2AT}{R} - A\frac{\mathrm{d}T}{\mathrm{d}R} - \frac{GM}{R^2} \tag{A.12}$$

There is a point $R_{\rm c}$ where the right-hand side of this equation vanishes, which implies that the derivative is zero or that $V_{\rm c}^2 = AT_{\rm c}$. When the later case occurs the point $R_{\rm c}$ is called a singularity or a critical point, since the derivative is given by an indetermination of the form $0/0$.

To overcome this indetermination it is necessary to classify the critical point. The first step is to normalize the equation to the critical point, by defining

$$a = \frac{R}{R_{\rm c}} \qquad \text{and} \qquad u = \frac{V}{V_{\rm c}} \tag{A.13}$$

getting the following expression for the momentum equation

$$\frac{1}{u}\left(u^2 - \tau\right)\frac{\mathrm{d}u}{\mathrm{d}a} = \frac{2\tau}{a} - \frac{\mathrm{d}\tau}{\mathrm{d}a} - \frac{GM}{R_{\rm c}V_{\rm c}^2 a^2} \tag{A.14}$$

where the fact that $V_{\rm c}^2 = AT_{\rm c}$ and the definition $\tau = T/T_{\rm c}$ have been used. At the critical point the right-hand side vanishes, i.e.,

$$2 - \left.\frac{\mathrm{d}\tau}{\mathrm{d}a}\right|_{\rm c} - \frac{GM}{R_{\rm c}V_{\rm c}^2} = 0 \tag{A.15}$$

The next step is to linearize the equation near the critical point ($a = 1$, $u = 1$), by defining

$$a = 1 + \delta \qquad \text{and} \qquad u = 1 + \epsilon \tag{A.16}$$

Since the radial distance is the only independent variable the temperature and its derivative can also be linearized by a Taylor's expansion around the "critical" temperature. Two different situations are possible, and are separately analysed in the following sections.

A.3 No explicit dependence of $\frac{d^2\tau}{da^2}\Big|_c$ on $\frac{du}{da}\Big|_c$

Assuming that the second derivative of the temperature does not depend explicitly on the derivative of the velocity the following linearized expressions are found

$$\tau = 1 + \frac{d\tau}{da}\bigg|_c \delta \qquad \text{and} \qquad \frac{d\tau}{da} = \frac{d\tau}{da}\bigg|_c + \frac{d^2\tau}{da^2}\bigg|_c \delta \tag{A.17}$$

and then the linearized momentum equation is

$$\left(-\frac{d\tau}{da}\bigg|_c \delta + 2\epsilon\right)\frac{d\epsilon}{d\delta} = \left[2\left(\frac{d\tau}{da}\bigg|_c - 1 + \frac{GM}{R_c V_c^2}\right) - \frac{d^2\tau}{da^2}\bigg|_c\right]\delta = \left(2 - \frac{d^2\tau}{da^2}\bigg|_c\right)\delta \tag{A.18}$$

Comparing with Eq. (A.1) the following expressions for the coefficients are found

$$\begin{aligned} b &= -\frac{d\tau}{da}\bigg|_c \\ c &= 2 \\ e &= 2 - \frac{d^2\tau}{da^2}\bigg|_c \\ f &= 0 \end{aligned} \tag{A.19}$$

A.4 Explicit dependence of $\frac{d^2\tau}{da^2}\Big|_c$ on $\frac{du}{da}\Big|_c$

$$\frac{d^2\tau}{da^2}\bigg|_c = \frac{\partial}{\partial a}\left(\frac{d\tau}{da}\right)\bigg|_c + \frac{\partial}{\partial u}\left(\frac{d\tau}{da}\right)\bigg|_c \frac{du}{da}\bigg|_c \tag{A.20}$$

A.4.1 Case a)

if $d\tau/da$ is linearized using

$$\frac{d\tau}{da} = \frac{d\tau}{da}\bigg|_c + \left[\frac{\partial}{\partial a}\left(\frac{d\tau}{da}\right)\bigg|_c + \frac{\partial}{\partial u}\left(\frac{d\tau}{da}\right)\bigg|_c \frac{du}{da}\bigg|_c\right]\delta \tag{A.21}$$

then the linearized momentum equation is:

$$\left[\left(\frac{\partial}{\partial u}\left(\frac{\mathrm{d}\tau}{\mathrm{d}a}\right)\Big|_{\mathrm{c}} - \frac{\mathrm{d}\tau}{\mathrm{d}a}\Big|_{\mathrm{c}}\right)\delta + 2\epsilon\right]\frac{\mathrm{d}\epsilon}{\mathrm{d}\delta} = \left[2\left(\frac{\mathrm{d}\tau}{\mathrm{d}a}\Big|_{\mathrm{c}} - 1 + \frac{GM}{R_{\mathrm{c}}V_{\mathrm{c}}^2}\right) - \frac{\partial}{\partial a}\left(\frac{\mathrm{d}\tau}{\mathrm{d}a}\right)\Big|_{\mathrm{c}}\right]\delta \quad \text{(A.22)}$$

and the coefficients

$$\begin{aligned} B &= \frac{\partial}{\partial u}\left(\frac{\mathrm{d}\tau}{\mathrm{d}a}\right)\Big|_{\mathrm{c}} - \frac{\mathrm{d}\tau}{\mathrm{d}a}\Big|_{\mathrm{c}} \\ C &= 2 \\ E &= 2 - \frac{\partial}{\partial a}\left(\frac{\mathrm{d}\tau}{\mathrm{d}a}\right)\Big|_{\mathrm{c}} \\ F &= 0 \end{aligned} \quad \text{(A.23)}$$

A.4.2 Case b)

if $\mathrm{d}\tau/\mathrm{d}a$ is linearized using

$$\frac{\mathrm{d}\tau}{\mathrm{d}a} = \frac{\mathrm{d}\tau}{\mathrm{d}a}\Big|_{\mathrm{c}} + \frac{\partial}{\partial a}\left(\frac{\mathrm{d}\tau}{\mathrm{d}a}\right)\Big|_{\mathrm{c}}\delta + \frac{\partial}{\partial u}\left(\frac{\mathrm{d}\tau}{\mathrm{d}a}\right)\Big|_{\mathrm{c}}\epsilon \quad \text{(A.24)}$$

then the linearized momentum equation is:

$$\left(-\frac{\mathrm{d}\tau}{\mathrm{d}a}\Big|_{\mathrm{c}}\delta + 2\epsilon\right)\frac{\mathrm{d}\epsilon}{\mathrm{d}\delta} = \left[2\left(\frac{\mathrm{d}\tau}{\mathrm{d}a}\Big|_{\mathrm{c}} - 1 + \frac{GM}{R_{\mathrm{c}}V_{\mathrm{c}}^2}\right) - \frac{\partial}{\partial a}\left(\frac{\mathrm{d}\tau}{\mathrm{d}a}\right)\Big|_{\mathrm{c}}\right]\delta - \frac{\partial}{\partial u}\left(\frac{\mathrm{d}\tau}{\mathrm{d}a}\right)\Big|_{\mathrm{c}}\epsilon \quad \text{(A.25)}$$

and the coefficients

$$\begin{aligned} b &= -\frac{\mathrm{d}\tau}{\mathrm{d}a}\Big|_{\mathrm{c}} \\ c &= 2 \\ e &= 2 - \frac{\partial}{\partial a}\left(\frac{\mathrm{d}\tau}{\mathrm{d}a}\right)\Big|_{\mathrm{c}} \\ f &= -\frac{\partial}{\partial u}\left(\frac{\mathrm{d}\tau}{\mathrm{d}a}\right)\Big|_{\mathrm{c}} \end{aligned} \quad \text{(A.26)}$$

the coefficients are related by: $B = b - f$, $C = c$ and $E = e$. The eigenvalues are :

$$\Lambda_{\pm} = \frac{B + F \pm \sqrt{(B-F)^2 + 4ce}}{2} \quad \text{(A.27)}$$

and

$$\lambda_{\pm} = \frac{b \pm \sqrt{b^2 + 4ce}}{2} = \Lambda_{\pm} + f \quad \text{(A.28)}$$

The eigenvalues obtained by the two methods differ by the quantity f, which can affect the nature of the critical point.

The critical slopes are given by:

$$\left.\frac{du}{da}\right|_c = \frac{\Lambda - B}{c} = \frac{-B \pm \sqrt{B^2 + 4CE}}{2C} \tag{A.29}$$

and

$$\left.\frac{du}{da}\right|_c = \frac{\lambda - b}{c} = \frac{-b + f \pm \sqrt{B^2 + 4CE}}{2C} = \frac{-B \pm \sqrt{B^2 + 4CE}}{2C} \tag{A.30}$$

which shows that the slopes obtained by the two different choices for the linearization of $d^2\tau/da^2$ are the same.

A.4.3 Changing nature of the critical point

In the previous Section it was shown that the nature of the critical point could depend on the choice of the linearization of $d\tau/da$. Looking at Table A.1 the only cases where this change can occur are case 1 and 2, improper node and saddle, respectively. Two different cases must be considered:

assume $\Lambda_- < 0 < \Lambda_+$ a saddle critical point

if $f > 0$ and $|\Lambda_-| < f$ then $0 < \lambda_- < \lambda_+$ improper node
if $f < 0$ and $\Lambda_+ < |f|$ then $\lambda_- < \lambda_+ < 0$ improper node

and conversely for the λ's

assume $\lambda_- < 0 < \lambda_+$ a saddle critical point

if $f > 0$ and $\lambda_+ < f$ then $\Lambda_- < \Lambda_+ < 0$ improper node
if $f < 0$ and $|\lambda_-| < |f|$ then $0 < \Lambda_- < \Lambda_+$ improper node

This shows that for $|f| > |\Lambda_\pm|$ or $|f| > |\lambda_\pm|$ the nature of the critical point seems to be undetermined, whether it is an improper node or a saddle, although the two different slopes allowed in these types of topology are independent of the method used for the linearization.

The solution for this ambiguity comes from the linearization of u:

$$u = 1 + \left.\frac{\mathrm{d}u}{\mathrm{d}a}\right|_{\mathrm{c}} \delta = 1 + \epsilon \tag{A.31}$$

in case b) the factor $\delta \cdot \mathrm{d}u/\mathrm{d}a|_{\mathrm{c}}$ is replaced by ϵ, while in case a) it is not. However, in case a) u is not linearized in the same way as $\mathrm{d}\tau/\mathrm{d}a$, if it were, then the linearized momentum equation will be:

$$\left[\left(2 + \frac{\partial}{\partial u}\left(\frac{\mathrm{d}\tau}{\mathrm{d}a}\right)\right|_{\mathrm{c}} - \left.\frac{\mathrm{d}\tau}{\mathrm{d}a}\right|_{\mathrm{c}}\right)\delta\Bigg]\frac{\mathrm{d}\epsilon}{\mathrm{d}\delta} = \left[2\left(\left.\frac{\mathrm{d}\tau}{\mathrm{d}a}\right|_{\mathrm{c}} - 1 + \frac{GM}{R_{\mathrm{c}}V_{\mathrm{c}}^2}\right) - \frac{\partial}{\partial a}\left(\frac{\mathrm{d}\tau}{\mathrm{d}a}\right)\right|_{\mathrm{c}}\Bigg]\delta \tag{A.32}$$

or, as $\mathrm{d}\epsilon/\mathrm{d}\delta = \mathrm{d}u/\mathrm{d}a|_{\mathrm{c}}$, and $\delta > 0$

$$2\left(\left.\frac{\mathrm{d}u}{\mathrm{d}a}\right|_{\mathrm{c}}\right)^2 + \left(\frac{\partial}{\partial u}\left(\frac{\mathrm{d}\tau}{\mathrm{d}a}\right)\right|_{\mathrm{c}} - \left.\frac{\mathrm{d}\tau}{\mathrm{d}a}\right|_{\mathrm{c}}\right)\left.\frac{\mathrm{d}u}{\mathrm{d}a}\right|_{\mathrm{c}} - 2\left(\left.\frac{\mathrm{d}\tau}{\mathrm{d}a}\right|_{\mathrm{c}} - 1 + \frac{GM}{R_{\mathrm{c}}V_{\mathrm{c}}^2}\right) + \frac{\partial}{\partial a}\left(\frac{\mathrm{d}\tau}{\mathrm{d}a}\right)\Bigg|_{\mathrm{c}} \tag{A.33}$$

this is a second order equation on $\mathrm{d}u/\mathrm{d}a|_{\mathrm{c}}$ and its solution gives the same expressions for the critical slopes as obtained before. But in this case it is not possible to classify the nature of the critical point.

From the previous discussion it is shown that case b) for the linearization of $\mathrm{d}^2\tau/\mathrm{d}a^2$ is the one to retain, as it is self-consistent, and therefore gives the true classification of the critical point.

Bibliography

Alazraki, G. and Couturier, P.: 1971, *Astron. Astrophys.* **13**, 380

Alcalá, J. M., Krautter, J., Covino, E., Neuhaeuser, R., Schmitt, J. H. M. M., and Wichmann, R.: 1997, *Astron. Astrophys.* **319**, 184

Alcalá-Estrada, J. M.: 1995, Ph.D. thesis, Ruprecht-Karls-Universitat, Heildelberg

Allphenaar, P. and van Leeuwen, F.: 1981, *Inf. Bull. Variable Stars* 1957

Appenzeller, I., Jankovics, I., and Östreicher, R.: 1984, *Astron. Astrophys.* **141**, 108

Attridge, J. M. and Herbst, W.: 1992, *Astrophys. J.* **398**, L61

Axford, W. I., Dressler, A. J., and Gottlieb, B.: 1963, *Astrophys. J.* **137**, 1268

Beals, C. S.: 1950, *Publ. Dom. Astrophys. Obs.* **9**, 1

Belcher, J. W.: 1971, *Astrophys. J.* **168**, 509

Belcher, J. W. and MacGregor, K. B.: 1976, *Astrophys. J.* **210**, 498

Benz, W. and Mayor, M.: 1981, *Astron. Astrophys.* **93**, 235

Beristain, G., Edwards, S., and Kwan, J.: 2001, *He emission from CTTS: dual origin in magnetospheric infall and hot wind*, accepted for publication by *Astrophys. J.*

Bertout, C.: 1989, *Ann. Rev. Astron. Astrophys.* **27**, 351

Biermann, L.: 1957, *Observatory* **77**, 109

Bouvier, J. and Bertout, C.: 1989a, *Astron. Astrophys.* **211**, 99

Bouvier, J. and Bertout, C.: 1989b, *Astron. Astrophys.* **218**, 337

Bouvier, J., Bertout, C., Benz, W., and Mayor, M.: 1986, *Astron. Astrophys.* **165**, 110

Bouvier, J., Cabrit, S., Fernández, M., Martín, E. L., and Matthews, J. M.: 1993, *Astron. Astrophys.* **272**, 176

Bouvier, J., Covino, E., Kovo, O., Martín, E. L., Matthews, J. M., Terranegra, L., and Beck, S. C.: 1995, *Astron. Astrophys.* **299**, 89

Boyce, W. E. and DiPrima, R. C.: 1986, *Elementary Differential Equations and Boundary Value Problems*, p. 443, John Wiley & Sons

Calvet, N., Hartmann, L., and Hewett, R.: 1992, *Astrophys. J.* **386**, 229

Canullo, M. V., Costa, A., and Ferro-Fontán, C.: 1996, *Astrophys. J.* **462**, 1005

Chamberlain, J. W.: 1961, *Astrophys. J.* **133**, 675

Choi, P. I. and Herbst, W.: 1996, *Astron. J.* **111(1)**, 283

Choudhuri, A. R.: 1998, *The Physics of Fluids and Plasmas: an Introduction for*

Astrophysicists, Cambdridge University Press

Cohen, M., Emerson, J., and Beichman, C.: 1989, *Astrophys. J.* **339**, 455

Cohen, M. and Kuhi, L. V.: 1979, *Astrophys. J., Suppl. Ser.* **41**, 743

Cook, D. M.: 1975, *The Theory of the Electromagnetic Field*, Prentice-Hall Physics Series, Prentice-Hall, New Jersey

Cook, J. W., Cheng, C.-C., Jacobs, V., and Antiochos, S. K.: 1989, *Astrophys. J.* **338**, 1176

Costa, V. M.: 2000, Ph.D. thesis, Universidade do Porto, Portugal

Couturier, P.: 1977, *Astron. Astrophys.* **59**, 239

Cox, D. P. and Tucker, W. H.: 1969, *Astrophys. J.* **157**, 1157

Cross, R.: 1982, *An Introduction to Alfvén Waves*, The Adam Hilger Series on Plasma Physics, Adam Hilger, Bristol and Philadelphia

Cuperman, S., Harten, A., and Dryer, M.: 1972, *Astrophys. J.* **177**, 555

Cuperman, S. and Metzler, N.: 1973, *Astrophys. J.* **182**, 961

Cuperman, S. and Metzler, N.: 1975, *Astrophys. J.* **196**, 205

Cuperman, S., Metzler, N., and Spiegelglass, M.: 1975, *Astrophys. J.* **198**, 755

Cuseri, I., Mullan, D., Noci, G., and Poletto, G.: 1999, *Astrophys. J.* **514**, 989

DeCampli, W. M.: 1981, *Astrophys. J.* **244**, 124

del Zanna, L.: 1998, Private communication

Dubath, P., Reipurth, B., and Mayor, M.: 1996, *Astron. Astrophys.* **308**, 107

Duncan, D. K.: 1993, *Astrophys. J.* **406**, 172

Durney, B. R.: 1971, *Astrophys. J.* **166**, 669

Durney, B. R.: 1973, *Sol. Phys.* **30**, 223

Dyck, H. M., Simon, T., and Zuckerman, B.: 1982, *Astrophys. J.* **255**, L103

Eaton, N. L., Herbst, W., and Hillenbrand, L. A.: 1995, *Astron. J.* **110(4)**, 1735

Edwards, S., Cabrit, S., Strom, S. E., Heyer, I., Strom, K. M., and Anderson, E.: 1987, *Astrophys. J.* **321**, 473

Edwards, S., Strom, S. E., Hartigan, P., Strom, K. M., Hillenbrand, L. A., Herbst, W., Attridge, J., Merrill, K. M., Probst, R., and Gatley, I.: 1993, *Astron. J.* **106(1)**, 372

Esser, R., Leer, E., Habbal, S. R., and Withbroe, G. L.: 1986, *J. Geophys. Res.* **91**, 2950

Favata, F., Micela, G., and Sciortino, S.: 1997, *Astron. Astrophys.* **326**, 647

Feigelson, E. and Nelson, P.: 1985, *Astrophys. J.* **293**, 192

Franchini, M., Magazzù, A., and Stalio, R.: 1988, *Astron. Astrophys.* **189**, 132

Gahm, G. F.: 1980, *Astrophys. J.* **242**, L163

Gameiro, J. F. and Lago, M. T. V. T.: 1993, *Mon. Not. R. Astron. Soc.* **265**, 359

Ghez, A. M., Neugebauer, G., Gorham, P. W., Haniff, C. A., Kulkarni, S. R., Matthews, K., Koresko, C., and Beckwith, S.: 1991, *Astron. J.* **102(6)**, 2066

Ghez, A. M., White, R. J., and Simon, M.: 1997, *Astrophys. J.* **490**, 353

Giovanardi, C., Lizano, S., Nattta, A., Evans II, N. J., and Heiles, C.: 1992, *Astrophys.*

J. **397**, 214

Grankin, K.: 1993, *Inf. Bull. Variable Stars* 3823

Grankin, K.: 1994, *Inf. Bull. Variable Stars* 4042

Grankin, K.: 1996, *Inf. Bull. Variable Stars* 4316

Grankin, K., Ibragimov, M., Melnikov, S., Shevchenko, V., and Yakubov, S.: 1991, *Inf. Bull. Variable Stars* 3658

Gray, D. F.: 1992, *The observation and analysis of stellar photosphres*, Cambridge University Press

Gregorio-Hetem, J., Montmerle, T., Casanova, S., and Feigelson, E. D.: 1998, *Astron. Astrophys.* **331**, 193

Grinin, V. P. and Mitskevich, A. S.: 1991, *Astrophys. Space. Sci.* **185**, 107

Grosso, N., Montmerle, T., Bontemps, S., André, P., and Feigelson, E. D.: 2000, *Astron. Astrophys.* **359**, 113

Guenther, E. W., Lehmann, H., Emerson, J. P., and Staude, J.: 1999, *Astron. Astrophys.* **341**, 768

Guenther, E. W., Stelzer, B., Neuhäuser, R., Hillwig, T. C., Durisen, R. H., Menten, K. M., Greimel, R., Barwig, H., Englhauser, J., and Robb, R. M.: 2000, *Astron. Astrophys.* **357**, 206

Hammer, R.: 1982a, *Astrophys. J.* **259**, 767

Hammer, R.: 1982b, *Astrophys. J.* **259**, 779

Hartigan, P., Strom, K. E., and Strom, S. E.: 1994, *Astrophys. J.* **427**, 961

Hartle, R. E. and Sturrock, P. A.: 1968, *Astrophys. J.* **151**, 1155

Hartmann, L.: 1982, *Astrophys. J., Suppl. Ser.* **48**, 109

Hartmann, L., Hewett, R., Stahler, S., and Mathieu, R. D.: 1986, *Astrophys. J.* **309**, 275

Hartmann, L., Soderblom, D., and Stauffer, J. R.: 1987, *Astron. J.* **93(4)**, 907

Hartmann, L. and Stauffer, J. R.: 1989, *Astron. J.* **97(3)**, 873

Hartmann, L. W., Calvet, N., Avrett, E. H., and Loeser, R.: 1990, *Astrophys. J.* **349**, 168

Hartmann, L. W., Edwards, S., and Avrett, E.: 1982, *Astrophys. J.* **261**, 279

Herbig, G. H.: 1952, *J.R.A.S. Can* **46**, 222

Herbig, G. H.: 1957, *Astrophys. J.* **125**, 612

Herbig, G. H.: 1962, *Adv. Astron. and Astrophys.* **1**, 47

Herbig, G. H.: 1977, *Astrophys. J.* **214**, 747

Herbig, G. H.: 1983, in R. Lucas, A. Omont, and R. Stora (eds.), *Birth and Infancy of Stars*, p. 535, Elsevier Science Publishers B. V.

Herbig, G. H. and Bell, K. R.: 1988, *Lick Obs. Bull.* **1111**, 1

Herbig, G. H. and Goodrich, R. W.: 1986, *Astrophys. J.* **309**, 294

Herbst, W., Booth, J. F., Chugainov, P. F., Barksdale, G. Z. W., Covino, E., Terranegra, L., and Vrba, F.: 1986, *Astrophys. J.* **310**, L71

Heyvaerts, J. and Priest, E. R.: 1983, *Astron. Astrophys.* **117**, 220

Hoff, W., Henning, T., and Pfau, W.: 1998, *Astron. Astrophys.* **336**, 242
Hollweg, J. V.: 1973, *Astrophys. J.* **181**, 547
Hollweg, J. V.: 1974, *J. Geophys. Res. A* **79**, 3845
Hollweg, J. V.: 1976, *J. Geophys. Res. A* **81**, 1649
Hollweg, J. V.: 1986, *J. Geophys. Res. A* **91**, 4111
Hollweg, J. V. and Johnson, W.: 1988, *J. Geophys. Res. A* **93**, 9547
Holzer, T. E.: 1977, *J. Geophys. Res. A* **82**, 23
Holzer, T. E. and Leer, E.: 1980, *J. Geophys. Res. A* **85**, 4665
Hood, A. W., Ireland, J., and Priest, E. R.: 1997, *Astron. Astrophys.* **318**, 957
Hu, Y. Q. and Low, B. C.: 1989, *Astrophys. J.* **342**, 1049
Ionson, J. A.: 1978, *Astrophys. J.* **226**, 650
Isobe, T., Feigelson, E., and Nelson, P.: 1986, *Astrophys. J.* **306**, 490
Jacques, S. A.: 1977, *Astrophys. J.* **215**, 942
Jacques, S. A.: 1978, *Astrophys. J.* **226**, 632
Jankovics, I., Appenzeller, I., and Krautter, J.: 1983, *Publ. Astron. Soc. Pac.* **95**, 883
Jones, B. F. and Herbig, G. H.: 1979, *Astron. J.* **84**, 1872
Joy, A. H.: 1942, *Publ. Astron. Soc. Pac.* **54**, 15
Joy, A. H.: 1945, *Astrophys. J.* **102**, 168
Joy, A. H.: 1949, *Astrophys. J.* **110**, 424
Kearns, K. E., Eaton, N. L., Herbst, W., and Mazzurco, C. J.: 1997, *Astron. J.* **114(3)**, 1098
Kenyon, S. and Hartmann, L.: 1990, *Astrophys. J.* **349**, 197
Khabibrakhmanov, I. K. and Mullan, D. J.: 1994, *Astrophys. J.* **430**, 814
Kiguchi, M., Narita, S., and Hayashi, C.: 1998, *Publ. Astron. Soc. Jpn.* **50**, 587
Kraus, J. D. and Carver, K. R.: 1986, *Electromagnetismo*, Editora Guanabara, Rio de Janeiro, second edition
Krishnamurthi, A., Pinsonneault, M. H., Barnes, S., and Sofia, S.: 1997, *Astrophys. J.* **480**, 303
Kudoh, T. and Shibata, K.: 1997, *Astrophys. J.* **474**, 362
Kuhi, L. V.: 1964, *Astrophys. J.* **140**, 1409
Lada, C. J.: 1985, *Ann. Rev. Astron. Astrophys.* **23**, 267
Lago, M. T. V. T.: 1982, *Mon. Not. R. Astron. Soc.* **198**, 445
Lago, M. T. V. T.: 1984, *Mon. Not. R. Astron. Soc.* **210**, 323
Lago, M. T. V. T.: 1988, in A. K. Dupree and M. T. V. T. Lago (eds.), *Formation and evolution of low mass stars*, NATO ASI-241, p. 209
Lamzin, S. A., Bisnovatyi-Kogan, G. S., Errico, L., Giovannelli, F., Katysheva, N. A., Rossi, C., and Vittone, A. A.: 1996, *Astron. Astrophys.* **306**, 877
Li, Z.-Y.: 1996, *Astrophys. J.* **465**, 855
Lim, J. and White, S. M.: 1996, *Astrophys. J.* **462**, L91

Lima, J. J. G., Priest, E. R., and K.Tsinganos: 2001, *An analytical MHD wind model with latitudinal dependences obtained using separation of the variables*, accepted for publication by *Astron. Astrophys.*

Lindsey, C. and Jefferies, J. T.: 1990, *Astrophys. J.* **349**, 286

Low, B. C. and Tsinganos, K.: 1986, *Astrophys. J.* **302**, 163

Lucas, R. D.: 1973, *Astrophys. J.* **186**, 275

MacGregor, K. B. and Brenner, M.: 1991, *Astrophys. J.* **376**, 204

Machado, L. J. R.: 1995, M.Sc. dissertation, Universidade do Porto, Portugal

Maihara, T. and Kataza, H.: 1991, *Astron. Astrophys.* **249**, 392

Mandel, G. N. and Herbst, W.: 1991, *Astrophys. J.* **383**, L75

Mestel, L.: 1968a, *Mon. Not. R. Astron. Soc.* **138**, 359

Mestel, L.: 1968b, *Mon. Not. R. Astron. Soc.* **140**, 177

Mestel, L. and Selley, C. S.: 1970, *Mon. Not. R. Astron. Soc.* **149**, 197

Mitskevich, A. S.: 1994, *Astron. Astrophys.* **281**, 471

Mitskevich, A. S.: 1995a, *Astron. Astrophys.* **298**, 219

Mitskevich, A. S.: 1995b, *Astron. Astrophys.* **298**, 231

Mitskevich, A. S., Natta, A., and Grinin, V. P.: 1993, *Astrophys. J.* **404**, 751

Montmerle, T., Koch-Miramond, L., Falgarone, E., and Grindlay, J. E.: 1983, *Astrophys. J.* **269**, 182

Mundt, R.: 1984, *Astrophys. J.* **280**, 749

Mundt, R., Walter, F., Feigelson, E., Finkenzeller, U., Herbig, G., and Odell, A.: 1983, *Astrophys. J.* **269**, 229

Munro, R. H. and Jackson, B. V.: 1977, *Astrophys. J.* **213**, 874

Natta, A.: 1989, *Rev. Mexicana Astron. Astrof.* **18**, 29

Natta, A.: 1992, in L. Drissen, C. Leitherer, and A. Natta (eds.), *Nonisotropic and Variable Outflows from Stars*, Vol. 22 of *ASP Conference Series*, p. 18, Astronomical Society of the Pacific

Natta, A. and Giovanardi, C.: 1990, *Astrophys. J.* **356**, 646

Natta, A., Giovanardi, C., Palla, F., and Evans II, N. J.: 1988a, *Astrophys. J.* **327**, 817

Natta, A., Giovanardi, C., and Palla, F.: 1988b, *Astrophys. J.* **332**, 921

Nerney, S. F. and Suess, S. T.: 1975, *Astrophys. J.* **196**, 837

Neuhäuser, R.: 1996, in *Roentgenstrahlung from the Universe*, p. 13

Neuhäuser, R., Sterzik, M. F., Schmitt, J. H. M. M., Wichmann, R., and Krautter, J.: 1995, *Astron. Astrophys.* **297**, 391

Neuhäuser, R., Torres, G., Sterzik, M. F., and Randich, S.: 1997, *Astron. Astrophys.* **325**, 647

Nisenson, P., Stachnik, R. V., Karovska, M., and Noyes, R.: 1985, *Astrophys. J.* **297**, L17

Nobili, L. and Turolla, R.: 1988, *Astrophys. J.* **333**, 248

Noble, L. M. and Scarf, F. L.: 1963, *Astrophys. J.* **138**, 1169

Osterloh, M., Thommes, E., and Kania, U.: 1996, *Astron. Astrophys. Suppl. Ser.* **120**, 267

Paatz, G. and Camenzind, M.: 1996, *Astron. Astrophys.* **308**, 77

Palla, F. and Stahler, S. W.: 1999, *Astrophys. J.* **525**, 772

Parker, E. N.: 1958, *Astrophys. J.* **128**, 664

Parker, E. N.: 1960, *Astrophys. J.* **132**, 175

Parker, E. N.: 1964, *Astrophys. J.* **139**, 93

Parker, E. N.: 1965, *Astrophys. J.* **141**, 1463

Parker, E. N.: 1988, *Astrophys. J.* **330**, 474

Penston, M. V. and Lago, M. T. V. T.: 1982, in E. J. Rolfe, A. Heck, and B. Battrick (eds.), *Third European IUE Conference*, p. 95, ESA SP-176

Petrov, P. P., Gullbring, E., Ilyin, I., Gahm, G. F., Tuominen, I., Hackman, T., and Lodén, K.: 1996, *Astron. Astrophys.* **314**, 821

Preibisch, T.: 1997, *Astron. Astrophys.* **320**, 525

Priest, E. R.: 1982, *Solar Magnetohydrodynamics*, Geophysics and Astrophysics Monographs, Reidel Publishing Company

Prosser, C., Shetrone, M., Dasgupta, A., Backman, D., Laaksonen, B., Baker, S., Marschall, L., Whitney, B., Kuijken, K., and Stauffer, J.: 1995, *Publ. Astron. Soc. Pac.* **107**, 211

Raymond, J. C., Cox, D. P., and Smith, B. W.: 1976, *Astrophys. J.* **204**, 290

Roberts, P. H. and Soward, A. M.: 1972, *Proc. R. Soc. London, Ser. A* **A328**, 185

Rosner, R., Tucker, W. H., and Vaiana, G. S.: 1978, *Astrophys. J.* **220**, 643

Roxburgh, I. W.: 1974, *Astrophys. J.* **191**, 557

Rydgren, A. and Vrba, F.: 1983, *Astrophys. J.* **267**, 191

Rydgren, A., Zak, D., Vrba, F., Chugainov, P., and Zajtseva, G.: 1984, *Astron. J.* **89(7)**, 1015

Sandbæk, Ø. and Leer, E.: 1994, *Astrophys. J.* **423**, 500

Sandbæk, Ø. and Leer, E.: 1995, *Astrophys. J.* **454**, 486

Sandbæk, Ø., Leer, E., and Hansteen, V. H.: 1994, *Astrophys. J.* **436**, 390

Sauty, C.: 1993, Ph.D. thesis, Université Paris VII, Paris

Sauty, C. and Tsinganos, K.: 1994, *Astron. Astrophys.* **287**, 893

Sauty, C., Tsinganos, K., and Trussoni, E.: 1999, *Astron. Astrophys.* **348**, 327

Schmitt, J. H. M. M., Fleming, T. A., and Giampapa, M. S.: 1995, *Astrophys. J.* **450**, 392

Shu, F., Najita, J., Ostriker, E., Wiljin, F., Ruden, S., and Lizano, S.: 1994a, *Astrophys. J.* **429**, 781

Shu, F. H., Najita, J., Ruden, S. P., and Lizano, S.: 1994b, *Astrophys. J.* **429**, 797

Simon, T., Vrba, F. J., and Werbst, W.: 1990, *Astron. J.* **100(6)**, 1957

Skumanich, A.: 1972, *Astrophys. J.* **171**, 565

Smith, M. A., Beckers, J. M., and Barden, S. C.: 1983, *Astrophys. J.* **271**, 237

Soderblom, D. R.: 1999, *Astrophys. Space. Sci.* **261**, 59

Soderblom, D. R. and Mayor, M.: 1993, *Astrophys. J.* **402**, L5

Soderblom, D. R., Stauffer, J. R., MacGregor, K. B., and Jones, B. F.: 1993, *Astrophys. J.* **409**, 624

Spitzer, L.: 1952, *Astrophys. J.* **116**, 299

Spitzer, L.: 1956, *Physics of fully ionized gases*, Interscience Publishers, Inc, New York

Spitzer, L.: 1962, *Physics of fully ionized gases*, Interscience Publishers, Inc, New York

Stassun, K. G., Mathieu, R. D., Mazeh, T., and Vrba, F. J.: 1999, *Astron. J.* **117**, 2941

Strom, K., Strom, S., Edwards, S., Cabrit, S., and Skrutskie, M.: 1989, *Astron. J.* **97(5)**, 1451

Strom, S. E.: 1972, *Publ. Astron. Soc. Pac.* **84**, 502

Suess, S. T. and Nerney, S. F.: 1973, *Astrophys. J.* **184**, 17

Trussoni, E. and Tsinganos, K.: 1993, *Astron. Astrophys.* **269**, 589

Trussoni, E., Tsinganos, K., and Sauty, C.: 1997, *Astron. Astrophys.* **325**, 1099

Tsinganos, K.: 1981, *Astrophys. J.* **245**, 764

Tsinganos, K.: 1982, *Astrophys. J.* **252**, 775

Tsinganos, K.: 1994, *An Introduction to Plasma Astrophysics*, University of Crete, Lecture Notes for 'A European Masters Degree in Astronomy'

Tsinganos, K. and Low, B. C.: 1989, *Astrophys. J.* **342**, 1028

Tsinganos, K. and Sauty, C.: 1992a, *Astron. Astrophys.* **255**, 405

Tsinganos, K. and Sauty, C.: 1992b, *Astron. Astrophys.* **257**, 790

Tsinganos, K. and Trussoni, E.: 1990, *Astron. Astrophys.* **231**, 270

Tsinganos, K. and Trussoni, E.: 1991, *Astron. Astrophys.* **249**, 156

Tu, C.-Y.: 1987, *Sol. Phys.* **109**, 149

Vogel, S. N. and Kuhi, L. V.: 1981, *Astrophys. J.* **245**, 960

Vrba, F. J., Chugainov, P. F., Weaver, W. B., and Stauffer, J. S.: 1993, *Astron. J.* **106(4)**, 1608

Vrba, F. J., Rydgren, A. E., Chugainov, P. F., Shakovskaya, N. I., and Weaver, W. B.: 1989, *Astron. J.* **97(2)**, 483

Vrba, F. J., Rydgren, A. E., Chugainov, P. F., Shakovskaya, N. I., and Zak, D. S.: 1986, *Astrophys. J.* **306**, 199

Walker, M. F.: 1990, *Publ. Astron. Soc. Pac.* **102**, 726

Walter, F. M., Brown, A., Mathieu, R. D., Myers, P. C., and Vrba, F. J.: 1988, *Astron. J.* **96(1)**, 297

Wang, Y. C. and Chang, C. C.: 1965, *J. Geophys. Res.* **70**, 4175

Wang, Y.-M.: 1993, *Astrophys. J.* **410**, L123

Wang, Y.-M.: 1994, *Astrophys. J.* **435**, L153

Weaver, W. B.: 1987, *Astrophys. J.* **319**, L89

Weber, E. J.: 1970, *Sol. Phys.* **14**, 480

Weber, E. J. and Davis, L. J.: 1967, *Astrophys. J.* **148**, 217

Weinberg, S.: 1962, *Phys. Rev.* **126**, 1899

Wichmann, R., Torres, G., Melo, C. H. F., Frink, S., Allain, S., Bouvier, J., Krautter, J., Covino, E., and Neuhäuser, R.: 2000, *Astron. Astrophys.* **359**, 181

Withbroe, G. L.: 1988, *Astrophys. J.* **325**, 442

Zakirov, M. M., Azimov, A. A., and Grankin, K.: 1993, *Inf. Bull. Variable Stars* 3898

Publications

ROTATION OF T TAURI STARS REVISITED

L.J.R.MACHADO
Centro de Astrofísica da Universidade do Porto
Rua do Campo Alegre, 823, 4150 Porto - Portugal

AND

M.T.V.T. LAGO AND J.J.G. LIMA
Centro de Astrofísica da Universidade do Porto
Departamento de Matemática Aplicada, FCUP

Abstract. This paper reviews the rotation of T Tauri stars. It summarizes the results of a complete bibliographical survey of all photometric and spectroscopic data available in connection with rotation studies of these stars. It is shown that T Tauri stars are slow rotators. More than half of the stars in the sample have been found to have $v \sin i < 25$ km/s.

Furthermore, the histogram for the photometric periods of rotation is clearly bimodal, with a peak at approximately 3 days and another at around 8 days.

1. Introduction

T Tauri stars (TTS) are low-mass (up to 3 $M_\odot$) pre-main-sequence stars of spectral types G to M (Herbig, 1983). They usually show H_α in emission and Li λ6707 in absorption, an indication of their youth. TTS can be separated in two classes: Classical TTS (CTTS) and Weak-line TTS (WTTS). CTTS have equivalent width of H_α ($W(H_\alpha)$) larger than 10Å and an infrared excess, WTTS have $W(H_\alpha) < 10$Å and a spectral energy distribution similar to that of a main-sequence star.

TTS were initially thought to rotate fast since being very young they would still be contracting towards the main-sequence. However the measurements of ($v \sin i$) made by Vogel and Kuhi (1981) showed for the first time that they are in fact slow rotators.

2. Rotational velocities and photometric periods

The rotational velocities can be measured either by the Fourier transform (Gray, 1992) or the cross-correlation methods (Benz and Mayor, 1981).

Combining the measurements of $v \sin i$ available in the literature we have built the histogram shown in Fig. 1 (left). The precision of the results

Astrophysics and Space Science is the original source of publication of his article. It is recommended that this article is cited as: *Astrophysics and Space Science* **261**: 69–70, 1999.

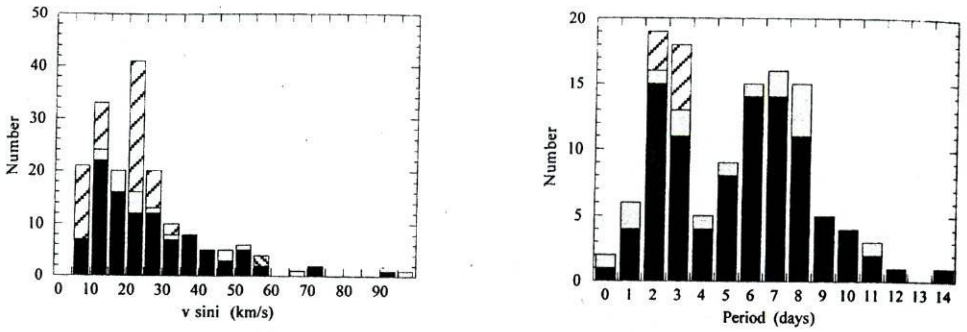

Figure 1. **left:** Histogram of the projected rotational velocity of TTS. **right:** Histogram of the rotational period of TTS. Dark grey are secure measurements of the quantity, light grey are uncertain measurements and the oblique stripes are upper limits.

has been taken into account. Around 62% of the 185 stars in this sample have $v \sin i < 25$km/s confirming the results of Vogel and Kuhi.

Some TTS show periodic changes in various photometric bands which are assumed to be associated with the presence of stellar spots. A periodogram is computed to determine the period.

The histogram shown in Fig. 1 (right) combines all available measurements of the rotational period. The distribution is clearly bimodal, with peaks around 3 and 8 days.

3. Discussion

Since TTS are slow rotators they must have lost angular momentum at some stage before this phase. An efficient way to loose angular momentum is through a magnetized stellar wind. However, to explain the slowest rotators another mechanism may in some cases be needed. A magnetic linkage at a very early phase between the protostar and a circumstellar disk is a possibility.

The bimodality in the histogram of the photometric period can be explained by the separation in the two classes CTTS and WTTS. On average CTTS rotate slower than WTTS. This could be due either to the presence of strong magnetic winds or a circumstellar disk.

Acknowledgments

L.J.R.M. acknowledges grant BD/5585/95 from PRAXIS XXI

References

Benz, W. and Mayor, M. (1981), *A&A*, **93**, p.235
Gray, D.F. (1992), in *The Observations and Analysis of Stellar Photospheres*
Herbig, G.H. (1983), in *Birth and Infancy of Stars*, p.535
Vogel, S.N. and Kuhi, L.V. (1981), *ApJ*, **245**, p.960

THE SIGNATURES OF STRUCTURED WINDS IN T TAURI STARS

MARIA TERESA V.T. LAGO AND JORGE F. GAMEIRO
Centro de Astrofísica da Universidade do Porto
Rua do Campo Alegre, 823, 4150 Porto - Portugal
Departamento de Matemática Aplicada, FCUP
VITOR M. COSTA
Centro de Astrofísica da Universidade do Porto
Departamento de Matemática, ISEP
AND
LEANDRO MACHADO AND ANTÓNIO PEDROSA
Centro de Astrofísica da Universidade do Porto

1. Introduction

The identification of He I lines λ 4471.5 Å, λ 5875.6 Å, λ 6678.1 Åand He II lines λ 4685.7 Åin emission in the optical spectra of T Tauri stars (e.g. Penston & Keavey 1977, Lago & Penston 1982) was the first clear indication for a temperature structure in the outer layers of these stars. Yet no immediate explanation was proposed for the presence of those high temperature regions in the atmosphere of late type stars.

The ultraviolet spectra later obtained with IUE showing emission lines from metals at various stages of ionization, for example, C I, C II, C III and CIV or Si II, Si III and Si IV, provided further evidence for the temperature structure in the atmosphere. An example is shown in Fig. 1 were the emission at various temperatures received from several T Tauri stars is displayed after normalization for the solar values. Moreover it allowed a quantification in terms of flux or emission measure from the regions contributing to the various lines.

Fig. 1 also shows that the emission from regions of temperature $\geq 10^4$ K far exceeds that observed in the Sun. Furthermore, while some T Tauri stars reach a peak emission just below T $\approx 10^5$ K, for other stars $f_*/f_\odot$

Astrophysics and Space Science is the original source of publication of his article. It is recommended that this article is cited as: *Astrophysics and Space Science* **261**: 107–116, 1999.

clearly keeps on rising until 10^7 K at least. This is an interesting result and a fundamental clue for the structure of the outer layers in T Tauri stars. Simultaneously it provides a tight constraint for the selection of mechanisms powering the activity, which is so very enhanced in these young stars. In this context we are analysing a sample of 25 T Tauri stars using both the IUE Newly Extracted Spectra (INES) and ROSAT Public Data Archives. A first paper focused on three TTS, namely, TW Hya, V410 Tau and CS Cha has been submitted (Costa et al. 1999).

We hope that the study of the UV and X-ray observations of such relatively large sample will help us to understand both the observed differences between the various T Tauri stars and the correlation of such differences with alternative mechanisms operating there.

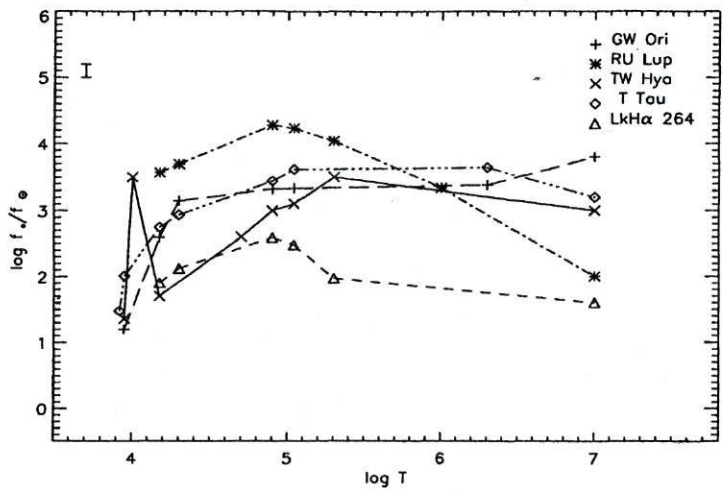

Figure 1. Ratio of stellar to solar surface fluxes for TTS as a function of temperature. For V410 Tau the X-ray flux is an average of two ROSAT observations. A typical error bar is shown in the upper left corner.

An aditional result from the UV data is the possibility to determine the stellar T_{eff} by fitting the observed continuum between $\approx$ 1200 and 3200 Å. Such fitting is very sensitive to the temperature adopted, mainly in the long wavelength band. It also allows the identification of other contributors such as free-free and free-bound emission from hydrogen and the respective temperature. For most T Tauri stars analysed so far the temperature of the plasma producing such emission is well above 10^4 K, in same cases reaching 5 10^4 K (Lago et al. 1984).

In a few cases, to achieve a good fitting it becomes necessary to introduce a third component. For example, in the case of TW Hya, as shown by Fig. 2,

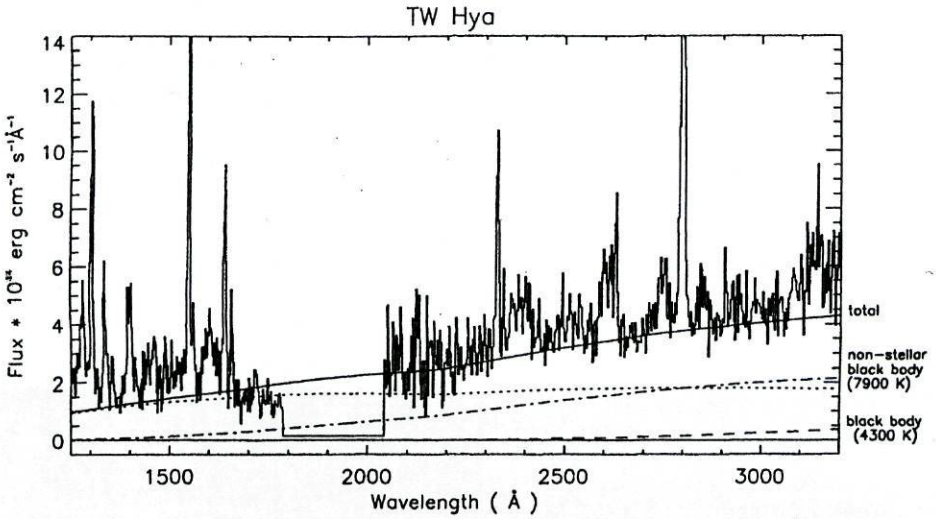

Figure 2. For the star TW Hya the continuum is the sum of hydrogenic free-free plus free-bound emission (dotted line) at 3×10^4 K plus a 4000 K black body emission and a third component - a black body emission at 7900 K covering approximately 5% of the stellar surface. The region around 2000 Å has been supressed due to the very high level of noise.

the third component is well adjusted by blackbody emission at 7 900 K but covering only $\approx$ 5 % of the stellar surface (Costa & Lago 1998).

2. Rotation

Fast rotation was at some point invoked in connection with the youth of T Tauri stars. However the observations have later shown that these stars are slow rotators.

Yet there are still unanswered questions in connection with the rotation in these early phases of evolution. It is therefore important to have a clear view of what the observations show us, namely the perception of their limitations and uncertainties. For that we have performed a global analysis of the whole set of data on rotation for T Tauri stars (185 stars) available in the literature. We have taken special attention in evaluating the uncertainties involved in the alternative observational techniques: photometry or spectroscopy. Due to the large number of papers involved we have chosen to give no references in this section.

Further to that we have also looked at the statistics in terms of period of rotation and $v \sin i$ versus spectral type. For this analysis confirmed binaries were excluded. The sample contains stars from G2 to M4 spectral types. As

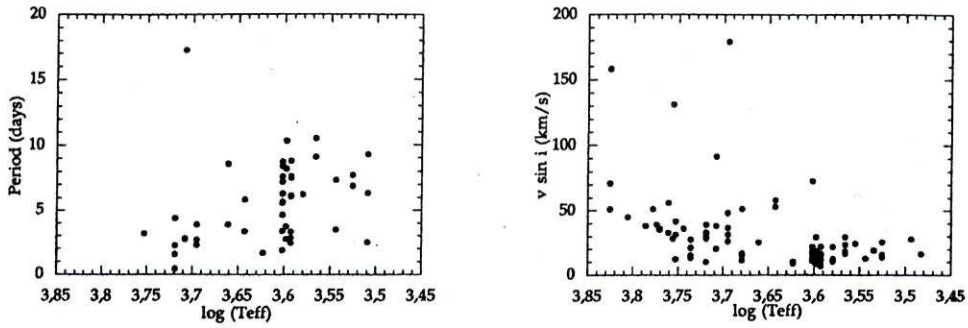

Figure 3. Scatter plots of P_{rot} vs. spectral type (left), and $v \sin i$ vs. spectral type (right).

shown on Fig. 3 there is a clear change of behavior around $\log T_{eff} \approx 3.6$ (corresponding to spectral types K7 - M0). For stars of earlier spectral type the period is ≤ 4 days, with very few exceptions. For later type stars there is a wider range of values for the period between ≈ 2 and 10 days. A similar behaviour is seen in the $v \sin i$ data: stars of $\log T_{eff} \leq 3.6$ display values centered around 20 km s^{-1}, for higher temperature stars the values of $v \sin i$ are systematically higher and seem to vary proportionally to the temperature. Is this an early sign of the well known difference in the rotation rate of main-sequence stars, where stars with a convective envelope rotate much slower than the ones with a radiative envelope?

Another interesting result from this large sample analysis is a clear bimodal distribution in terms of the photometric period, seen in the corresponding histogram. This histogram displays two peaks, one centered around 2 days and another around 8 days. When looking at the histograms relative to the Weak-line T Tauri stars (WTTS) and the Classical T Tauri stars (CTTS), we see that the WTTS show a tendency to rotate faster than the CTTS (see article 'Rotation of T Tauri Stars Revisited' in this volume). However, this is not a clear cut: being a CTTS (WTTS) does not mean that the star will be a slow (fast) rotator.

3. Variability

In T Tauri stars variability is a well established fact. These stars vary in terms of their brightness and of their spectra. Spectral variability affects both the continuum and the lines, the later variations occurring in terms of both the lines intensity and profile.

3.1. THE ULTRAVIOLET

Although limited by the relative scarcity and lack of systematic observations, the variations in the flux of the lines observed with IUE are an important result. This is so because the spectra include lines covering a very wide range of temperatures. In some cases, variations up to 60 % are reported for the strong Mg II lines for observations obtained several months apart. Although no variations were detected on much shorter timescales $\simeq$ 2,5 hours (Penston & Lago 1983). Variations in the flux of higher excitation lines have also been detected, in some cases involving factors as high as 4.

The variations in the continuum, not detectable on scales of one day, are quite remarkable on scales of several months (Lago et al. 1984; Gameiro et al. 1993).

Unfortunately the number of stars for which coherent information is available is very small. However one result is clear: even if variations in the continuum are observed, the variations measured in the lines are real and not just the result of the changes in the continuum.

Of course the limited resolution of IUE does not allow to check whether the variations in the lines were also accompained by any changes in the shape of the profile.

3.2. THE OPTICAL

We selected a sample of 10 T Tauri stars for repeated high resolution observations of Hα, He I and Na I D lines over one week, on time scales ranging from 1 day down to $\approx$ 16 minutes. These lines were selected since they constitute good diagnostic tools for regions of very different temperature. Furthermore, their wavelength proximity allows an almost simultaneous observation. We have analysed the variability of these lines in terms of equivalent width and shape of the profiles.

We will present here the results for one of the stars in the sample, LkHα 264, the closest known T Tauri star (Gameiro et al. 1993, Lago & Gameiro 1998). This star has magnitude $m_V \approx 12.46$ and is located in the Lynds 1457 - 8 dark cloud, at a distance of $\approx$ 65 pc.

Results for other stars in the sample are also presented in another paper (Spectral Variability of T Tauri Stars in the Optical).

3.3. THE Hα LINE PROFILE

LkHα 264 displays a very strong (with equivalent width, $80 \leq W \leq 120\AA$) and broad Hα line (FWHM $\geq$ 300 Km s^{-1}). The line shows a typical III B profile, as do most T Tauri stars (over 33% in the large sample of Reipurth, Pedrosa & Lago, 1996).

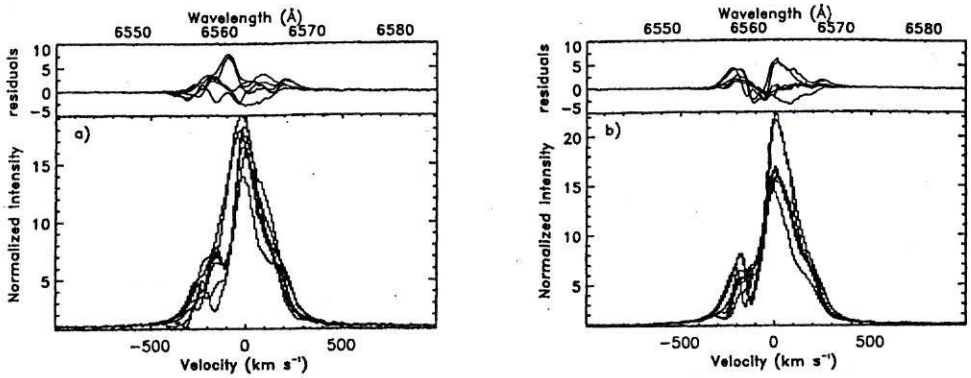

Figure 4. Overlap of the Hα line profiles. The top panel shows the residuals relative to the first profile in the series. a) run of 1990 October, b) run of 1993 November

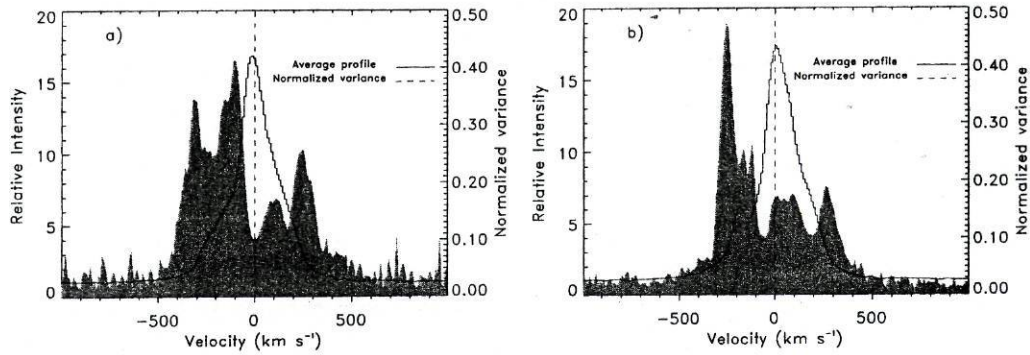

Figure 5. Average profile of Hα and normalized variance. a) Run of 1990 October, b) run of 1993 November.

Fig. 4 shows the variations of the Hα line profile over one week in two different epochs (1990, October 1 to 7 and 1993, November 26 to 30). The lower panels display an overlap of the individual profiles and the upper panels show the residuals relative to the first profile in each set.

The analysis is probably made more clear if we use the normalized variance, as shown in Fig. 5 a) and b). We have also ploted there the average profile for comparison. However, while the data for the first epoch covers only observations $\approx$ 24 h apart, in the second epoch (1993) observations on much shorter time scales are also included.

Fig. 6 shows the normalized variance profiles where we have separated observations on shorter timescales from those 1 day apart. The results show that on longer time scales (1 day) the variations of the Hα line are stronger on the blue side, altough some variability also occurs on the red side. On

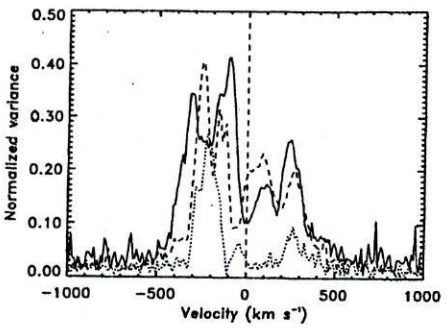

Figure 6. Normalized variance profiles for the Hα observations of 1990 October (solid line), 1993 November (time-scale of 1 d) (dashed line) and the night 1993 November 26 - 27 (dotted line).

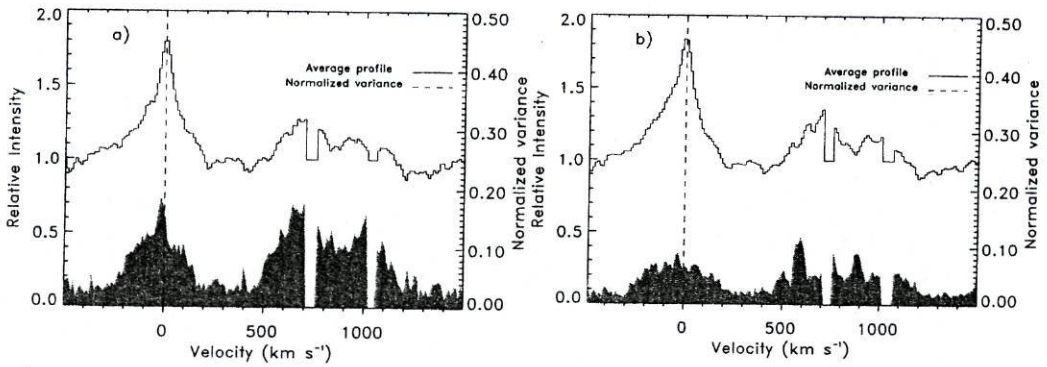

Figure 7. The average and normalized variance profiles of the He I and Na I D lines for (a) 1990 October, (b) 1993 November. The artifact seen on top of the Na I D lines results from the removal of the interstellar components.

short time scales, however, the variations of the Hα line profile are only seen on the blue wing and over a very narrow range of velocities, centered at ≈ -210 Km s^{-1}.

3.4. THE HE I LINE

The He λ 5876 Å line is quite strong ($1.5 \leq W \leq 4.5$ Å) and wide (FWHM$\geq$250 Km s^{-1}). Although the line varies considerably in strength the variations occur over the profile as a whole, the width at the base of the line remains very constant. The variations on short time scales are very small and, once more, take place over the whole profile. The behaviour of the He I line is

therefore different from that of the Hα. Fig. 7 displays the average profile for the He I and Na D lines and the normalized variance profile for both runs after removal of the interstellar bands.

3.5. THE NA I λ 5890, 5896 LINE PROFILES

The Na I D lines are more complex and difficult to study, owing to the narrow interstellar bands which have been removed to avoid difficulties while normalizing to the continuum. During the second run the blue side of the normalized variance shows discrete peaks at velocities where absorption features appear at certain times. These peaks, centered at $\approx +600$ Km s^{-1} and $+900$ Km s^{-1} (≈ -150 Km s^{-1} relative to the interstellar components) coincide with the absorption features seen in Hα at similar velocities.

4. Discussion and conclusions

It is interesting to analyse the behaviour of the various optical lines in terms of their equivalent widths as shown in Fig. 8. Fig. 8 a) deals with time scales of $\approx$1 day. The results show that there is a strong correlation between W_{HeI} and W_{NaI} on both epochs. This implies a common region of origin and a collision dominated regime since the lines differ so much in terms of excitation energy. In previous work we were able to identify this region as being very close to the surface of the star, between 1.1 and 1.2 r_* (Gameiro et al. 1993).

On the first epoch, when the global level of activity in the star as measured by the amplitude of the variations was larger, the Hα seems to behave in a very different way of both the He I and Na I D lines. However, on the second epoch while the global variations are much smaller, the variations in the $W_{H\alpha}$ also correlate well with those of the other two lines.

On shorter time scales the results as shown on Fig. 8 b) are different. There the observations correspond to time scales ranging from less than 20 minutes to hours. The correlation found for $W_{H\alpha}$, W_{HeI} and W_{NaI} seems to hold for time scales of $\approx$ 1 hour. However, the correlation between W_{HeI} and W_{NaI} seems to hold down to time scales of 1 to 2 hours but not for shorter time scales. On these shorter time scales W_{HeI} changes by $\approx$ 10 % yet W_{NaI} remains constant. Even on time scales of 1 to 2 hours the variations of the HeI line appear already systematically larger than those of the NaI lines. Therefore, a consistent picture emerging from the global analysis and our conclusion is that the He I and Na I D emission lines are produced in one (same) narrow region, close to the star, very dense and highly variable. On the contrary, the Hα line has a double origin: part of the emission is produced in a relatively small region, close to the star, not too different from the one producing He I and Na I D lines. This can only be seen

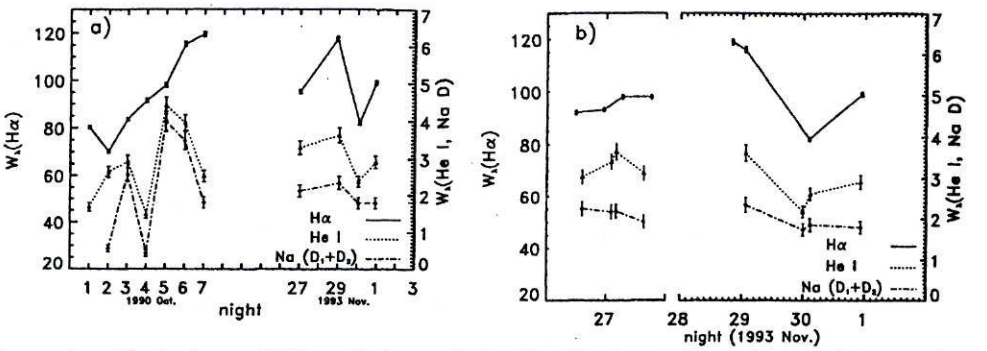

Figure 8. Equivalent width variations of the Hα, He I and Na I (D_1+D_2) lines; **a)** during 1990 October and 1993 November, on time scales of the order of 1 d; **b)** during 1993 November on time-scales shorter than 1 d, ranging from less than 20 min to several hours.

when the global level of activity is low. The atmosphere is then transparent allowing to sample the local behaviour with time. The remaining of the emission in Hα is produced in a more extended region, therefore insensitive to whatever causes the variations in the level of emission of the He I and Na I D lines. This component dominates when the general level of activity of the star is higher and the lower transparency of the upper regions "covers up" the contribution from the inner region.

This is in fact not so different from the results obtained by speckle interferometry for T Tau.

We are pursuing this type of analysis for the remaining stars in the sample. The coherent analysis of such large sample will certainly allow us to clarify several questions still not answered for T Tauri stars:

- the location and characterization of the structure and dynamics of the various temperature regions in the outer layers of TTS,
- through the use of time series analysis to constrain the presence of flows, in terms of direction, structure, dimension, energy and momentum transfer to the circumstellar environment.

The aim is to apply those answers and take advantage of physically sound models of line/continuum formation and transfer of radiation in order to build a comprehensive picture of this early phase of stellar evolution.

References

Costa V.M., Lago M.T.V.T., 1998, Proceedings of the Conference Ultraviolet Astrophysics Beyond the IUE Final Archive, Sevilla, Spain ESA SP-413, 113
Costa V.M., Lago M.T.V.T., Norci L., Meurs E.J.A., 1999, To be submitted
Gameiro J.F., Lago M.T.V.T., Lima N.M., Cameron A.C., 1993, MNRAS, 261, 11

Lago M.T.V.T., Gameiro J.F. , 1998, MNRAS, 294, 272
Lago, M.T.V.T., Penston, M.V., Johnstone, R. (1984), in *Proceedings of Fourth European IUE Conference, Rome, Italy*, p. 233
Penston, M.V., Lago, M.T.V.T., 1983, MNRAS, 202, 77
Reipurth, B., Pedrosa, A., Lago, M.T.V.T. 1996, A&AS, 120, 229